Understanding reaction mechanisms of electrochemical metallization processes used for silicon photovoltaic cells.

Cécile Molto

université PARIS-SACLAY

Understanding reaction mechanisms of electrochemical metallization processes used for silicon photovoltaic cells

Thèse de doctorat de l'université Paris-Saclay

École doctorale n° 573 Interfaces : matériaux, systèmes, usages
Spécialité du doctorat : Chimie
Unité de recherche : Université Paris-Saclay, UVSQ, CNRS, Institut Lavoisier de Versailles, 78000, Versailles, France
Référent : Université de Versailles-Saint-Quentin-en-Yvelines

Thèse présentée et soutenue à Palaiseau, le 04/06/2020, par

Cécile MOLTO

Composition du Jury

Daniel LINCOT Professeur, CNRS	Président du jury
Danièle BLANC-PELISSIER Chargée de recherche, INL	Rapportrice
Pere ROCA i CABARROCAS Professeur, Ecole Polytechnique	Rapporteur
Laure FILLAUD Maître de conférences, UPMC	Examinatrice
Loïc TOUS Chercheur, IMEC	Examinateur
Anne-Marie GONCALVES Maître de conférences, UVSQ, ILV	Directrice de thèse
Pierre-Philippe GRAND Ingénieur-Chercheur, EDF	Co-Encadrant

Thèse de doctorat

NNT : 2020UPASV016

À ma maman,

Acknowledgments

La rédaction des remerciements est un moment attendu de chaque doctorant car il symbolise la fin de ce parcours éprouvant de thèse. En ce qui me concerne, cette thèse a été particulièrement difficile car, entre autres, mes expériences ont été retardées par un déménagement de laboratoire et la pandémie de Covid-19 a compliqué la procédure de soutenance. Aujourd'hui je suis fière d'avoir persévéré et d'être arrivée jusqu'au bout mais cela n'aurait pas été possible sans les personnes que je m'apprête à remercier.

Tout d'abord, je remercie les entités qui m'ont accueilli et m'ont permis de réaliser mes travaux de thèse dans leurs locaux à savoir, L'Institut Lavoisier de Versailles (ILV), EDF et l'Institut Photovoltaïque d'Ile de France (IPVF). Je remerie EDF pour le financement de cette thèse et notamment Stéphanie MULLER (chef du département EFESE) et Cédric GUERARD (Chef du groupe R17), qui ont veillé à ce que je travaille dans les meilleures conditions possibles.

J'adresse également mes remerciements aux membres de mon jury de thèse qui ont accepté d'évaluer mon travail et se sont prêtés de manière inédite à l'exercice de la soutenance de thèse en visioconférence partielle. Merci donc à mes rapporteurs Pere ROCA i CABARROCAS (Ecole Polytechnique) et Danièle BLANC PELISSIER (INL) ainsi qu'à mes examinateurs Daniel LINCOT (CNRS), Laure FILLAUD (UPMC) et Loïc TOUS (Imec) pour leurs commentaires constructifs et leurs félicitations.

Je remercie tout particulièrement Pierre-Philippe GRAND (encadrant, EDF) et Anne-Marie Gonçalves (directrice de thèse, ILV) qui m'ont suivi avec bienveillance tout au long de ce parcours et se sont beaucoup investis dans ma thèse. Cela n'a pas été facile tous les jours mais nous avons constitué un trio efficace pour s'adapter aux imprévus et anticiper certains problèmes. Anne-Marie, je te remercie notamment pour le temps que tu m'as consacré jusque tard le soir à l'ILV pour parler des interfaces semiconducteur/electrolyte et pour ta relecture attentive de mon manuscrit. Pierre-Philippe, je te suis très reconnaissante de m'avoir rassurée et soutenue moralement quand il le fallait. Tu m'as laissé l'autonomie dont j'avais besoin pour cette thèse tout en te rendant disponible lorsque c'était nécessaire ce qui m'a motivé à donner le meilleur de moi-même.

Je remercie Jan NEKARDA, Varun ARYA et Benjamin GRUEBEL (Fraunhofer ISE) ainsi que Arnaud DEVOS (Menapic) pour leur apport scientifique dans le cadre de nos collaborations.

Je souhaite ensuite remercier les personnes de l'ILV et notamment Arnaud ETCHEBERRY, Solène BECHU, Muriel BOUTEMMY et Davina MESSOU qui ont réalisé les mesures XPS et Auger et ont partagé toute leur expertise dans ce domaine. Merci particulièrement à Solène et Muriel qui se sont également impliquées

dans la rédaction de mon premier article et la correction de mon manuscrit avec une précision remarquable. Je n'oublie pas Damien, Yohan, Nathalie, Mathieu, Jean-Claude et Cendra avec qui j'ai pu échanger sur différents sujets et passer de bons moments.

A l'IPVF, vous avez été nombreux à m'épauler et parfois me supporter aussi. Un grand merci à Sophie GAILLARD et Valérie DANIAU qui ont remué ciel et terre pour que le laboratoire re-fonctionne correctement au plus vite. Vous êtes toutes les deux d'une gentillesse extrême et d'une aide précieuse, pour les doctorants en particulier. Merci à Thibault HILDEBRANDT, Aurélien DUCHATELET, Jean ROUSSET, Daniel ORY qui m'ont m'aidé dans mes expériences, dans l'analyse de mes résultats ou encore la correction de mes rapports et présentations. Merci à Etienne DRAHI qui a supervisé le projet A dans lequel m'a thèse s'est inscrite. Une dédicace particulière à Karolien SALIOU, qui a travaillé sur la métallisation électrochimique avec moi durant quelques mois à la fin de ma thèse. Ton implication dans mon projet de thèse m'a permis de trouver l'énergie et la motivation nécéssaires pour affronter les "nombreux" problèmes rencontrés en fin de thèse. L'équipement Laser nous a joué des tours à plusieurs reprises mais heureusement Salim MEJOUARI nous a apporté son aide sur ce problème.

Merci aux grimpeurs aguéris Olivier FOURNIER, Anatole DESTHIEUX, Valentin ACHARD et Marta CHROSTOWSKI. Ces moments à Arkose avec vous ont été plus que bénéfiques pour évacuer les tensions. Une mention spéciale pour Marta qui a rédigé sa thèse en même temps que moi. Tu étais la mieux placée pour comprendre mon stress durant cette phase de rédaction et nous nous sommes mutuellement soutenues.

Merci aussi à Jorge, Samuel, Sébastien, Marie et Fréderique avec qui j'ai pu rire et discuter, durant la pause déjeuner ou autour d'un verre. Je ne doute pas que vous trouverez meilleure partenaire que moi pour les parties de babyfoot mais promis je vais essayer de progresser.

Parce que nous étions tous dans le même bateau et que vous m'avez soutenue durant ces trois et plus années, je remercie les doctorants EDF: Sophie, Emilie, Margaux, Arpit, Adrien, Fabien, Harold ainsi que Salim, Anatole, Valentin et Oliver déjà cités. Je vous souhaite à tous bon courage, surtout pour ceux n'ayant pas terminé leur thèse. Je tiens à remercier tout particulièrement Oliver, Anatole et Harold qui ont partagé mon bureau à l'IPVF et qui parfois ont du supporter mes râleries. J'ai toujours apprécié nos échanges que ce soit pour des conversations sérieuses sur le photovoltaique ou sur divers sujets parfois un peu farfelus. Merci à mes autres co-bureau: Katherine pour sa gentillesse et ses petits chocolats, Dhanushika et Jung Eun pour les pauses cafés détentes et Romaric qui m'a aidé à rédiger ma thèse avec LaTeX.

Je vais passer maintenant aux remerciements plus personnels pour mes amis Cynthia, Canelle, Blandine, Laurène. Vous m'avez apporté votre soutien chacune à votre manière et les moments passés avec vous ont été des parenthèses nécessaires pour me changer les idées. Merci également à Florent avec qui j'ai partagé presque 10 ans de ma vie et bien que nos chemins se soient séparés je te suis reconnnaissance d'avoir été présent pour moi en toutes circonstances.

Le plus important des remerciements revient bien évidemment à ma famille. La fierté dans vos yeux représente un immense bonheur pour moi et m'a donné la force d'arriver jusque là. Merci à mon grand-père, mon plus grand fan car c'est à lui que je dois ma curiosité sans limites. Tu sais que j'aurais voulu que

mamie puisse se rendre compte de ce que la petite fille dont elle a tant pris soin a accompli. Merci à mes parents qui ont fait de moi ce que je suis aujourd'hui, m'ont permis de réaliser de longues études et m'ont toujours comblé de leur amour sans failles. Papa, les goûts musicaux que tu m'a transmis m'ont suivi tout au long de mon parcours et je dois dire que la musique à eu une place particulièrement importante ces trois dernières années. Maman, je te remercie infiniment de me soutenir quelques soient mes choix. Sache que le courage et la persévérance qui m'ont permis d'en arriver là, je les tiens de toi.

List of acronyms

Acronyms	Description	Acronyms	Description
c-Si	Crystalline Silicon	RTA	Rapid Thermal Annealing
Mono-Si	Mono-crystalline Silicon	LIPSS	LASER-Induced Periodic Surface Structures
mc	Multi-crystalline	PLA	Post-Laser Annealing
Poly-Si	Polycrystalline Silicon	HAZ	Heat Affected Zone
a-Si	Amorphous Silicon	PL QSS-PC	PhotoLuminescence calibrated with Quasi-Steady-State Photoconductance
VB	Valence Band	XPS	X-ray Photoelectron Spectroscopy
CB	Conduction Band	SAM	Scanning Auger Electron Microscopy
SCR	Space Charge Region	APiC	Acoustics Picosecond Colored
STC	Standard Testing Conditions	CLSM	Confocal Laser Scanning Microscopy
SQ	Shockley–Queisser	SEM	Scanning Electron Microscopy
AM	Air Mass	EDS	Energy Dispersive Spectroscopy
Al-BSF	Aluminum Back Surface Field	TLM	Transmission Line Measurement
PERC	Passivated Emitter Rear Cell	OCP	Open Cicruit Potential
PERL	Passivated Emitter Rear Locally diffused	SHE	Standard Hydrogen Electrode
PERT	Passivated Emitter Rear Totally diffused		
HJT	HeteroJunction Technology		
IBC	Interdigitated Back-Contacted cell		
ARC	Anti-Reflection Coating		
SP	Screen-Printing		
PP	Parasitic Plating		
PSG	Phosphosilicate Glass		
BSG	Borosilicate Glass		
PECVD	Plasma-Enhanced Chemical Vapor Deposition		
ALD	Atomic Layer Deposition		
SWCT	Smart-Wire Connection Technology		
LIP	Light-Induced Plating		
FBP	Forward Biais Plating		

List of symbols

Symbols	Description	Units	Symbols	Description	Units
σ	Conductivity	S.m^{-1}	$N_{D,A}$	Semiconductor doping level (acceptors or donors)	at.cm^{-3}
E_{ph}	Photon energy	eV	ρ_c	Contact resistivity	Ω.cm^2
E_G	Bandgap energy	eV	R_m	Metal resistance	Ω
E_C	Energy level of conduction band	eV	R_{sc}	Semiconductor resistance	Ω
E_V	Energy level of valence band	eV	ρ_{sc}	Semiconductor resistivity	Ω.cm
$\overrightarrow{E}$	Electric field	V.m^{-1}	L_T	Transfer length	m
J_{ph}	Photo-generated current density	A.cm^{-2}	J'_0	AM 1.5 spectra irradiance	W.m^{-2}.nm^{-1}
Δ V	Potential difference	V	R	Reflectivity	%
V_{OC}	Open-circuit voltage	V	R_{eff}	Effective reflectivity	%
J_0	Diode saturation current density	A.cm^{-2}	ρ_m	metal density	g.cm^{-3}
T	Temperature	K	E^0	Standard redox potential	V
R_s	Series resistance	Ω	E_F	Fermi level energy	eV
R_{sh}	Shunt resistance	Ω	E_{redox}	Redox potential	V
R_{sheet}	sheet resistance	Ω/sq	$E_{F,redox}$	Redox Fermi level	eV
n′	Diode ideally factor	no unit	$\mathcal{E}_C$	Anchoring level of CB	eV
A	Area	cm^2	$\mathcal{E}_V$	Anchoring level of VB	eV
J_{SC}	Short-circuit current density	A.cm^{-2}	ϕ_{el}	Electrolyte work function	eV
FF	Fill Factor	%	λ_S	Reorganization energy	eV
pFF	Pseudo Fill Factor	%	V_{fb}	Flatband potential	eV
η	Power conversion efficiency	%	C_{SC}	Capacity in the SCR	F
$\eta_{h,max}$	Maximum harvesting efficiency	%	C_H	Capacity in Helmholtz layer	F
$\eta_{STC,max}$	Maximum efficiency in STC	%	C_{OX}	Capacity in the oxide layer	F
n	Refractive index	no unit	Q	Charge	C
λ	Wavelength	nm	Q_H	Charge in Helmholtz layer	C
V_{SC}	Potential drop in semiconductor	eV	J_i	Flux of species i	mol.cm^{-2}.s^{-1}
W	SCR thickness	m	D_i	Diffusion coefficient	cm^2.sec^{-1}
ϕ_B	Schottky barrier	eV	D_{th}	Thermal diffusivity	m^2.s^{-1}
ϕ_S	Semiconductor work function	eV	v(x)	Velocity of species along x-axis	cm.sec^{-1}
ϕ_M	Metal work function	eV	β	Current efficiency	%
χ_S	Semiconductor affinity	eV			

z	number of electrons involved	no unit
I	Current	A
α	Absorption coefficient	m^{-1}
m	mass	g
d	density	$g.L^{-1}$
C_i	Concentration of species i	$mol.L^{-1}$
I_d	Thermal penetration depth	m
F_{peak}	Laser peak fluence	$J.cm^{-1}$
f	Frequency	Hz
ω	Pulsation	$rad.s^{-1}$
ϵ	relative permittivity	no unit
α'	Optical absorption coefficient	no unit
E_{BE}	Electron binding energy	eV
E_{KE}	Electron kinetic energy	eV
α_T	charge transfer coefficient	no unit

List of constants

Constant	Description	Value
q	Electron elementary charge	$1.605.10^{-19}$ C
k_B	Boltzmann's constant	$1.380.10^{-23}$ J.K^{-1} or $8.617.10^{-5}$ eV.K^{-1}
R	Universal gas constant	8.314 J.mol^{-1}.K^{-1}
F	Faraday's constant	96485 C.mol^{-1}
h	Planck's constant	$6.63.10^{-34}$ J.s
c	Light celerity	3.10^{8} m.s^{-1}
ϵ_0	Vacuum permittivity	$8.85.10^{-12}$ F.m^{-1}
N_C	Effective density of states in silicon conduction band	$2.8.10^{19}$ at.cm^{-3}
N_V	Effective density of states in silicon valence band	$1.9.10^{19}$ at.cm^{-3}

Table of contents

General introduction

On June 23 1988, the influence of human activities on climate change has been mentioned publicly for the first time by James E. Hansen. In front of the members of the United States Senate, the NASA climatologist warned the authorities that abnormally high temperatures are not the natural variability of climate, but human greenhouse gases emissions into the atmosphere which are heating up the Earth's atmosphere [1]. Although public awareness has been slow, it is now undeniable that climate change is happening and is threat to human societies and natural ecosystems. This is reflected by the loss of biodiversity, the disappearance of certain species, the melting of polar ice or the spread of natural disasters.

To address global warming and climate change, societies must fundamentally change their patterns of energy use in order to reduce greenhouse gas emissions. The greenhouse gases emitted by human activities are carbon dioxide (CO_2), methane, nitrous oxide and fluorinated hydrocarbons. The amount of CO_2 emitted, mainly due to consumption of fossil fuels, significantly exceeds the emission of other greenhouse gases with more than 36 billions tonnes of CO_2 equivalents emitted per year [2]. It is therefore crucial to reduce CO_2 emissions over the coming years. In this context, the Paris agreement came into force on November 16^{th}, 2016 with the aim to limit global warming to a rise of average temperatures at $2°\mathrm{C}$ maximum [3]. To meet this target, a recent study suggests that a third of oil reserves, half of gas reserves and over 80% of current coal reserves should remain unused from 2010 to 2050 [4]. However, fossils fuels are currently overused and are running out quickly, as shown in Table 1 established from Knoema data platform [5]. In addition, the world population constantly grows and the global energy demand continues to increase (+ 2.3% in 2018) [6]. The remaining extraction times calculated in Table 1 might be therefore even lower. As a result, there is no doubt that the development of renewable energy technologies is essential to meet future energy demand and limit global warming.

Table 1: Estimation of remaining extraction time of fossil fuel ressources [5].

	Coal (billions tones)	**Natural gas (billions of m^3)**	**Crude oil (billions of barrels)**
World proven reserves in 2018	1054.78	196850	1729.74
Annual world consumption in 2018	8.01	3848.86	35.44
Remaining extraction time (years)[1]	**131.64**	**51.14**	**48.8**

Since the 1970s, the total energy consumption in the world largely comes from fossil fuel burning and still accounted for 79.7% in 2017 as described in Figure 1. Fortunately, public awareness has risen over the last years and renewable energies development is growing up wit more and more renewable power

[1] considering that the consumption remains the same over the next years

generating capacity installed. In particular, the generation of electricity by renewable energies is of great interest, especially with the development of electrical vehicles having the potential to significantly reduce CO_2 emissions.

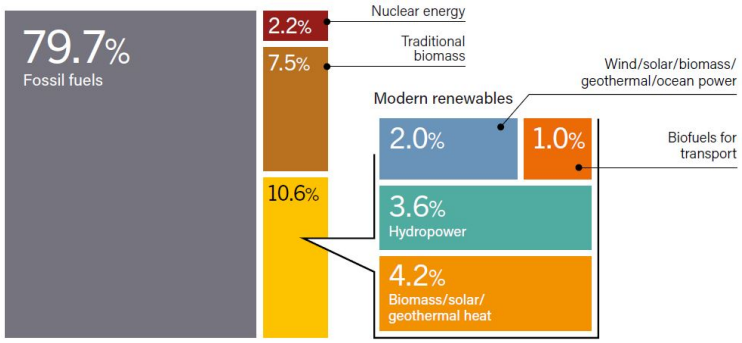

Figure 1: Renewable and non renewable share of the world total energy consumption in 2017 [6].

In 2018, renewable power generating capacity saw its largest annual increase ever with an estimated 181 GW installed worldwide according to the last REN21 report (see Figure 2 a)) [6]. By the end of the year, the overall global renewable power generating capacity reached 2,378 GW, which represents over 33% of the global power generating capacity as shown in Figure 2 b) [6].

a)

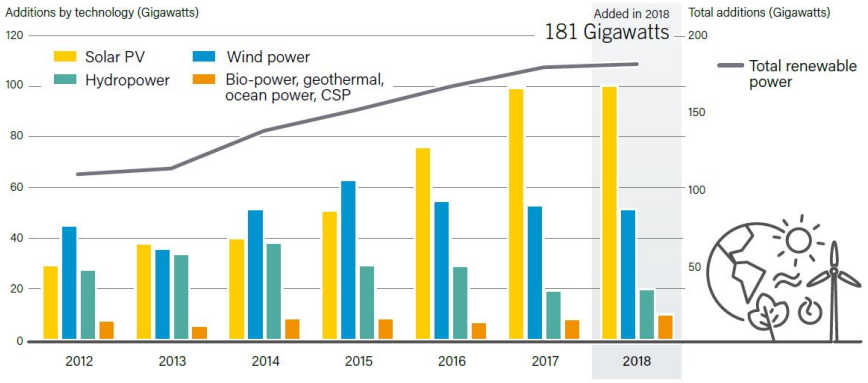

b)

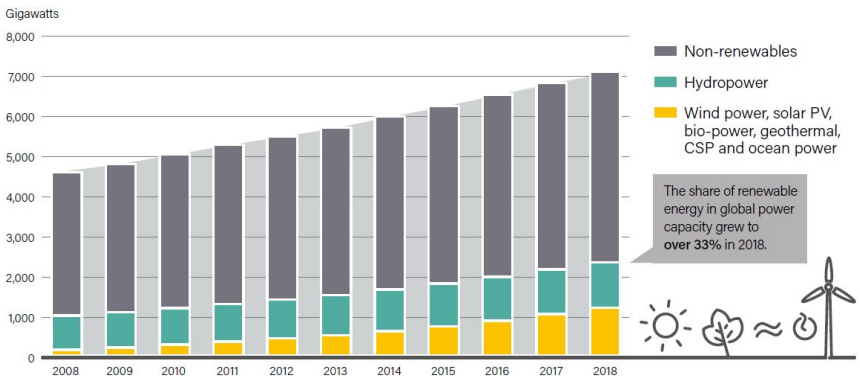

Figure 2: a) Annual additions of renewable power capacity from 2012 to 2018, b) Global power generating capacity from 2008 to 2018 [6].

This evolution is driven by the constant reduction of electricity cost from renewable technologies. According to the International Renewable Energy Agency (IRENA), the electricity cost for all commercial re-

newable power generation technologies is within the range of fossil fuel power generation cost, that is 0.049 - 0.174 USD/kWh, and is expected to decrease year by year [7]. Meanwhile, promising progress on battery development will enable to store more efficiently the electricity from renewable energies [8].

With 505 GW installed in the world in 2018, solar photovoltaic (PV) energy has demonstrated the highest increase over the last years compared to other renewable energies (see Figure 3) [6]. Most of the current PV technologies produce electricity within the range of fossil fuel power generation cost and it is expected that over four-fifths of solar PV capacity installed in 2020 produce cheaper electricity than any fossil fuel option [7]. Solar PV will thus be a significant contributor to satisfy electricity demands over the next years.

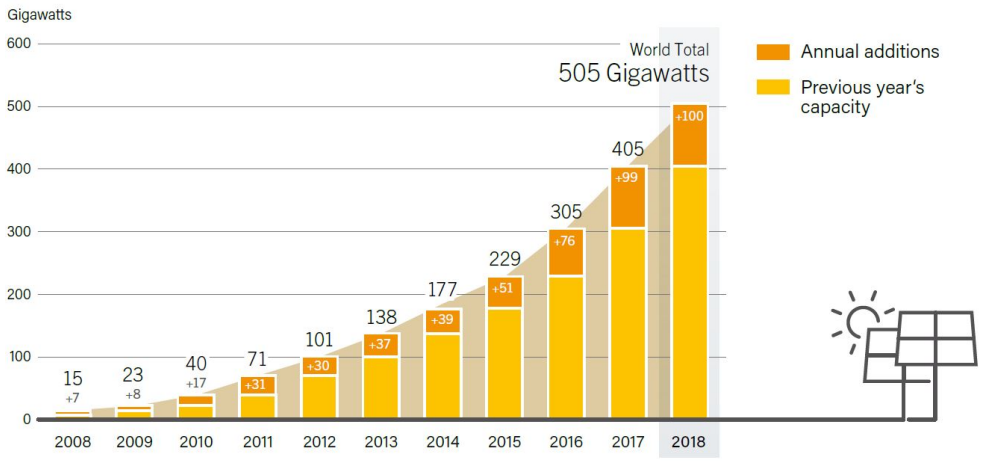

Figure 3: Solar PV global world capacity and annual additions from 2008 to 2018 [6].

Finally, thanks to cheaper production costs and development of batteries, renewable energies are expected to account for 62% of total generated electricity by 2050. Solar energy is expected to show the most significant growth, rising from 2% of today's world electricity generation, to 22% in 2050 as represented in Figure 4 [9]. Renewable energies are intermittent and still show lower conversion efficiency than fossil fuels or nuclear energy. On this basis, researchers and manufacturers aim to develop storage systems and make renewable energies more and more efficient with lower costs.

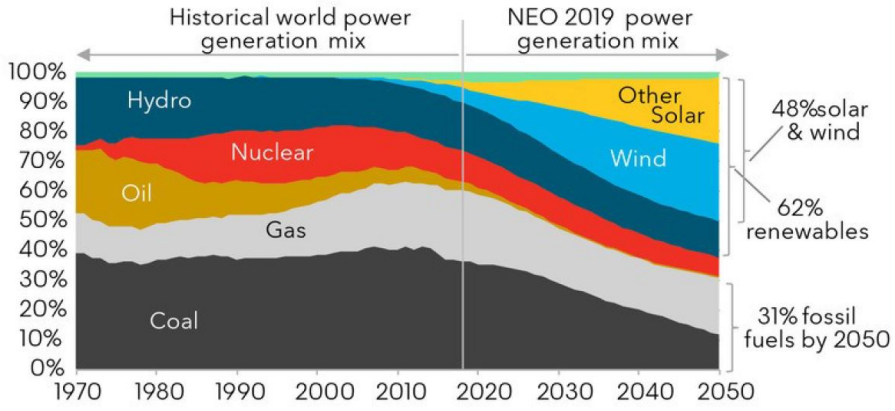

Figure 4: Electricity power generation mix from 1970 to today and predicted trend within 2050 [9].

The different solar cell technologies can be classified into three categories as represented in Figure 5. Hybrid solar cells can also be obtained by assembling two or more solar cell technologies to form multi-junctions devices having an high efficiency potential.

1. Crystalline silicon solar cells (c-Si): This technology is based on silicon (mono-crystalline (mono-Si) or multi-crystalline (mc)) as the semiconductor converting light into electricity. c-Si solar cells have been the first developed, in particular because Si is the second most abundant element on Earth after oxygen, but also because it demonstrates great efficiencies in industry with robust manufacturing process. c-Si based PV technology largely dominates the market with around 95% of the total production in 2018 [10].
2. Thin film solar cells: Thin film solar cells are obtained by successive depositions of thin layers of semi-conducting materials to form the PV device. Main advantages are that thin films use less materials and can be deposited on flexible substrates, allowing new applications with relatively low production costs. The main issue is that good conversion efficiencies (around 20%) obtained at laboratory scale (small surface) drastically fall down when the cell area is increased (industry scale). As a result, the market for thin films PV continues to grow but only accounts for 5% [10].
3. Emerging solar cells: This category regroups several PV technologies mainly developed at laboratory scale: Organic cells, Dye-sensitized cells, quantum dots and perovskites. These technologies have the main advantage to be low cost but demonstrate low efficiencies. However, fast improvements of perovskites device efficiency (hybrids organic-inorganic material) have been observed over the last years, making this technology promising. The main disadvantage of perovskites cells is the stability issue [11].

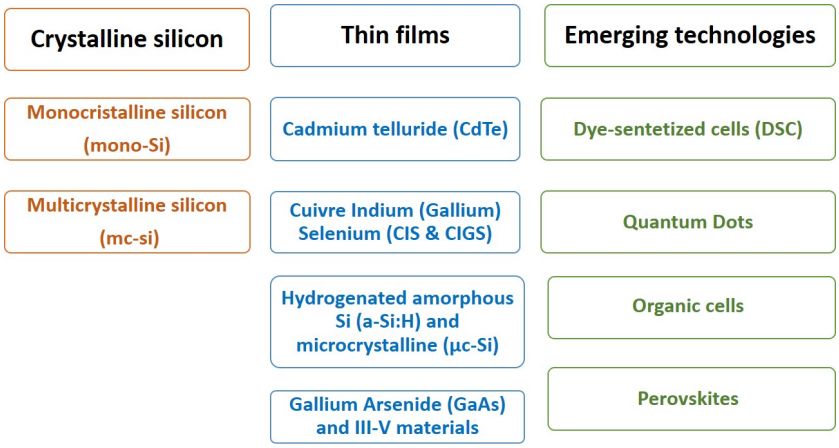

Figure 5: Classification of different solar cell technologies.

As the most mature solar technology, c-Si solar cells are of particular interest with researchers constantly working to improve efficiency and reducing the production costs. From c-Si feedstock to PV module, significant improvements can be realized. For instance, the metallization step has the potential to improve cell efficiencies by increasing the quality of metallic contacts (higher conductivity, lower contact resistance, reduced shadowing effect etc.). Moreover, silver (Ag) and aluminum (Al) based pastes are currently used

for the metallization of c-Si cell technologies and represent the most expensive non-silicon materials used [10]. Significant cost reductions are thus possible by lowering paste consumption and/or modifying their composition. Nowadays, screen printing (SP) is the mainstream metallization technology to produce industrial c-Si solar cells, as represented in Figure 6. This method has the advantages to be simple, fast and well implemented in industry. However, it relies on silver containing pastes, an expensive metal (19.31 USD/once in September 2019 [12]) with a fluctuating cost, and has almost reached its limitations in terms of metallic contact quality. The development of SP derivatives and new techniques, such as electrochemical metallization (also called "plating"), is essential to go even further in the improvement of c-Si solar cells.

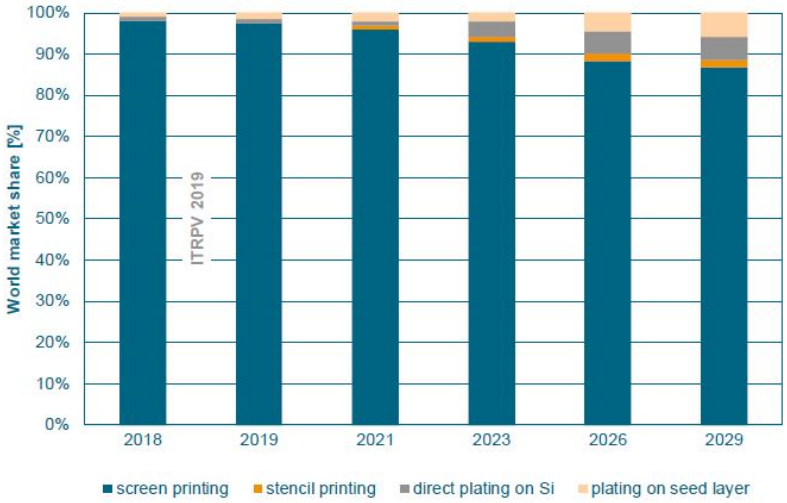

Figure 6: Market share of front side metallization technologies and estimation until 2029 [10].

In this way, plating is a good alternative to standard SP metallization and is under investigation by recognized research institutes such as Fraunhofer ISE (Institute for Solar Energy) and Imec (Institut de MicroElectronique et Composants). First, plating gives a solution to metal cost reduction by using cheaper metals, such as nickel (Ni) and copper (Cu) (0.53 USD/once and 0.15 USD/once respectively in September 2019 [12]). While nickel is used as seed layer, copper represents the conductive part of the metallic contact with an electrical conductivity very close to the one of silver (σ_{Cu} = 5.96 x 10^7 S/m; σ_{Ag} = 6.30 x 10^7 S/m). Provided that processing and depreciation costs are similar to SP process, cost savings can be realized with Ni/Cu plating [13]. Secondly, SP relies on high temperature process steps (800-900°C) which are not suitable for some Si solar cells architectures (heterojunction cell for example) and induces a non negligible thermal budget. Ni/Cu plating is more suitable as temperatures needed do not exceed 350°C. Finally, plating has the potential to overcome SP limitations and achieve higher metallic contact quality. Absolute efficiency gains of 0.5% have already been demonstrated in literature in comparison with SP [14]. For all these reasons, plating is expected to gain progressively market share and account for $\approx$ 10% in 2029 according to the International Technology Roadmap for PhotoVoltaics (ITRPV) (Figure 6). Despite its great potential, plating is in an introductory phase because several issues need to be addressed before implementation in mass production such as risks of junction shunting, poor adherence or parasitic plating (PP). Improvements in terms of reliability and process scalability are also necessary.

The aim of this thesis is to investigate the Ni/Cu plating process steps to 1) identify the factors affecting the solar cell 2) understand the physico-chemical phenomenon involved and 3) develop an optimized Ni/Cu plating process to achieve similar cell efficiency than reference SP cells. The first steps needed to prepare the Si surface before Ni/Cu plating are of great importance and receive particular emphasis in this study as well. This work is organized in five chapters, each including a summary of the main conclusions.

The first two chapters give background knowledge.

Chapter 1 is dedicated to the scientific background on c-Si solar cells. The working principle is explained and the different factors limiting efficiency are detailed. The process flow for a standard industrial c-Si solar cell is also introduced and current advancements to achieve high efficient c-Si solar cells are reviewed. Finally, key elements to reduce production costs are discussed.

Chapter 2 is focused on metallization techniques for c-Si solar cells. The standard screen-printing process as well as corresponding drawbacks and limitations are presented. The possibility to increase c-Si solar cell efficiency while reducing production cost by improving the metallization step is highlighted. In that way, existing SP derivatives and alternative electrochemical metallization (plating) are described. The background on semiconductor/metal and semiconductor/electrolyte interfaces is presented and finally the methodology of this thesis work is introduced.

The following chapters concern the experimental results. Two chapters are dedicated to Si surface preparation before plating and the last chapter deals with Ni/Cu deposition and the development of a whole plating process with optimized conditions.

In **Chapter 3**, the impact of selective laser ablation of dielectric layers before plating is investigated. Various laser parameters are tested and their impact on Si surface morphology, composition and electrical properties is characterized. A laser ablation mechanism is proposed and optimized laser parameters are selected.

Chapter 4 concerns the next plating process steps which are silicon surface deoxidation and activation. Etching of silicon oxides in two fluoride media are studied. Meanwhile, the impact of these fluoride media on dielectric layers is also investigated for potentially improved selectivity. Silicon surface activation through palladium deposition is then extensively studied to understand nucleation and growth mechanisms and improve the activation bath composition.

In **Chapter 5**, Ni electroless deposition is studied and factors affecting the homogeneity and adherence are highlighted. In collaboration with the Fraunhofer ISE, the adherence of three different Ni electroless deposition processes is compared using the Acoustics Picosecond Colored (APiC) method. To complete the plating process, Cu is deposited electrolytically. Subsequently, cells are annealed to investigate the impact of non optimized laser parameters and annealing temperature on cell efficiency. Finally, the optimized processing conditions studied in this work are implemented to achieve cell efficiencies comparable to SP references.

Finally, the main conclusions of this thesis are summarized, while future work and perspectives are detailed in a brief outlook.

Chapter 1

Background on crystalline silicon solar cells

CONTENTS

1.1 Introduction

This chapter introduces the main knowledge on crystalline silicon solar cells needed to fully understand the approach and the results of this thesis work. The working principle of a c-Si solar cell is detailed and limiting-efficiency factors are reported. A standard process flow is presented, areas of improvement in terms of conversion efficiency are reviewed and some elements to lower the production costs are given. In this way, main materials and cell architectures under investigation in the PV field are presented. That brings to understand the material choice for this work and the concern about c-Si metallization step.

1.2 Structure and working principle

The working principle of a c-Si solar cell is based on the photovoltaic effect, discovered in 1839 by Edmond Becquerel. The photovoltaic effect is responsible for the creation of voltage in a material in response to an electromagnetic radiation. In this manner, a c-Si solar cell converts light energy into electricity by means of three mechanisms [15]:

1. Photons absorption in the silicon material and generation of charges carriers.

A photon is absorbed when its energy is superior to the Si bandgap energy (E_G (Si) = 1.12 eV at ambient temperature). That promotes the excitation of an electron in the Si material from an initial state (E_i) in the valence band (VB) to a final state (E_f) in the conduction band (CB) as illustrated in Figure 1.1. A positively charged particle is created in the VB and is called a hole.

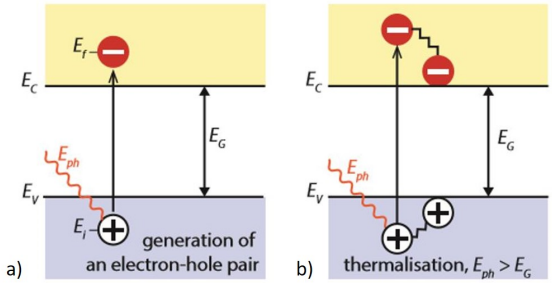

Figure 1.1: a) Photon absorption and generation of an electron-hole pair ($E_{ph} \geq E_G$), b) when $E_{ph} > E_G$, a part of the energy is thermalized [15].

In a real semiconductor, the valence and conduction bands are not flat but vary depending on the electron momentum (k-vector) as described in Figure 1.2. The maximum of the VB and the minimum of the CB occur at the same momentum in case of a direct gap semiconductor but not for an indirect one. In indirect gap semiconductors, such as silicon, electron excitation necessitates a change of electron momentum and so the absorption coefficient is much lower than the one of a direct semiconductor. Silicon based absorber must be consequently relatively thick and the optimal c-Si thickness has been calculated to be about 100 µm [16]. However, c-Si thickness is in the range of 150-200 µm in industry to limit mechanical issues and bowing effect [17].

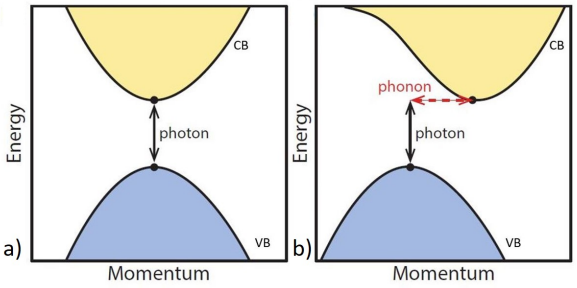

Figure 1.2: Electron excitation in a) direct gap semiconductor, b) indirect gap semiconductor [15].

2. Subsequent separation of the photo-generated charges carriers.

Usually, the photo-generated electrons fall back to their initial energy level E_i and the energy is released either as a photon (radiative recombination) or transferred to other electrons or holes or to the lattice (non radiative recombination). A p-n junction is thus needed to promote photogenerated charges separation on the both side of the cell and their collection by metallic contacts. The formation of a p-n junction is illustrated in Figure 1.3 a). A n-doped area is formed by introducing phosphorous (P) atoms into the silicon wafer. As phosphorous is a 5-valence dopant, the four outer electrons combine with each electron of Si atom, while the fifth electron is free to move and serves as charge carrier. Due to the higher number of free electrons, those are also named as majority charges carriers, while free mobile holes are named as the minority charges carriers. The p-doped area is formed by introducing boron (B) atoms into the silicon wafer. As boron is a 3-valence dopant, that results in an higher number of free holes (majority carriers). When a n-type and a p-type Si are in contact, the following phenomenon happens at the interface: the majority carriers respectively diffuse towards the p and n areas. On the n-side, near to the interface, free electrons in the CB are gone because they have diffused to p-type area and also due to recombinations with diffused holes from the p-side. On the p-side, free holes in the VB are also gone by a similar process. This leads to the apparition of the so called Space Charge Region (SCR), where only the fixed impurity atoms and the neutral Si atoms remain. This area is also called "depletion region" in reference to the depletion of majority charges carriers. The charges of fixed ions create an electric field $\overrightarrow{E}$ in the SCR and a potential difference ΔV blocking the diffusion of charges carriers (see Figure 1.3 b)).

Under light, photogenerated charges are created which leads to the Fermi level splitting into a Fermi level of electrons (E_{Fn}) and a Fermi level of holes (E_{Fp}). The photo-generated minority charges carriers reach the SCR thanks to $\overrightarrow{E}$ and diffuse towards the p area for photo-generated holes and n area for photo-generated electrons (see Figure 1.3 c)). The increase of holes concentration on p side and electrons on n side results in an electric field opposited to the one of the junction and a photo-generated current density (J_{ph}). ΔV remains unchanged in short-circuit conditions as photo-generated current can properly flow. Otherwise, ΔV is lowered by a voltage drop called the photo-potential. In open-circuit conditions, photo-generated current can not flow through external circuit so the photo-generated current must be balanced by a recombination current. As a result, ΔV will be reduced by an amount of V_{OC} corresponding to the open-circuit potential.

The behavior described in Figure 1.3 is relative to no bias voltage conditions but when an external reverse

bias voltage is applied, ΔV is increased and the SCR becomes wider. On the contrary, by applying a forward bias voltage ΔV is decreased and the SCR becomes narrower (minority-carrier injection).

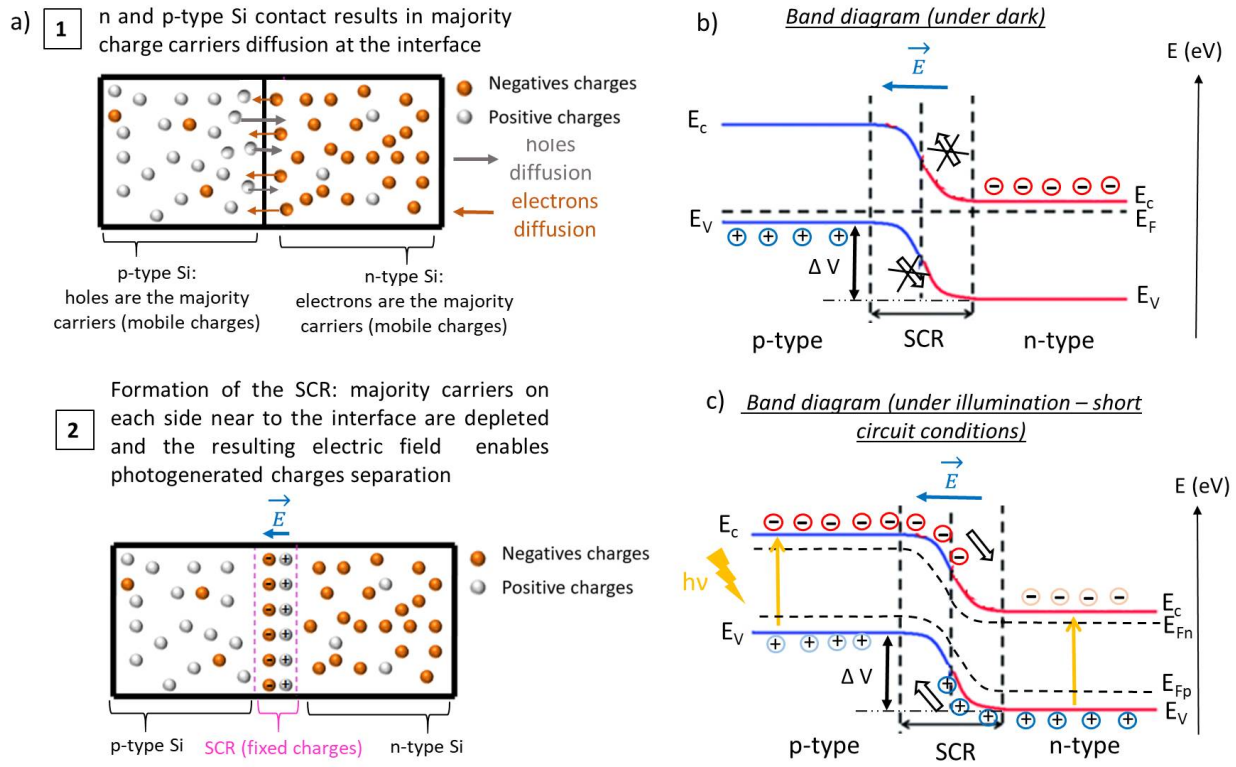

Figure 1.3: a) Illustration of p-n junction formation, b) Corresponding band diagram in dark, c) Corresponding band diagram under illumination in short circuit conditions.

3. Collection of the photogenerated charges carriers in an outside electric circuit.

Finally, the photogenerated charges carriers are extracted by the metallic contacts: the photo-generated electrons are collected on the n side and pass through the circuit to be recombined with the photo-generated holes collected on the p side. An outside current is thus generated. The working principle of a c-Si solar cell is summarized in Figure 1.4.

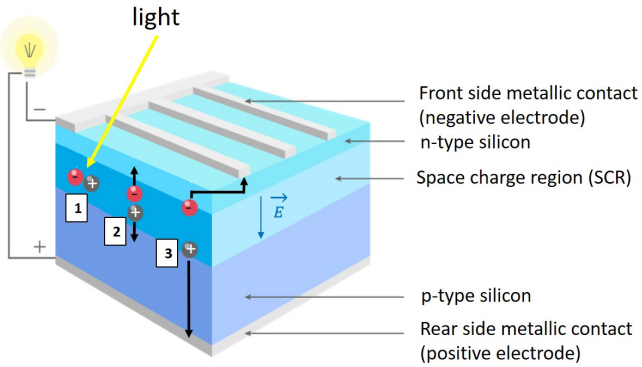

Figure 1.4: Illustration of c-Si solar cell working principle.

Contrary to the rear side, the front side is not fully metallized to allow light absorption. It is generally metallized according to so called "H-pattern" where thin metallic lines (fingers) are perpendicular to thicker ones (busbars) as shown in Figure 1.5.

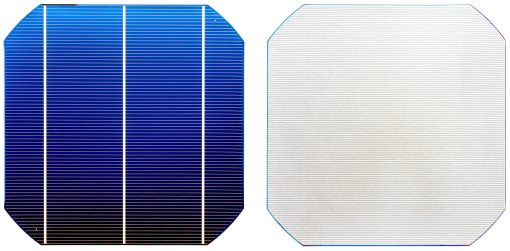

Figure 1.5: Image of a monofacial Si solar cell. Front side on the left is metallized according to H-pattern and rear side on the right is fully metallized.

1.3 Performance measurements of c-Si solar cells

1.3.1 Equivalent circuit

An ideal solar cell can be represented by the equivalent circuit in full line in Figure 1.6 (one diode model). A current source is connected in parallel with a diode enabling the current to only pass in one direction. This diode represents the recombination losses and is characterized by the saturation current density J_0 (in order to remove the dependence of the solar cell area onto measured current it is preferable to use the current density (J) instead of current I). In this ideal case, the equation 1.1 links the current density to the voltage[18]:

$$J = J_{ph} - J_0(e^{\frac{nqV}{k_B T}-1}) \tag{1.1}$$

With J_{ph} the photo-generated current density, J_0 the diode saturation current density, n the diode ideally factor, q the electron elementary charge, V the applied voltage, k_B the Boltzmann's constant and T the temperature.

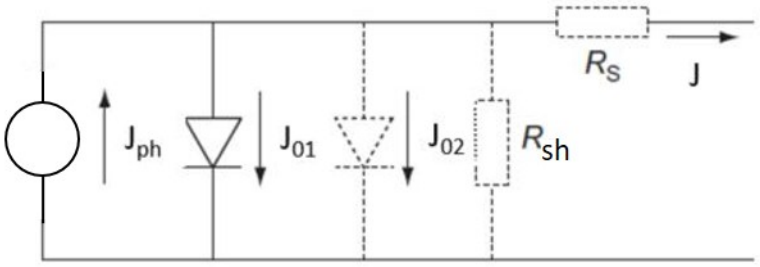

Figure 1.6: Equivalent circuit of an ideal solar cell (full lines). Non ideal components are shown by the dotted lines [18].

In practice, the two-diode model must be used as equivalent circuit to take into account the contribution of a second diode (J_{02}), series resistances (R_s) and parallel resistances (shunt resistance R_{sh}). These additional components are represented in dotted lines in Figure 1.6. The second diode represents the recombination losses in the SCR and is characterized by the saturation current density J_{02}. Series resistances are ohmic resistances from the metallic contacts, the semiconductor and the semiconductor-metal interface.

They must be lowered. Parallel resistances are due to shunts in the SCR or current leakage. The relation between current density and applied voltage becomes [18]:

$$J = J_{ph} - J_{01}(e^{\frac{q(V-AJR_s)}{n'_1 k_B T}-1}) - J_{02}(e^{\frac{q(V-AJR_s)}{n'_2 k_B T}-1}) - \frac{V - AJR_s}{R_{sh}} \tag{1.2}$$

With J_{ph} the photo-generated current density, J_{01} and J_{02} the diodes saturation current densities, q the electron elementary charge, V the applied voltage, A the solar cell area, R_s the series resistance, R_{sh} the parallel resistance, n'_1 and n'_2 the diodes ideally factors (1 in ideal case), k_B the Boltzmann's constant and T the temperature.

1.3.2 I-V measurement

Main parameters used to characterize the performance of a solar cell can be extracted from illuminated current-voltage (I-V) curves. A voltage ramp is applied in forward bias direction and the corresponding generated current is measured. I-V curves are performed under standard testing conditions (STC) where irradiation = 1000 W/m^2, T = 25°C, Air Mass = 1.5. The air mass (AM) measures how absorption in the atmosphere affects the spectral content and intensity of the solar radiation reaching the Earth's surface. Just above Earth's atmosphere, the radiation intensity is about 1.253 kW/m^2 and the corresponding spectral distribution is referred as AM0. A widely used standard to compare solar cells performances is the AM1.5 spectrum, normalized to a total power intensity of 1 kW/m^2. A typical I-V curve is represented in Figure 1.7 and the main parameters extracted (V_{OC}, I_{SC}, FF and η) are detailed below.

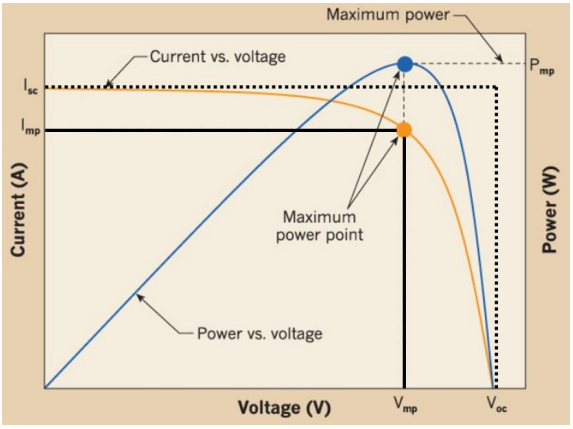

Figure 1.7: Typical I-V curve and graphical representation of the main solar cell parameters extracted [19].

- The open-circuit voltage (V_{OC}): It corresponds to the maximum voltage that a solar cell can deliver when no current is flowing. According to equation 1.1, V_{OC} is impacted by J_0, which depends on recombinations in the solar cell. V_{OC} thus reflects the amount of recombination in the device.

- The short-circuit current (I_{SC}): It is the current density flowing through the external circuit when electrodes are short circuited. It depends on the incident photon flux, optical properties and recombination rate of the solar cell. It is often expressed as short-circuit current density J_{SC}. In the ideal case, J_{SC} = J_{ph}. The maximum J_{SC} is 46 mA/cm^2 for a c-Si cell under AM 1.5 [15].

- The fill factor (FF): It is essentially a measure of the quality of the solar cell. The ideal FF is equal to 1 in case of no series resistances, infinite parallel resistances and diodes ideally factor equal to 1 (ideally factor is a measure of the junction quality and the type of recombination in a solar cell). FF is given by the ratio between dot square and full line square areas represented in Figure 1.7 such as:

$$FF = \frac{P_{mp}}{I_{SC} \times V_{OC}} \tag{1.3}$$

- The power conversion efficiency η: It is calculated by the ratio between the maximal generated power (P_{mp}) and the incident power (P_{in} = 1000 W/m^2 in STC) as shown in equation 1.4:

$$\eta = \frac{P_{mp}}{P_{in} \times A} = \frac{FF \times V_{OC} \times I_{SC}}{P_{in} \times A} \tag{1.4}$$

Various parameters can affect the I-V characteristic such as the p-n junction quality, the minority carriers recombination rate, the series and parallel resistances and the optical properties of the solar cell. An example is given in Figure 1.8 when series and parallel resistances are increased.

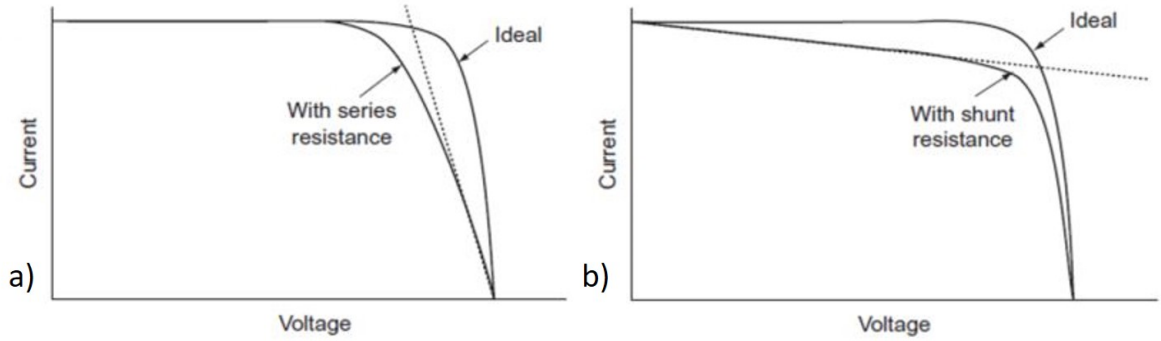

Figure 1.8: Effect of a) series and b) parallel resistances on a solar cell I-V characteristic [18].

1.3.3 Dark I-V measurement

Dark I-V measurement consists of carriers injection into the solar cell by an electrical current instead of light illumination. In this way, noise measurement due to small fluctuations in the light intensity is reduced. Despite it does not provide short-circuit current value, dark I-V measurement is more sensitive to determine other parameters (series resistance, shunt resistance, diode factors, diode saturation currents).

1.3.4 SunV_{OC} measurement

SunV_{OC} measurement enables to determine the I-V curve without the effect of series resistance. The cell is illuminated using a flash lamp with a slow decay and the V_{OC} is measured for various illuminations. The measure is performed at the open circuit so it is free from series resistance effect. By shifting the SunV_{OC} curve along the current density axis by J_{SC} (1 sun) the pseudo illuminated curve and the virtually series resistance free pseudo fill factor (pFF) are obtained. The difference between FF and pFF gives the fill factor losses due to the series resistance.

1.4 Limiting-efficiency factors

1.4.1 Maximum theoretical efficiency

The conversion of the light energy illuminating a solar cell is not complete and the yield is limited. The maximum efficiency achievable is affected by various factors, which are intrinsic or technological and are further described. Moreover, the environment temperature affects the cell behavior and the spectral density of the solar spectrum is different at various locations in the world which changes the incident power reaching the solar cell.

An accurate determination of the maximum efficiency for five solar technologies has been realized by Ian Marius Peters et al. [20] by taking into account the world climate conditions in 2015. The as-determined maximum efficiency is called the "maximum harvesting efficiency" ($\eta_{h,max}$), in opposition to the maximum efficiency determined in Standard Testing Conditions ($\eta_{STC,max}$). The calculated median values of η_{STC} and η_h are reported in Figure 1.9 for the five tested solar cell technologies having different bandgap values.

It appears that η_h is always inferior to η_{STC}, especially for materials with smaller bandgap such as silicon. The behavior of solar cells with small bandgap is thus more affected by environmental conditions such as humidity and temperature. Their efficiency is more sensitive to location in the globe and fluctuations of climate conditions which is interesting to keep in mind.

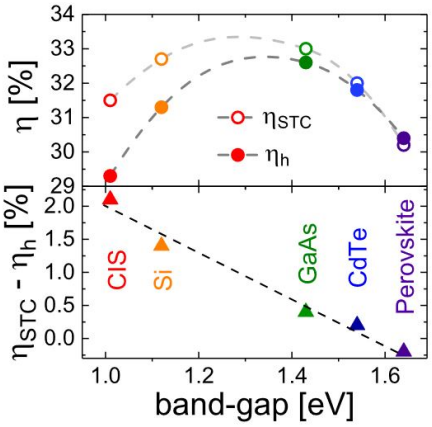

Figure 1.9: Comparison of harvesting efficiencies and STC efficiencies as a function of cell technology bandgap. The lower part shows the difference $\eta_{STC} - \eta_h$ [20].

In addition, by taking into account climate conditions all around the world, the ideal bandgap for maximizing the energy yield to 33% is equal to 1.35 eV (see Figure 1.10). This value is consequently a target for solar technologies where the bandgap value can be modulated.

The maximum efficiency in the STC ($\eta_{STC,max}$) is generally called the Shockley–Queisser (SQ) limit. Usually, only radiative recombinations are present in SQ limit calculation, but in silicon, Auger recombinations (non radiative process) are dominant and the SQ limit is not directly applicable [15], [21]. Some papers have determined the SQ for Si solar cell by approximations to take into account Auger recombinations and values around 29% have been obtained [16] (29.43% [15], 29.8% [22]). These values are below the ones proposed by Ian Marius Peters et al. ($\eta_{STC} \approx$ 32-33% in Figure 1.9) for which Auger recombinations have not

been considered, which raises the importance to take into account these recombinations. Overpassing the conversion efficiency limit requires tandem or multi-junctions structures and an example is given in section 1.5.2.

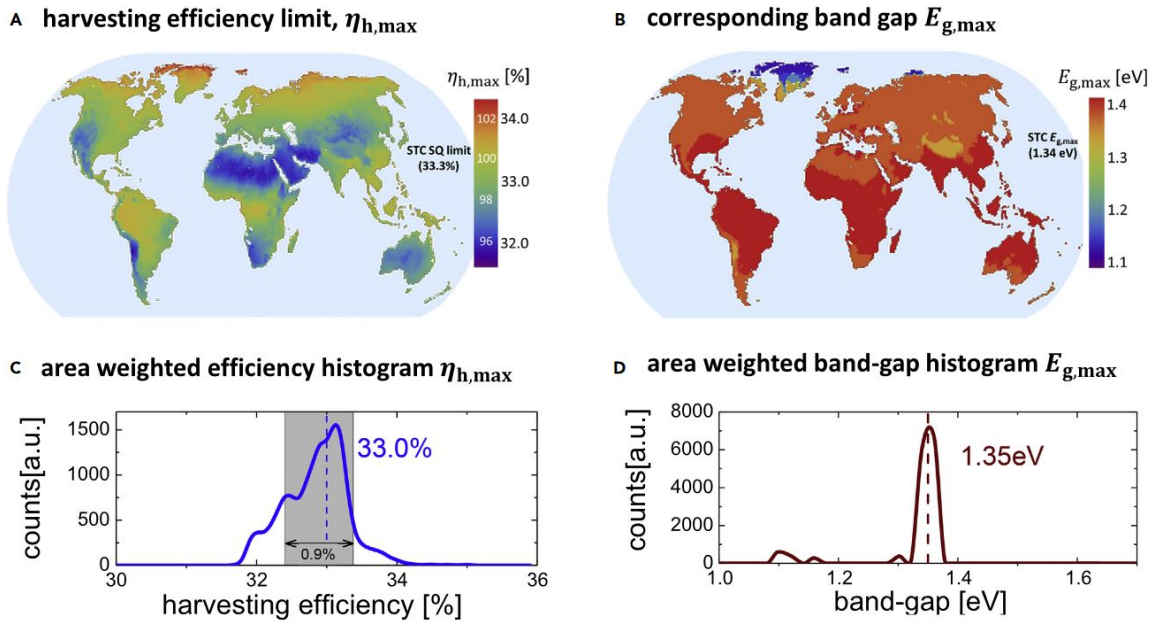

Figure 1.10: Global harvesting efficiency limits and corresponding bandgap. A and B: calculated harvesting efficiency limit $\eta_{h,max}$ and bandgap $E_{g,max}$ for which this limit is achieved. C and D: Area-weighted histograms of the occurring efficiency $\eta_{h,max}$ and bandgap, $E_{g,max}$ (D) values [20].

1.4.2 Intrinsic limiting-efficiency factors

Unavoidable intrinsic losses limit the conversion efficiency of c-Si solar cells and have four origins:

- **Incomplete absorption of photons:** when photons energy is smaller than the one of the Si bandgap, they are not absorbed and do not contribute to the creation of electron-hole pairs. That leads to about 27% loss in the yield as depicted in Figure 1.11.
- **Excess energy of photons:** photons with energy greater than the Si bandgap loose their energy in excess by thermalization and does not participate in the creation of electron-hole pairs. This results in a yield loss of about 28% (see Figure 1.11).

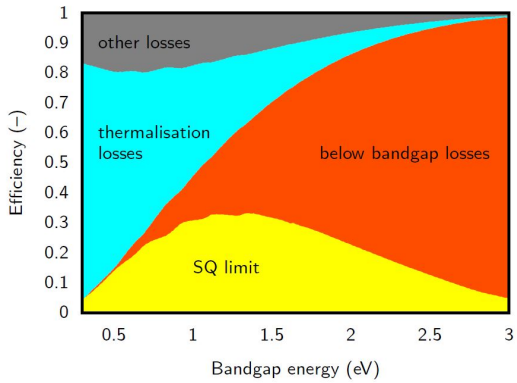

Figure 1.11: Major loss mechanisms considered in the SQ limit determination [15].

Non absorption of photons having $E_{ph} < E_G$ and thermalization losses due to $E_{ph} > E_G$ are the two main losses. They are both related to the spectral mismatch between the energy distribution of photons in the solar spectrum and the Si bandgap as represented in Figure 1.12.

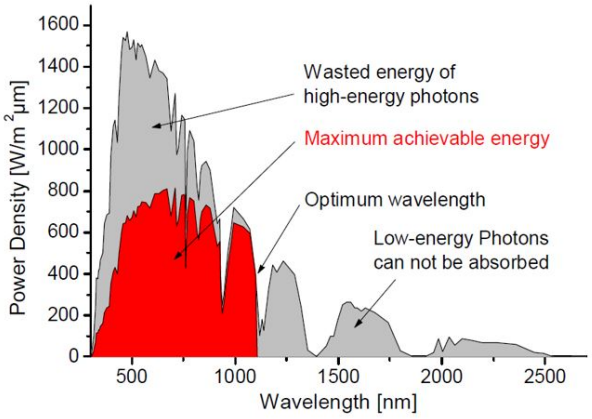

Figure 1.12: Spectral mismatch between the energy distribution of photons in the solar spectrum (AM 1.5) and the Si bandgap: the red part represents the fraction converted by a c-Si solar cell with E_G = 1.12 eV at ambient temperature [23].

- **Reduction of the maximum achievable V_{OC} by thermal radiation:** the maximum V_{OC} for a c-Si solar cell is related to its bandgap and is equal to 1.12 V at ambient temperature. It must also be taken into account that the cell temperature is not equal to $0K$, which further limits the V_{OC} value [24]. Indeed, the solar cell is in thermal equilibrium with its surroundings, so it absorbs thermal radiation according to the ambient temperature and also emits the same amount of radiation (blackbody radiations). That leads to a recombination current different from zero, and a reduction of the maximum V_{OC}.
- **Fill factor (FF) limitation:** ideally, FF is equal to 1. However, recombination currents limit its value to 0.85 [21]. These both last intrinsic losses are part of "other losses" mentioned in Figure 1.11.

1.4.3 Technological limiting-efficiency factors

Technological losses can be avoided and are divided into three categories: optical losses, recombination losses and resistive losses. They can occur at cell level but also at module level, resulting in cell to module power losses until $2\%_{abs}$ [25]. This value can be reduced by using advanced interconnection technologies (see section 1.5.3).

- **Optical losses:**

  - Reflection on the metallic contacts: the metallic grid pattern must be optimized to collect efficiently photo-generated carriers while limiting the shadowing effect. Bifacial solar cell concept (see section 1.5.2) and interdigitated back-contacted cells (IBC) (see section 1.5.2) enable to significantly reduce these losses;

  - Reflection on the Si surface: average reflectivity is $\geq$35% in the wavelength range 250-850 nm on polished Si but a texturing treatment reduces this value at 11% by increasing the path length of the photons [26]. By combining a texturation treatment with an anti-reflection coating (ARC), average reflectivity lower than 2.5% can be obtained [27]. The optimal refractive index of the ARC (n_{ARC}) depends on re-

fractive index n_1 and n_2 (respectively relative to environment in which the incident and refracted light propagates) according to equation 1.5. The optimal thickness e_{ARC} at a specific wavelength λ is calculated by equation 1.6 [28]:

$$n_{ARC} = \sqrt{n_1 \times n_2} \tag{1.5}$$

$$e_{ARC} = \frac{\lambda}{4 \times n_{ARC}} \tag{1.6}$$

- Absorption of photons by the rear metallic face at high wavelengths: to promote absorption of low energy photons, thanks to multiple reflections between the rear and front metallic contacts, the refractive index of the metal must be as high as possible;
- Optical losses in the module: reflection and absorption in the glass, encapsulating material and interconnection tabs lead to optical losses.

At the cell level, an analysis of optical losses in terms of current density has been carried out on industrial PERC (Passivated Emitter and Rear Cell) by Müller et al. [29]. Results, described in Figure 1.13, show that optical losses mainly come from reflection on fingers, busbars and rear side metallization. Minimizing busbar and finger widths is thus essential to limit optical losses.

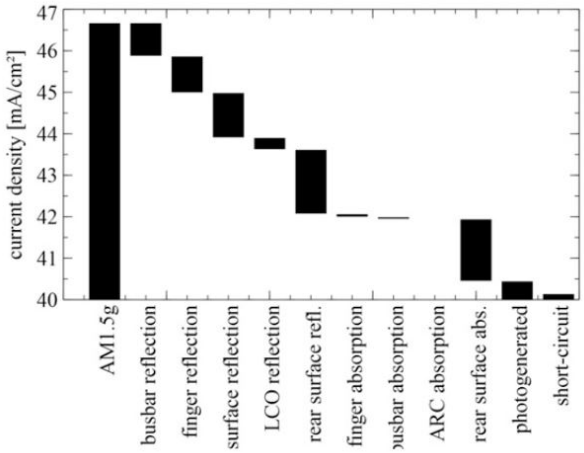

Figure 1.13: Optical losses analysis in terms of current density [29].

- **Recombination losses:** It refers to the annihilation of electron hole pairs, the reverse process of charges carriers generation. The average time for this reverse process is called the carrier's lifetime. High lifetime is required to allow the separation of photogenerated charges. The four main recombination mechanisms are schematized in Figure 1.14 and described below:
  - Radiative recombination: it corresponds to the recombination between an electron in the CB and a hole in the VB, followed by a photon emission. As Si has an indirect gap, it must simultaneously emit a photon and a phonon to conserve both energy and momentum. Radiative recombination is thus a four-particles process and is unlikely to occur (it can be neglected).
  - Auger recombination: the excess of energy, produced by the recombination between an electron in the CB and a hole in the VB, is transferred to another electron or hole. The particle thus activated, emits this energy under the form of phonons in the Si matrix. The probability of this phenomenon increases with

the Si doping. As silicon has an indirect bandgap, Auger recombination are dominant.

- Bulk Recombination through defects: the presence of defects within the semiconductor crystal (impurities atoms, lattice defects) produces discrete energy levels within the bandgap. These 'trap' levels facilitate recombination, which are commonly named Shockley-Read-Hall recombination.

- Surface recombination through defects: the Si surface represents a severe discontinuity in its crystalline structure. The large number of partially bonded Si atoms gives rise to many dangling bonds. Therefore, a large density of defect levels are found within the bandgap near to Si surface.

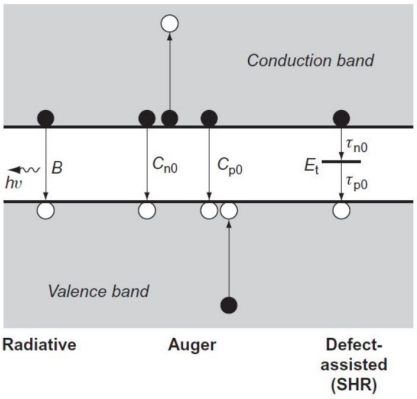

Figure 1.14: Schematic representation of recombination mechanisms in a c-Si solar cell [18].

Recombination losses impact directly the solar cell efficiency and must be limited. Radiative and Auger recombinations are intrinsic to the material and can not be reduced, but surface and bulk recombinations through defects are extrinsic and can be lowered by improving the fabrication process. For instance, application of appropriate dielectric layers on Si surface, such as silicon oxide (SiO_x), hydrogenated-silicon nitride (SiN_x:H) or aluminum oxide (AlO_x), significantly reduces recombination through passivation of dangling bonds (see section 1.5.2). SiN_x:H layers also release hydrogen upon high annealing temperature, which passivates trap level into the bulk. Recombinations can be reduced by minimizing the minority carrier concentration at the surface through doping or by creating an electric field to repel minority carriers thanks to dielectric layers with fixed charges. For more details, the reader is referred to the review in reference [30]. In addition, advanced structures such as selective emitters (see section 1.5.2) and passivating contacts (see section 1.5.2) enable to reduce the recombination losses.

- **Resistive losses:** They include shunt R_{sh} and series R_s resistances. R_{sh} are due to another current path for the light-generated current, because of leaks from the edges or short-circuited emitter. Less current flows through the junction and efficiency is reduced. R_s corresponds to the different individual resistances of the cell summarized in Figure 1.15. Ideally, R_{sh} should be infinite and R_s should be zero. Both of them impact the conversion efficiency and metallic contacts are largely involved in R_s. Electrical losses also occur by the Joule heating effect in module interconnections. In this work, shunt resistance can be typically involved in resistive losses through copper diffusion into silicon in case of non optimized plating process. We will also particularly investigate the resistances related to metallic contacts such as contact resistance and line resistance of fingers and busbars.

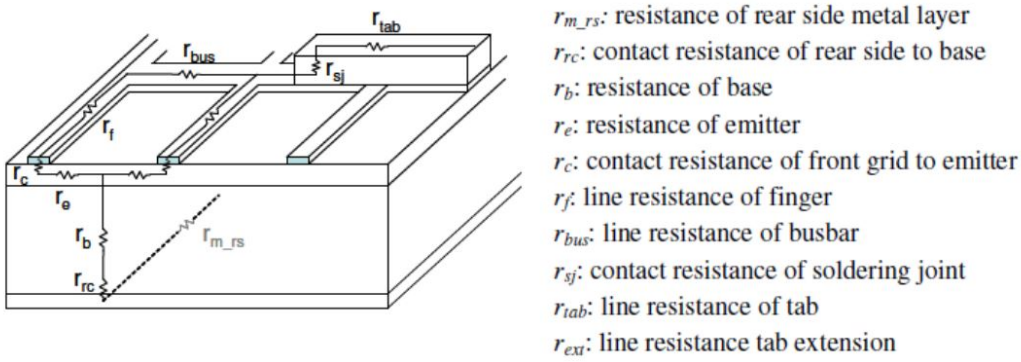

Figure 1.15: Schematic representation of series resistance contribution in a c-Si solar cell [31].

1.5 On the road to highly efficient c-Si solar cells and modules

Silicon solar cell efficiency can be improved by means of light absorption optimization, efficient collection of photo-generated carriers or reduction of recombinations and resistance losses. In that way, researchers and industry are developing new architectures and materials to achieve highly efficient c-Si solar cells. Meanwhile, to reduce manufacturing costs, efforts are made to use low cost materials and equipments, reduce process temperatures, reduce breakage risks and increase throughputs. Metrology techniques are also constantly improved to identify defects into c-Si solar cells all along the process line. Improvements to achieve highly efficient Si solar cells are described under the different manufacturing steps.

1.5.1 Making silicon substrates

The making of Si substrates involves three successive steps: feedstock, ingot and wafer production. To improve the quality of Si substrates, researchers aim to limit impurities incorporation and failure modes during these three steps by upgrading metrology techniques and process equipments. To lower production costs, a great attention is also paid on limiting the quantity of material damaged when ingots are sliced into wafers because this damaged part must be then removed (Kerf-losses). In that way, diamond wire sawing process is more and more used to slice Si ingots into wafers as this technique reduces the depth of damages and so the Kerf-losses [32] compared with conventional abrasive slurry sawing.

Standard c-Si solar cells are mainly based on multi-crystalline (mc-Si) because it is less expensive to manufacture. However, less defects (grain boundaries, dislocations, metallic impurities) are observed with mono-Si. The current trend is thus to go from mc-Si to mono-Si and efforts are ongoing to lower the manufacturing costs.

P-type wafers took the lead historically because at the beginning of its development, the solar technology was mainly used for spacial applications and p-type structure presents better resistance to radiations. However, n-type wafers are more tolerant to metallic contaminations and show higher minority carrier's lifetimes. N-type wafers also do not suffer from light-induced degradation as the degradation mechanism is based on boron-oxygen complex formation. Both types have their advantages and drawbacks, which are well described by Pietro P.Altermatt [33], but n-type is more suitable to achieve highly efficient c-Si solar

cells. Moreover, the price of n-type wafers, which was above 30% higher than for p-type a few years ago, is now only above 5% [34]. The trend is therefore to go from p-type to n-type wafers and most of the advanced cell architectures are based on n-type wafers.

1.5.2 Cell manufacturing

Aluminum Back Surface Field (Al-BSF) has been the 1^{st} architecture developed in industry and was considered as a standard for many years. The process flow for an Al-BSF structure is shown in Figure 1.16.

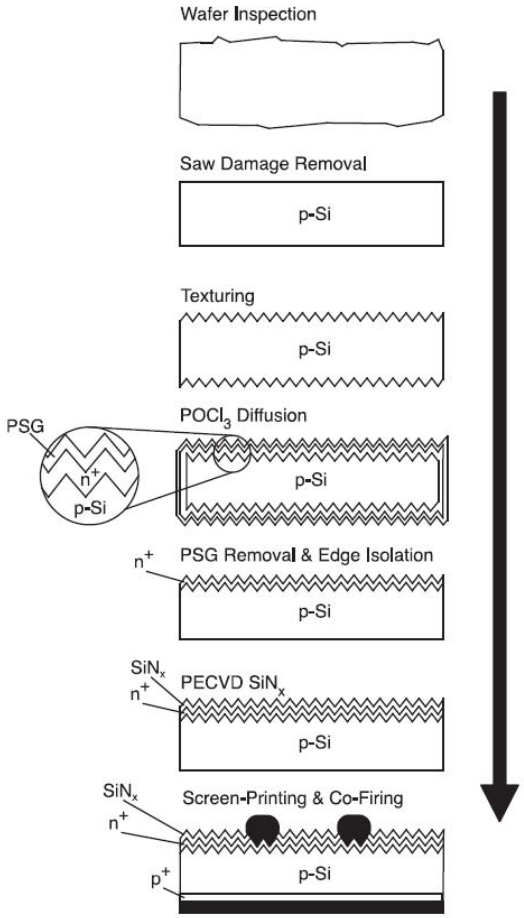

Figure 1.16: Typical cell manufacturing flow for an industrial Al-BSF c-Si solar cell [35].

156 x 156 mm^2 size mono-Si or mc-Si p-type Si wafers are used to form the base with a resistivity around 1 Ω.cm. To absorb efficiently the incoming photons, base thickness is commonly in the range of 180-200 μm. Firstly, **saw damage removal** and **texturing** are needed to respectively remove saw marks arising from ingots slicing and reduce optical losses. This is performed through wet chemical processes and the purity of chemicals used is essential to limit impurities incorporation [35].

To separate the generated charges carriers, the p-n junction is created through the widely used **$POCl_3$ diffusion**. A $POCl_3$ liquid is turned into vapor by N_2 gas flow and reacts with a simultaneously introduced gas flow of O_2. The process is performed at around 800-900°C and results in phosphorus pentoxide formation which coats the Si wafer and acts as P dopant source. As a result, the Si surface is highly doped with phosphorus atoms up to a depth of around 500 nm and is called the n^+ emitter. To reduce emitter re-

combination losses, while preserving a good metal contact, researchers seek to obtain low surface dopants concentration with deep emitters. Emitter formation is a critical step and temperature profile, pressure and deposition time must be carefully optimized to avoid risk of shunts.

The phosphosilicate glass (PSG) layer formed during diffusion process acts as recombination center and impacts the cell reflectance. Thus, **PSG removal** is performed using an HF-based solution to etch selectively the PSG without damaging the emitter below. Moreover, $POCl_3$ diffusion occurs on the entire cell and **edge isolation** through wet chemical process is necessary to remove n^+ area formed on the rear side and edges.

Next step consists of dielectric layers deposition to promote **antireflection and passivation properties** on the front side. An amorphous hydrogenated silicon nitride **(SiN_x:H)** layer (generally around 75 nm thick) is commonly used as it plays both roles. Finally, metallic contacts are formed to collect the photogenerated charges carriers. **Screen-printed Ag paste** is used for the front side, according to an H-pattern design, and the rear side is fully metallized by a **screen-printed Al paste**. During the **final co-firing** at high temperatures (800-900°C), two phenomena happen: 1) On the rear side, a BSF is created and consists of an higher doped region due to diffusion of Al atoms. The interface between the highly and lowly doped regions behaves like a p^+-p junction and an electric field is formed. Thus, the flow of minority carrier to the rear surface is blocked and recombinations are limited, 2) On the front side, glass frit component present in the Ag paste provides the etching of dielectric layers and the formation of Si/Ag contact. Mechanisms occurring during co-firing are further detailed in section 2.4.

Recently, Ki Hyung Kim and al. achieved a record p-type mono-Si Al-BSF solar cell efficiency of 20.29% (M2 size cell: 244.3 cm^2) [36]. However, the full-area Al-BSF demonstrates a moderate passivation quality and only about 70% of the infrared light reaching the rear contact is reflected back into the silicon [37]. Furthermore, industrial Al-BSF solar cell hardly exceeds 20% efficiency. For a long time, Al-BSF structure was the mainstream c-Si technology but currently, the majority of c-Si solar cells is produced according to advanced PERC architecture (described in section 1.5.2). To improve c-Si solar cell efficiency and/or reduce production costs, new materials and architectures have been developed and are constantly improved.

- Alternative doping technologies:

Ion implantation and silicon epitaxial growth both enable to control more precisely the doping profile compared to standard $POCl_3$ diffusion. Better emitter quality can be achieved through more homogeneous doping profile and sharper interface. Even though implantation is the most sophisticated doping technique, it is still too slow and expensive to be widely implemented in industry [35]. Silicon epitaxial growth requires high-temperature processes ($> 800°C$) to obtain high quality epitaxial layers, which can lead to unintentional dopant and impurity diffusion and implies an high thermal budget. To tackle these issues, researchers are focusing on PECVD (Plasma-Enhanced Chemical Vapor Deposition) to promote gases dissociation at lower temperatures but further investigations are still needed to understand growth mechanisms and optimize plasma conditions [38], [39].

- Efficient passivation layers and rear passivated cell devices [30], [37]:

SiN_x:H films were the first dielectric layers developed in solar cell industry as they demonstrate passivation properties through hydrogen release associated with anti-reflection properties. Now, other passivation layers have been developed and demonstrate higher passivation level such as SiO_x, Al_2O_3 or amorphous hydrogenated silicon (a-Si:H). Nevertheless, SiN_x:H is still used with SiO_x, Al_2O_3 or a-Si:H as capping layer to promote anti-reflection properties and additional passivation effect through hydrogen release.

High level of chemical passivation can be achieved for n^+ emitters with thermally grown SiO_x layer. This is explained by the obtention of a layer with a stoechiometry x = 2. Thermally grown SiO_2 can be used in combination with a SiN_x:H layer for highly efficient solar cell devices, but high temperature processes are needed and growth rate is low. Another method, more suitable for industrialization, consists of SiO_x deposition through low temperature PECVD process but slightly lower passivation levels are obtained.

For p^+ emitters, Al_2O_3 layers demonstrate efficient field effect passivation thanks to negative fixed charges. They are mainly deposited by Atomic Layer Deposition (ALD), resulting in low deposition rates but high rate ALD deposition concepts such as spatial ALD are under development. Al_2O_3 PECVD deposition is also under investigation. Boron silicate glass (SiO_x:B) deposited by PECVD can act both as boron source for the p^+ emitter diffusion and as passivation layer in combination with SiN_x:H layer.

a-Si:H layers with $> 10\%$ hydrogen content provide chemical passivation for both p^+ and n^+ emitters with the main advantage to necessitate low PECVD temperatures (around 225°C). Figure 1.17 illustrates some passivation scenarios for both n^+ and p^+ emitters.

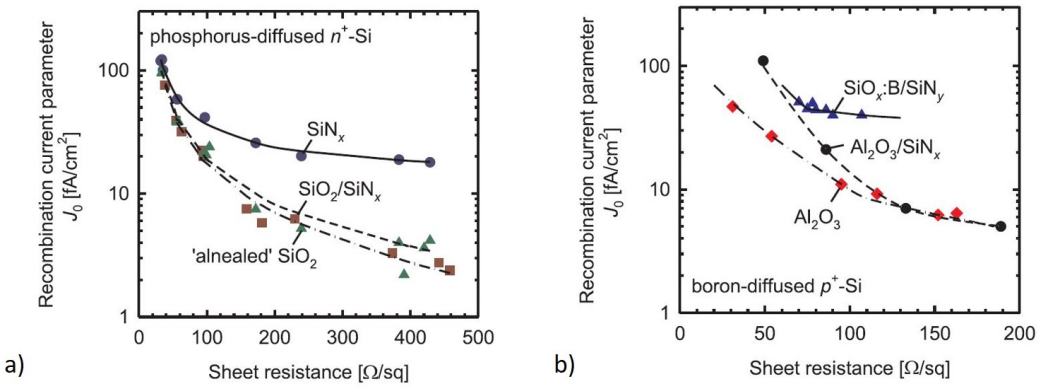

Figure 1.17: Measured recombination current density as a function of the sheet resistance for a) phosphorus-diffused n^+ emitter, b) boron-diffused p^+ emitter [30].

In order to improve light reflection from the backside of the cell into the solar cell, while limiting recombination at Si/metal interface, passivation layers can be applied on the rear side. This is the working principle of **PERC, PERL (passivated emitter and rear locally diffused) and PERT (passivated emitter and rear totally-diffused) cell devices** schematized in Figure 1.18. The front side is identical to the Al-BSF structure, but the rear side is improved by applying dielectric layers to enhance internal reflection and passivation properties.

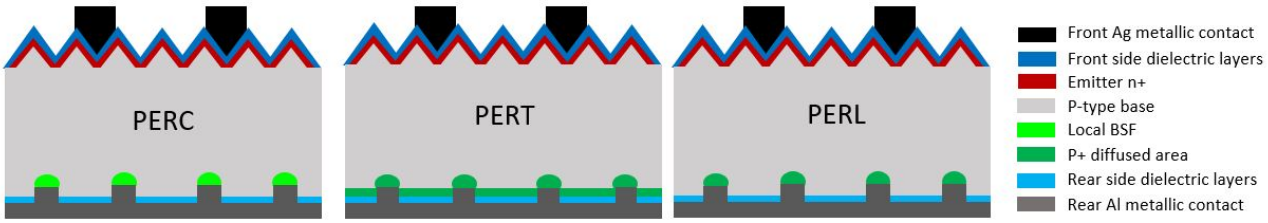

Figure 1.18: PERC, PERT and PERL advanced architectures for monofacial c-Si solar cells.

In PERC structure, LASER or chemicals are used to selectively open the rear passivation before SP of Al paste. A BSF is then locally formed through Al atoms diffusion during the firing process. Al_2O_3/SiN_x:H and SiO_2/SiN_x:H dielectric stacks are commonly used for rear side passivation. The SiN_x:H is used as capping layer to decrease surface recombination velocity, protect the passivation layer from Al etching during firing process and improve the internal optical reflectance. PERC has been the first rear passivated device developed and has now replaced the standard Al-BSF as mainstream architecture. This evolution is driven by an higher added value of these cells compared to increased production costs [37]. In January 2019, LONGI solar has achieved a new bifacial mono-Si PERC (PERC+) world record conversion efficiency of 24.06% on 156 x 156 mm^2 cells (M2-sized) [40].

For their part, PERT and PERL are expected to gain importance in the future. Meyer Burger is currently developing industry-proven PERT and PERL equipments, in collaboration with recognized research institutes [41]. Unlike Al-BSF and PERC, which both use an Al-alloy BSF, PERT and PERL structures have a diffused rear surface as described in Figure 1.18. The created field-effect, allows to strongly limit contact recombinations by reducing minority carrier concentrations. Such a local junction provides better passivation performances than local Al-BSF used in PERC [37]. Moreover, to promote rear side back surface field formation through Al atom diffusion, PERC cells require p-type wafer. PERT and PERL, can be adapted to n-type wafers which are more suitable for highly efficient Si solar cells. In April 2019, Imec announced that its n-PERT bifacial solar cells developed with Jolywood manufacturer, have reached front side conversion efficiency of 23.2% (M2-sized cells) [42]. Thus, the PERT structure has been chosen for this thesis work.

- Selective emitters:

Locally highly doped areas can be obtained into the emitter, most of the time, by means of laser doping. They are noted n^{++} or p^{++} areas and allow to achieve better contact quality because highly doped Si surfaces are easily contacted. This point is further explained in section 2.2. In addition, emitter between fingers can be lowly doped to limit recombination and improve the blue spectral response. Laser doped selective emitters combined with PERC structure have shown an absolute gain from 0.15 to 0.28% in average cell efficiency compared to standard PERC cells [43].

-Passivating contacts and Heterojunction Si solar cells technology (HJT) [44]–[46]:

Passivating contacts consist of placing a layer stack between c-Si and the metallic contacts to suppress charges carriers recombination at Si/metal interface while simultaneously allowing charges extraction from

the c-Si absorber. Promising materials for passivating contacts applications include a-Si:H, SiO_2/doped polycrystalline silicon (poly-Si) stack and transition metal oxides.

a-Si:H materials are used in HJT solar cells and the as-obtained passivating contact structure largely explains the high conversion efficiency of these solar cells. Contrarily to homojunction c-Si solar cells, HJT uses two different semiconductor materials (a-Si:H and c-Si) to create the p-n junction as represented in Figure 1.19. Firstly, a thin intrinsic a-Si:H layer is deposited by PECVD on c-Si, followed by a p-type or n-type doped a-Si:H layer. The intrinsic a-Si:H layer provides chemical passivation of the c-Si surface, while the doped a-Si:H layer provides carrier selectivity by inducing band bending in the c-Si. Usually, a transparent conductive oxide, acting as ARC on the front side, is needed to improve lateral conductivity. Main drawbacks of a-Si:H materials are the significant optical absorption losses and the poor thermal stability. HJT can be processed at low temperatures ($\leq 200°C$) compared to homojunction cells. Therefore, very thin wafers can be used without damaging substrates and the thermal budget is reduced. HJT are however not suitable for high process temperatures such as SP metallization. Low-temperature Ag pastes are needed but are more expensive. HJT has already the potential to produce highly efficient Si solar cells with competitive production costs, but this potential could be largely increased by reducing Ag paste consumption or developing more compatible metallization technologies.

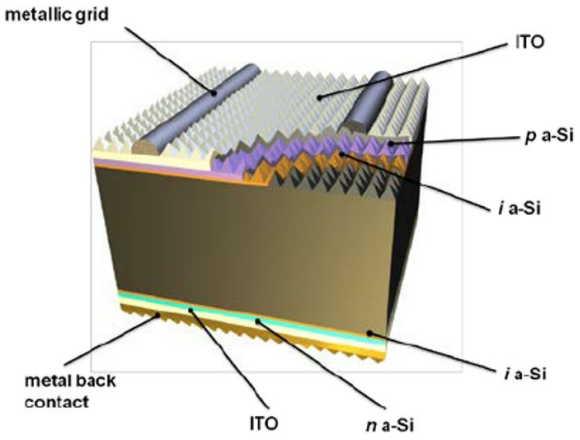

Figure 1.19: Schematic representation of HJT c-Si solar cell structure [47].

Another passivating contact structure is the SiO_2/poly-Si stack and an example is given in Figure 1.20 with the TOPCon structure. An ultrathin oxide, typically grown by chemical or thermal oxidation, provides chemical passivation at the c-Si/oxide interface and acts as a barrier toward dopant diffusion from poly-Si to c-Si. The thickness is well controlled to provide current flow through tunnel effect. The poly-Si layer increases the conductivity of one type of charges carriers depending on its doping type. This passivation stack is currently being implemented in industry but it requires high processing temperatures ($\approx 900°C$) to achieve high crystallization and the desired doping level in the poly-Si layer. Significant absorption losses are observed for both a-Si:H and SiO_x/poly-Si passivating contact structures, and the use of more transparent materials such as transition metal oxides, is interesting especially for front side application.

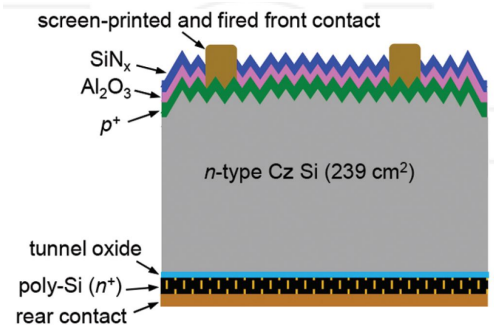

Figure 1.20: Schematic representation of passivating contacts on TOPCON c-Si solar cell structure [48].

- Interdigitated back-contacted cells (IBC):

The principle of IBC is to put emitter, BSF doped area and all metallic contacts on the rear side by using an interdigitated structure as shown in Figure 1.21. Compared to other structures described above, IBC demonstrates better light absorption and increases the J_{SC} due to suppression of optical shading losses on the front side. IBC cells have a great high-efficiency potential and become more and more attractive. They are also suitable for tandem applications as bottom cells. Main challenge for IBC cells is to reduce process complexity and costs for large scale industrialization. Kaneka Corporation has achieved the world's highest conversion efficiency of 26.63% in a practical size (180 cm^2) c-Si solar cell with a HJT-IBC architecture [49].

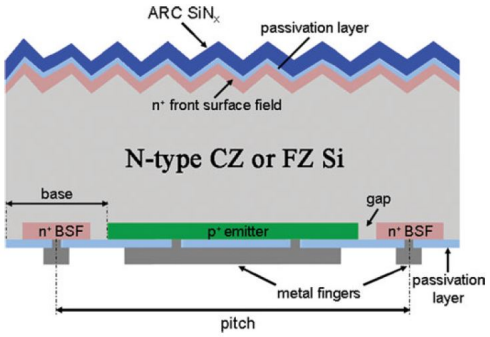

Figure 1.21: Illustration of IBC structure of c-Si solar cell [37].

-Tandem c-Si solar cells:

A tandem c-Si solar cell consists of using a c-Si solar cell, as bottom cell with another solar cell technology as top cell. The top cell must have an wider bandgap than the bottom cell to absorb high energy photons and be transparent to provide low energy light absorption by the bottom cell. This concept enables to increase the overall cell efficiency by limiting thermalization losses. Using two junctions gives the possibility to overpass the SQ limit depicted for a single junction c-Si solar cell. Several solar cell technologies can be used as top cell such as perovskites, III-V cells or thin films thanks to their higher bandgap compared to silicon (see Figure 1.9). Perovskites are a choice of interest as they absorb visible light but transmit IR and near IR to the Si bottom cell as illustrated in Figure 1.22. Main challenges of Si/perovskite devices are 1) the stability of the perovskite towards temperature, humidity and UV radiations 2) optimization of the semi-transparency for the perovskite rear side metallic contact 3) the connection of both sub-cells (2 terminals structure is more promising than 4 terminals one but perovskite growth directly onto Si cell remains challenging). The Energy

research Centre of the Netherlands (ECN) has achieved 30.2% equivalent conversion efficiency for a bifacial Si/perovskite tandem solar device **[50]**.

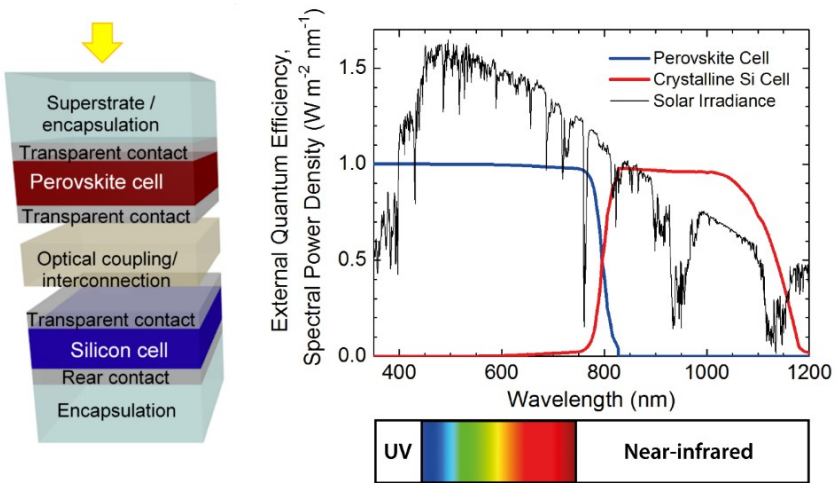

Figure 1.22: Illustration of a perovskite/Si tandem cell and resulting external quantum efficiency [51].

More than two sub-cells can be used, and it is called multi-junction solar cells, but this technology is mainly used with thin films solar cell technology. As increased production costs are not compensated by the efficiency gains, multi-junction solar cells are not yet industrially suitable.

-Bifacial solar cells [52]:

Bifacial solar cell is a promising technology that increases the production of electricity through absorption of the light reflected on the ground (albedo). It necessitates to not fully metallize the rear side of the cell which also limit the recombinations at metal/Si interface. By shifting from monofacial to bifacial modules, the energy output can by increased by until 30% [18]. These cells are able to operate at lower temperatures than monofacial ones, resulting in an increased maximum power output. For these reasons, bifacial technology has the potential to significantly reduce the Levelized Cost of Electricity [53] and is expected to share more than 50% of the market by 2029 according to ITRPV [10] (see Figure 1.23). For these reasons, this work will be focused on bifacial n-PERT cells.

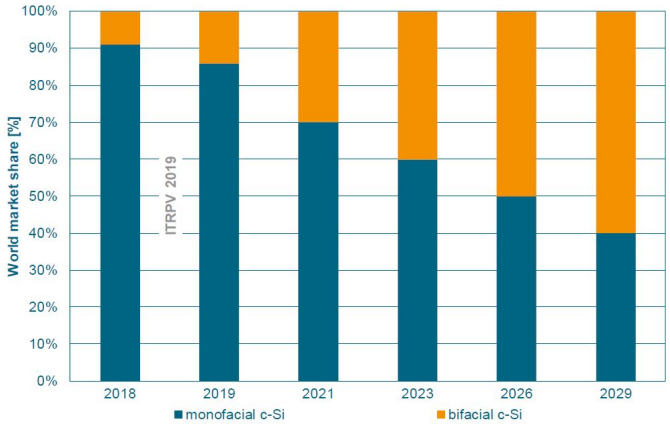

Figure 1.23: Predicted worldwide market share for bifacial Si solar cell technology [10].

All solar cell concepts described above can be adapted to bifacial structure [53]. However, as the BSF of PERC cells is formed by Al paste diffusion under firing, adaptation to bifacial structure requires to locally remove the dielectric layers and SP Al paste with an accurate alignment. n-PERT, HJT and IBC cell concepts are mainly based on n-type wafers and do not suffer from Light-Induced degradation which is even more beneficial in bifacial structure. The measure of bifacial solar cell efficiency is still largely discussed in the PV community but it is clear that bifaciality has the potential to improve significantly solar cell efficiency. The most accurate characterization methods, for standardized testing of bifacial solar cells and modules, are described in reference [52]. Simultaneous irradiation of both sides of the cell using back mirror and simulating different albedo conditions, is recommended. For now, the accepted practice is to measure the solar cell from the front side in STC and add another 20% of this illumination from the rear side [50].

The market share of the different advanced technologies described above is expected to significantly increase, especially for the rear passivated cells, as shown in Figure 1.24. Current cell records are summarized in Table 1.1. On top of all these advancements, improvement of metallization step has also the potential to increase the conversion efficiency and limit production costs which has motivated this thesis work. The chapter 2 is dedicated to a background on metallization techniques for c-Si and presents the advancements to achieve higher metallic contact quality, and so higher solar efficiencies.

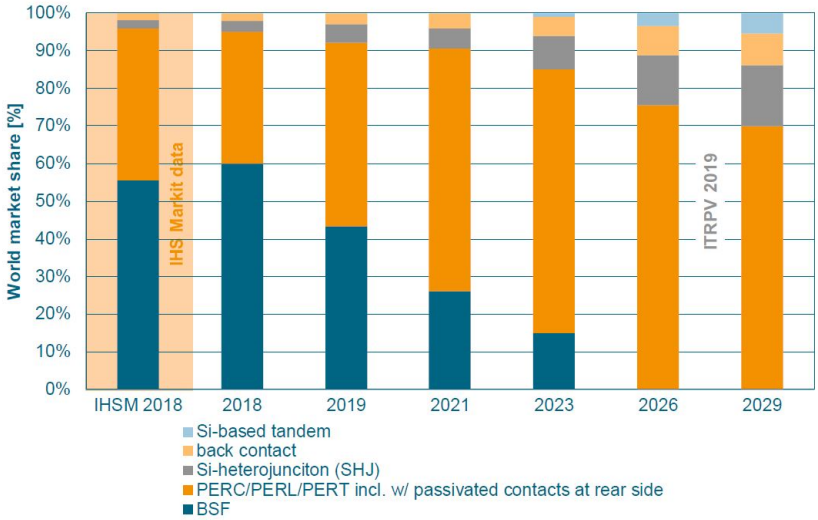

Figure 1.24: Predicted worldwide market share for different c-Si solar cell technologies [10].

Table 1.1: Current conversion efficiencies records for different c-Si solar cell architectures.

Cell architecture	Efficiency (%)	Area (cm^2)	Description	Date and research center
Monofacial Al-BSF	20.29	244.3	p-type, mono-Si	2017, Korea's Shinsung solar [36]
Bifacial PERC (PERC+)	24.06	244.3	p-type, mono-Si	2019, LONGI Solar [40]
Bifacial PERT	23.2	244.3	n-type, mono-Si	2019, IMEC [42]
HJT-IBC	26.63	180	n-type, mono-Si	2017, Kaneka [54]
Tandem Perovskite/Si	30.2	-	-	2019, ECN [50]

1.5.3 PV module manufacturing

The processing of cells into modules involves three steps: 1) interconnection of solar cells (stringing and tabbing) 2) encapsulation of interconnected cells (lamination) 3) integration of the junction box and bypass diodes. PV module manufacturing is a critical step because both power losses and gains can occur. The cell-to-module power ratio is used to quantify the general loss/gain percentage in a PV module. It corresponds to the ratio of module power to cell power multiplied by the number of cells integrated into the module [55]. Additional optical and resistance losses due to interconnection and encapsulation schemes must be limited as much as possible. In this aim, different geometries of interconnection tabs are developed, such as round or textured tabs, to redirect the reflected light into the cell. With textured tabs, total current and power of a module can be enhanced by 3% [25]. Furthermore, new interconnection schemes are under investigation to replace the traditional interconnection with Cu ribbons. Indeed, this interconnection technology is cheap, robust and reliable but demonstrates several problems: 1) there are important resistive losses, 2) shading losses are caused by ribbons and 3) high stress is induced in the cells during soldering process. Moreover, traditional soldered interconnections are inappropriate or ineffective for some cell structures such as HJT, which cannot sustain conventional soldering temperatures [56].

Two interconnection technologies have drawn attention these last years: Smart-wire connection technology (SWCT) and shingling technology. SWCT enables to reduce shading losses by 25% and increases the module efficiency by up to 5.7% [57]. This technology is based on wire bonding where round Cu-based wires are embedded in a polymer foil and applied directly on the cell surface (see Figure 1.25 a)). Optical losses are significantly limited due to the wires shape (see Figure 1.25 b)) and all fingers are connected together so busbars are not required. Bursbarless cells enable to realize cost savings by reducing metal consumption and and simplifying the process steps. Stress induced by connection process with SCWT is reduced as lower temperatures are used. Less breakage risks are also reported so thinner wafers can be used [57].

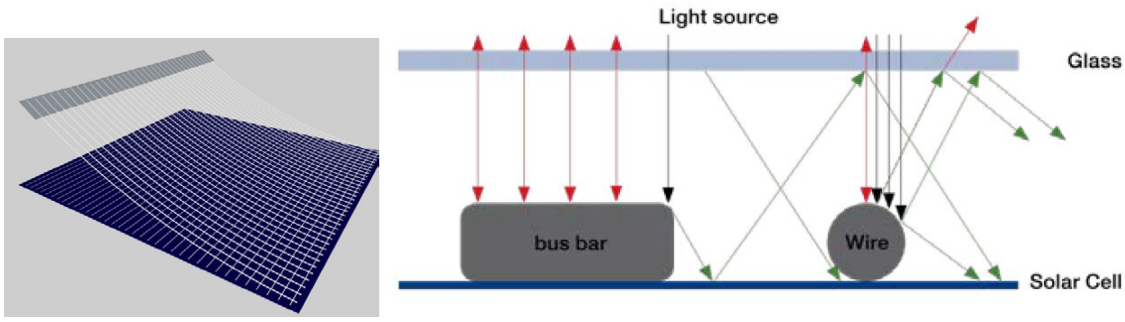

Figure 1.25: a) SWCT schematic representation, b) Comparison of light reflection on module with busbar or wire for fingers connection tab [57].

In the shingled cells module structure, a cell is cut into 3 to 6 stripes (so called shingles) which are assembled by connecting the front of each shingle to the back of the next one by using an electrically conductive adhesive. As a result, the cells slightly overlap with each other as represented in Figure 1.26. Contrary to conventional modules, there is no spacing between cells and the active area is highly increased [58]. Ohmic

losses are also reduced as smaller areas are connected in series. Curing of ECA requires lower temperatures than Cu ribbon soldering, which limits stress and makes shingled interconnection suitable for thin wafers [59]. Efficiency and power of shingled modules are consequently higher than for conventional modules (+ 1.86%$_{abs}$ +33 Wp) [60].

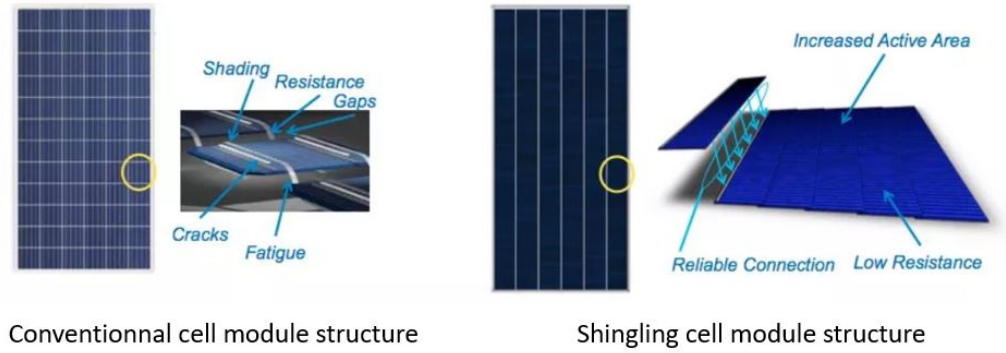

Figure 1.26: Comparison of conventional and shingling cell module interconnection schemes [61].

According to ITRPV, SWCT and Shingled cells market share are expected to increase significantly by replacing traditional Cu ribbon as reported in Figure 1.27.

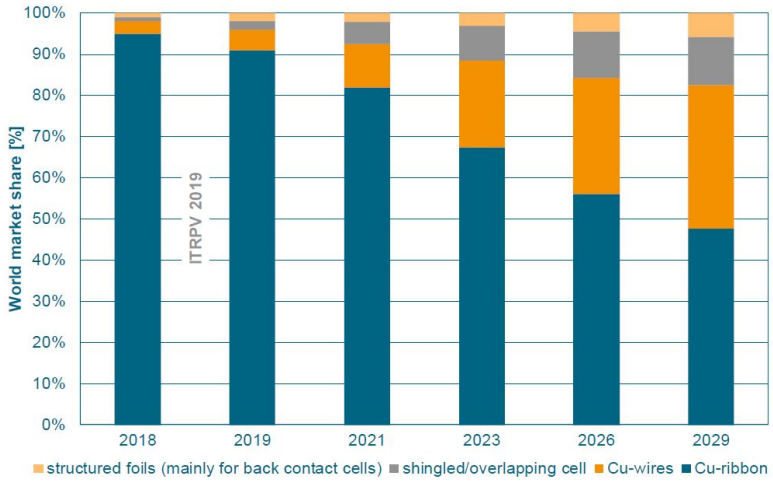

Figure 1.27: Expected market share for different interconnection technologies by 2029 [10].

1.6 Key elements to lower the production costs

Development of advanced technologies for c-Si solar cells now provides high cell efficiencies up to $\geq$ 25%. However, production costs can be increased due to more complex processes or requirement of new equipments. To be implemented in mass production, a c-Si device must meet one of these conditions in regards to current mainstream c-Si technology 1) the efficiency gain compensates the increased process complexity and cost (for instance, by increasing the conversion efficiency, less surface covered by solar cells will be necessary to supply the same output power) or 2) higher efficiencies are obtained with similar or

lower production costs and similar or higher throughputs. Few changes on the production line (especially in terms of equipments) must be required.

In parallel to the development of advanced c-Si concepts, production costs can reduced by using cheaper materials, reducing process temperatures or simplifying the manufacturing process. As it will be seen in Chapter 2, metallization step has the potential to reduce the production costs by reducing metal consumption or using cheaper metals.

In addition, cost savings are possible through recycling of PV modules and cells which can be re-used for solar cells manufacturing [62], [63]. Recycling is also primordial to keep a low environmental impact of PV technologies. Great progresses have been realized over the past 20 years in this field and a mass-recovery rate of 96% is now achievable as shown in Figure 1.28.

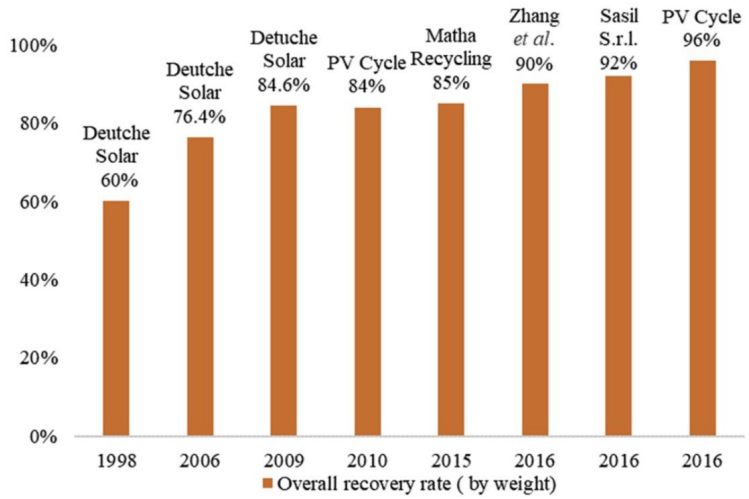

Figure 1.28: Progresses in the mass recovery of c-Si PV modules recycling over the past 20 years [62].

Due to its intermittency, solar energy requires storage devices so that the excess of energy produced during the day can be re-used latter (i.e. during the night). By increasing the charges capacity and the storage efficiency of batteries the electricity cost produced by solar energy could be reduced. Meanwhile, PV panels lifetime is also an important point to consider. The majority of manufacturers offer a 25-years standard solar panel warranty, which means that power output should not be less than 80% of rated power after 25 years. This number should be higher for PV panels installed nowadays thanks to research efforts.

MEMENTO

When a c-Si solar cell is illuminated, photons are absorbed and charges carriers (electron-hole pairs) are generated. These photogenerated charges carriers are separated by a p-n junction and then collected by metallic contacts. The two-diode model is mostly used as equivalent circuit to correlate the current density to the applied voltage according to the following relation:

$$J = J_{ph} - J_{01}(e^{\frac{q(V-AJR_s)}{n_1 k_B T}-1}) - J_{02}(e^{\frac{q(V-AJR_s)}{n_2 k_B T}-1}) - \frac{V - AJR_s}{R_{sh}}$$

Performance of a c-Si solar cell can be characterized by I-V measurements under Standard Testing Conditions to extract the main parameters which are V_{OC}, I_{SC}, FF, η, R_s and R_{sh}. Mainly due to intrinsic losses, maximum achievable efficiency is limited to around 30% for a single junction c-Si solar cell. To approach this limit, technological losses (optical, recombination and resistive losses) can be reduced through improvement of cell and module manufacturing process. In this way, the development of advanced cell structures (PERC, PERT, IBC, HJT etc.) and interconnection schemes (SWCT, shingled cells) are primordial.

Al-BSF was the mainstream architecture for a long time but it has been recently overpassed by PERC structure. PERT is gaining more and more interest as it demonstrates better passivation performances and are based on n-type wafers which are more and more preferred to p-type ones. In addition, bifacial cells are progressively replacing monofacial ones and PERT can be easily adapted in bifacial structure. Metallization step is of special interest because it has the potential to increase cell efficiency while reducing production costs. For all these reasons, this thesis will be focused on metallization of bifacial n-PERT c-Si solar cells as explained in more details in the next chapter.

Chapter 2

Metallization technologies for crystalline silicon solar cells

CONTENTS

2.1 Introduction

Metallization step has the potential to increase c-Si solar cell conversion efficiency by improving metallic contact quality: higher line conductivity, lower contact resistance, smaller line width etc. In addition, cost savings can be realized by using cheaper metals, reducing metal consumption and lowering process temperatures. This chapter 3 presents the metallization technologies for c-Si solar cells and reviews their respective advantages and drawbacks. Background knowledge on metal-semiconductor and semiconductor-electrolyte interfaces are introduced to help understanding the reaction mechanisms at Si surface investigated in this work. The working principle of the mainstream SP metallization is detailed and the need to develop alternative metallization ways is discussed. That brings to present the SP derivatives and the electrochemical metallization (plating). The potential of Ni/Cu plating to improve metallic contact quality is highlighted and the current issues to be tackled are discussed. Finally, the objectives and the methodology of this thesis are detailed.

2.2 Background on metal/semiconductor interface

2.2.1 The Schottky model

To define the requirements for a good metallic contact, the metal/semiconductor interface must be described by introducing the Schottky model [64]. In 1938, Walter Schottky elaborated a theory to explain the rectifying behaviour of metal/semiconductor contacts by introducing the notion of energy barrier between two materials. The Schottky model is illustrated in Figure 2.1 in case of n-type semiconductor.

When the metal and the semiconductor are in contact, the respective Fermi levels will equalize. This is associated with either accumulation (Figure 2.1 c)) or depletion of majority carriers (Figure 2.1 a)) at the vicinity of the surface, depending on respective initial position of metal and semiconductor bands. When charges carriers are depleted, fixed charges appear due to remaining ionized dopants (positives and negatives fixed charges for n-type and p-type semiconductor respectively). In both accumulation and depletion regimes, semiconductor bands are bent and a potential drop V_{SC} is created in a region called the Space Charge Region (SCR) having a thickness W. In depletion regime, a Schottky barrier is formed (ϕ_B) and the metal/semiconductor junction is said "rectifying", making a device known as a Schottky diode. On the contrary, accumulation regime leads to a non-rectifying junction and the device is called an Ohmic contact. As its name implies, the flatband regime corresponds to a behavior with no band bending (Figure 2.1 b)). This regime is mainly obtained by applying an external potential.

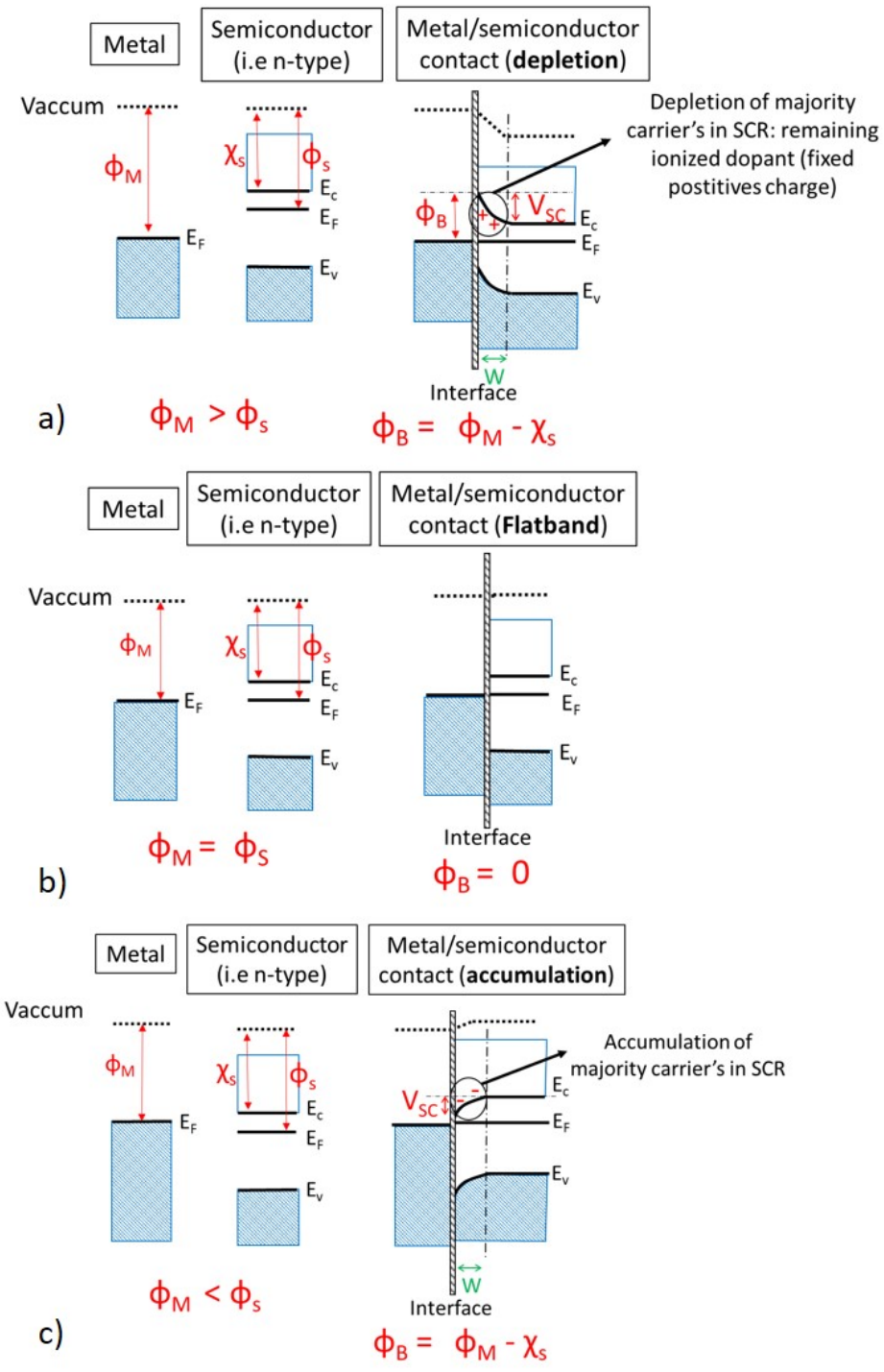

Figure 2.1: Energy band diagram of n-type semiconductor before and after contact with a metal according to the Schottky model. Three behaviors can be observed a) Depletion, b) Flatband, c) Accumulation. ϕ_M is the metal work function, χ_S the semiconductor affinity, ϕ_S the semiconductor work function, V_{SC} the potential drop, W the SCR thickness and ϕ_B the formed Schottky barrier such as $\phi_B = \phi_M - \chi_S$.

2.2.2 Comparison of metal/Si barrier heights

The graph in Figure 2.2 a) shows that a device metal/Si has a rectifying behavior ($\phi_B > 0$) with most of the metals. At first approximation, Schottky model predicts that the barrier ϕ_B should vary directly with the metal work function ϕ_M but for common semiconductors such as silicon, this relationship is not verified

due to interfacial surface states. An extension of the Schottky model taking into account these surface states is described in reference [64]. However, it appears that for silicides, the Schottky model is approached, meaning that less surface defects are present (Figure 2.2 b)) [64].

As a consequence, better contact quality with less interfacial surface states are expected for Ni plated contact as a NiSi layer is formed during the final annealing step (see section 2.5.2). In addition, Ag/Si barrier height ($\approx$ 0.8 eV) is higher than NiSi/Si one ($\approx$ 0.6 eV), which highlights the potential of Ni/Cu plating process to obtain better metallic contact quality. Copper also demonstrates low barrier height with Si ($\approx$ 0.45 eV) but can not be directly applied onto Si as Cu can diffuse into Si and act as recombination center. This is why plating is based on a Ni/Cu stack where nickel is the seed layer and Cu the conductive layer. Al has a lower barrier height ($\approx$ 0.45 eV) than NiSi but it is less suitable for front side metallization due to its lower conductivity compared Ag and Cu.

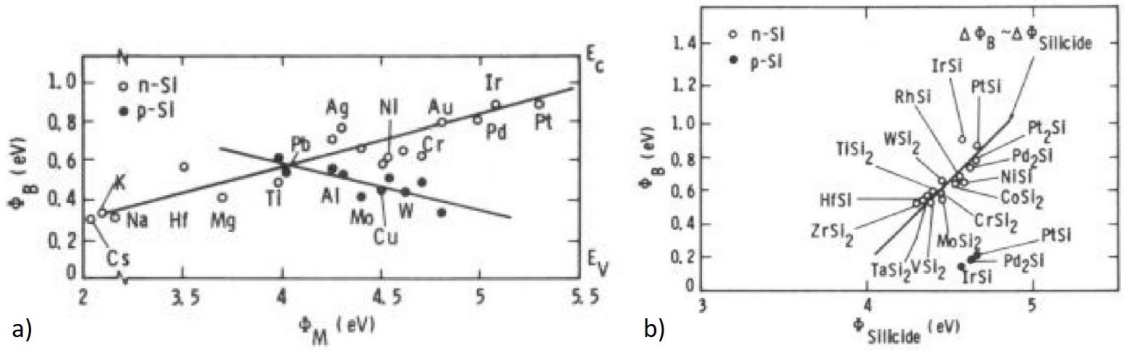

Figure 2.2: Barrier height ϕ_B for n and p type Si as a function of a) various metal work function ϕ_M and b) silicide work function $\phi_{silicide}$. Silicide work function is calculated assuming Si_4 stoechiometry [64].

In a metal/semiconductor device having a rectifying behavior, current can flow through three mechanisms depending on semiconductor doping level $N_{D,A}$ as represented in Figure 2.3.

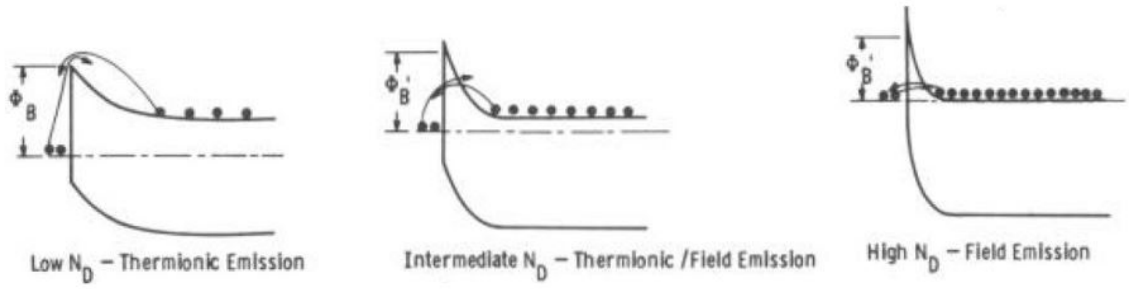

Figure 2.3: Schematic representation of current flow as function of the doping level N_D in case of rectifying contact between a metal and n-type semiconductor [64].

- With low $N_{D,A}$ ($\leq 10^{17}$ at.cm^{-3}) current flows by thermionic emission. The material needs thermal energy to overcome the Schottky barrier ϕ_B.
- An intermediate $N_{D,A}$ (10^{17} at.cm$^{-3} \leq N_{D,A} \leq 10^{20}$ at.cm^{-3}) leads to thermionic field emission.
- With high $N_{D,A}$ ($\geq 10^{20}$ at.cm^{-3}) current flows by field emission. The width of the SCR is thin enough to promote quantum tunneling and allows the charges to pass through the Schottky barrier ϕ_B.

When ϕ_B is too high, a alternative is to increase the semiconductor doping level to increase the band bending in the SCR and promote current flow through field emission. This is especially used for Ag/Si devices because lowly doped emitters are difficult to contact. As ϕ_B is lower with NiSi, lowly doped emitters are easily contacted with Ni/Cu plating compared to SP. The quality of the metal/semiconductor contact can be characterized by its contact resistivity ρ_c. This latter is expressed in $\Omega.cm^2$ according to the equation 2.1 [64] and must be as low as possible to enable the current to flow easily at metal/semiconductor interface.

$$\rho_c = (\frac{\partial V}{\partial J})_{V=0} \tag{2.1}$$

with V is the applied voltage across the contact and J the flowing current density .

The Transmission Line Measurement (TLM) technique is mostly used to determine ρ_c of metallic contacts on c-Si solar cells. It has been described for the first time by Shockley [65] and further developed by Berger [66]–[68]. In reference [69], authors have not only detailed this technique but they have also investigated the factors influencing measurements accuracy. Based on this reference, TLM technique is presented in Appendix A.1.

2.3 Background on semiconductor/electrolyte interface

This section is based on literature [70]–[73]. For simplicity, we consider an ideal case with no surface states or interfacial dipoles at semiconductor/electrolyte interface.

2.3.1 Correspondence between solid and electrolyte energy scales

To explain the phenomena occurring at the semiconductor/electrolyte interface, it is necessary to find a correlation between both energy scales. Indeed, the solid energy scale is defined in eV in reference to vacuum level, while in solution energy scale is defined in Volts and the redox potential is in relation to a reference redox potential. To correlate both energy scales, the "Fermi level in solution" concept must be introduced.

Electronic states in the electrolyte are assimilated to localized electronic states of ions or molecules of redox species. Oxidant species gain easily electrons, so empty electronic states are associated with a low energy level. On the contrary, reducing species release easily electrons and the occupied electronic states are associated with an high energy level. Thus, electron energy scale and redox potential scale have opposite signs. Some authors have determined the energy associated with equilibrium in equation 2.2 in the solid energy scale and agreed to retain the value of - 4.5 eV. The correlation between solid and electrolyte energy scales is thus given by relation 2.3 and represented in Figure 2.4 a). The position of E_C and E_V in silicon in both scales is given in Figure 2.4 b).

$$\frac{1}{2}H_2 = H^+ + e^- \tag{2.2}$$

$$E_{F,redox} = -qE_{redox} - 4.5 \tag{2.3}$$

With $E_{F,redox}$ the redox Fermi level in eV, E_{redox} the redox potential in Volts and q the elementary charge.

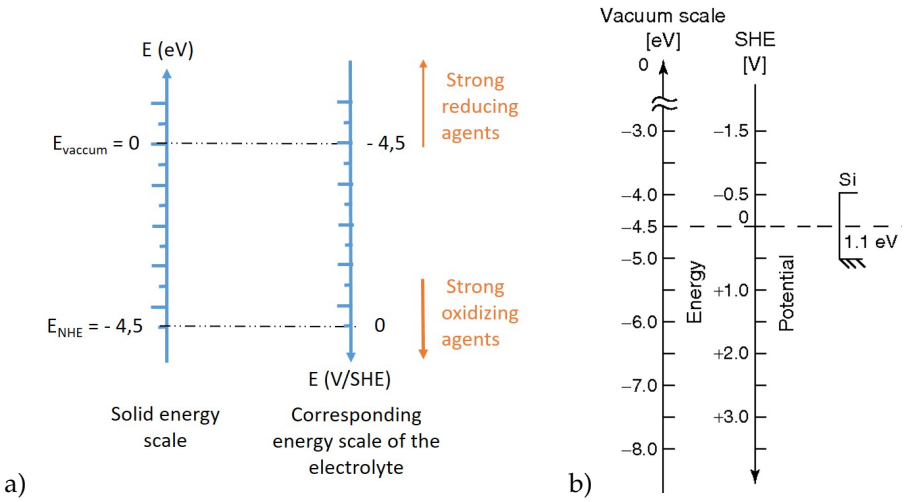

Figure 2.4: a) Correlation between solid energy scale (eV) and electrolyte scale in case of Standard Hydrogen reference electrode (SHE) (V), b) Position of E_C and E_V of Si on both energy scales [74].

A semiconductor is defined by its Fermi level E_F and the level of E_C and E_V (such as E_C - E_V corresponds to the semiconductor energy bandgap). The corresponding band diagram depends on the temperature and the doping level as illustrated in Figure 2.5 for Si material. The relative position of Fermi level towards CB and VB can be calculated with equation 2.4 and the Si band diagram on both solid and SHE scale can be drawn as exampled in Figure 2.6.

$$\mu_C = E_C - E_{F,n} = k_B \times T \times Ln(\frac{N_C}{N_D}) \qquad \mu_V = E_{F,p} - E_V = k_B \times T \times Ln(\frac{N_V}{N_A}) \tag{2.4}$$

with μ_C and μ_V the energy differences between the Fermi level and the majority carriers band, k_B the Boltzmann's constant, T the temperature, N_D and N_V the density of donors and acceptors, N_C and N_V the effective density of states in conduction and valence band.

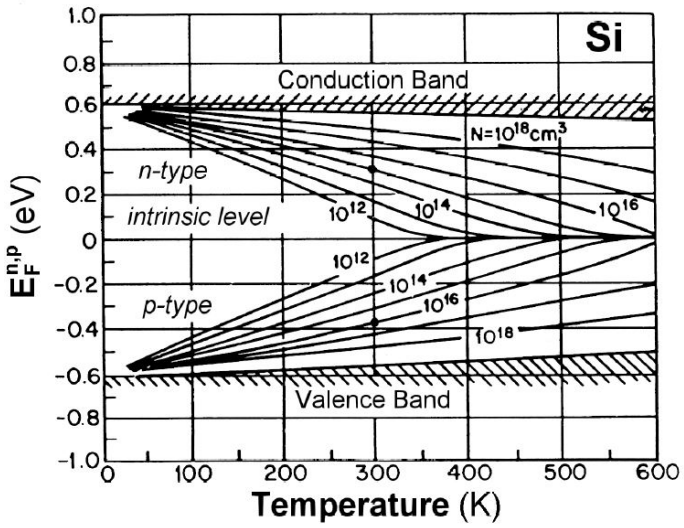

Figure 2.5: Fermi level positions for n and p-type Si as function of doping density and temperature [71] (this graph is not relative to vacuum scale as the 4.5 constant (see equation 2.3) has been already added).

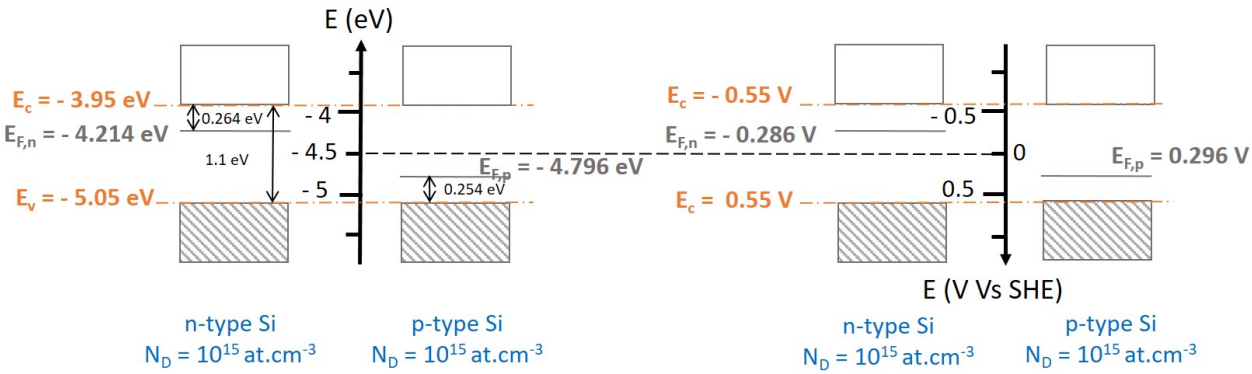

Figure 2.6: Si band diagrams for n and p-type Si with $N_{D,A}$ = 10^{15} at.cm^{-3} at 300 K, relatively to solid energy scale on the left and SHE energy scale on the right.

At equilibrium, the electrolyte is defined by a redox potential E_{redox} in solution given by the **Nernst's relation**:

$$E_{redox,eq} = E^0 + \frac{RT}{zF} ln(\frac{[Ox]_{eq}}{[Red]_{eq}}) \tag{2.5}$$

With E_0 the standard redox potential, R the universal gas constant, T the temperature, z the number of electrons exchanged, F the Faraday's constant, $[Ox]_{eq}$ and $[Red]_{eq}$ the molar concentration of redox species at equilibrium.

By applying the equation 2.3, the corresponding redox Fermi level $E_{F,redox}$ can be determined and the electrolyte can be described by $E_{F,redox}$, the work function ϕ_{el} and the energy level of occupied (E_{ox}) and vacant states (E_{red}) (see Figure 2.7). In the electrolyte, ions and molecules interact with redox species such as solvent molecules are polarized around ions to form an "outer solvatation shell". It has been stated that thermal fluctuations into the electrolyte lead to fluctuation of ion polarization. Consequently, electronic energy states in electrolyte are not statics but fluctuate around a most probable value (E_{ox}) or (E_{red}).

In addition, charges exchanges require rearrangement or relaxation of the solvatation shell (Franck-Condon electron energy shift) thanks to reorganization energy λ_S given by equation 2.6. λ_S depends on the ion radius and solvent dielectric constant and is difficult to measure. However, it can be approximated to $\approx$ 1 eV. The density of occupied and empty states in the electrolyte (D_{ox} and D_{red} respectively) can be described by a Gaussian distribution according to equation 2.7.

$$\lambda_S = \frac{E_{ox} - E_{red}}{2} \tag{2.6}$$

$$\begin{aligned} D_{ox} &= D^0_{ox} \frac{1}{\sqrt{4\pi\lambda_s k_B T}} \exp\left(-\frac{(E - E_{ox})^2}{4\lambda_S k_B T}\right) \\ D_{red} &= D^0_{red} \frac{1}{\sqrt{4\pi\lambda_S k_B T}} \exp\left(-\frac{(E - E_{red})^2}{4\lambda_S k_B T}\right) \end{aligned} \tag{2.7}$$

With D^0_{ox} and D^0_{red} normalizing factors, k_B the Boltzmann's constant, T the temperature, λ_S the reorganization energy, E_{ox} and E_{red} the most probable electronic energy states of redox species.

2.3.2 Band bending in the semiconductor

When a semiconductor is immersed in an electrolyte, the respective Fermi levels will equalize through electronic exchanges. That leads to a band bending into the semiconductor and specific charges distribution in the electrolyte. Similarly to the behavior observed at metal/semiconductor interface (see section 2.2), the potential drop V_{SC} is mainly supported by the semiconductor in a SCR having a thickness W. Three behaviors are observed depending on the relative Fermi level position before contact as illustrated in Figures 2.7 and 2.8 for n-type and p-type semiconductor respectively.

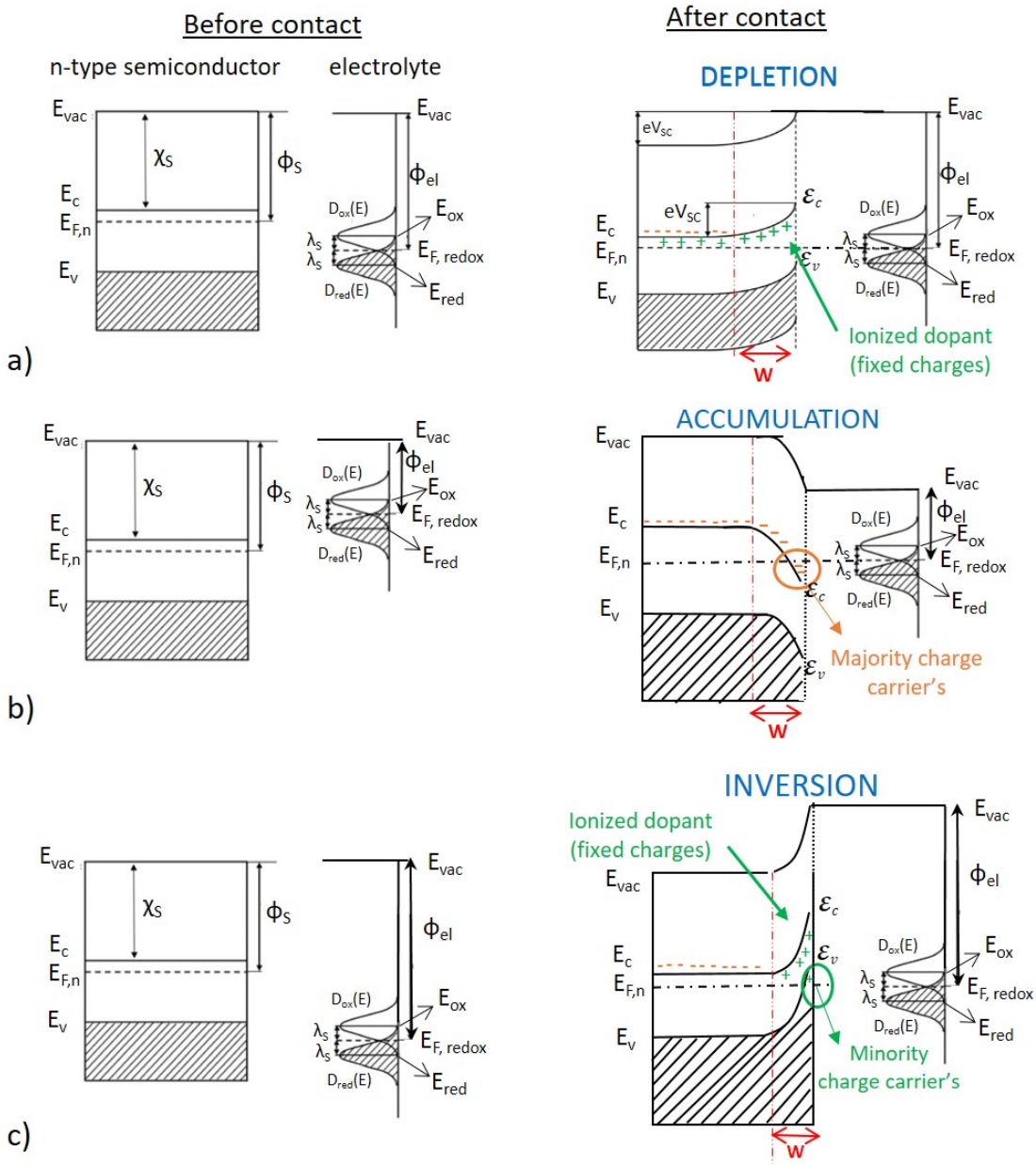

Figure 2.7: Schematic representation of a) Depletion, b) Accumulation, c) Inversion behaviors when a n-type semiconductor is in contact with an electrolyte. W represents the SCR's thickness.

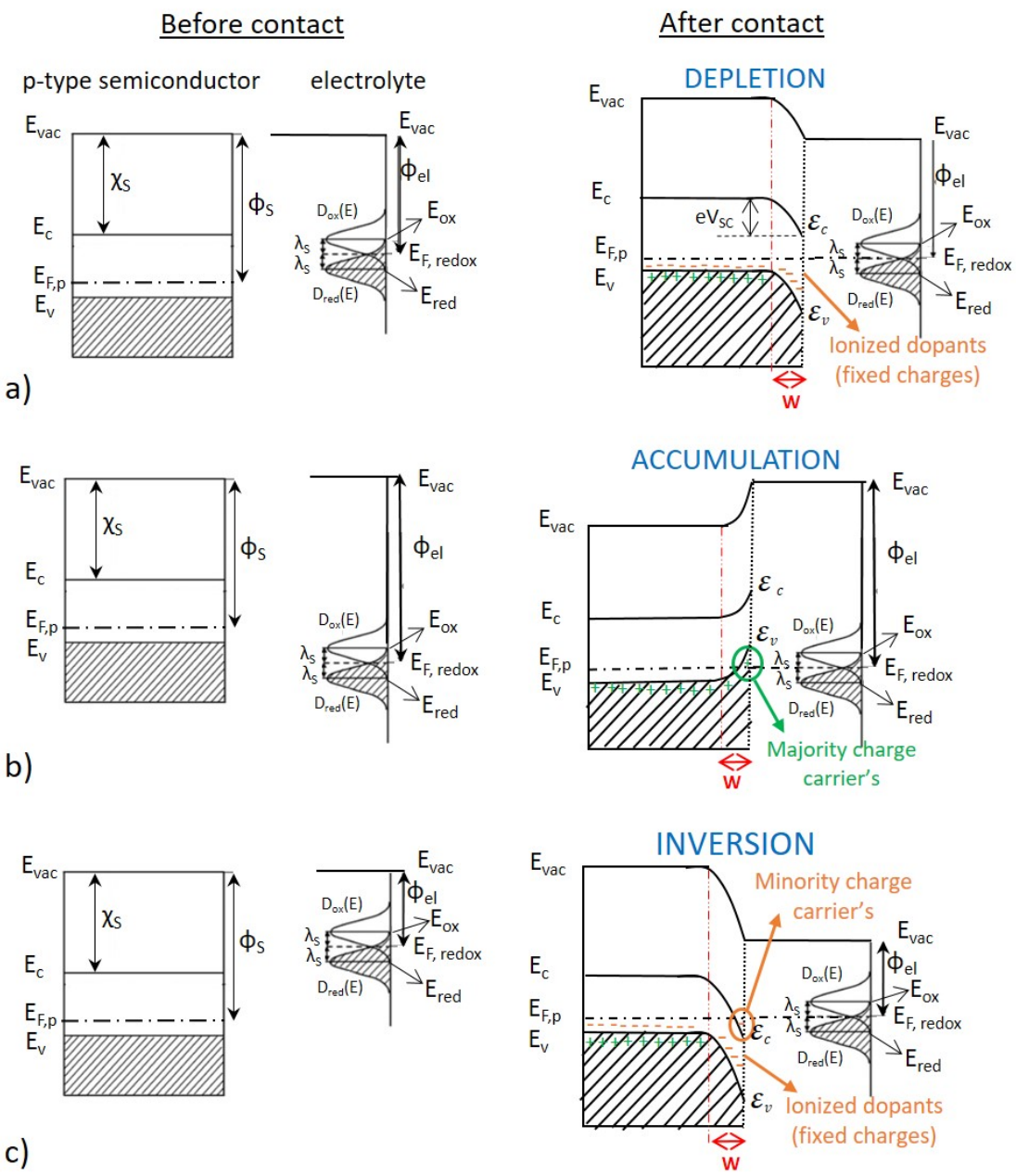

Figure 2.8: Schematic representation of a) Depletion, b) Accumulation, c) Inversion behaviors when a p-type semiconductor is in contact with an electrolyte. W represents the SCR's thickness.

- Depletion (Figure 2.7 a) and 2.8 a)): The surface is depleted of the majority carriers leading to a positive or a negative band bending for n-type and p-type semiconductor respectively. Depleted zone has no mobile charges but contains remaining fixed charges from ionized dopants in the SCR.
- Accumulation (Figure 2.7 b) and 2.8 b)): The surface has an excess of majority carriers and negative band bending is observed on n-type semiconductor while p-type semiconductor demonstrates a positive band bending.
- Inversion (Figure 2.7 c) and 2.8 c)): It is a specific case of depletion regime. Here, the Fermi level equalization requires a potential drop higher than the semiconductor bandgap. The semiconductor Fermi level crosses the minority carriers band, leading to accumulation of mobile minority carriers at the

surface. Inversion is sometimes difficult to obtain due to slow generation of minority carriers and we rather observe a regime called "deep depletion regime".

- Flatband: This regime corresponds to the case where no band bending is observed. The potential associated with this behavior is called the flatband potential (V_{fb}).

After contact, the SCR on the semiconductor is equivalent to a capacitor C_{SC} (in Farad) with a thickness W. C_{SC} is given by equation 2.8 and W can be determined with equation 2.9.

$$C_{SC} = \frac{dQ_{SC}}{dV} = \frac{\epsilon\epsilon_0}{W} \tag{2.8}$$

With Q_{SC} the charge in the SCR, V the potential, ϵ the material permittivity and ϵ_0 the vacuum permittivity.

$$W = [\frac{2\epsilon\epsilon_0}{qN_{D,A}}(|(V - V_{fb})| - \frac{k_B T}{q}]^{\frac{1}{2}} \tag{2.9}$$

With $N_{D,A}$ the dopant concentration, ϵ the material permittivity, ϵ_0 the vacuum permittivity, q the electron elementary charge, V the applied voltage, V_{fb} the flatband potential, k_B the Boltzmann's constant and T the temperature.

2.3.3 Charges distribution in the electrolyte: the "double layer" model

On the electrolyte side, the charges distribution at the semiconductor surface is different than in the bulk solution. The "double layer" model describes this charges distribution as represented in Figure 2.9 and two layers can be distinguished: The Helmholtz layer and the Gouy-Chapman layer.

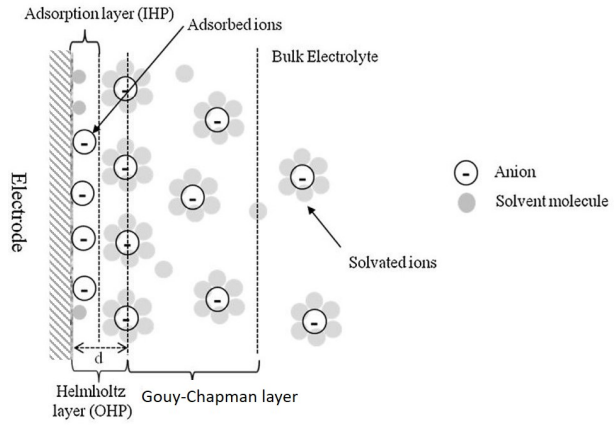

Figure 2.9: Illustration of the "double layer model" to describe the charges distribution in an electrolyte in contact with a semiconductor [75].

- **Helmholtz layer**: This compact layer is directly adjacent to the electrode and mainly contains solvent molecules. It comprises an "Inner Helmholtz Plan" (IHP), where dipolar solvent molecules and ions are adsorbed onto the electrode, and an "Outer Helmholtz Plan" (OHP) comprising solvated or complexed ions inversely polarized to the electrode. The potential drop mainly occurs in this Helmholtz layer which is equivalent to a capacitor C_H such as:

$$C_H = \frac{dQ_H}{dV} = \frac{\epsilon\epsilon_0}{d} \tag{2.10}$$

Where Q_H is the accumulated charges in Helmholtz layer, ϵ the material relative permittivity, ϵ_0 the vacuum permittivity and d the Helmholtz layer thickness ($\approx$ 5 - 10 Å in most cases).

- **Gouy-Chapman layer**: This is a diffused layer formed by solvated or complexed ions inversely polarized to the electrode and free to move up to the OHP. It appears when accumulated charges in the Helmholtz layer do not compensate the counter-charge in the semiconductor. In concentrate electrolytes ($\geq$ 0.1 M), the Gouy-Chapman layer is so compact that it can be confounded with the Helmholtz layer and becomes negligible.

The possibility to exchange charges between the semiconductor and the electrolyte depends on the relative position of E_{ox} and E_{red} to anchoring band $\mathcal{E}_C$ and $\mathcal{E}_V$ after that Fermi level have been equalized. Thus, four charges transfers mechanisms are possible as illustrated in Figure 2.10. Electrons flow from the CB to the oxidized species in solution or from the reduced species to the CB. Holes can flow from the VB to the reduced species in solution or from oxidized species to VB. Finally, the semiconductor undergoes cathodic and/or anodic decomposition or is stable for both reactions.

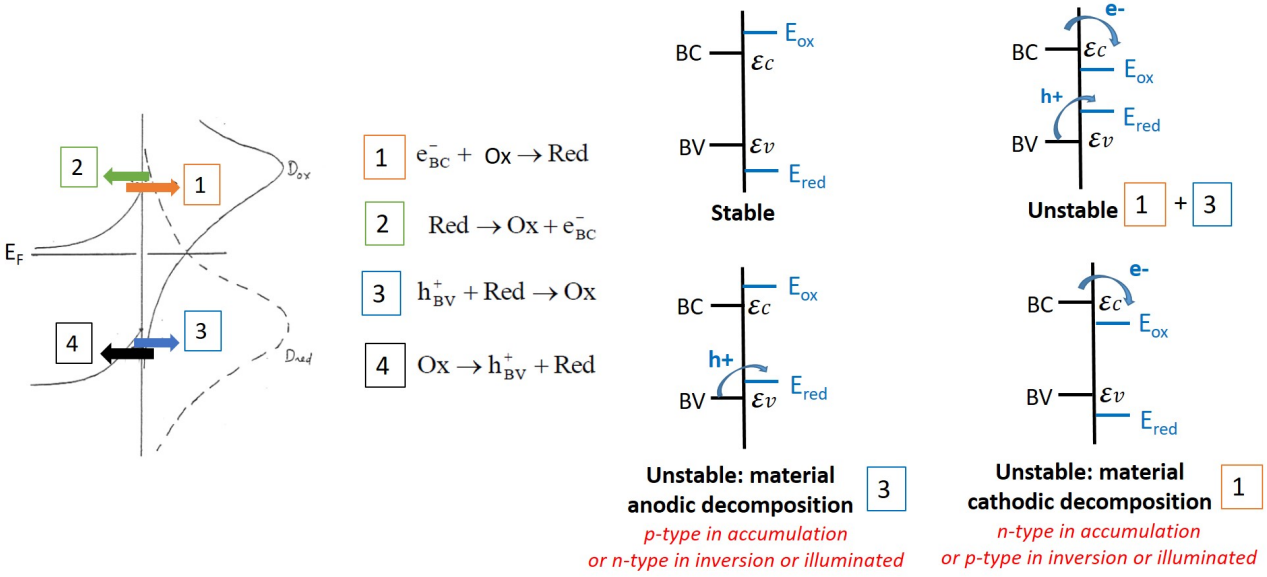

Figure 2.10: Illustration of possible charges transfers at semiconductor/electrolyte interface. Reactions 1 and 3 are the most common but reactions 2 and 4 can occur in case of strong reducing or oxidant agents respectively.

Finally, the total capacitance (C_T) of the device semiconductor/electrolyte can be described according to the semiconductor capacitance (C_{SC}) and the capacitance of the double layer (C_{DL}) by equation 2.11:

$$\frac{1}{C_T} = \frac{1}{C_{SC}} + \frac{1}{C_{DL}} \tag{2.11}$$

Most of the time, $\frac{1}{C_{DL}} \ll \frac{1}{C_{SC}}$ and the junction capacity is approximately equal to the semiconductor capacity. In addition, the semiconductor capacity C_{SC} is related to the potential drop into the SCR (V_{SC}) according to the Mott-Schottky relation:

$$\frac{1}{C_{SC}^2} = \frac{2}{\epsilon\epsilon_0 q N_{D,A}}((|(V - V_{fb})|) - \frac{k_B T}{q}) = \frac{2}{\epsilon\epsilon_0 q N_{D,A}}(|V_{SC}| - \frac{k_B T}{q}) \tag{2.12}$$

With ϵ the material permittivity, ϵ_0 the vacuum permittivity, q the electron elementary charge, $N_{D,A}$ the density of dopants, V the applied voltage, V_{fb} the flatband potential, V_{SC} the potential drop in the semiconductor, k_B the Boltzmann's constant and T the temperature.

2.4 Metallization of c-Si solar cells: screen-printing

2.4.1 Working principle

Solar cells using SP for metallization were first developed in the 1970's. Nowadays, SP is the most mature and the mainstream metallization technology for c-Si solar cells. For the front side, Ag-based pastes are preferred because Ag is the best electrical conductor (σ_{Ag} = 6.2 x 10^7 S/m) while cheaper Al-based pastes are used on the rear side to promote BSF formation. Metallic pastes for SP are commonly made up of:

- metallic particles of the metal to be deposited;
- solvents to limit particles clustering;
- organic binders to adjust the paste viscosity and cohesion of the components;
- glass frit (glass silicates + lead oxide (PbO)) to penetrate the paste through dielectric layers and promote metallic contact formation. Glass frit is necessary in case of Ag-paste as front side metallization requires the etching of dielectric layers but Al pastes do no need glass frit.

The working principle for Ag silver paste SP on the front side of a c-Si solar cell is illustrated in Figure 2.11.

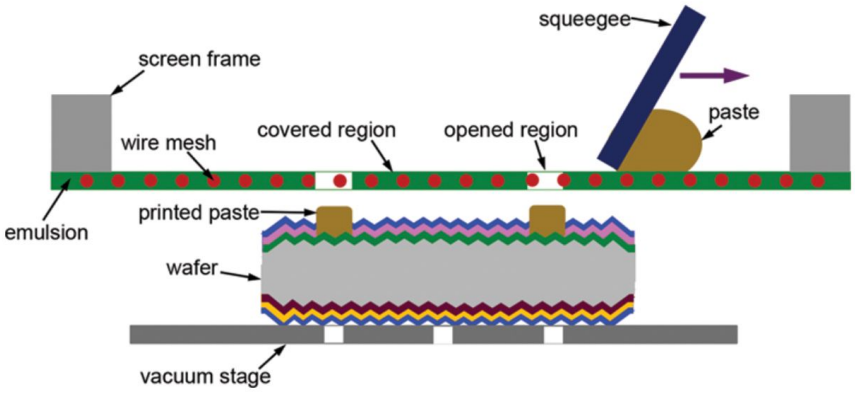

Figure 2.11: Working principle of screen-printing metallization process [76].

The mesh of the screen is on top of the Si substrate and a flood-bar distributes the metallic paste to fill the mesh. Then, the paste is pushed into the open area by a squeegee. After paste deposition, sample is dried in an air oven at 150-270°C to evaporate solvents and is placed in a convector belt furnace for the co-firing of screen-printed front and back contacts and the formation of the metallic contacts (sintering step).

Physico-chemical mechanisms involved in Ag/Si contact formation are complex and still under investigations to adjust the firing process. However, a global mechanism is described in literature (see Figure 2.12). Firstly, a temperature plateau between 300 and 500°C allows the pastes to solidify. From 500°C, the frit melts and wets the Ag/SiN_x interface. Between 500 and 650°C, the PbO reacts and penetrates the SiN_x ARC according to reaction 2.13 (see Figure 2.12 a)):

$$2PbO + SiN_x \rightarrow 2Pb + SiO_2 + \frac{x}{2}N_2 \tag{2.13}$$

Ag can also etch the SiN_x after dissolving in frit as silver oxide (Ag_2O) according to reaction 2.14:

$$SiN_x + 2Ag_2O \rightarrow 4Ag + SiO_2 + \frac{x}{2}N_2 \tag{2.14}$$

Ag-Pb alloy formed during this process assists in liquid-phase the sintering of Ag (see Figure 2.12b)). Above 650°C, Ag dissolves into the frit and diffuses towards the emitter surface. In the vicinity of the Si emitter surface, Ag ions are consumed to oxidize Si into SiO_2 and deposit metallic Ag on the emitter surface (Figure 2.12 c)). This requires to first oxidize Ag (reaction 2.15) before Si oxidation (reaction 2.16):

$$2Ag + \frac{1}{2}O_2 \rightarrow Ag_2O \tag{2.15}$$

$$2Ag_2O + Si \rightarrow SiO_2 + 4Ag \tag{2.16}$$

The formed SiO_2 is incorporated into the molten frit. During the cooling, the solubility of Ag in the melt decreases and nanocrystals precipitate within the glass matrix (see Figure 2.12 d)).

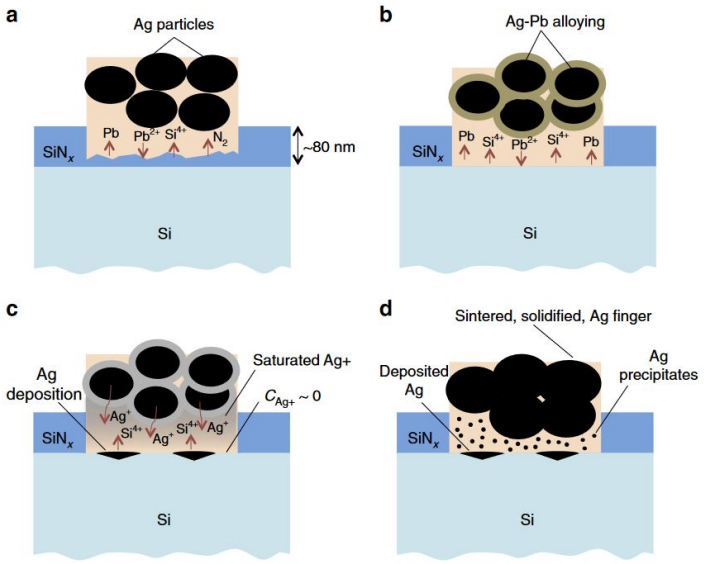

Figure 2.12: Stages of Ag-Si contact formation during firing (a) SiN_x etching by PbO in the frit, (b) Ag-Pb alloying, (c) Ag^+ transport through molten frit and deposition at the Si surface, (d) Resulting fired-contact morphology, with inclusion of small Ag precipitates within the glass intermediate layer [77].

Concerning the annealing of SP Al paste, the Al-Si phase diagram [78] indicates that the eutectic point occurs at 12.2%$_{at}$ Al at 577°C. Thus, at temperatures above this eutectic point, Al and Si interdiffuse which creates the Back Surface Field on the rear side of the cell.

During the co-firing of SP contacts, hydrogen also diffuses from SiN_x:H layer to Si underlying which provides passivation properties.

2.4.2 Screen-printing advantages and drawbacks

Main advantages of SP are its simplicity and quickness, enabling to achieve throughputs $>$ 6000 wafers/hour in the market [10]. SP has been constantly improved regarding the standard Al-BSF architecture and is well implemented in industry. However, some limitations remain in terms of process conditions and quality of metallic contacts:

- Around 70% of SP pastes still contain lead [10]. With respect to the 2011 legislation on the Restriction of use of hazardous substances, it is primordial to go towards lead-free metallization ways.
- SP relies on expensive Ag pastes. For instance, calculations based on the last ITRPV roadmap evidence the need to considerably reduce Ag consumption in order to develop a sustainable PV technology at the multi-TeraWatt level. Ag consumption varies from 100 to 270 mg/cell depending on the cell concept, which represents 3.6 to 9.7 g/module (36 cells/module). In the last three years, around 100 GW PV capacities have been installed per year, corresponding to 317.46 million additional modules if we consider a production of 315 W/module. On this basis, PV industry requires 1142 to 3079 tons of Ag/year, so 4.66 to 12.58% of annual Ag production (24468 tons of Ag produced in 2018 [5]). Considering a scenario where PV contributes to a 100% renewable energy-based power sector (ITRPV scenario 3), the objective would be to achieve 10 TW of PV capacity within 2035. That represents an increase of around 600 GW/year and a consumption of 28 to 75% of Ag produced per year. Paste consumption therefore needs to be reduced and ITRPV estimations for Ag consumption are given in Figure 2.13 [10]. Following this trend requires the improvement of SP technique or the development of alternative metallization technologies. The need to reduce metal consumption and/or use cheaper metals is also important in case of Si/perovskite tandem solar cells where the aim is to have a low cost Si bottom cell. It is worth to mention that SP can be based on other metals (Cu, Ni or Zn) but this necessitates optimization of paste formulation and process temperatures which is not tackled [79], [80].

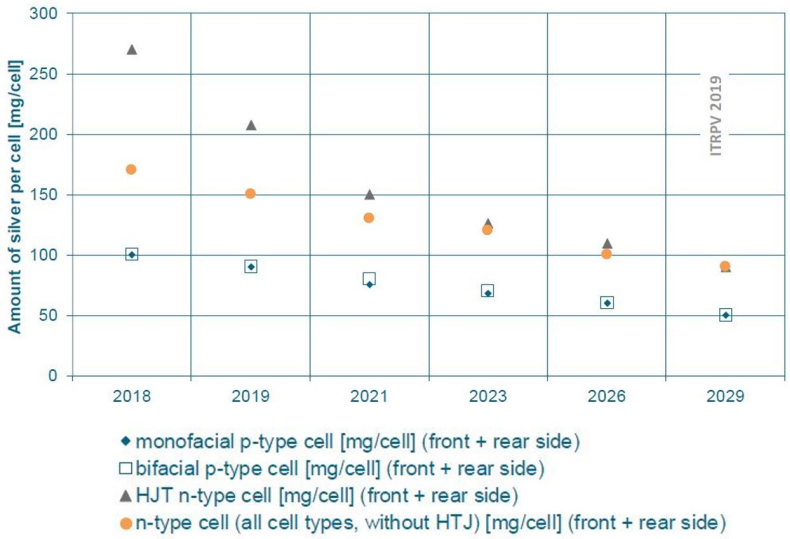

Figure 2.13: Trends for Ag consumption per cell (156.75 x 156.75 mm^2) for various c-Si cell concepts [10].

- SP pastes lead to porous contacts which increases contact and line resistances.
- Contacting lowly doped emitters with Ag SP pastes remains a challenge. As explained in section 2.2, higher surface doping concentrations are needed to decrease the SCR thickness and increase the possibility of quantum mechanical tunneling of the charges carriers through the Schottky barrier.
- Boron emitters remain difficult to contact with common Ag SP pastes. This is probably due to a lack of surface defects compared to phosphorus emitters where precipitation of P atoms on the surface

induces Ag crystal growth [81]. Addition of Al in Ag pastes facilitates contact formation but causes shunt risks due to Al spiking into Si. As a reminder, advanced c-Si technologies presented in Chapter 1 (PERT, HJT, IBC ...) are based on n-type wafers having boron emitters.

- Finger line width is within the range of 35-40 µm [10] but it becomes more and more difficult to be lowered. Finger line width must be as narrow as possible to limit shadowing effect and reduce metal consumption. In addition with the trend to go to multi-busbar and busbarless cells, SWCT introduced in section 1.5.3 necessitates narrower finger lines or other metallization scheme [57] to significantly improve conversion efficiency. To achieve efficient current conduction, high aspect ratios (height/width) are also needed and conventional SP pastes achieve values ranging from 0.2 to 0.5 [82]. As explained in Chapter 1, bifacial c-Si solar cells are progressively replacing the monofacial ones, which necessitates to improve alignment accuracy of metallic contacts. Figure 2.14 represents ITRPV expectations for finger width and alignment precision within 2029.

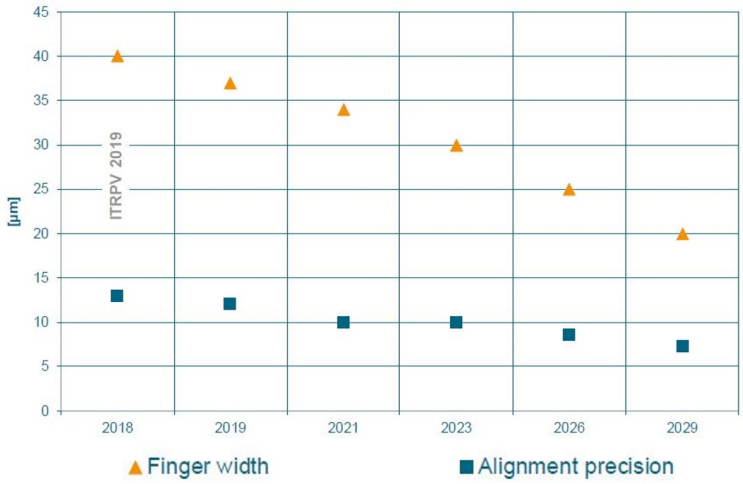

Figure 2.14: Predicted trend for finger width and alignment precision from 2018 to 2029 [10].

- Front and rear sides can not be metallized at the same time and two printing sequences are needed.
- To decrease production costs, the trend is to reduce progressively wafers thickness. As a pressing process, SP leads to breakage risks which is an issue to process thin wafers.
- Shuntings are observed in case of SP metallization for c-Si cells with Poly-Si passivated contacts [83]. SP firing-through pastes must be adapted to avoid etching of Poly-Si stacks.
- SP requires high annealing temperatures ($\approx 800°C$). Not only it implies a thermal budget, but it is also not well adapted for HJT cells which are destroyed under high temperatures. Low temperature Ag pastes are under development but are still expensive [56].

To overcome SP limitations, researchers continue to improve SP process and investigate derivative techniques based on ink or pastes. To improve the metallic contacts quality, the aim is to achieve lower line width, better aspect ratio, higher metal density, lower metal contact resistivity and reduced shunt risks. To lower the production costs, the metallization process can be simplified with lower temperatures, reduced metal consumption and/or cheaper metals. Recent advancements are presented in the next section.

2.4.3 Screen-printing improvements and derivatives techniques

Screen-printing improvements:

R&D efforts are made to better understand the reactions involved in contact formation with Ag pastes and to control Ag nanocrystals microstructure. For instance, to know the temperature at the solar cell surface during firing steps, in-situ IR thermography can be used. In addition, some experiments have shown that Ag nanocrystals microstructures can be controlled by supplying electrons at the interface during firing [84].

Researchers also aim to optimize pastes chemistry. In particular, the replacement of the traditional PbO glass frit by tellurium oxide is one of the major improvement in the last years [84]. Lower line widths are achievable through paste rheology optimization (capillary suspensions [85]), screen angle modification [84], [86] or screen design [84]. Reactive Ag inks are also under investigation. They are composed of the chemical reaction precursors instead of particles in suspension in a solvent, which enables to reduce process temperatures, Ag consumption, metal resistivity and porosity.

To increase throughputs, new approaches are under development such as rotary SP (see Figure 2.15) and Volo Flood SP [84]. Both of them do not necessitate a double printing sequence (flooding and printing) as for standard flatbed SP. So far, rotary SP is only mature for full area metallization and optimization is needed to metallize H-patterns in mass production. In addition, double printing, consisting of repeating printing pattern twice, is more and more applied in industry due to improvement of printer alignment accuracy [82]. Double printing allows to achieve better aspect ratio with limited fingers interruptions.

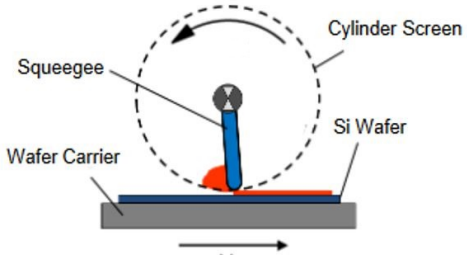

Figure 2.15: Schematic representation of rotary screen-printing concept [82].

Constant SP improvements explain that this technique is going to stay the mainstream one in the near future. However, to overcome current SP limitations, derivative techniques using pastes or inks are studied. They are sometimes more suitable to print fingers and can be used in a dual-printing process where fingers and busbars are printed separately with two different techniques.

Screen-printing derivatives:

1. **Stencil printing** [82], [87]: the use of stencil screen instead of mesh screen provides 100% open finger area (60% for SP) and enables an excellent paste transfer. Finger height is increased, width is reduced (better aspect ratios) and efficiencies up to 21.1% on PERC cells have been already demonstrated which represents a gain of 0.2%$_{abs}$ compared to SP. Stencil printing is especially suitable for finger printing where very narrow printed areas are required. However, stencils are more expensive and sensitive

than mesh screens and thus necessitate a careful monitoring. Stencil printing is not yet ready for mass production but is promising and could share 2-3% of the market by 2029 [10].

2. **Flexographic printing** [82], [88], [89]: a ink is deposited on a cylindrical flexible relief printing plate to be transferred onto the solar cell (see Figure 2.16). This technique has the potential to achieve higher throughputs than SP while providing low finger width and low printing pressure. It is also more precise for rough substrates like textured Si wafers. However, insufficient paste transfer is observed leading to high lateral finger resistance. As a result, contacts must be thickened with another printing process. Flexographic printing could be especially suitable for busbarless cell concept where lower lateral finger resistance are needed. However, this technique is not yet used in mass production.

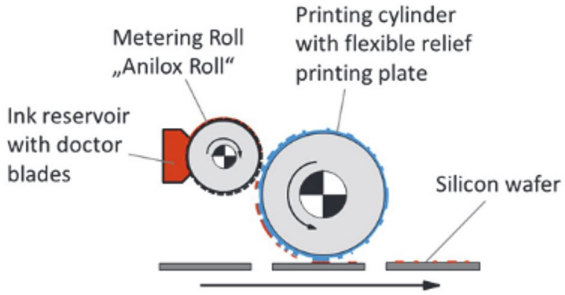

Figure 2.16: Schematic representation of flexographic printing concept [88].

3. **Dispensing** [82], [85], [90]: this contactless method consists of metallic paste ejection from several nozzles thanks to an high pneumatic pressure (see Figure 2.17). It is flexible, fast and provides narrow fingers with high aspect ratios. SP pastes must be adapted to prevent paste spreading and intermittent dispensing and nozzle clogging issues must be tackled for mass production implementation [84].

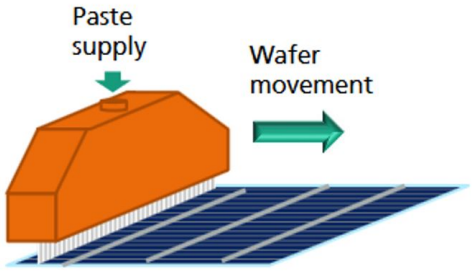

Figure 2.17: Schematic representation of dispensing printing concept [82].

4. **Aerosol jet printing and inkjet printing** [72], [82]: Both are contactless methods consisting of fluid ejection through a nozzle (as droplet ink or aerosol form). They are less attractive in comparison with dispensing because as-obtained contacts are thin and need to be thickened.

5. **Pattern Transfer Printing (PTP)** [84], [91]: a laser irradiation is used to transfer a paste, patterned in a molded polymer, to the wafer surface as described in Figure 2.18. Reproducible contacts with 20 µm line width and a 50% aspect ratio can be obtained but commercial SP pastes are not suitable for this technique and new paste formulations must be investigated.

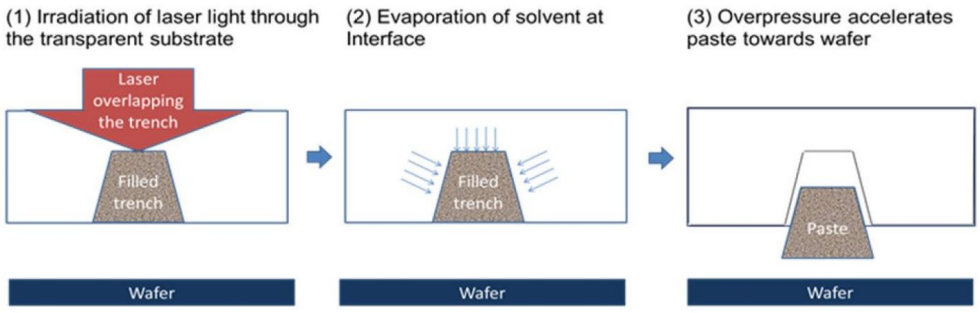

Figure 2.18: Schematic representation of the pattern transfer printing technology [82].

Current improvements of SP metallization and SP derivatives techniques are summarized in Table 2.1.

Table 2.1: Advantages and drawbacks of screen-printing metallization and current improvements.

SP advantages	SP drawbacks	Area of improvement	
		SP improvements	SP derivatives
- Simple - Fast - Well implemented in industry	- Expensive Ag pastes - 70% pastes contain lead - Porous contacts (increases contact and line resistances) - Difficult to further reduce finger width - Difficult to contact lowly doped and boron emitters - Pressing process - Not well adapted to HJT - Alignment accuracy must be increased	- Better understanding of reaction mechanisms - Rotary SP and Volo Flood SP - Paste chemistry optimization - Paste rheology improvement (capillary suspensions) - Development of reactive inks - Change of screen angle - Modification of screen design - Double printing process - Investigation of low temperature Ag pastes	- Stencil - Flexographic - Dispensing - Aerosol - Inkjet - Paste transfer

Besides, metallization techniques not relying on pastes/inks have been studied as an alternative to SP. Plating is a promising one and is detailed in the next section. Others exist but most of them are not really used in Si solar cell industry:

- Photolithography: Despite that good contact quality can be achieved, the numerous steps and the process complexity make this technique too expensive and not compatible with industry.
- Physical vapor deposition: It can be used to fully metallize the rear side but requires a mask and implies an important waste of metal for specific patterns. In addition, this process is slow and expensive.
- Metal powder sintering with laser: This technique can damage the sample and deposited metal is thin and need to be thicken by another technique.

2.5 Metallization of silicon solar cells: Plating

2.5.1 Working principle of plating

Plating consists of electrochemical deposition of metals on a conductive or semiconductive surface. The surface is immersed in an electrolyte bath containing the metal cations which are reduced and deposited on the surface. Depending on electrons source, we can distinguish three electrochemical deposition reactions illustrated in Figure 2.19.

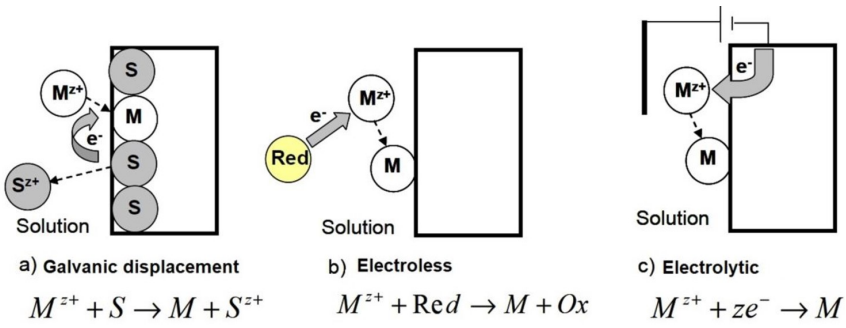

Figure 2.19: Electrochemical deposition methods: a) Galvanic displacement, b) Electroless, c) Electrolytic [92].

- **Galvanic displacement deposition:** $M^{2+} + S \rightarrow M + S^{2+}$
  Electrons are provided by the substrate (see reaction 1 in Figure 2.10) and deposition is performed in Open Circuit Potential (OCP) conditions. Galvanic displacement is thermodynamically possible when the standard redox potential of the metal to be deposited is superior to the one of the base material ($E_{(M^{2+}/M)} > E_{(S^{2+}/S)}$). The base material is dissolved meanwhile the metallic ions are reduced on the surface [93]. When $E_{(M^{2+}/M)}$ is very high (strong oxidizing agent), the deposition can occur through holes injection into the VB (see reaction 4 in Figure 2.10). The process is auto-limitated and stops as soon as the base material is completely recovered. Deposited film follows precisely the surface roughness and its thickness is typically within the range of hundreds nanometers.

- **Electroless deposition:** $M^{2+} + Red \rightarrow M + Ox$
  Electrons come from a reducing agent in the solution and deposition is performed in Open Circuit Potential (OCP) conditions. Provided that the standard redox potential of the metallic cations is higher than the one of the reducing agent, this reducing agent is spontaneously oxidized, providing electrons for metallic cations reduction. To avoid substrate dissolution, the redox potential of the base material must be preferably higher than the one of metallic ions such as $E_{(S^{2+}/S)} > E_{(M^{2+}/M)} > E_{(ox/red)}$. As long as there are reducing agent and metallic cations in the solution, the deposited film continues to grow and the final thickness mainly depends on the deposition time.

- **Electrolytic deposition:** $M^{2+} + ze^{-} \rightarrow M$
  Electrons are provided by an external current or voltage source. The external voltage or current is applied between two electrodes, one of these being the base material. The properties of the deposited film, as well the deposition rate, depend on electrolytic bath formulation and applied current or voltage. Contrary to electroless deposition, current distribution is not uniform along the surface but higher deposition rates are achievable.

Electrochemical deposition processes are composed by three successive phenomena: mass transfer, surface reactions and charges transfer to the substrate (see Figure 2.20). Among this three phenomena, the slower one determines the kinetic of the deposition process. In addition, parasitic reactions can occur (i.e hydrogen evolution) and limit the current efficiency of the deposition process.

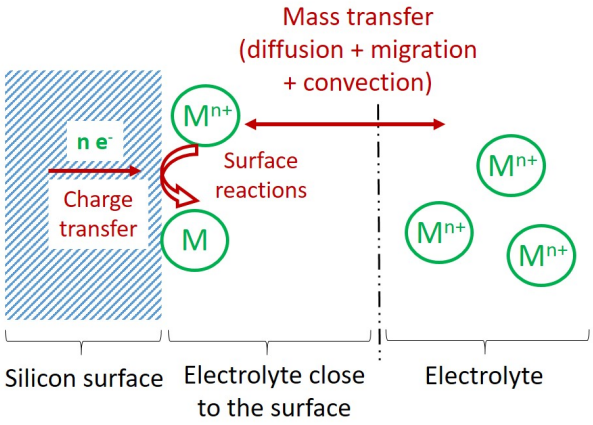

Figure 2.20: Phenomena involved in electrochemical deposition of M^{n+} cations on a silicon surface.

The mass transfer of species to an electrode can be described by the Nernst-Planck theory [94] where three mass transfer modes are involved: migration induced by an electric field, diffusion induced by a concentration gradient and convection induced by pressure, temperature or stirring. For one-dimensional mass transfer of species *i* along the x-axis, the **Nernst-Planck equation** 2.17 is:

$$J_i(x) = -D_i \frac{\partial C_i(x)}{\partial x} - \frac{z_i F}{RT} D_i C_i \frac{\partial \phi(x)}{\partial x} + C_i v(x) \tag{2.17}$$

Where J_i is the flux of species i, D_i the diffusion coefficient, $\frac{\partial C_i(x)}{\partial x}$ the concentration gradient, $\frac{\partial \phi(x)}{\partial x}$ the potential gradient, z_i and C_i the charge and concentration of species respectively, v(x) the velocity.

Surface reactions occur after mass transfer and include metallic seeds growth reactions and adsorption-desorption at the electrodes. It is followed by the charges transfer at electrodes surface.

In case of electrolytic deposition process, the quantity of substances released during electrode electrolysis is proportional to the time and the electric current according to Faraday's laws. The mass and the height of deposited material are given by equation 2.18 and 2.19 respectively [31]:

$$m = \beta \frac{MQ}{zF} = \beta \frac{MIt}{zF} \tag{2.18}$$

$$h = \beta \frac{MQ}{\rho_m A_m zF} = \beta \frac{Mjt}{\rho_m zF} \tag{2.19}$$

With m the deposited mass, β the current efficiency, M the molar mass of deposited metal, Q the charge, z the number of electron exchanged, F the Faraday's constant, I the current exchanged, t the deposition time, h the height of deposited metal, ρ_m metal density, A_m the metallized area and j the current density associated with cathodic reduction.

The current density j (if not directly applied) can be determined for an elementary reaction by equation 2.20. When reactions are not limited by mass-transfer, which means that the concentration of the electroactive species at the surface is equal to the one in the bulk this equation can be simplified as the so-called **"Butler-Volmer equation"** (equation 2.21).

$$j = j_0 \left(\frac{[Red]_{el}}{[Red]_{bulk}} exp\left(\frac{\alpha_T z F}{RT} (E - E_{eq}) \right) - \frac{[Ox]_{el}}{[Ox]_{bulk}} exp\left(-\frac{(1-\alpha_T) z F}{RT} (E - E_{eq}) \right) \right. \tag{2.20}$$

$$j = j_0(exp(\frac{\alpha_T zF}{RT}(E - E_{eq}) - exp(-\frac{(1-\alpha_T)zF}{RT}(E - E_{eq})) \quad (2.21)$$

Where j_0 the exchange current density, $[Red]_{el}$ and $[Ox]_{el}$ the concentrations of redox species at electrode surface, $[Red]_{bulk}$ and $[Ox]_{bulk}$ the concentrations of redox species in the bulk solution, α_T the charges transfer coefficient, z the number of electrons exchanged, F the Faraday's constant, R the universal gas constant, T the temperature, E the electrode potential and E_{eq} the potential at equilibrium.

2.5.2 Ni/Cu plating process steps

Typically, Ni/Cu plating applied to Si solar cells consists of seven steps illustrated in Figure 2.21. This part gives an overview of the physico-chemical reactions involved in Ni/Cu plating metallization and more details are provided in the next chapters.

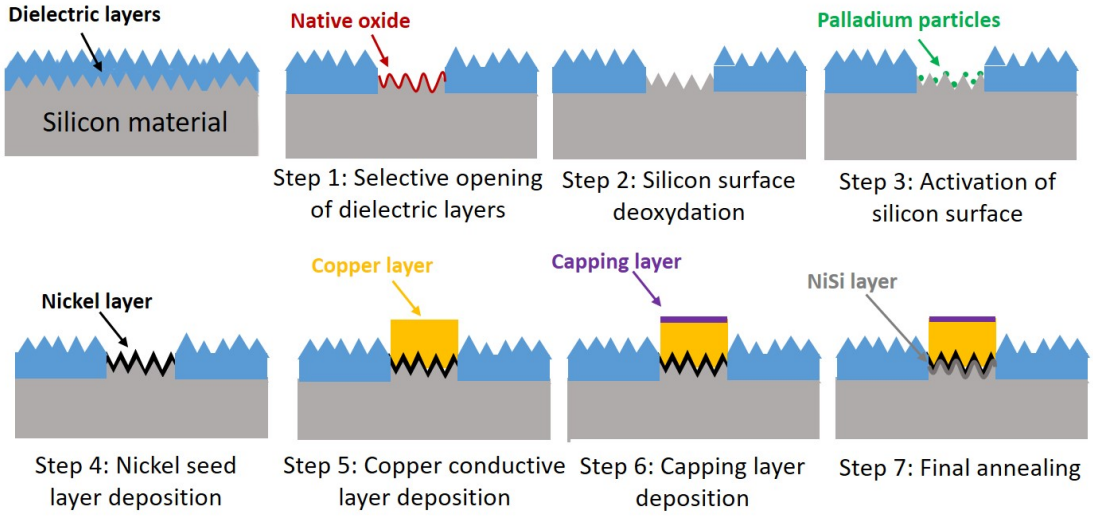

Figure 2.21: Schematic representation of a typical Ni/Cu plating process (not in scale).

Step 1: Localized opening of dielectric layers

Dielectric layers (passivation layers and ARC) must be locally removed according to a grid pattern to promote further metal deposition directly on the silicon surface. Opened area must be as narrow as possible to reduce plated finger width and limit shadowing effect. In addition, the Si underlying must not be damaged during localized opening of dielectric layers.

Laser ablation is the most widely used technique to open the dielectric layers. The main issue is the risk of emitter damaging if laser parameters are not optimized. Laser technology can be reliably integrated into production lines with high throughputs while maintaining low production costs [95]. Different type of lasers can be used such as nanoseconds, picoseconds or femtoseconds and the laser source is generally a UV, green or IR one. Laser choice is still an area of study but the trend is to move to UV-ps laser.

Localized opening of dielectric layers can be also performed using photolithography, etching pastes or mechanical scribing but these methods are not suitable for industrial applications. Photolithography enables to achieve low opened widths but photoresins are expensive and processing steps are numerous. Etching pastes are too expensive and mechanical scribing is not recommended due to the weakness of Si substrates.

Step 2: Silicon surface deoxidation

Silicon surface is spontaneously oxidized under air atmosphere according to the reaction 2.22 and can also be oxidized during the laser ablation process performed under air atmosphere.

$$Si + 2H_2O = SiO_2 + 4H^+ + 4e^- \quad \text{(E = - 0.85 - 0.0591 pH (V/SHE) [73], [96])} \tag{2.22}$$

Silicon oxide hinders further plating process step and must be removed. An ineffective removal can lead to poor adherence of plated contacts and high contact resistivity. The most widely chemical treatment used is the hydrofluoric acid (HF) (see reaction 2.23 [73], [97]). However, fluoride-based solutions can also damage the dielectric layers such as SiN_x [98] so concentration and immersion time must be well controlled.

$$SiO_2 + 6HF = SiF_6^{2-} + 2H^+ + 2H_2O \tag{2.23}$$

Step 3: Silicon surface activation through Pd deposition by galvanic displacement

It is known that palladium facilitates further Ni deposition by lowering the activation energy barrier for Ni nucleation [13], [93], [99]–[101]. Indeed, hydrogen affinity of Pd particles provides a relatively high hydrogen conversion [102] which facilitates oxidation of the reducing agent in the Ni plating bath. Nickel layers are also more adherent and uniform with prior Pd activation [103]. Activation solution contains generally a source of Pd ions and a source of fluoride ions to continuously remove SiO_x formed in aqueous media. Palladium galvanic displacement on Si in fluoride media involves two reactions: reduction of palladium ions (see reaction 2.24) and parallel Si surface oxidation (see reaction 2.22).

$$Pd^{2+} + 2e^- = Pd \quad \text{(E = 0.987 + 0.0295 log([Pd}^{2+}\text{]) (V/SHE) [96])} \tag{2.24}$$

Step 4: Nickel seed layer deposition

Nickel is deposited as a seed layer for two main reasons. Firstly, nickel acts as a barrier to prevent detrimental Cu diffusion into Si. Secondly, Ni and Si atoms interdiffuse during the final annealing, creating a nickel silicide layer with a low contact resistance. Thus, the mechanical and electrical contact with the silicon is formed. Ni seed layer thickness is generally ≤ 1 µm as a too thick Ni layer reduces the conductivity of the metallic stack (Ni conductivity is four times lower than Cu one). Various deposition techniques, such as thermal evaporation or laser assisted deposition [104], can be used but electroless deposition is preferred as a well-established and suitable process. Electroless Ni plating bath is generally composed of [105], [106]:

- A source of nickel: nickel sulfate ($NiSO_4$) is commonly used;
- A reducing agent: sodium hypophosphite ($NaPO_2H_2$) is preferred but three other sources are sometimes used: sodium borohydride ($NaBH_4$), Dimethylamineborane and hydrazine;
- Complexing agents: they are necessary to control the concentration of free nickel ions, prevent the precipitation of nickel salts and exert a buffering action. Organic acids, inorganic pyrophosphate anion or ammonium ion are examples of complexing agents used.
- Stabilizers: their role is to avoid the spontaneous decomposition of the bath. Most effective stabilizers comprise compounds of group VI elements such as sulphur and compounds containing heavy metals such as lead ions.

- Additives: for instance, accelerators can increase reducing agent reactivity and wetting agents enhance H_2 release by modifying liquid surface tension.
- Buffer agent: it is needed to maintain a constant pH value. Electroless plating can be made on either acidic or alkaline bath but alkaline baths are generally preferred.

The reactions taking place involve metals cations reduction (see reaction 2.25) and electrons are supplied by the oxidation of the reducing agent. According to the potential-pH diagram of phosphorus given in Appendix F.2, the oxidation of the reducing agent $H_2PO_2^-$ is based on various reactions depending on the solution pH (see reaction 2.26 to 2.36).

Reduction of nickel ions [96]

$$Ni^{2+} + 2e^- = Ni \quad \text{(E = - 0.25 + 0.0295 log([Ni}^{2+}\text{]) (V/SHE)} \tag{2.25}$$

Oxidation of hypophosphite ions [96]

At pH < 1.98 :

$$H_2PO_2^- + H^+ = H_3PO_2 \tag{2.26}$$

$$H_3PO_2 + H_2O = H_3PO_3 + 2H^+ + 2e^- \quad \text{(E = - 0.499 - 0.0591 pH + 0.0295 log } (\frac{[H_3PO_3]}{[H_3PO_2]}) \text{ (V/SHE))} \tag{2.27}$$

$$H_3PO_3 + H_2O = H_3PO_4 + 2H^+ + 2e^- \quad \text{(E = - 0.276 - 0.0591 pH + 0.0295 log } (\frac{[H_3PO_4]}{[H_3PO_3]}) \text{ (V/SHE))} \tag{2.28}$$

At 1.98 < pH < 6.13 :

$$H_2PO_2^- + H_2O = H_2PO_3^- + 2H^+ + 2e - \quad \text{(E = - 0.504 - 0.0591 pH + 0.0295 log } (\frac{[H_2PO_3^-]}{[H_2PO_2^-]}) \text{ (V/SHE))} \tag{2.29}$$

$$H_2PO_3^- + H_2O = H_2PO_4^- + 2H^+ + 2e - \quad \text{(E = - 0.260 - 0.0591 pH + 0.0295 log } (\frac{[H_2PO_4^-]}{[H_2PO_3^-]}) \text{ (V/SHE))} \tag{2.30}$$

At 6.13 < pH < 7.19 :

$$H_2PO_2^- + H_2O = HPO_3^{2-} + 2e^- + 3H^+ \quad \text{(E = - 0.323 - 0.0886 pH + 0.0295 log } (\frac{[HPO_3^{2-}]}{[H_2PO_2^-]}) \text{ (V/SHE))} \tag{2.31}$$

$$HPO_3^{2-} + H_2O = H_2PO_4^- + 2e^- + H^+ \quad \text{(E = - 0.447 - 0.0295 pH + 0.0295 log } (\frac{[H_2PO_4^-]}{[HPO_3^{2-}]}) \text{ (V/SHE))} \tag{2.32}$$

At 7.19 < pH < 12.03 :

$$H_2PO_2^- + H_2O = HPO_3^{2-} + 2e^- + 3H^+ \quad \text{(E = - 0.323 - 0.0886 pH + 0.0295 log } (\frac{[HPO_3^{2-}]}{[H_2PO_2^-]}) \text{ (V/SHE))} \tag{2.33}$$

$$HPO_3^{2-} + H_2O = HPO_4^{2-} + 2e^- + 2H^+ \quad \text{(E = - 0.234 - 0.0591 pH + 0.0295 log } (\frac{[HPO_4^{2-}]}{[HPO_3^{2-}]}) \text{ (V/SHE))} \tag{2.34}$$

At 12.03 < pH

$$H_2PO_2^- + H_2O = HPO_3^{2-} + 2e^- + 3H^+ \quad \text{(E = - 0.323 - 0.0886 pH + 0.0295 log } (\frac{[HPO_3^{2-}]}{[H_2PO_2^-]}) \text{ (V/SHE))} \tag{2.35}$$

$$HPO_3^{2-} + H_2O = PO_4^{3-} + 2e^- + 3H^+ \quad \text{(E = 0.121 - 0.0886 pH + 0.0295 log } (\frac{[PO_4^{3-}]}{[HPO_3^{2-}]}) \text{ (V/SHE))} \tag{2.36}$$

In addition, two main parallel reactions can occur: hydrogen evolution (see reaction 2.37) and phosphorus incorporation into the nickel layer (see reaction 2.38).

Parallel reactions: hydrogen evolution and phosphorus incorporation [96])

$$2H_2O + 2e^- = H_2 + 2OH^- \quad \text{(E = 0 - 0.0591 pH - 0.0295 log(P}_{H_2}\text{) (V/SHE))} \tag{2.37}$$

$$H_2PO_2^- + 2H_2O + e^- = P + 4OH^- + 2H^+ \quad \text{(E = - 0.391 - 0.1182 pH + 0.0591 log ([H}_2PO_2^-\text{]) (V/SHE))} \tag{2.38}$$

Electroless nickel plating can be performed at atmospheric pressure and does not necessitate high temperatures (80°C are usually sufficient). On the one hand, the deposition rate increases exponentially with temperature [106] but on the other hand, overplating (overflow of plated area) and parasitic plating (PP) (plating out of desired area which means on dielectric layers) are more likely to occur at high temperatures [92]. Parameters that must be well controlled and optimized are the composition and concentration of bath components, the pH, the temperature, the immersion time and the stirring.

Two alternatives worth to be mentioned: Light Induced Plating (LIP) [107], [108] and Forward Bias Plating (FBP) illustrated in Figure 2.22) a) and b) respectively. These methods are more related to electrolytic deposition mechanisms. LIP is based on the intrinsic capacity of Si to generate a current under illumination to perform Ni seed layer deposition on monofacial cells. In case of standard Al-BSF cell for instance, illumination of the solar cell enables to generate electrons which are drifted on the n-type area. These electrons provide reduction of nickel ions. On the contrary, photogenerated holes are drifted to p-type area causing rear side Al metal dissolution which can be prevented by contacting the rear side and applying a positive cathodic potential. FBP is used to metallize p-type Si surfaces. A forward bias current is applied from n to p type area and solar cell illumination is not necessary. Both techniques are not suitable to metallize both sides of the solar cell at the same time contrary to electroless method.

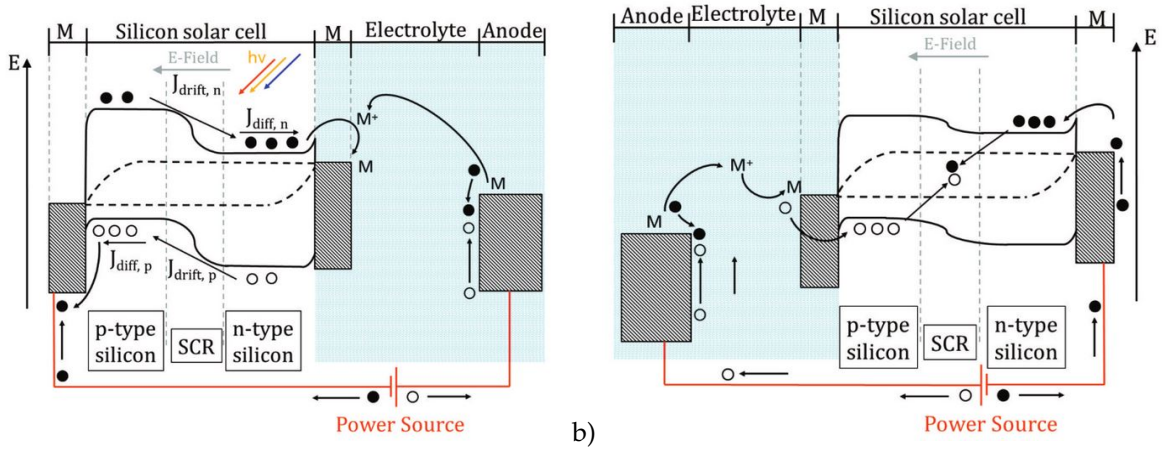

Figure 2.22: Illustration of a) Light Induced Plating (LIP) and b) Forward Bias Plating (FBP) [108].

Step 5: Copper conductive layer deposition

As explained in the introduction of this thesis, copper is a good choice to replace silver as conductive layer because it is cheaper and has a similar conductivity. However, Cu atoms can easily travel into Si

and become deep level impurities. The traps generated by these impurities act as recombination centers, decreasing the minority carrier lifetime [107]. This is prevented by deposition of Ni seed layer as described above. Cu conductive layer must be thicker than Ni seed layer to achieve low line resistance of the metallic contacts. Calculation have demonstrated that optimal Cu thickness is ≈ 10 µm [92] so electrolytic deposition method, having higher deposition rates, is the most suitable technique. The main difficulty of this method is to contact the cell without damage or break it.

A three electrode system is used with a reference electrode, a counter electrode acting like an anode and the contacted solar cell as working electrode and acting as a cathode. These three electrodes are immersed in an electrolytic bath containing [109]:

- A source of Cu ions: copper sulfate ($CuSO_4$) is mostly used. It is dissolved in the electrolyte to give free hydrated cupric ions Cu^{2+} which are reduced into copper metal on the silicon surface.
- Sulfuric acid: it is usually added to increase solution conductivity and improve surface wetting. A more conductive electrolyte leads to more homogeneous copper layers.
- Additives: accelerators, suppressors and levellers are mostly used. Accelerators are mercapto containing species which locally accelerate the current. Suppressors are polymers such as polyethylene glycol which tend to form a current suppressing film on the entire wafer surface when they are combine with chloride ions. Leveler enable to less suppress the current at isolated mass transfer locations such as the inside of a via, while protruding surfaces or corners (to which mass transfer by diffusion or migration is more efficient) are more suppressed. To obtain a conformal growth of copper, it is preferable to use these three additives as represented in Figure 2.23.
- A pH buffer: needed to maintain constant pH value. Cu electrodeposition is performed in acid baths.

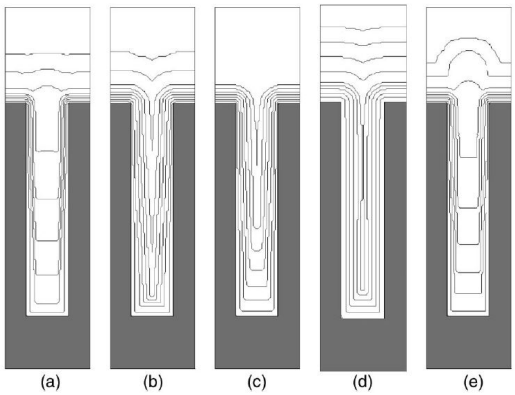

Figure 2.23: Simulated (kinetic Monte Carlo Model) shape evolution of trench fill during copper electrodeposition with various additive compositions a) accelerator, suppressor and leveller, b) only suppressor, c) no leveller and high concentration of accelerator, d) only accelerator, e) no leveller [110].

By supplying electrons through an external circuit or by applying an external voltage, Cu ions are reduced at nickel surface according to reaction 2.39. The controllable parameters of an electroplating bath are the same as for electroless deposition plus the current or voltage applied which control the deposition rate. In some cases, pulse or pulse reverse plating, consisting of applying the current as series of short pulses, can be used to improve the quality of the layer deposited [111], [112].

$$Cu^{2+} + 2e^- \rightarrow Cu \quad \text{(E = 0.337 + 0.000295 log ([Cu}^{2+}\text{]) (V/SHE) [96]} \tag{2.39}$$

Step 6: Capping layer deposition

To prevent Cu oxidation, tin or silver capping layer is deposited over Cu. That also facilitates the soldering of interconnecting tabs and limits interactions between Cu and encapsulating material.

Step 7: Final annealing

Final annealing step allows to form the nickel silicide layer through Ni/Si atoms interdiffusion. Adherence and contact resistivity of the metallic contacts are enhanced after this process [113] (see Figure 2.24).

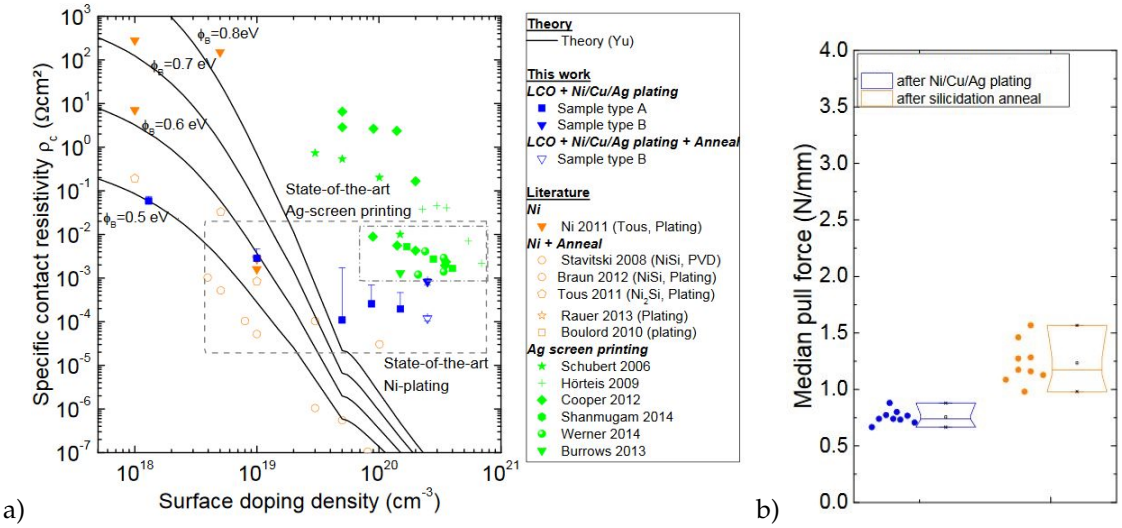

Figure 2.24: Impact of annealing process on a) contact resisitivity, b) adherence of metallic contacts [113].

Depending on annealing parameters, such as temperature and annealing time, nickel silicide stoechiometry and thickness are different. Silicide formation on solar cells from plated Ni layers is still not completely understood and the temperature ranges for nickel silicide formation proposed in literature are slightly different. Regarding the ranges in references [13], [92], [114], we propose that Ni_2Si is formed between 200 and 350°C, NiSi between 400 and 530°C and $NiSi_2$ above 650°C. The different phases are formed successively when temperature is increased and various phases can be present after annealing process as illustrated in Figure 2.25. The NiSi phase is desired because it has the lowest resistivity and Schottky barrier [114], [115].

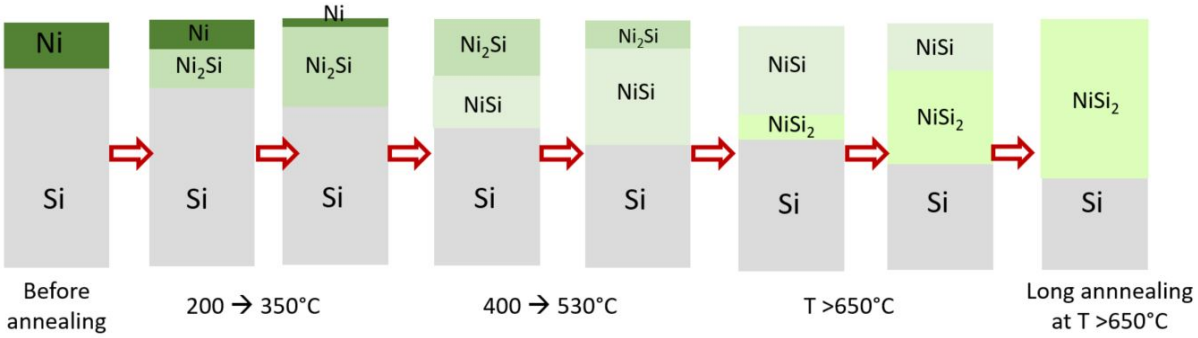

Figure 2.25: Silicidation process during annealing of plated Ni layer on Si surface (from [116], [117]).

2.5.3 Advantages and drawbacks

The different advantages and drawbacks of plating metallization described in literature [107], [118]–[120] are reported below and summarized in Table 2.2.

PLATING ADVANTAGES

Plating metallization has cost savings potential compared to standard SP and this has been already demonstrated for three or more busbars concepts [119]. Some authors have estimated that 7.5% of the cell production costs could be saved with Ni/Cu plating compared to SP, provided that the rest of the process costs remain unchanged [13]. The following advantages are related to potential cost savings:

- Silver can be replaced by **cheaper metals (Ni/Cu stack)** and only thin silver capping layer remains necessary to prevent Cu oxidation;
- **Lower final annealing temperature**. Contacts are usually formed between 250°C and 400°C with Ni/Cu plating while SP needs temperatures around 750-850°C. Thus, the thermal budget is reduced with Ni/Cu plating;
- Plating is a **selective metallization process**. It does not need masks or screens and metal waste is limited;
- Plating can **simultaneously metallize both sides** of the solar cell, reducing processing steps;
- **Costs of plating equipments are potentially lower**. Authors are however divided on this point. Some authors claim that plating equipments are cheaper (or at least do not imply additional costs) compared to SP ones [118], [119], while others are more sceptical [84];
- Plating has a great added value for SWCT and shingling interconnections as it is more **flexible** thanks to laser ablation process (flexible pattern and accurate alignments of opened areas on both sides).

Plating has also the potential to achieve better metallic contact quality, and therefore higher solar cell conversion efficiencies:

- Plated **contacts are denser**, leading to lower line resistances;
- **Finger widths are narrower**, limiting shadowing and metal consumption. For instance, 5 µm laser opened widths can be achieved with laser, leading to metallized contacts width $\approx$ 20 µm [121];
- As shown in Figure 2.24 **lower contact resistivity** can be obtained thanks to Nickel silicide formation;
- Lowly doped emitters are easily contacted due to smaller Schottky barrier ϕ_B of nickel silicides;
- Thanks to lower process temperatures, plating is more **suitable for HJT concept** [111], [122], [123]. Bifacial HJT metallized with Cu plating and having conversion efficiencies $\geq$ 24% with FF $\geq$ 82% [84] have been demonstrated. Lower temperatures process are also less detrimental for passivation layers.

PLATING DRAWBACKS

Despite its great potential, Ni/Cu metallization is still at an introductory phase and needs some improvements to be implemented in production mass:

- **Laser ablation can damage Si underlying**. Laser induced defects (cracks/dislocations, surface amorphization etc.) lead to recombination losses and, in the worst case, junction shunting [124]–[128]. Laser induced damages can provide a sink for Cu diffusion inducing an early ageing of the cell [129], [130].
- **Parasitic plating (PP)**. Plating is a selective process but it sometimes occurs on dielectric layers. That affects adversely the cell performances: 1) shading losses are increased and J_{SC} is reduced 2) there are more recombinations where PP is present and resistance losses (R_s) are increased, affecting V_{OC} 3) junction can be shunted if Cu diffuses into Si where PP is present (this is likely to occur on the cell edges when passivation is not sufficient).
- **Inhomogeneity:** Both Ni and Cu deposition rates are affected by the geometry of contact opened areas. In addition, plating is not homogeneous due to uneven laser ablation (especially on textured side) or presence of residues. As Ni/Si interdiffusion is deeper for thicker Ni layers, Ni thickness inhomogeneity can lead to junction shunting [131].
- **Poor contact adherence** of plated metallic contacts can be observed and originates from: 1) generation of voids between Ni and nickel silicide interface during annealing [114] , 2) hindering of nickel silicide formation due to presence of oxides at Ni/Si interface [114], [132], 3) Cu self-anneal at room temperature, transitioning from fine-grained to coarse-grained material. This creates stress and is detrimental for adherence [56] or 4) a lack of anchoring points on flat surfaces.
- One of the main issues restricting the commercialization of the Ni/Cu plating process is the **long term reliability issue** due to Cu ability to diffuse into Si. Few studies have been carried out to characterize Ni/Cu plated cells after thermal ageing but further investigations are needed to attest the reliability of the process [130], [133]–[136]. It has been demonstrated that Cu can also diffuse into Ag capping layer, which forms voids and induces resistance losses [135].
- **Scalability** of the process is still a subject of debate. Some manufacturers, such as Sunpower, have successfully realized plating in production lines which may serve as a proof of concept [118]. Manufacturers are however still sceptical as plating process implies to use other equipments and can be more complex that standard SP. In addition, the need to contact the cells for Cu electroplating is also challenging (risks of breakage or inefficient contact).

Table 2.2: Advantages and drawbacks of Ni/Cu plating for c-Si solar cells.

Plating advantages	Plating drawbacks
Cheaper metals (Ni/Cu)	Laser induced damages
Lower temperatures (cost savings + suitable for HJT)	Parasitic plating
Selectivity and both sides metallized at the same time	Inhomogeneous metallization
Potential lower cost equipments	Shunting risks
Denser contacts (higher line conductivity)	Poor adherence
Narrow fingers (less shadowing)	Reliability and scalability
Lower contact resistivity	
Lowly doped and boron doped emitters easily contacted	
More suitable for SWCT and shingled interconnections	

2.5.4 Area of improvements

In order to improve the plating process, lines of research for each drawback stated above are presented:

Reduction of laser-induced damages

Type and source of laser must be carefully chosen. Ultra-short laser pulses are potentially more suitable to reduce laser induced damages by limiting thermal impact into underlying silicon [127], [137]. Moreover, UV laser radiations create laser induced defects with a shallower spatial distribution [127], [138]. An alternative to limit laser induced damages is to add a buffer layer, having a low thermal diffusivity (as a-Si), between the dielectric layers and Si. The laser energy will be absorbed into the buffer layer and limit Si damages [139]. Bailly et al. have proposed another alternative by using an a-Si etch mask deposited on the SiN_x layer [140]. The mask is selectively laser ablated and a chemical treatment is performed to remove underlying SiN_x layers without damaging Si underlying. Finally, the a-Si mask is chemically removed. Good results are obtained but this alternative needs several process steps. In addition, it has been demonstrated that a post-laser annealing is beneficial through recrystallization of a-Si formed during laser ablation [141].

Limitation of Parasitic Plating (PP)

Inhomogenities of dielectric layers are mainly responsible for PP [118]. In particular, top of pyramids have sometimes thinner dielectric layers and are more susceptible to present PP. To address this issue, a double layer ARC can be used. In addition, PP can be also due to dielectric layers defects after deoxidation treatment during plating process because fluoride-based treatments also attack the SiN_x layers. Precautions must also be taken during handling to limit damage through mechanical stress. Some authors proposed to suppress deoxidation treatment and metallize the cell directly after laser contact opening. This method is called "easy-plating" [141], [142] but the added value is not clear yet.

Improvement of homogeneity

Inhomogeneity issues come from different Ni/Cu plating rates on finger and busbars. Electrolyte volume contributing to diffusional mass transfer is semi-cylindrical for narrow structures (fingers) while it is rectangular for larger structures (busbars) [118] which impacts the deposition rates. Moreover, Cu electrolytic deposition on fingers can be higher than on busbars due to lower current density on larger area. Higher concentration of electrical field lines on cell edges also leads to thicker Cu deposition on edges compared to center of the cell [118]. An alternative to these issues could be to develop plating on busbarless cells (SWCT). Furthermore, texturation step can be optimized to achieve smaller and more uniform pyramids size and thus favor homogeneous laser ablation on textured surfaces [118], [143].

Reduction of shunting risks

To reduce the risks of shunting, the homogeneity of plated contacts must be improved, parasitic plating must be limited and a suitable annealing process must be used.

Improvement of adherence

To prevent voids formation at Ni/Nickel silicide interface during annealing, the plating process can be modified so that: annealing is performed just after Ni deposition, un-reacted nickel is then removed and Ni re-plating is realized with a prior HF treatment. This alternative enables to achieve better adherence [133] but it implies additional process steps. Surface roughening through laser process is also an alternative to overcome poor adherence, especially on polished Si surface [144], [145]. In addition, performing a rapid thermal annealing (RTA) in N_2 after Cu plating enables to improve crystallinity and conductivity of fingers while removing internal stress caused by Cu self anneal at room temperature [146].

2.6 Methodology of thesis work

For all the reasons described previously, this work is focused on n-PERT cell architecture and Ni/Cu plating is performed on both sides to obtain bifacial n-PERT solar cells. Nevertheless, results obtained could be applied to other cell architectures thanks to the flexibility of the Ni/Cu plating process. The purpose of this thesis is to develop a Ni/Cu plating process for bifacial n-PERT c-Si solar cells and achieve conversion efficiencies close to the one of reference screen-printed cells. That implies to identify the factors affecting the solar cell during the process and understand the physico-chemical phenomenon involved to further optimize the successive Ni/Cu plating process steps. Characterization techniques used all along this work are detailed in Appendices.

IPVF laboratory can not provide n-PERT precursors (n-PERT cells without metallization) so they have been purchased at the International Solar Energy Research Center Konstanz (ISCK). The cell architecture is illustrated in Figure 2.26.

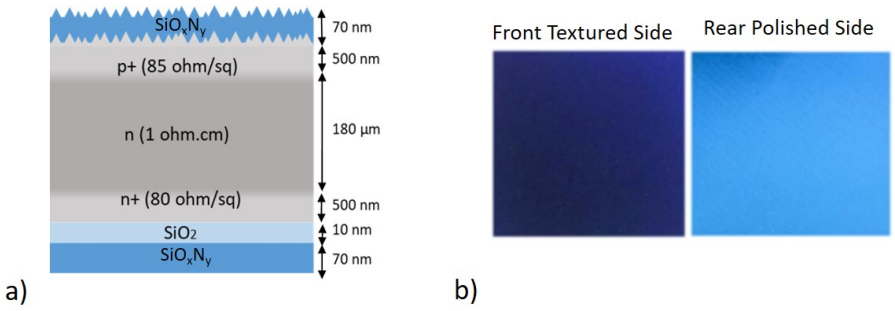

Figure 2.26: a) Structure of n-PERT precursor from ISC Konstanz, b) Picture of the both sides.

N-PERT precursors consist of a large area (156 x 156 mm^2) n-type mono-Si with a 180 µm thick base resistivity of 1 Ω.cm. The p^+ emitter is 500 nm thick with a sheet resistance (R_{sh}) ≈ 85 Ω/sq. The phosphorus doped area is 500 nm thick with a sheet resistance ≈ 80 Ω/sq. The front side is textured with random pyramids and a 70 nm thick silicon oxi-nitride (SiO_xN_y) is deposited by PECVD for passivation and antireflection properties. Its refractive index is about 2.03 according to the supplier. It is worth to mention that a thin BSG layer is kept before SiO_xN_y deposition on the front side to improve passivation properties. The rear side is polished and a PECVD oxi-nitride stack is deposited. Silicon oxide (SiO_x) is ≈ 10 nm thick and SiO_xN_y is ≈ 70 nm thick. The thickness of SiO_xN_y and SiO_xN_y/SiO_x stack have been confirmed by sectional SEM pictures.

This cell architecture implies that plating process is likely to be different on both sides. Indeed, physico-chemical mechanisms involved will depend on texturation and doping type of Si surface. In the ISC Konstanz process flow, the rear side dielectric stack is used as diffusion barrier during boron doping on the front side. As a result, it has underwent an additional thermal treatment and optical properties have been modified. The final refractive index on the rear side was not given by the supplier but is further determined.

As it is not clear yet if the rear side should be preferably polished or textured in bifacial architecture to increase light absorption, we also ordered same n-PERT precursors having both sides textured. For both precursors, reference SP cells performances given by the supplier are shown in Table 2.3. R_s and R_{sh} have

been multiplied by the surface to enable further comparison with smaller samples metallized in this work.

Cell parameters of double textured n-PERT SP references are significantly worse than the one on textured/polished cells. To explain this, it is worth mentioning that SP process at ISC Konstanz is optimized for textured/polished cells. As explained before, the dielectric layers on the rear side are used as a barrier during front side Boron diffusion. When the rear side is textured, the surface covering by dielectric layers is not as efficient as on a polished surface which can lead to shunts on the rear side after boron diffusion step and explain the lower cell parameters.

Table 2.3: Main cells parameters of 156 $\times$ 156 mm textured/polished and double textured n-PERT screen-printed reference cells given by ISC Konstanz (mean of three cells).

SP references	J_{SC} (mA.cm^2)	V_{OC} (mV)	FF (%)	η (%)	R_s ($\Omega.cm^2$)	R_{sh} ($\Omega.cm^2$)
Textu/polished	38.65 $\pm$ 0.013	655 $\pm$ 0.5	80.46 $\pm$ 0.1	20.38 $\pm$ 0.01	0.5 $\pm$ 0.02	2214 $\pm$ 1165
Textu/textu	35.94 $\pm$ 0.053	618 $\pm$ 0.3	78.11 $\pm$1	17.35 $\pm$ 0.3	0.75 $\pm$ 0.13	25408 $\pm$ 20400

Normally, passivation properties of dielectric layers are activated through hydrogen release after SP final annealing at high temperature ($\approx 800°C$). However, plated contacts can not stand such high temperatures and an annealing step prior to plating is needed on both n-PERT precursors. With the framework of a 6 months internship at EDF before this thesis, these annealing conditions have been optimized to achieve best carriers lifetimes on textured/polished n-PERT precursors. Best conditions are the following: 30 sec temperature build-up to 750°C under N_2 followed by cooling with a Jipelec Jetfirst furnace from Semco technology.

Meanwhile, some experiments have required non passivated wafers:

- n-type Si wafer, mirror polished, base resistivity $\approx$ 1.5 Ω.cm (Syltronix);
- polished and textured n and p-type wafers with 1 and 2 Ω.cm bulk resistivity respectively (ISCK);
- polished and textured n/n$^+$ and n/p$^+$ wafers wafers with 1 Ω.cm bulk resistivity and various doped area R_{sheet} (70 - 90 - 120 Ω/sq) (ISCK)

The Table 2.4 gives a global view of the thesis work objectives.

Table 2.4: Overview of thesis work objectives at each Ni/Cu plating process step.

Process step	Objectives
LASER ABLATION	- Identification of laser induced damages and impact on cell efficiency - Understanding of ablation mechanism - Optimization of laser parameters
DEOXIDATION AND ACTIVATION	- Determination of SiO_x and SiO_xN_y etching mechanisms in two fluoride media - Optimization of deoxidation bath composition to limit ARC damages - Analysis of parameters affecting Pd galvanic displacement - Optimization of activation bath composition to limit Pd consumption while achieving satisfying surface activation
NI/CU PLATING	- Identification of parameters affecting the homogeneity and adherence of plated contacts - Comparison of deposition rates on both sides - Optimization of Ni/Cu deposition conditions
FINAL ANNEALING	- Highlight the impact of annealing parameters on contact resistivity and cell efficiency - Optimization of annealing parameters

MEMENTO

Screen-printing (SP) is the mainstream metallization technology for c-Si solar cells and consists of applying a metallic paste through a mask. This technique is simple, fast and well implemented in industry but some limitations remain in term of metallic contacts quality and expensive Ag pastes are needed. SP derivative techniques, such as stencil printing and dispensing, should gain interest in the near future.

Alternative electrochemical metallization (Ni/Cu plating) is expected to gain market share as better metallic contact quality with reduced production costs are achievable compared to SP. Indeed, plating relies on cheaper metals (Ni/Cu), cost equipments are potentially reduced, process temperatures are lower, lowly doped and boron emitters are easily contacted (lower Schottky barrier), plated contacts are denser with lower contact resistivity and narrower line width. Common plating process comprises successively: the selective ablation of dielectric layers, the Si surface deoxidation and activation, the nickel electroless deposition, the copper electrolytic deposition and the final annealing.

Si/electrolyte interface is characterized by specific charges distribution into the electrolyte (Helmholtz and Gouy-Chapman layers) and a band bending into the semiconductor to equalize respective Fermi levels. Redox potential into the electrolyte is given by:

$$E_{redox,eq} = E^0 + \frac{RT}{nF} ln(\frac{[Ox]_{eq}}{[Red]_{eq}}) \qquad \text{(Nernst's relation)}$$

Into the silicon, a depletion regime is most of the time observed with a space charge region equivalent to a capacitor having a capacitance C_{SC}. In case of electrolyte concentration $\geq$ 0.1 M, C_{SC} can be related to the semiconductor flatband potential with Mott-Schottky relation:

$$\frac{1}{C_{SC}^2} = \frac{2}{\epsilon\epsilon_0 q N_{D,A}}(|V_{SC}| - \frac{k_B T}{q}) \qquad \text{(Mott-Schottky relation)}$$

charges exchanges between silicon and the electrolyte depend on valence and conduction band positions respectively to energy level of oxidized and reduced species.

Despite the great potential of Ni/Cu plating, following issues must be tackled: laser induced damages, poor adherence of plated contacts, shunt risks, parasitic plating, metallization inhomogeneity and scalability and reliability issues. This work aims to developed a Ni/Cu plating process on bifacial n-PERT Si solar cell and achieve conversion efficiencies close to the ones of reference SP cells. For that purpose, the different process steps are investigated to understand the physico-chemical phenomena involved and optimize the factors impacting the solar cell integrity and performance.

Chapter 3

Selective laser ablation of dielectric layers

CONTENTS

3.1 Introduction

In this chapter, the first step of plating process, which consists of selectively remove the dielectric layers by laser ablation, is investigated. A background on laser/matter interactions is first presented and the choice of laser type and source employed for this work is explained. Dielectric layers on both sides of textured/polished n-PERT precursors are then laser opened with various laser parameters and several characterization techniques are used to identify the laser induced damages and understand the ablation mechanism (morphological characterizations, analysis of fine chemical surface compositions and environments, electrical properties characterizations). The impact of a post laser annealing and a deoxidation treatment in fluoride media on Si surface after laser ablation is also studied. Results have enabled to optimize the laser ablation parameters on both sides of n-PERT precursors and have been published in reference [147].

3.2 Background on laser/matter interactions

The working principle of LASER (Light Amplification by Stimulated Emission of Radiation) has been described for the first time by Einstein in 1917 and is based on "stimulated emission" as illustrated in Figure 3.1 c). Contrary to absorption process, which attenuates the incident wave by photons absorption (see Figure 3.1 a)), stimulated emission amplifies the incident wave. When an electron in an excited state encounters an incident radiation resonating at the same transition frequency, it decays by emitting a photon with the same radiation mode than the incident photons (same direction and phase). A process called "pumping" is necessary to maintain the electrons in an excited state and prevent spontaneous emission in which excited electrons quickly return to their ground state by emitting photons in random directions (see Figure 3.1 b)). Pumping consists of supplying energy through an electric current or as light at different wavelengths.

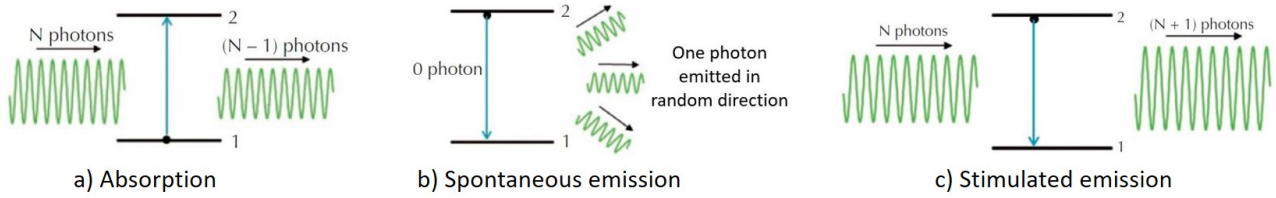

Figure 3.1: Illustration of three light-matter interactions processes: a) Absorption, b) Spontaneous emission and c) Stimulated emission.

Interaction process between the laser beam and a material depends on:

- The monochromatic laser source: the main ones are UV, green and infrared (IR);
- The pulse duration: femtoseconds (fs), picoseconds (ps) or nanoseconds (ns) pulses are mostly used;
- The laser beam energy, called the fluence (J/cm^2): it represents the quantity of photons at each x-position of the laser beam and depends on the laser frequency and power;
- The overlap of laser pulses which can be modulated by the scan rate;
- The material properties: the bandgap determines the capacity to absorb the laser energy and absorption properties modulate the quantity of photons absorbed.

The incident laser beam energy can be determined by the Planck-Einstein relation (equation 3.1). Energy of UV, green and IR laser beams have been calculated by using this equation and results are given in Table 3.1. Since silicon has a bandgap of 1.12 eV at 300 K and 1 eV = 1.60 10^{-19} J, an energy E $\geq$ 1.12 x 1.60 10^{-19} = 1.79 10^{-19} J is required to be absorbed into silicon material. UV, green and IR radiations can therefore be absorbed by silicon material.

$$E_{ph} = h\nu = h\frac{c}{\lambda} \tag{3.1}$$

With h the Planck's constant, ν the frequency, c the light celerity and λ the wavelength of incident wave.

Table 3.1: Calculated energies of UV, Green and IR laser beam.

Wavelength (nm)	355 (UV)	532 (green)	1064 (IR)
Photon energy (J)	5.6 x 10^{-19}	3.7 x 10^{-19}	1.9 x 10^{-19}
Photon energy (eV)	3.5	2.3	1.2

Normally, a laser beam having an energy lower than the material bandgap can not be absorbed, but, this becomes possible in specific conditions. At high optical intensity, the bandgap can be bridged by simultaneous absorption of two or more lower-energy photons, if the sum of their energies exceeds the bandgap (see Figure 3.2). This non-linear optical phenomenon is called "multi-photon absorption" and is more likely to happen with ultra-short or short laser pulses, combined with high laser intensities (high fluences) [148], [149].

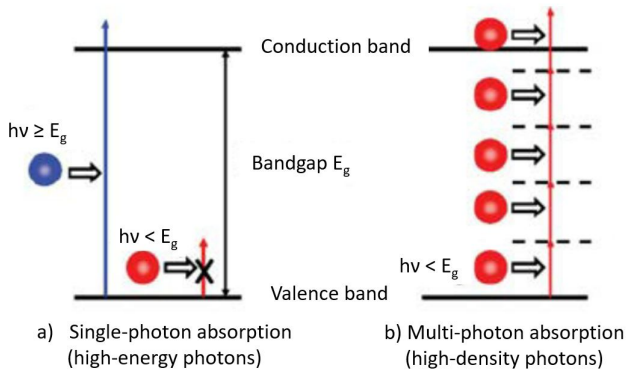

Figure 3.2: Illustration of photon absorption through a) single-photon absorption when $E_{ph} \geq E_g$, b) multi-photon absorption in case of high photon flux with $E_{ph} \leq E_g$ [149].

After photons absorption, excited electrons can collide each others, leading to electron temperature increase. Excited electrons can also interact with the lattice and transfer their energy with a phonon emission and an increased lattice temperature. When the material is thermalized and turns into a liquid phase due to the laser process, its optical properties are modified. Indeed, material bandgap is smaller when the temperature increases, so more carriers are produced, reinforcing the absorption process (cascade-like effect) [148]. Matter thermalization also leads to phase transition and ablation of the material. The transition from solid to gas phase can occur by melting of the solid (fusion) followed by evaporation of the liquid or, under specific conditions, by a direct transition from solid to gas phase (sublimation) [150]. It can be accomplished by a very rapid heating of solid matter to temperatures higher than the critical point.

Considering that the time scale for electron cooling and energy transfer to the lattice is within the range of ps, very short pulse duration (fs) associated with an high fluence can lead to material sublimation without thermal conduction into the lattice. Indeed, when the fluence is high enough, an high quantity of excited electrons transfer their energy to the lattice (non-radiative electron-phonon transfer) in a very short time scale, so that the lattice is heated at a ps scale and matter is directly sublimated. In this case, thermal conduction into the rest of the sample can be neglected [127], [150].

Laser ablation of dielectric layers on c-Si solar cells have been studied for various pulse duration and wavelengths. The possible laser induced damages impacting the cell efficiency, such as dislocations/crack formation, surface melting, dopant redistribution and surface amorphization, have been identified [124], [125], [128], [151]–[153]. UV lasers have been revealed to be less aggressive towards Si surface than green and IR ones thanks to smaller optical penetration depth, which leads to shallower spatial distribution of defects [127], [138], [154]. Regarding the pulse duration, ns-lasers have been first studied and optimized but ultra-short laser pulses are currently under investigation because of their potential to reduce the laser induced damages by limiting the thermal impact on Si underlying. Indeed, the extent of thermal diffusion depends on the pulse duration according to the following relation [148]:

$$I_d = \frac{1}{\alpha} + \sqrt{D_{th} t} \tag{3.2}$$

where I_d is the thermal penetration depth, α the absorption coefficient, D_{th} the thermal diffusivity and t the laser pulse duration.

Heinrich et al. have worked on laser ablation of SiN_x layers for c-Si solar cells and they have described three mechanisms: direct ablation, partial lift-off and lift-off, as illustrated in Figure 3.3 [155]–[158].

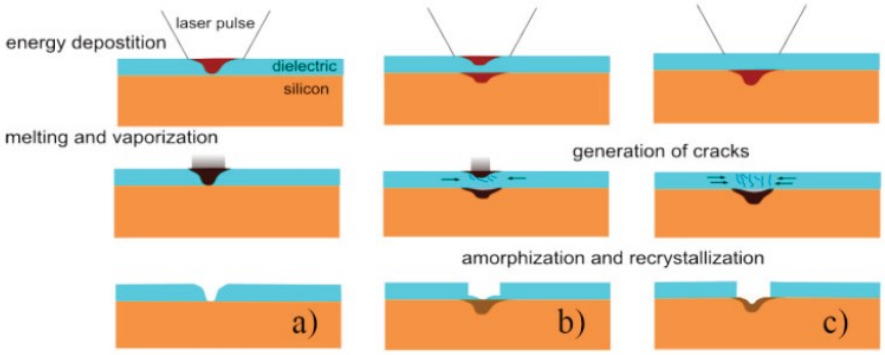

Figure 3.3: Illustration of laser ablation of dielectric layers by a) direct ablation, b) partial lift-off and c) lift-off according to Heinrich et al. [156].

Ps-laser ablation of SiO_2 layers on Si substrates has been also investigated by Hermann et al.[159] and these studies have been helpful to understand ablation mechanisms investigated in this thesis. However, modification of the laser source, pulse duration or dielectric layers properties can completely change the ablation mechanism and related laser induced damages. Hence, an accurate determination of the most suitable laser processing parameters requires a specific study for the materials to be ablated.

3.3 Experimental approach

In this work, laser ablation of dielectric layers on textured/polished n-PERT precursors have been studied using a UV-ps laser. The aim is to efficiently remove the dielectric layers while limiting the laser impact on Si underlying, and understand the related ablation mechanism. Laser source and type have been chosen regarding the literature mentioned above. Indeed, smaller optical penetration depths are observed with UV radiations and ultra-short or short pulse durations limit the thermal impact on Si below the dielectric layers. Since fs-lasers are expensive, delicate and difficult to operate, they are still under development for PV industry applications and ps-laser is the best choice for this work.

Dielectric layers have been ablated in air atmosphere using a UV-ps laser from Coherent (HyperRapid laser with a Gaussian beam profile having 20 µm diameter, pulse duration is 10 ps and frequency is 400 kHz). Two studies have been carried out independently to determine the laser impact on the front and rear side. The originality of this work lies in the multi-approach of laser interaction as two different dielectric material stacks and two surface roughnesses (polished and textured) have been investigated.

Several laser ablations have been performed by varying the peak fluence (F_{peak}) in the range of 0.130 J/cm^2 to 2.159 J/cm^2 and the distance between two centers of lasered spots (d) from 4 µm to 36 µm to test various overlapping conditions. The F_{peak}, which referred to the maximum fluence value on the Gaussian shape of laser beam, depends on the average power supplied by the laser as explained in Figure 3.4. The fluence threshold (F_{th}) corresponds to the minimum fluence needed to ablate the dielectric layers.

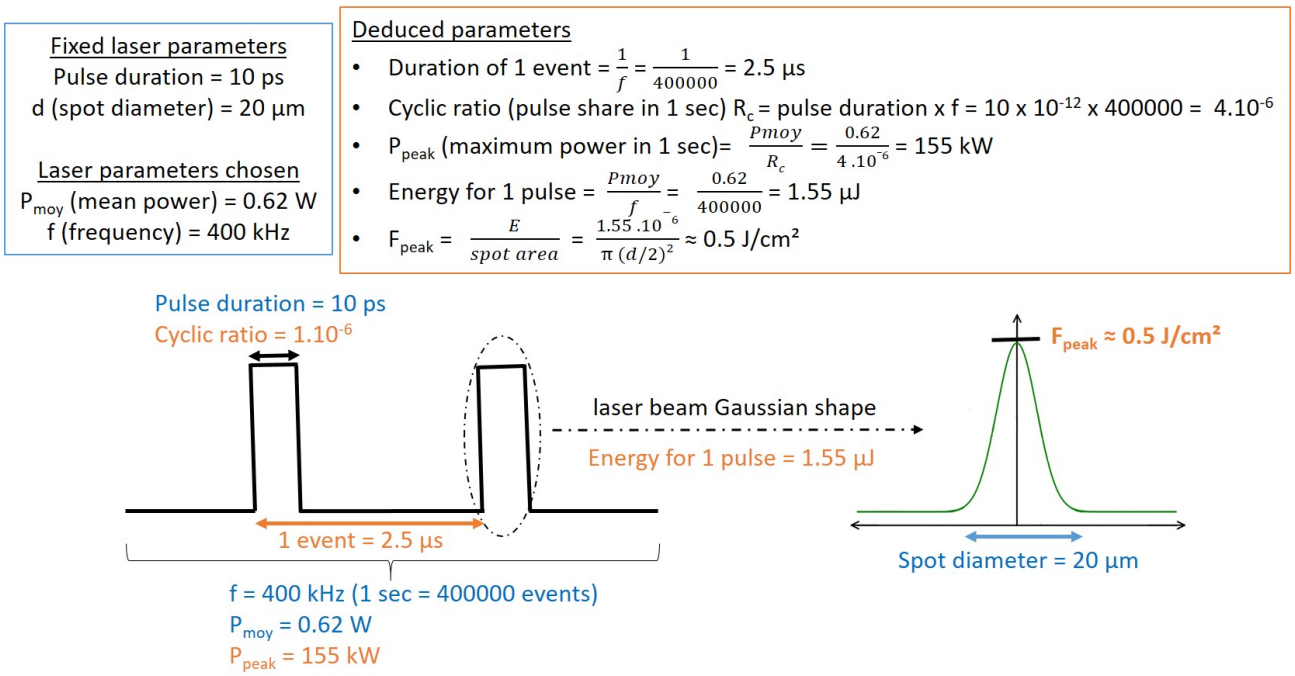

Figure 3.4: Methodology to calculate the F_{peak} from laser parameters used.

Thus, 90 parameter combinations have been tested as summarized in Appendix B, and samples have been characterized by several methods to highlight laser induced damages and understand the related ablation mechanism. The experimental setup is described in Figure 3.5.

Furthermore, the short annealing step needed to activate the passivation properties of dielectric layers through hydrogen diffusion (built-up at 750°C under N_2 flow) (see section 2.6) is performed after laser ablation (and not before) or not performed at all. That enables to investigate the possible impact of this annealing, named post-laser annealing (PLA) on the laser impacted silicon surface. Finally, samples have been immersed in a fluoride-based solution ($NaHF_2$ $1\%_{(wt/wt)}$) 2 min) to characterize the Si surface just before metallic deposition (palladium, nickel and copper). Polished n-type bare Si wafers with a 500 nm n^+ doped layer have been also used as reference to study the laser impact on Si without the contribution of the dielectric layers.

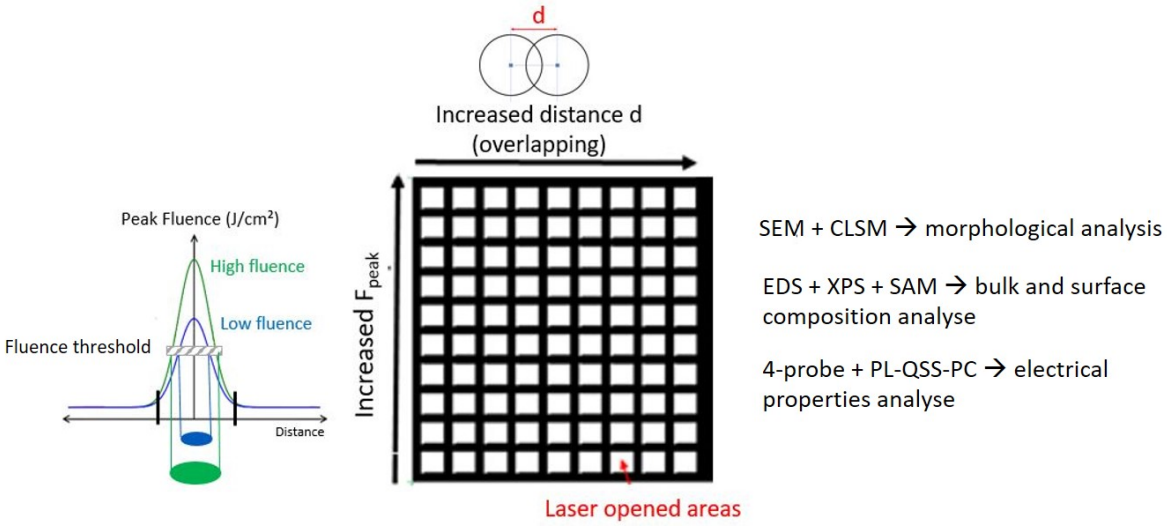

Figure 3.5: Illustration of patterns used for dielectric layers laser ablation. F_{peak} (J/cm^2): 0.130, 0.269, 0.448, 0.505, 0.668, 0.766, 0.896, 1.385, 1.809, 2.159 from bottom to top. Distance between two spot centers (µm): 4, 8, 12, 16, 20, 24, 28, 32, 36 from left to right.

Ellipsometry measurements have been performed on the dielectric layers to determine their refractive index and optical bandgap. These both parameters are of primary importance to understand the ablation mechanism. Surface morphology of ablated samples have been characterized by Confocal Laser Scanning Microscopy (CLSM) and Scanning Electron Microscopy (SEM).

Then, chemical bulk composition has been determined by Energy Dispersive Spectroscopy (EDS) and surface composition and chemical environment by X-ray Photoelectron Spectroscopy (XPS) and Scanning Auger electron Microscopy (SAM) analysis.

Finally, electronic properties have been investigated with four-probe measurements to determine Si surface sheet resistance and PhotoLuminescence calibrated with Quasi-Steady-State PhotoConductance (PL QSS-PC) has been used to measure charges carriers lifetime. To remove the contribution of recombination on bare Si surface, ablated samples have been re-passivated with Hydrogenated amorphous silicon (a-Si:H). 40 nm of a-Si:H have been deposited by PECVD at 175°C using an SiH_4 and H_2 gas mixture flow in the Octopus II tool from Indeotec. Prior to a-Si:H deposition, a HF cleaning is performed (HF 5%, 15 seconds) to remove silicon oxide layer.

The Table 3.2 summarizes the wafers used and process steps realized in this work.

Table 3.2: Summary of the successive process steps performed on textured/polished n-PERT precursors and n/n$^+$ bare Si wafers to study the impact of laser ablation.

	Studied materials		
	Polished n/n⁺ bare Si n (1 ohm.cm) n+ (80 ohm/sq)	Polished/textured n-PERT precursor SiNx p+ (85 ohm/sq) n (1 ohm.cm) n+ (80 ohm/sq) SiO_2 SiNx	Polished/textured n-PERT precursor SiNx p+ (85 ohm/sq) n (1 ohm.cm) n+ (80 ohm/sq) SiO_2 SiNx
	Process steps		
1: LASER	Yes	Yes	Yes
2: Characterization	SEM, CLSM, XPS	SEM, CLSM, XPS, SAM, PL-QSS PC, 4-probe	PL-QSS PC
3: PLA	Yes	Yes	No
4: Characterization	XPS, CLSM	SEM, CLSM, XPS, PL-QSS PC, 4-probe	No
5: $NaHF_2$ treatment	Yes	Yes	Yes
6: Characterization	XPS	XPS, PL-QSS PC, 4-probe	No
7: a-Si:H passivation	No	Yes	Yes
8: Characterization	No	PL-QSS PC	PL-QSS PC

3.4 Laser impact on silicon surface morphology

3.4.1 CLSM characterization

Results on textured/polished n-PERT precursors: rear polished side analysis

Samples have been ablated using various F_{peak}, without any overlapping of laser opened area. Results of CLSM characterization are shown in Figure 3.6 for five F_{peak} tested. Optical and laser images, recorded through optical and laser excitation (405 nm) respectively, are both displayed because they give complementary information. Typically, surface appears in dark grey on laser intensity images where the dielectric layers are removed.

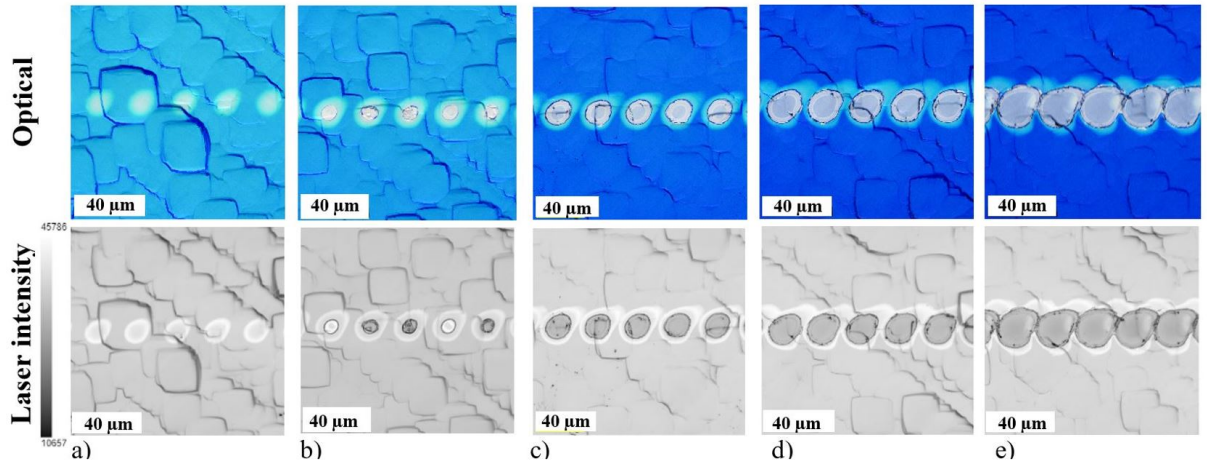

Figure 3.6: Optical and laser intensity CLSM images on the rear polished side after laser ablation using d = 24 µm and various F_{peak} a) 0.130 J/cm^2, b) 0.269 J/cm^2, c) 0.505 J/cm^2, d) 0.896 J/cm^2, e) 2.159 J/cm^2.

The surface morphology depends on the F_{peak} used. A $F_{peak} \leq 0.130$ J/cm^2 is not sufficient to remove

the dielectric layers as observed in Figure 3.6 a). Nevertheless, the surface is impacted with the appearance of a light blue area. Then, by increasing the F_{peak} to 0.269 J/cm^2, the dielectric layers start to be partially removed (see Figure 3.6 b)), meaning that F_{th} is close to this value. The non-continuous ablation with $F_{peak} \approx F_{th}$ originates from small pulse to pulse deviations and variation of effective F_{th} due to material inhomogeneities. At $F_{peak} \geq F_{th}$ (see Figure 3.6 c) to e)), the dielectric layers seem to be completely removed and three different areas can be discriminated. Two of them correspond to the removal of dielectric layers and the third one is an area where dielectric layers are not removed. These areas are illustrated in Figure 3.7 a) and named to facilitate further explanations.

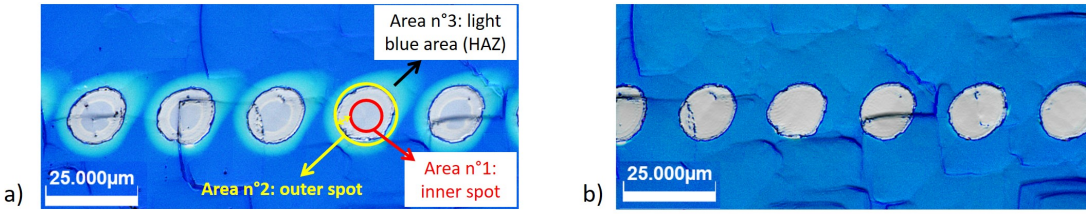

Figure 3.7: Optical CLSM images representing the different surface morphologies after laser ablation (d = 24 µm, F_{peak} = 0.505 J/cm^2) a) before PLA, b) after PLA.

Given the Gaussian shape of the laser beam (see Figure 3.9), these three areas have not received the same photons quantity and are differently impacted:

- **Area n°1: inner spot.** In this area, at the laser beam center, more photons are received. As a result, this area is the most impacted one.
- **Area n°2: outer spot**. This area is a corona around the inner spot where dielectric layers are also removed. However, this area is less impacted due to lower quantity of photons received.
- **Area n°3: light blue area**. This part is affected but not ablated and is called the heat-affected zone (HAZ). This morphology has already been observed in literature and probably corresponds to amorphous silicon (a-Si) under dielectric layers [129], [141], [155], [156], [158]. Laser parameters do not enable energy absorption by the dielectric layers contrary to underlying Si. As a result, Si is locally melted and the fast cooling prevents Si re-crystallization, leading to Si amorphization. When the PLA is performed, this light blue area completely disappears for all laser parameters tested as exampled in Figure 3.7 b). This behavior supports the hypothesis of a-Si formation in this region as a-Si starts to crystallize at 640°C and the PLA is performed at 750°C [160]. Area n°1 is much less visible after PLA but does not completely disappear (visible on laser intensity images not shown here).

Respective sizes of observed areas have been determined for the different F_{peak} tested. The evolution of the opened spot diameter (area n°1 + area n°2) with F_{peak} is plotted in Figure 3.8 a). Two linear trends can be observed: 1) from $F_{peak} = F_{th}$ to $F_{peak} \approx 1$ J/cm^2, the opened spot diameter increases until around 19 µm which corresponds approximately to the laser beam spot diameter 2) above $F_{peak} \geq 1$ J/cm^2, the opened spot diameter becomes higher than the laser beam spot thanks to lateral thermal dissipation. However, the opened area diameter increases three times slowly with F_{peak} which suggests that a maximum opened area diameter will be reached for maximum lateral thermal dissipation ability.

The Figure 3.8 b) gives information on respective sizes of the different areas identified before. We can observe that the ratio of opened spot/inner spot diameter decreases indicating that inner area (n°1) becomes more and more important compared to outer area (n°2) when F_{peak} increases. In the same way, the ratio of total impacted area (opened spot + light blue area)/opened spot decreases showing that the light blue area (n°3) becomes thinner when F_{peak} increases. This is also visible in Figure 3.6 but the graph in Figure 3.8 b) highlights that this phenomenon is more significant for $F_{peak} \geq 0.896$ J/cm^2, when the opened spot diameter is higher than the laser beam spot diameter. Therefore, the inner area fills almost the entire opened area with a very thin HAZ (blue light area). A schematic representation is given in Figure 3.9 to illustrate this phenomenon related to the Gaussian shape of the laser beam.

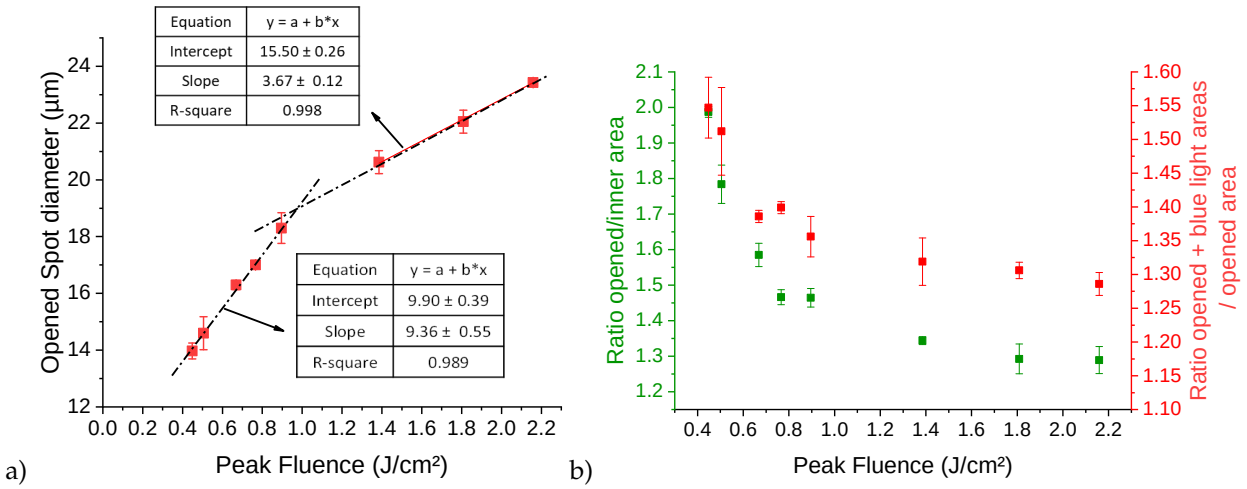

Figure 3.8: a) Evolution of laser opened spot diameter with F_{peak} b) Evolution of areas ratio with F_{peak}.

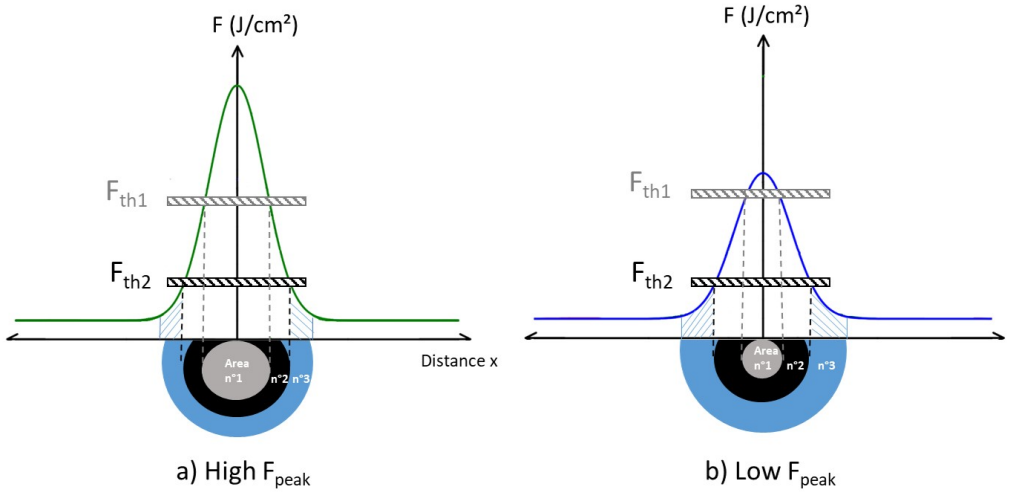

Figure 3.9: Schematic representation of area n°1, n°2, n°3 sizes as function of F_{peak}.

Now, if we take into account laser spot overlapping, areas n°1 and 2 are progressively replaced by double impacted areas, named area n°4 as visible in Figure 3.10 b), c) and d). On these double impacted areas, the surface seems to be melted and thus more damaged. It is especially observable at high F_{peak} (see Figure 3.10 d)). With F_{peak} = 0.130 J/cm^2 ($< F_{th}$), there is not enough energy to ablate the dielectric layers, even with

overlapping (see Figure 3.10 a)). However, it can be notice in Figure 3.10 b) that overlapping promotes a complete removal of dielectric layers at $F_{peak} \approx F_{th}$ for which laser ablation was observed to be partial with no overlapping.

Overlapping also implies a bigger light blue area (HAZ), which confirms the higher thermal impact. This is observable in Figure 3.11 since evolution of the opened area diameter is similar with and without overlapping while the ratio of total impacted area (opened + light blue area) to opened area is higher with overlapping.

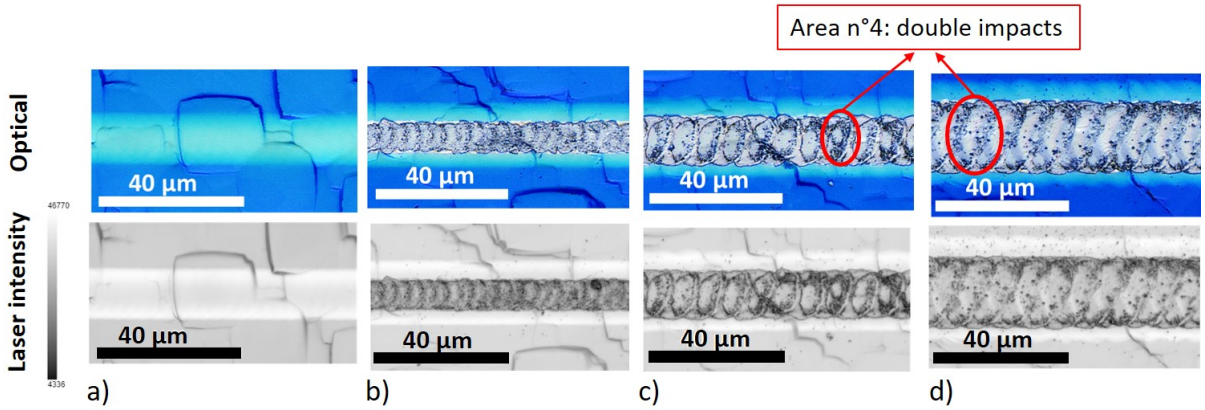

Figure 3.10: Optical and laser intensity CLSM images on the rear polished side after laser ablation with 50% overlapping a) F_{peak} = 0.130 J/cm^2, b) F_{peak} = 0.269 J/cm^2, c) F_{peak} = 0.505 J/cm^2, d) F_{peak} = 1.385 J/cm^2.

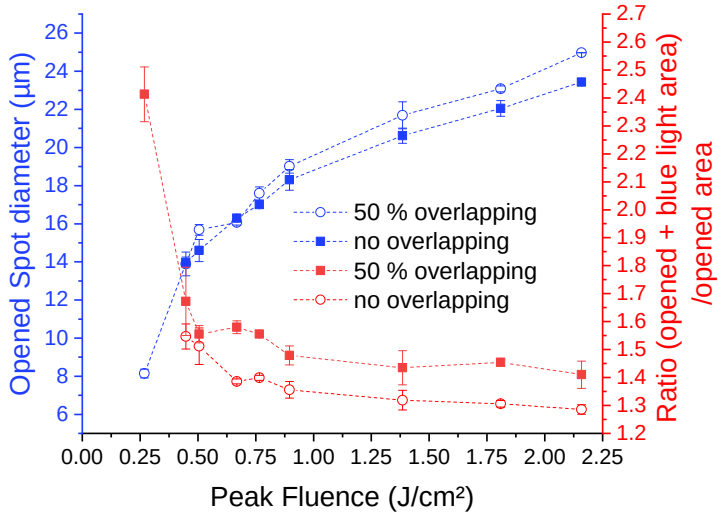

Figure 3.11: Evolution of opened area diameter (blue curve) and (opened + light blue area)/opened area diameter ratio (red curves) as a function of F_{peak}. Results are displayed with no overlapping or 50% overlapping.

Results on n/n$^+$ polished bare silicon (reference for rear side of n-PERT precursors)

CLSM measurements have been realized after laser ablation on bare polished Si samples (n/n$^+$ wafers) to investigate the laser impact without the contribution of dielectric layers. These results serve as 'reference' for the rear polished side of n-PERT precursors. Two laser parameters have been tested with 50% overlapping: F_{peak} = 1.809 J/cm^2 and F_{peak} = 0.448 J/cm^2. The corresponding CLSM images for F_{peak} = 1.809 J/cm^2

before and after PLA are displayed in Figure 3.12 c) and d) respectively. For comparison, CLSM images after ablation in the same conditions on the rear polished side of n-PERT precursors are also presented in Figure 3.12 a) and b).

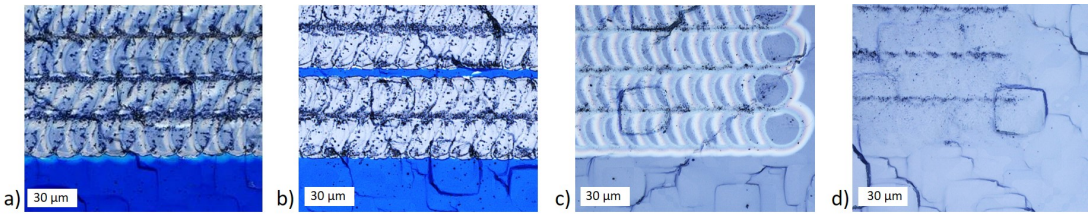

Figure 3.12: Optical CLSM images after laser ablation with F_{peak} = 1.809 J/cm^2 and 50% overlapping. a) and b): rear polished side of n-PERT precursors before and after PLA respectively. c) and d): n/n$^+$ bare Si wafer before and after PLA respectively.

A color contrast is visible on n/n$^+$ bare Si wafer after laser ablation (see Figure 3.12 c)) and it disappears after PLA (see Figure 3.12 d)). As for n-PERT precursors, it suggests the formation of a-Si which is recrystallized after PLA at 750°C. As a result, a-Si would be induced by the laser impact independently of the presence of dielectric layers. Otherwise, laser impact on the Si surface morphology is higher when dielectric layers are present. Indeed, double impacted areas are more melted on n-PERT precursors than on n/n$^+$ bare Si wafer as observable by comparing Figures 3.12 a) and c) or Figures 3.12 b) and d). This has been confirmed by SEM characterization. As the laser energy is absorbed onto underlying Si, the thermal energy hardly dissipated because of the dielectric layers above. Thermal impact on Si is thus higher compared to bare Si wafers for which the thermal energy is easily dissipated. Moreover, more energy impacts the passivated wafers due to the presence of dielectric layers which limits the reflection process.

Results on textured/polished n-PERT precursors: front textured side analysis

The front side is more delicate to analyse due to optical diffusion mechanisms induced by pyramids texturing. Nevertheless, CLSM images after ablation with several F_{peak} are presented in Figure 3.13 and bring some information. As for the rear polished side, a $F_{peak} \leq 0.130$ J/cm^2 is not sufficient to ablate the dielectric layers (see Figure 3.13 a)) but a light blue area is still visible, suggesting a thermal impact on the silicon underlying. This light blue area is present around the laser opened areas and its width decreases with F_{peak} (see Figure 3.13 b) compared to Figure 3.13 d) as observed on the rear polished side. However, contrary to the rear side, this light blue area seems to disappear only partially after PLA (see Figure 3.13 c)).

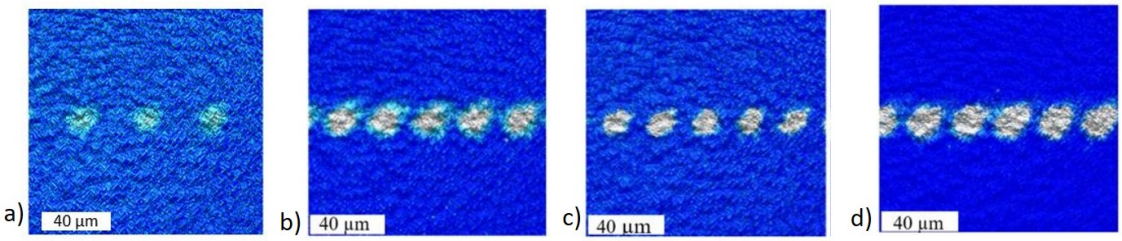

Figure 3.13: Optical CLSM images on the front textured side after laser ablation using F_{peak} a) 0.130 J/cm^2, b) 0.448 J/cm^2, c) 0.448 J/cm^2, d) 0.896 J/cm^2. Images are obtained before PLA except for image c).

3.4.2 SEM characterization

SEM images have been realized to characterize in more details the surface morphology after laser ablation on both sides.

Results on textured/polished n-PERT precursors: rear polished side analysis

Representative SEM images obtained after laser ablation on the rear polished side with different parameters are presented in Figure 3.14. The difference of material crystallinity can not be detected through SEM measurements so the HAZ (area n°3) observed with CLSM before PLA is not visible here. However, area 1 and 2 as well a double impacted area named area 4 identified on CLSM images are still visible. An additional impacted area, consisting of a thin external corona, can also be observed and is named area n°2_{bis}.

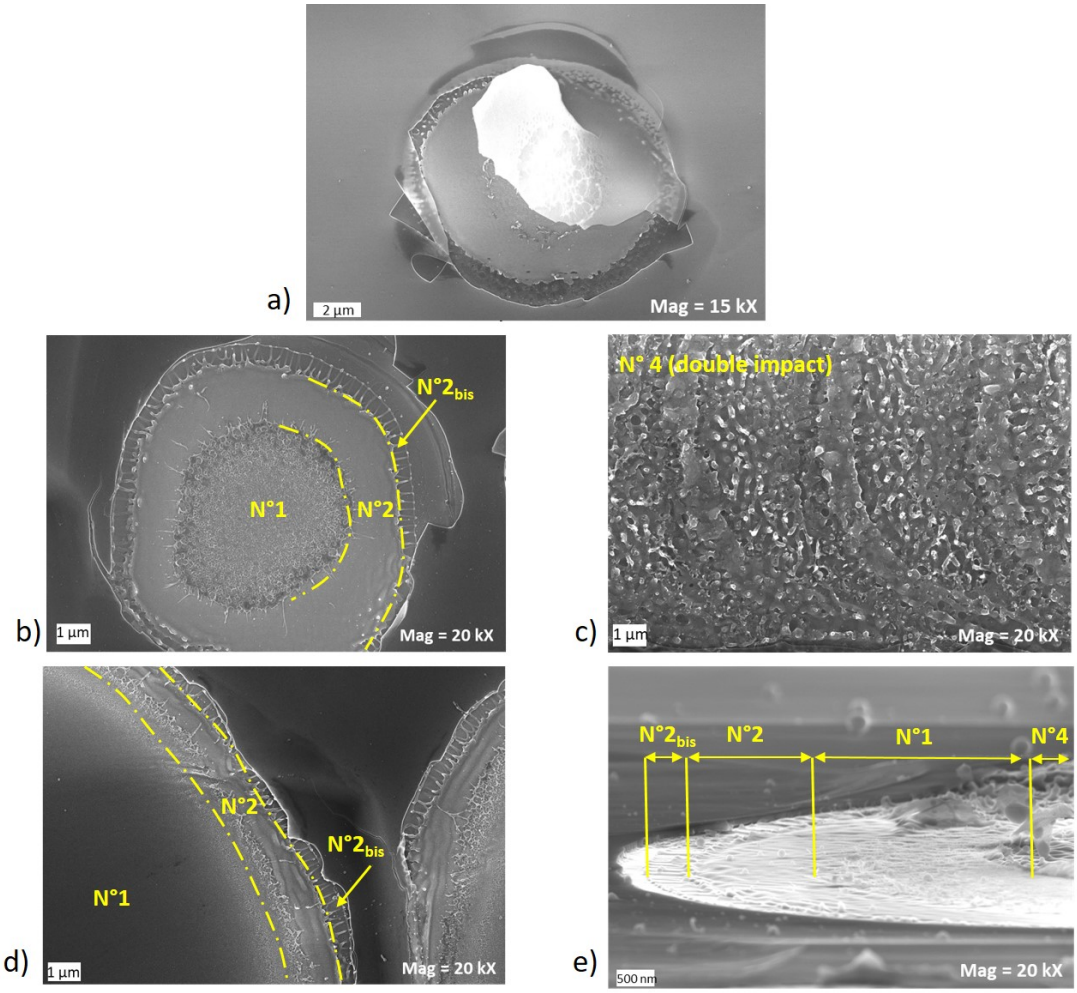

Figure 3.14: SEM images after laser ablation on the rear polished side a) F_{peak} = 0.269 J/cm^2, b) F_{peak} = 0.448 J/cm^2, c) F_{peak} = 0.448 J/cm^2 with 50% overlapping, d) F_{peak} = 1.809 J/cm^2, e) Sectional image F_{peak} = 1.809 J/cm^2 with 10% overlapping.

In Figure 3.14 a), $F_{peak} \approx F_{th}$ and dielectric layers are partially removed. A fragment not completely removed is visible and borders of the partially opened area are sharp. In addition, the fragment seems to have been damaged in its center. This morphology suggests that dielectric layers have been ablated through a partial lift-off or lift-off process.

A chemical contrast can be discerned where dielectrics layers have been removed (see Figures 3.14 b), d) and e)) which could be due to the presence of SiO_x in areas 1 and 2. In Figure 3.14 b) and d), dielectric layers have been completely removed by using F_{peak} = 0.448 J/cm^2 and F_{peak} = 1.809 J/cm^2 respectively. As demonstrated previously, area n°1 diameter is bigger when F_{peak} increases. At the frontier between area n°1 and n°2, melted residues are visible and are likely to correspond to redeposited melted dielectric layers. In area 2_{bis}, dielectric layers seems to have been lifted off the silicon surface and it is expected to detect a smaller mount of silicon oxide in this area. This point will be verified through further SAM analysis.

In Figure 3.14 c), laser ablation has been performed using F_{peak} = 0.448 J/cm^2 with 50% overlapping so that the morphology of double impacted area (area n°4) can be observed. In this area, the laser thermal impact is more important and induces surface melting, increasing the surface roughness.

Finally, a sectional SEM image is represented in Figure 3.14 e). Laser parameters have been chosen so that all identified impacted areas are visible (F_{peak} = 1.809 J/cm^2 with 10% overlapping). Thus, area 1, 2, 2_{bis} and 4 can be observed as well defined separated area having different morphologies and probably different chemical compositions.

Results on textured/polished n-PERT precursors: front textured side analysis

Representative SEM images obtained after laser ablation on the front textured side with different laser parameters are presented in Figure 3.15.

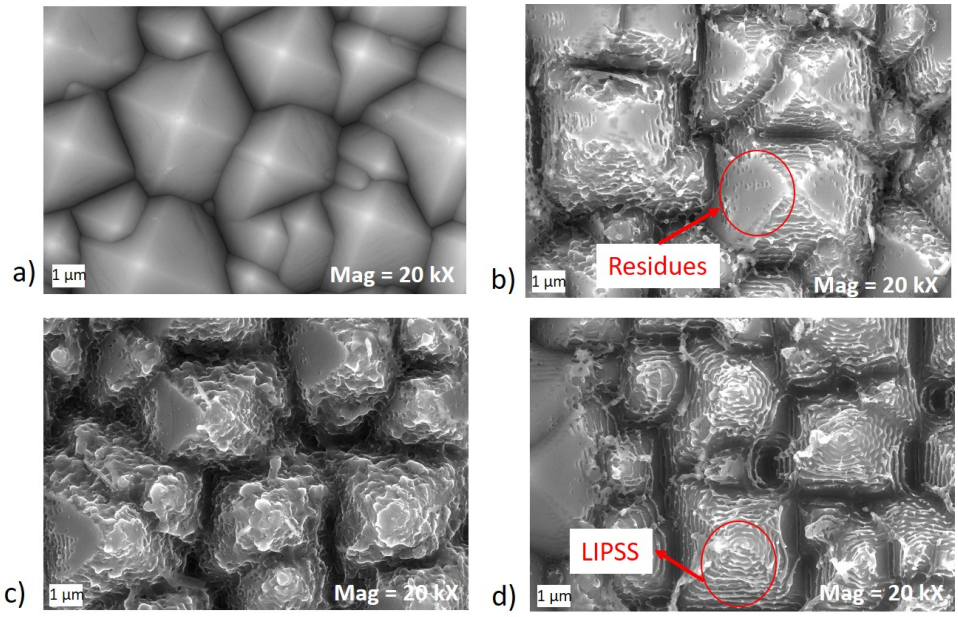

Figure 3.15: SEM images on the front textured side before laser ablation (a) and after laser ablation with b) F_{peak} = 0.505 J/cm^2 no overlapping, c) F_{peak} = 0.505 J/cm^2 50% overlapping, d) F_{peak} = 1.809 J/cm^2 no overlapping.

In Figure 3.15 b), it appears that ablation mechanism preferentially concerns edges, base and top of pyramids while dielectric layers residues remain on pyramids sides. This can be attributed to optical diffusion mechanisms on pyramids, causing uneven distribution of energy impacting the surface. This ablation structure on textured surfaces is characteristic and has already been explained and quantified by Knor et al. using

rigorous coupled wave analysis (RCWA) simulations [161].

In addition, ablated areas show a specific surface morphology called LASER-induced periodic surface structures (LIPSS) and highlighted in Figure 3.15 d). This structure has already been described in literature [129], [132], [156], [162], [163] and is said to originate from an interference between the incident light and a surface wave generated by scattering. It leads to periodic modulation of the absorbed intensity and consequently to modulated ablation. LIPSS increase the surface roughness.

Without overlapping, pyramids start to be highly damaged (especially the little ones) at $F_{peak} \geq 0.766$ J/cm^2. When laser spots overlap, the Si layer is highly damaged as demonstrated by the melted top of pyramids, even at low fluence as visible in Figure 3.14 c). Overlapping, is thus more critical on the front textured side where thermal impact induced by overlapping is exacerbated by optical diffusion processes.

3.4.3 Conclusions

On both sides: The peak fluence needed to start removing the dielectric layers (F_{th}) is around 0.269 J/cm^2. It is however recommended to use slightly higher F_{peak} to obtain a continuous laser opened area when no spot overlapping is used. For higher F_{peak} tested ($\geq$ 0.448 J/cm^2), laser contact opening is continuous on both sides with a width $\geq$ 14 µm. Continuous ablation is also achieved with F_{peak} = 0.269 J/cm^2 using overlapping $\geq$ 50%. It presents the advantage to lead to very narrow laser contact opening width (9 µm) and increases surface roughnesses.

On the rear polished side: Four different rather concentric areas have been identified after laser ablation (area 1, 2, 2_{bis} and 3). This morphology is linked to the laser fluence spatial distribution and the relative proportion of each area depends on F_{peak} used. With overlapping, doubled impacted area (area n°4) undergoes an higher thermal impact and appears to be melted with more roughness. This can be an advantage by favoring the adherence of the metallic contacts deposited afterwards. The area n°3 (light blue area) becomes bigger with overlapping and disappears after a PLA, confirming that it is related to a thermal process. Thus, area n°3 is likely to correspond to a-Si formation, which is recrystallized after PLA. This area is also observed on laser impacted n/n$^+$ bare Si wafer, which means that a-Si is formed independently of the presence of dielectric layers. However, the thermal impact on Si underlying is more significant when dielectric layers are present due to more difficult dissipation of thermal energy. SEM images suggest that dielectric layers are removed by lift-off or partial lift-off and that areas 1, 2 and 2_{bis} have different chemical surface compositions. Initial SiO_x dielectric layer may have not been completely removed and/or SiO_x layer has been formed under laser impact. Complementary chemical analysis have been performed and are presented in the next section to refine the morphological study and help understanding the ablation mechanism.

On the front textured side: Pyramid texturing induces optical diffusion process which leads to LIPSS morphology and preferential ablation areas. Roughness is thus increased but more dielectric layers residues are observed compared to the rear polished side. Optical diffusion processes also lead to an increased thermal impact, in particular when spot overlapping is used. As for the rear side, laser ablation seems to occur by lift-off or partial lift-off. The area n°3 (light blue area) is also observed, suggesting that underlying Si is amorphized during the laser process. Unlike the rear polished side, this area n°3 does not completely disappear after PLA which seems to indicate an incomplete Si recrystallization.

3.5 Laser impact on silicon surface composition

In this section, EDS and SAM analysis have been performed on the rear polished side of n-PERT precursors after laser ablation to investigate the chemical composition of the different areas identified before (EDS as a first approach followed by accurate SAM analysis). Then, XPS analysis have been realized on both sides of n-PERT precursors as well on n/n^+ bear Si wafers to study the chemical composition and environments of double impacted areas.

3.5.1 EDS characterization

EDS analysis have been first performed on the different areas identified after laser ablation on the rear polished side of n-PERT precursors. Results obtained in case of F_{peak} = 0.448 J/cm^2 and F_{peak} = 1.809 J/cm^2 are shown in Figure 3.16 and evidence the presence of Si, O and C in laser opened areas. Nitrogen is sometimes detected but only for measurements performed closed to laser spot edges. This can be explained by the spatial resolution of the technique, which does not enable to perform local analysis at submicrometric scale. Thus, Nitrogen is most likely attributed to the dielectric layers contribution on the sides. Carbon signal originates from surface contamination.

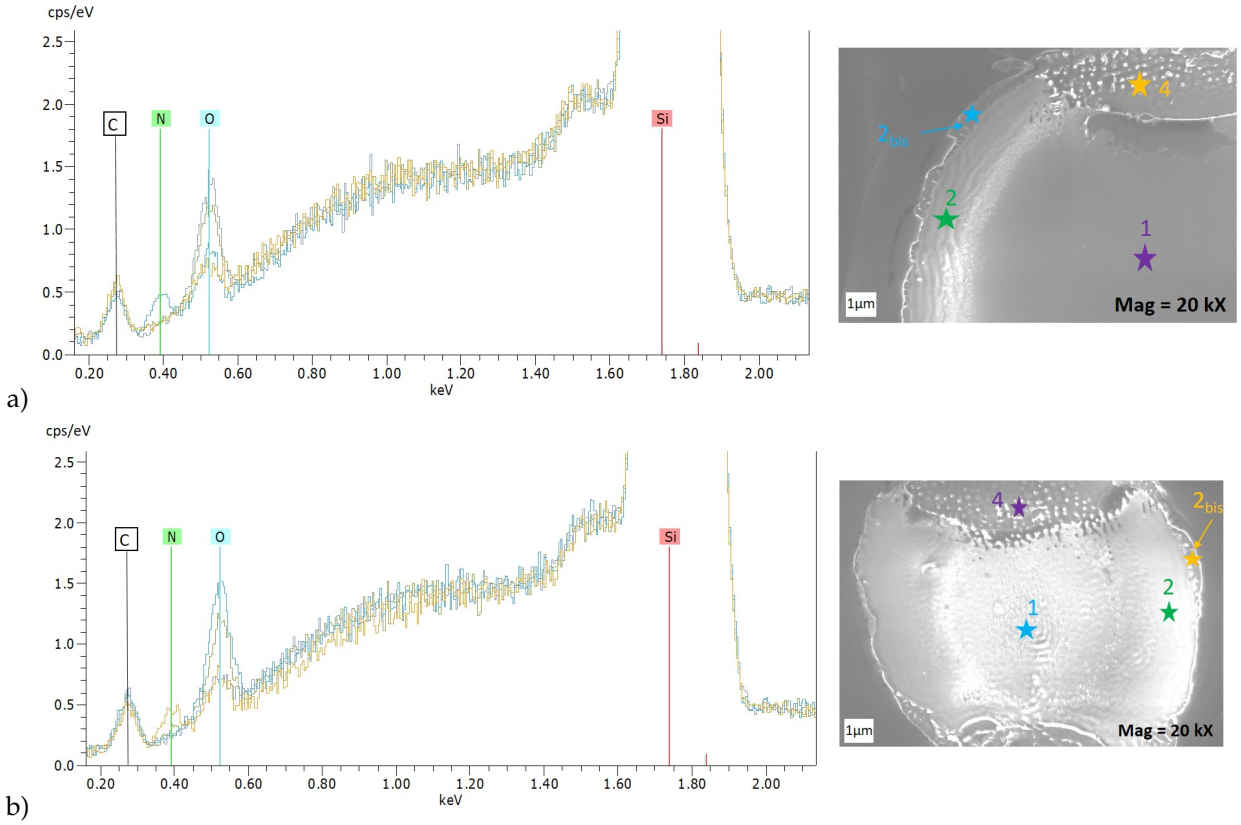

Figure 3.16: SEM images and corresponding EDS analysis at various location for laser ablation using a) F_{peak} = 1.809 J/cm^2, b) F_{peak} = 0.448 J/cm^2 on the rear polished side. Analysed areas are numbered according to areas identified before.

A significant amount of oxygen is detected into the opened area with a signal intensity varying on the different parts. At all F_{peak} tested, area n°1 demonstrates the higher O signal intensity on EDS spectra,

followed by area n°2 and then area 2_{bis} and double impacted area. As suspected after SEM analysis, silicon oxide is present on silicon surface after laser ablation, in particular in area n°1 and n°2. The different oxygen amounts detected by EDS could be due to different SiO_x stoechiometries and/or thicknesses on the different areas. Two hypothesis can be proposed:

1. Initial SiO_x dielectric layer has not been completely removed in area 1 and 2, explaining the higher amounts of Oxygen. Oxygen detected in area 2_{bis} and 4 could be due to Si surface reoxidation under laser heat effect.
2. Dielectric layers have been completely removed in the four areas and Si surface has been more or less oxidized under laser heat effect due to the Gaussian shape of laser beam. This is less probable as double impacted areas should demonstrate the higher O amount in this case.

To go even further on the chemical composition analysis and quantify the different elements detected, analytical techniques more adapted to the dimensions of the system are required such as SAM and XPS.

With a spot diameter of 12 nm and a 4 nm depth analysed, SAM analysis allows to investigate the fine surface chemistry evolution after LASER opening on the four identified areas independently. However, the quantification and spectra treatment with SAM is not as direct as what can be done for XPS spectra treatment. It requires the acquisition of reference spectra representative of each compound to determine the spectroscopy signature and refine sensitivity factors tacking account for possible matrix effects.

XPS analysis enables to access precisely chemical compositions and environments with a quantitative aspect. However, the spot diameter is 400 µm with 10 nm depth analysed. Thus, only the double impacted areas can be analysed independently by using samples with several opened lines with 50% overlapping.

3.5.2 SAM analysis

SAM measurements have been carried out on samples after various laser ablations on the rear polished side. Results obtained in the case of F_{peak} = 1.809 J/cm^2 with no overlapping are presented in Figure 3.17.

The different areas in the laser opened spot have been investigated at local scale as described in Figure 3.17 a). As for EDS analysis, four elements are identified: O, N, Si and C. The low C content is associated to superficial contamination. The specific spectroscopic signatures in each area for N-KLL, O-KLL and Si-KLL transitions are given in Figure 3.17 b). Reference spectra from JEOL database (Si and SiO_2 spectra in Figure 3.17 c)) and the reference spectrum for SiO_xN_y layer (measurement point n°1) have been used to qualitatively interpret the Auger spectra. The AES atomic percentages have been also determined using the sensitivity factors of the constructor to help the phases identification. AES atomic percentages are displayed in Figure 3.17 d). Two phases have been identified, SiO_xN_y and SiO_x, and both peaks shapes and quantitative data are intimately linked and remain constant for similar positions, even on different samples, which confirms the existence of these phases. The acquisition of reference spectrum for initial SiO_x dielectric layer and for Si wafer would have been necessary to analyse the SiO_x phase stoechiometry. In addition, the SiO_x compound is not stable under electron beam irradiation and its reduction occurs practically instantaneously. Consequently, the AES percentages must be analysed in term of SiO_x and SiO_xN_y phase proportions.

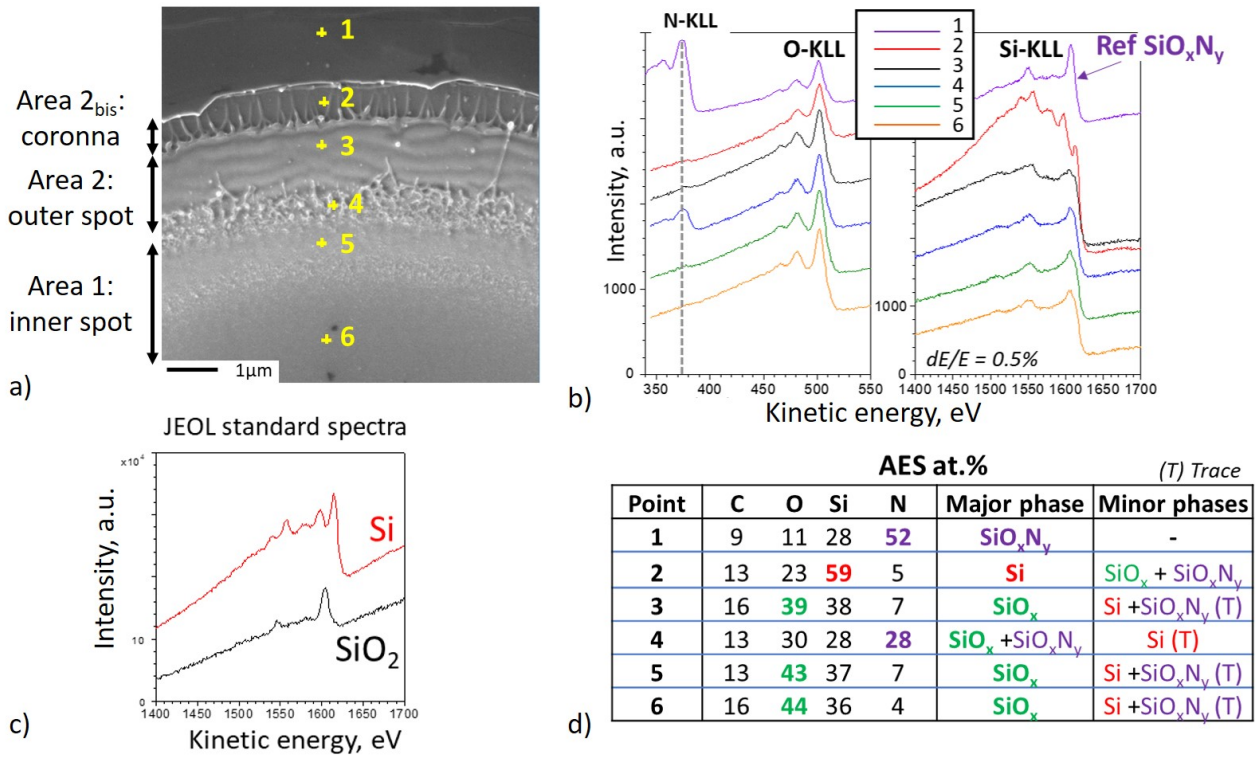

AES at.% (T) Trace

Point	C	O	Si	N	Major phase	Minor phases
1	9	11	28	52	SiO_xN_y	-
2	13	23	59	5	Si	SiO_x + SiO_xN_y
3	16	39	38	7	SiO_x	Si +SiO_xN_y (T)
4	13	30	28	28	SiO_x +SiO_xN_y	Si (T)
5	13	43	37	7	SiO_x	Si +SiO_xN_y (T)
6	16	44	36	4	SiO_x	Si +SiO_xN_y (T)

Figure 3.17: SAM results on a sample after laser ablation using F_{peak} = 1.809 J/cm^2 (no overlapping). a) Microscopy image showing the analysed points, b) Corresponding spectra for N-KLL, O-KLL and Si-KLL transitions, c) Si and SiO_2 JEOL standard spectra, d) SAM atomic percentages obtained using C-KLL, O-KLL, Si-KLL and N-KLL transitions and sensitivity factors of JEOL library.

The measurement point n°4 has been performed on a melted residue and a significant amount of Nitrogen is found, which confirms that SiO_xN_y layer is melted during the laser ablation process.

Spectra obtained for points n°5 and 6 are similar as they are both in area n°1 (inner spot). SiO_x is the main phase and has an higher Oxygen content in comparison with SiO_x phase in area 2 (outer spot) (measurement point n°3) as already observed with EDS measurements. At this stage, the origin of this silicon oxide layer can not be confirmed but these observations will be completed with further XPS analysis.

Spectrum obtained in area 2_{bis} (measurement point n°2) indicates that Si is the major phase but SiO_x is still present. Given that SAM depth analysis is < 4 nm, the detection of Si wafer indicates that SiO_x layer is thinner than 4 nm in area 2_{bis}. Consequently, in this area, not only the dielectric layers have been more efficiently removed but no significant Si surface oxidation has occurred under laser heat effect. Results obtained on sample ablated with F_{peak} = 0.448 J/cm^2 (no overlapping) have led to the same conclusions.

Double impacted areas have also been analysed on a sample ablated with F_{peak} = 0.448 J/cm^2 and 50% overlapping. Results are displayed in Figure 3.18. In this case, no more Nitrogen is detected, suggesting that residues have been completely melted and removed from the surface by the second laser impact. A significant amount of Oxygen is observed and associated with the SiO_x phase. In double impacted areas, the thermal impact is increased so it is likely that the SiO_x phase observed mainly comes from Si surface oxidation under laser impact. It appears that relative proportion of oxygen and silicon are similar to the

one observed in area n°1 (inner spot) for samples with no overlapping (comparison of measurement points n°5 and 6 in Figure 3.17 d) with measurement point n°1 in Figure 3.18 d)). Therefore, it can be assumed that SiO_x phase observed in area n°1 (inner spot) and area n°4 (double impacted area) are similar and both originate from Si surface oxidation by laser impact.

Moreover, the shape of Si-KLL peak in double impact area (see Figure 3.18 b)) is different and less structured in comparison with Si-KLL peak observed when there is no overlapped area (see Figure 3.17 b)). It could be due to silicon surface amorphization induced by the double laser impact and its associated energy.

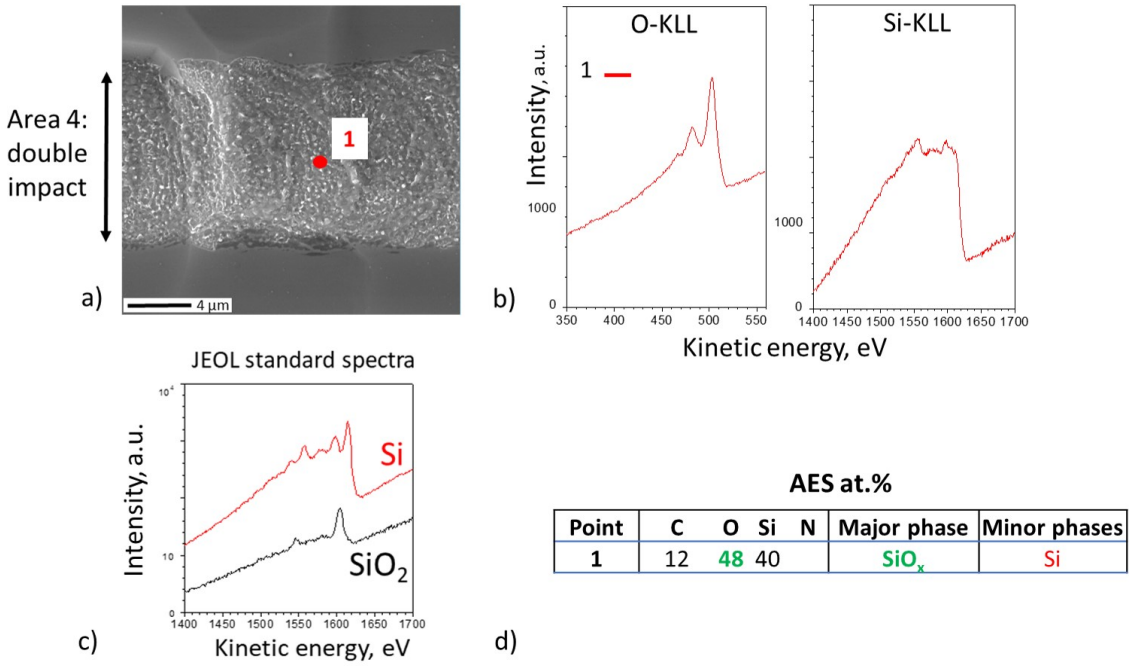

AES at.%

Point	C	O	Si	N	Major phase	Minor phases
1	12	48	40		SiO_x	Si

Figure 3.18: SAM results on a sample after laser ablation using F_{peak} = 0.448 J/cm^2, 50% overlapping. a) Microscopy image showing the analysed point, b) Corresponding spectra for O-KLL and Si-KLL transitions, c) Si and SiO_2 JEOL standard spectra, d) SAM atomic percentages obtained using C-KLL, O-KLL and Si-KLL transitions and sensitivity factors of JEOL library.

3.5.3 XPS analysis

XPS analysis have been then performed in order to investigate in more details the fine chemical surface composition and environments on double laser impacted areas. First, analysis have been realized on laser impacted polished n/n^+ bare Si wafers which serve as reference for the rear polished side of n-PERT precursors. Then, XPS profiling analysis on the rear side of n-PERT precursors will enable to characterize the initial SiO_x dielectric layer. Finally, XPS analysis have been performed after laser ablation on both side of n-PERT precursors. In this part, the effect of PLA and $NaHF_2$ $1\%_{wt/wt}$ treatment is also investigated.

XPS results on polished n/n^+ bare Si wafers

To better understand the laser ablation mechanism, XPS measurements have been performed on bare polished n/n^+ Si wafers to investigate the laser impact without the contribution of the dielectric layers. Measurements have been realized on doubled impacted areas before PLA, after PLA and after PLA + $NaHF_2$

chemical treatment. CLSM images of analysed sample are given in Figure 3.12 c) (before PLA) and Figure 3.12 (after PLA). An non laser impacted area has also been analysed. In this part, results obtained in case of laser ablation using F_{peak} = 1.809 J/cm^2, 50% overlapping are presented but similar results have been obtained with other F_{peak}.

From the survey spectra (not shown here), 3 elements are detected: Si, O, and C. Carbon presence is attributed to sample inherent superficial contamination. High resolution spectra of Si2p obtained on the non impacted area and the impacted area after laser, PLA and $NaHF_2$ treatment have been superimposed in Figure 3.19.

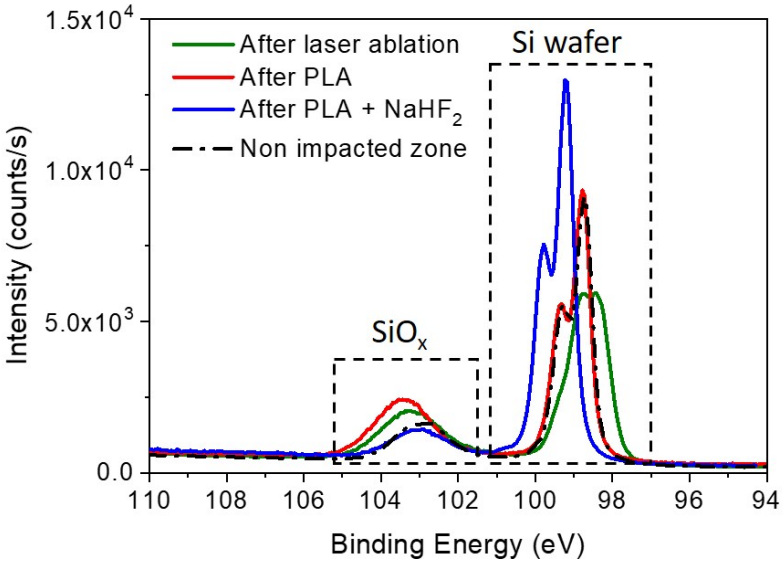

Figure 3.19: High energy resolution XPS spectra of Si2p after ablation on n/n$^+$ bare Si wafers with F_{peak} = 1.809 J/cm^2, 50% overlapping followed by PLA and $NaHF_2$ treatment. A non impacted zone is also analysed.

Two main environments can be observed: the first one, at around 99 eV, is attributed to the c-Si wafer [164] and the second one, at around 103.5 eV corresponds to SiO_x phases [165]. As both contributions are distinct, the spectra fit deconvolution is not presented here.

The detection of the Si substrate signal indicates that the oxidized layer is either inhomogeneous, or presents a thickness $\leq$ 10 nm. This signal brings also information about the atomic arrangement. Indeed, the spin-orbit splitting of $Si2p_{3/2}$ and $Si2p_{1/2}$ contributions observed after laser ablation is lost which suggests a disorganization of the atomic network, whose probably originates from the interaction with laser, leading to Si surface amorphization. This confirms the formation of a-Si on n/n$^+$ bare Si wafer under laser impact, independently of the presence of dielectric layers above. In comparison with the Si2p spectra of non impacted area, a slight shift of Si wafer contribution towards lower energies can be observed after laser ablation. This behavior could be explained by surface modification of the material related to the dopant type and concentration. Indeed, the Si2p peak for a p-type Si is positioned at lower energies than for a n-type Si [164]. It suggests that after laser ablation the Si surface is less n-type doped, which could be due to dopant

profile modification of oxygen diffusion into Si wafer during the laser process.

After PLA, the spin-orbit splitting is recovered which indicates that a-Si has been recrystallized. The position of $Si2p_{3/2}$ and $Si2p_{1/2}$ contributions are also similar to the one for the non impacted area. Thus, it seems that the PLA enables to recover the initial network organization and doping properties of silicon wafer under the SiO_x layers. However, after the $NaHF_2$ chemical treatment, a slight shift towards higher energies is observed. It is likely that $NaHF_2$ treatment had etched SiO_x layers but also the extreme Si surface which is doped (etching of silicon in fluoride media is supposed to be very low [97] on unbiased conditions).

SiO_x contribution after laser ablation is more intense than the one of non impacted area. It confirms that laser impact leads to Si surface oxidation. After PLA, SiO_x contribution is slightly increased. The PLA is performed under N_2 but during cooling step, the chamber returns to air atmosphere before complete cooling which can cause a slight additional Si oxidation. After $NaHF_2$ treatment, SiO_x contribution decreases and is similar to the one of non impacted area. It suggests that SiO_x layers have been properly removed and remaining SiO_x contribution corresponds to a native silicon oxide layer.

Atomic percentages and SiO_x stoechiometry after laser ablation are depicted in Table 3.3. Results obtained with another F_{peak} (0.448 J/cm^2) with 50% overlapping are also given for comparison. The laser formed SiO_x on n/n^+ bare Si wafer has a stoechiometry close to 2 for both F_{peak} tested, so it is similar to a thermal oxide. Technically, we are not supposed to found a O/Si ratio > 2 and to explain our higher values, we can hypothesize: 1) a standard deviation of XPS measurements 2) oxygen incorporation, through O_2 diffusion or surface hydration, which complicates the analysis.

Table 3.3: XPS atomic percentages and SiO_x stoechiometry obtained after reconstruction of the XPS spectra of laser ablated bare silicon n/n^+ wafers.

	F_{peak} (J/cm^2)	0.448	1.809
Contamination	**C (C1s)**	8.7%	7.1%
	O (O1s)	4.5%	5.3%
SiO_x	**O (O1s)**	37.5%	35.37%
	Si (Si2p sub-oxide + Si2p SiO_x)	17%	15.8%
SiO_x stoechiometry	**O/Si**	2.20	2.23
Si wafer	**$Si2p_{3/2}$**	32.3%	36.5%

XPS profiling results to analyse the initial SiO_x layer on the rear polished side of n-PERT precursors

In order to further analyse the stoechiometry of SiO_x layers observed on Si surface after laser ablation on the rear side of n-PERT precursors, it is necessary to know the initial stoechiometry of the SiO_x dielectric layer. For that purpose, the 70 nm SiO_xN_y layer must be progressively etched by sputtering with Ar gun (2000 eV) to analyse the underlying SiO_x layer. Due to the important density of SiO_xN_y layer on the rear side, it has been necessary to first chemically etch a part of it in HF $5\%_{wt}$ during 1h30 to avoid too long XPS profiling analysis. The pre-etched sample is then analysed by XPS during sputtering of the surface and the evolution of atomic percentages with sputtering time is displayed in Figure 3.20.

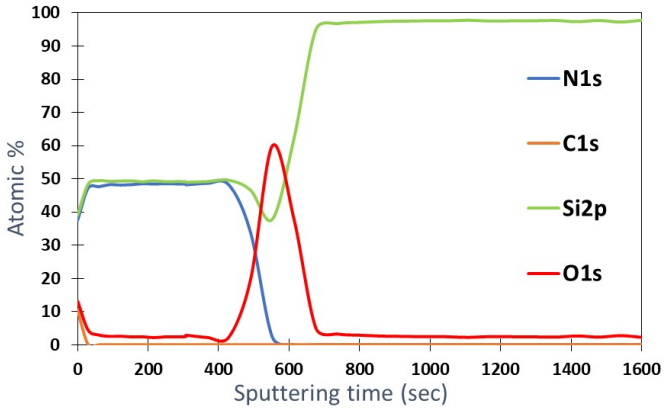

Figure 3.20: Evolution of atomic percentages with sputtering time of SiO_xN_y/SiO_x dielectric stack on n-PERT rear polished side.

As expected, the amount of nitrogen progressively decreases and after 600 seconds sputtering the entire SiO_xN_y layer has been removed. The amount of oxygen starts to increase after 400 seconds, indicating that the SiO_xN_y/SiO_x interface has been reached. After 700 seconds, both dielectric layers have been completely removed and only the Si bulk is analysed. To determine the SiO_x layer stoechiometry, the XPS spectrum realized at 600 seconds sputtering has been analysed. Indeed, at this moment the SiO_xN_y layer has been completely etched and the oxygen amount is maximum so conditions are ideal to analyze the SiO_x layer. Atomic percentages and SiO_x stoechiometry obtained after reconstruction of the XPS spectrum are shown in Table 3.4. Values depend on the methodology used to fit the XPS spectra but the same methodology has been used for all XPS analysis in this thesis. Fitting details are not given here but are identical to the one explained just after for the analysis of XPS spectra after laser ablation on rear side of n-PERT precursors.

The SiO_x layer in the initial dielectric stack has been deposited by PECVD and O/Si ratio obtained with this technique are generally comprised between 1.5 and 2 [166]. The stoechiometry found in Table 3.4 is equal to 1.65 which is consistent and corresponds to a refractive index of ≈ 1.5 according to literature [166].

Table 3.4: XPS atomic percentages and SiO_x stoechiometry after reconstruction of the XPS spectra at 600 seconds sputtering time.

SiO_xN_y	**O (O1s oxinitride)**	3.6%
	Si (Si2p oxinitride)	1.9%
	N (N1s)	2%
Si wafer	**$Si2p_{3/2}$**	1.4%
SiO_x	**O (O1s)**	56.8%
	Si (Si2p sub-oxide + Si2p SiO_x)	34.4%
SiO_x stoechiometry	**O/Si**	1.65

Results on textured/polished n-PERT precursors: rear polished side analysis

Then, XPS measurements have been performed on samples with 50% overlapping at four different F_{peak}: 0.269 J/cm^2, 0.448 J/cm^2, 1.809 J/cm^2 and 2.159 J/cm^2. CLSM images of analysed samples are depicted in Figure 3.21.

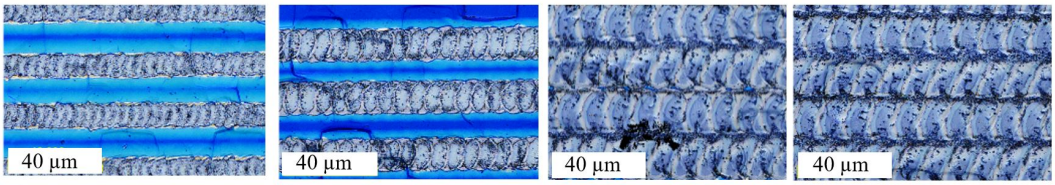

Figure 3.21: CLSM optical images of laser ablated samples (50% overlapping) analysed by XPS. a) F_{peak} = 0.269 J/cm^2, b) F_{peak} = 0.448 J/cm^2, c) F_{peak} = 1.809 J/cm^2, d) F_{peak} = 2.159 J/cm^2.

High energy resolution spectra obtained after laser ablation using F_{peak} = 1.809 J/cm^2 (50% overlapping) are displayed in Figure 3.22 with the details of fitting. From the survey spectra (not shown here), 4 elements are detected: Si, O, N and C. Carbon presence (7.2 at.%) is attributed to sample inherent superficial contamination.

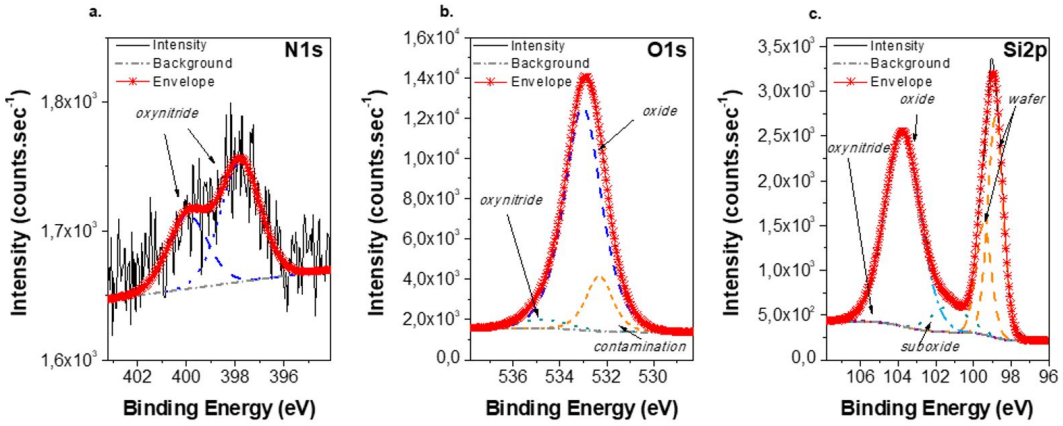

Figure 3.22: High energy resolution XPS spectra after laser ablation at F_{peak} = 1.809 J/cm^2 (50% overlap).

The Si2p spectrum (Figure 3.22 c)) shows two main environments, the first one, at 98.5 eV (Si2p$_{3/2}$ contribution), is attributed to the crystalline Si wafer [164], the second one, at 103.5 eV fitted using only one contribution, corresponds to oxide phases [165] in agreement with O1s predominant oxide contribution at 532.7 eV. A minor suboxide phase at 100.9 eV is also detected as well as a very low SiO_xN_y oxynitride contribution at 105.2 eV. This is coherent with the low signal levels of O1s contribution at 534.4 eV and N1s photopeak, visible by using XPS contrarily to EDS, and presenting a specific double structure assigned to the oxynitride organization [167]. The last O contribution at 532.0 eV corresponds to the O involved in the C contamination layer. The detection of the Si substrate signal indicates that the oxidized layer is thinner than 10 nm or either inhomogeneous. The spin-orbit splitting is not visible which suggests a disorganization of the atomic network (silicon surface amorphization) as observed on n/n$^+$ Si wafers.

Similar photopeak reconstructions are obtained for all F_{peak} studied, but with a variability of the different contributions proportion and stoechiometry, as evidenced on the Figure 3.23 presenting the superimposition of the Si2p, O1s and N1s regions. The qualitative comparison of Si2p peak envelops shows a SiO_xN_y contribution for 0.269 and 0.448 J/cm^2 which becomes negligible compared to the oxide and substrate ones at higher F_{peak}. This is confirmed by looking at O1s and N1s peaks. This can be attributed to a lack of over-

lapping between spot lines as seen in Figure 3.21 a) and b). The atomic percentages are depicted in Table 3.5 and the SiO_x stoechiometry has been calculated.

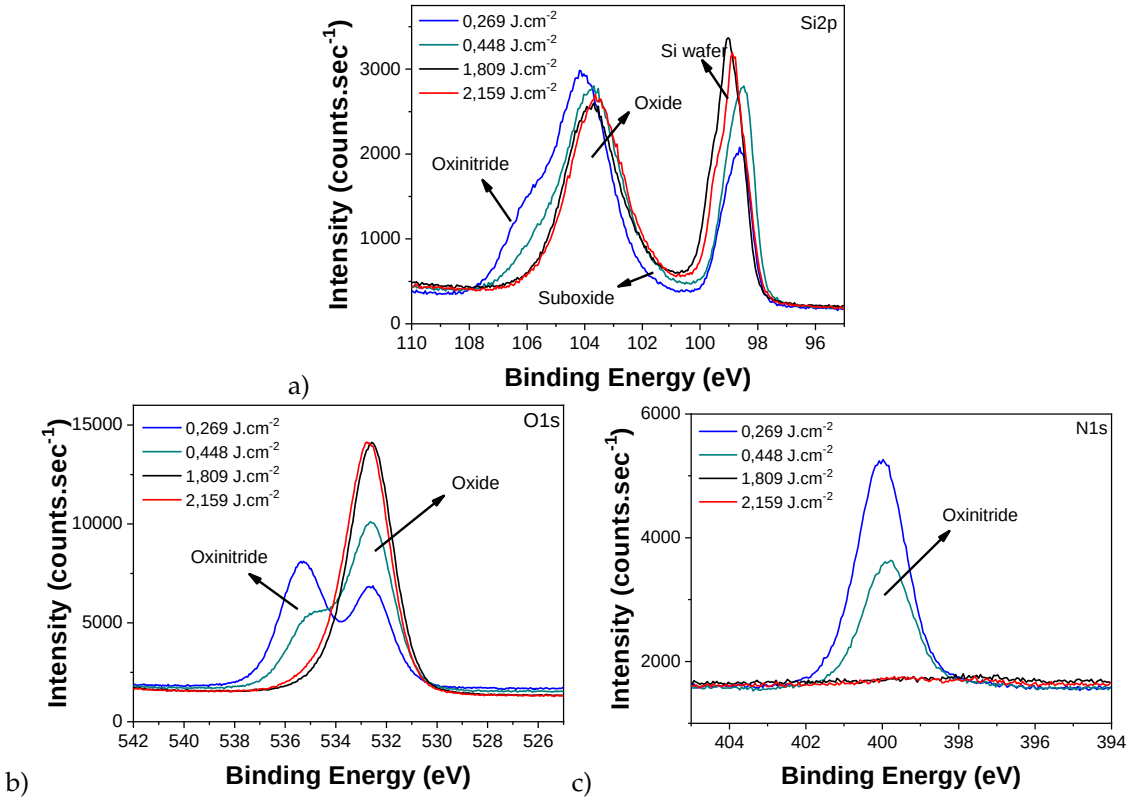

Figure 3.23: High energy resolution XPS spectra of a) Si2p, b) O1s and c) N1s after laser ablation on the rear side for different F_{peak}.

Table 3.5: XPS atomic percentages and SiO_x stoechiometry obtained after reconstruction of the XPS spectra of rear side laser ablation on n-PERT precursors using various F_{peak}.

	F_{peak} (J/cm^2)	0.269	0.448	1.809	2.159
Contamination	**C (C1s)**	5.6%	5.5%	7.2%	6.9%
	O (O1s)	2.6%	5.3%	7.3%	7.5%
SiO_x	**O (O1s)**	13.4%	23.5%	41.5%	39%
	Si (Si2p sub-oxide + Si2p SiO_x)	13.7%	16.2%	24.7%	25.8%
SiO_x stoechiometry	**O/Si**	0.98	1.45	1.68	1.51
SiO_xN_y	**O (O1s oxinitride)**	22.6%	15%	2.1%	4.9%
	Si (Si2p oxinitride)	17.9%	12.9%	0.1%	0.1%
	N (N1s)	15.3%	9%	0.9%	1%
Si wafer	**$Si2p_{3/2}$**	8.2%	12.6%	16.3%	15%

The O/Si ratios corresponding to the SiO_x environment, rise with F_{peak} from 0.98 to 1.68, which is globally lower than the stoechiometry of initial SiO_x layer. These values are also lower than the stoechiometry of laser formed SiO_x layer (see Table 3.3 for XPS analysis on n/n^+ bare Si wafers). Moreover, the comparison of Si2p spectra after laser ablation on n-PERT precursors with the one after laser ablation on n/n^+ bare Si wafers (not shown here) always demonstrates a lower contribution of the Si wafer with an higher contribution of SiO_x contribution in case of ablation on n-PERT precursors. This indicates that SiO_x layers present on ablated n-PERT is thicker than the one created under laser heat effect on n/n^+ bare Si wafers.

Based on these results, it can be hypothesized that the oxide in double impacted areas is a mixed of remaining initial SiO_x, probably modified by the laser impact, with a laser formed SiO_x layer. Due to the presence of dielectric layers above silicon during the first laser impact and the presence of remaining SiO_x layer during the second laser impact, less Oxygen can be incorporated to oxidized the silicon surface during the laser process.

Concerning the SiO_xN_y environment, the oxynitride contribution is very low for high F_{peak} (1.809 and 2.159 J/cm^2) which indicates that dielectric layers have been well removed. Nitrogen is however still detected, probably due to presence of some residues.

Then, XPS analyses have also been carried out after PLA and $NaHF_2$ treatment ($1\%_{wt/wt}$ 2 min). Results are similar for the four F_{peak} tested and spectra obtained at F_{peak} = 1.809 J/cm^2 are shown in Figure 3.24.

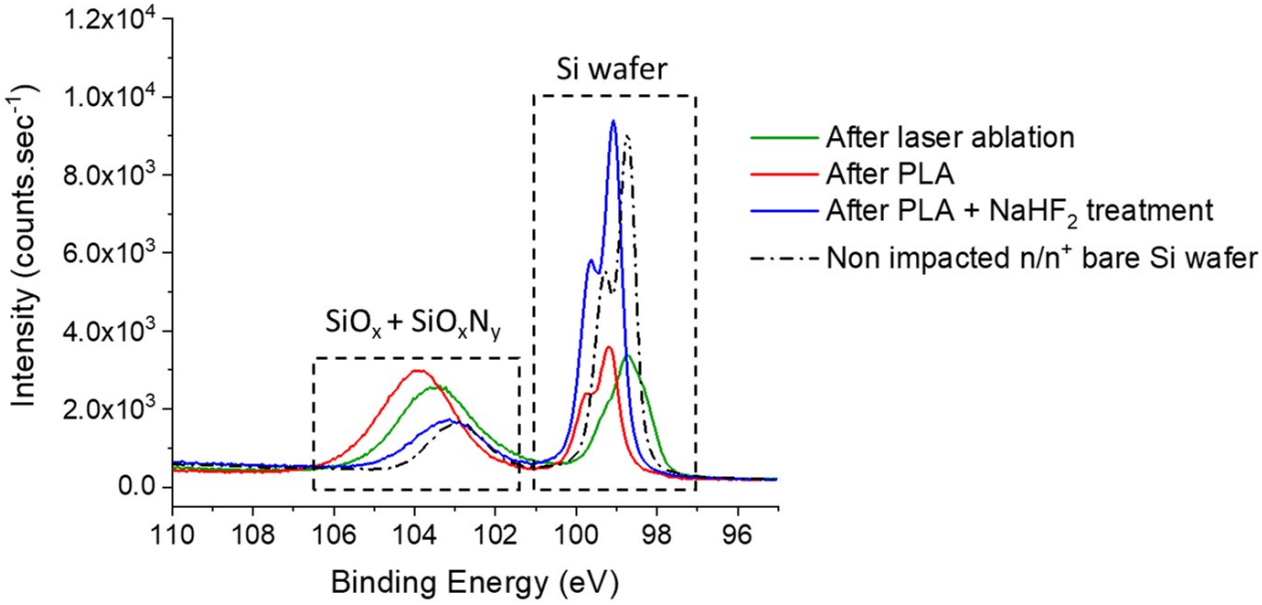

Figure 3.24: High energy resolution XPS spectra of Si2p after ablation with F_{peak} = 1.809 J/cm^2, 50% overlapping followed by PLA and $NaHF_2$ treatment. The Si2p spectra obtained on non impacted n/n$^+$ bare Si wafer is also represented as reference.

Observations are similar to the one described on n/n$^+$ bare Si wafers. The laser seems to have an impact on the dopants at Si surface because the $Si2p_{3/2}$ peak contribution (attributed to the c-Si wafer) is shifted to lower energies (green curve in Figure 3.24). After the PLA, the $Si2p_{3/2}$ peak contribution is shifted towards higher energies and starts to recover its spin orbit splitting (red curve). This is consistent with the a-Si re-crystallization and suggests a modification of the dopant profile after PLA. However, it seems that Si crystallinity is better but not completely recovered because the shape of $Si2p_{3/2}$ peak is still slightly different from the initial state (non impacted n/n$^+$ Si surface (see black curve in Figure 3.24)).

After the fluoride treatment, it appears that SiO_x contribution is significantly reduced while c-Si wafer one is increased (blue curve in Figure 3.24). As SiO_x on the surface has been etched by $NaHF_2$, analysed depth mainly comprises c-Si wafer which explains this observation. The observed SiO_x contribution after $NaHF_2$ treatment is similar to the one on non impacted n/n$^+$ bare Si wafer. Therefore, SiO_x layers present

after laser ablation have been properly removed by the fluoride treatment and only native oxide remains.

Results on textured/polished n-PERT precursors: front textured side analysis

XPS analysis have also been performed on double impacted areas on the front side of n-PERT precursors. Pyramids texturing complicates XPS analysis and results interpretation due to electrons reflections. High energy resolution XPS spectra of Si2p after laser ablation for four F_{peak} tested is represented in Figure 3.25. Table 3.6 gives atomic percentages and the SiO_x stoechiometry obtained.

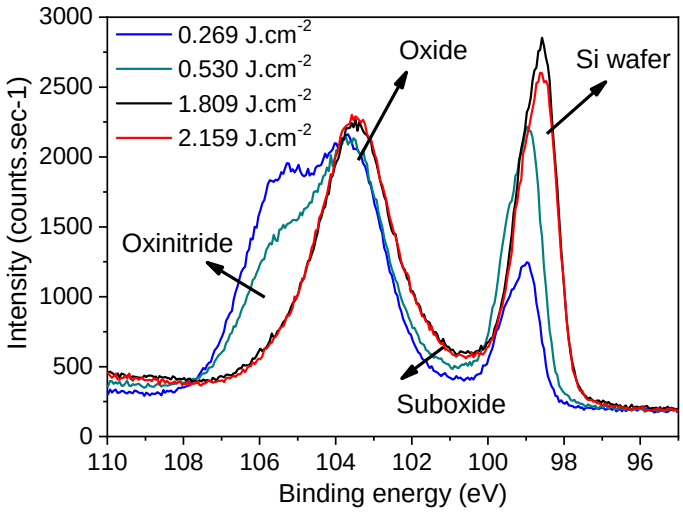

Figure 3.25: High energy resolution XPS spectra of Si2p after laser ablation on the front textured side of n-PERT precursors with different F_{peak}.

Table 3.6: XPS atomic percentages and SiO_x stoechiometry obtained after reconstruction of the XPS spectra of front side laser ablation of n-PERT precursors.

	F_{peak} (J/cm^2)	0.269	0.448	1.809	2.159
Contamination	**C (C1s)**	8.7%	8.3%	9.7%	9%
	O (O1s)	1.4%	1.7%	6.9%	7.6%
SiO_x	**O (O1s)**	6.3%	14.7%	33.5%	33.8%
	Si (Si2p sub-oxide + Si2p SiO_x)	15.7%	20.2%	25.5%	25.2%
SiO_x stoechiometry	**O/Si**	0.40	0.73	1.31	1.34
SiO_xN_y	**O (O1s oxinitride)**	33.3%	25.5%	6.2%	5.7%
	Si (Si2p oxinitride)	16.5%	9.6%	1.1%	1.9%
	N (N1s)	13.0%	9.8%	3.0%	3.2%
Si wafer	**Si2p$_{3/2}$**	5.1%	10.3%	14.2%	13.5%

SiO_xN_y contribution is globally more important on the front side compared to the rear side, even at high fluences, suggesting an higher proportion of dielectric layer residues. This observation is consistent with previous SEM observations. Furthermore, for low fluences (F_{peak} = 0.269 and 0.448 J/cm^2), SiO_xN_y contents are still important which is due to remaining dielectric layers between laser opened line, as observed for the rear side. Similarly to the rear side, the spin-orbit of Si2p$_{3/2}$ peak contribution is not observed, suggesting silicon amorphization under laser impact. However, it is possible that the spin-orbit of Si2p$_{3/2}$ peak

contribution does not appear even on non impacted textured silicon surface. It would therefore have been necessary to perform XPS analysis on a bare textured p-type side wafer to verify if the spin-orbit of Si2p$_{3/2}$ peak contribution appears.

A SiO$_x$ layer $\leq$ 10 nm is also observed after ablation but its stoechiometry is different than on the rear polished side. Globally, SiO$_x$ appears less rich in oxygen on the front textured side. Knowing that this side is more thermally impacted due to diffusion mechanisms on pyramids, we would expect O/Si ratios being higher on the front side since higher thermal impact would increase silicon reactivity towards oxygen incorporation. However, the initial SiO$_x$ layer on the front side is different (BSG) than the one on the rear side and its stoechiometry is not known which limits the analysis to hypothetical statements. As for the rear polished side, it is possible that SiO$_x$ observed on double impacted area correspond to a mix of remaining BSG layer, probably modified by the laser impact, with a laser formed SiO$_x$ layer.

As shown in Figure 3.26, no significant modifications of Si2p spectra are observed after the PLA. As explained above, it is possible that spin-orbit of Si2p$_{3/2}$ peak contribution does not appear in any case due to pyramid texturing. Another explanation can be proposed regarding the different crystal orientation on the front (111) and rear side (100). Yet, Csepregi et al. [168], have observed experimentally that re-crystallization of a-Si layer on top of c-Si substrate was favored on (100) orientation over (111) one. Therefore, PLA may be not suitable to bring enough energy for re-crystallization on (111) crystal orientation.

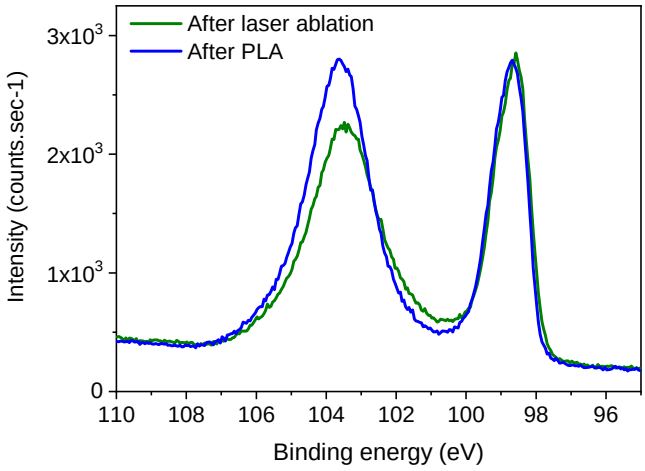

Figure 3.26: High energy resolution XPS spectra of Si2p after laser ablation on the front textured side using F$_{peak}$ of 1.809 J/cm^2 and 50% overlapping and followed by a PLA.

3.5.4 Conclusions and perspectives

The fine surface chemistry on the four areas identified before (1, 2, 2$_{bis}$ and 4) after laser ablation on the rear polished side of n-PERT precursors has been analysed by SAM. The melted residues observed on SEM pictures correspond to SiO$_x$N$_y$ melted residues, which confirms that this layer is thermally impacted during the laser process. Moreover, SiO$_x$ phase has been detected in the four areas with different amounts of Oxygen. The lower oxygen content was found in area 2$_{bis}$ in which dielectric layers seem to have been efficiently removed without a significant surface reoxidation under laser heat effect. Results indicate higher

amounts of Oxygen in area 1 and 2, suggesting that SiO_x is thicker or has an higher stoechiometry in these areas. It is likely that initial SiO_x dielectric layer has not been completely removed in area n°2. In area n°1, amounts of Oxygen are similar to the one in double impacted areas and may contain a mix of remaining initial SiO_x dielectric layer, probably modified by the laser impact, with a laser formed SiO_x layer.

Indeed, double impacted areas have been analysed by XPS and more information have been obtained, especially concerning atoms chemical environments and Si network organization. The Si/O ratio is increased when F_{peak} increases, which suggests that the SiO_x is, at least partially, formed under laser heat effect. However, the SiO_x stoechiometry remains lower than the one on double impacted areas on bare n/n^+ Si wafers and has been assimilated to a thermal oxide. The SiO_x stoechiometry also stays lower than the one of initial SiO_x dielectric which has been determine to be equal to 1.65 according to XPS profiling results. This supports the hypothesis of a mixed SiO_x layer on double impacted areas (remaining initial SiO_x dielectric layer modified by the laser impact + laser formed SiO_x layer).

XPS results also confirmed that underlying Si was amorphized during ablation process at least on the rear polished side and independently of the presence of dielectric layers above it. A PLA is beneficial by promoting partial a-Si recrystallization on the rear polished side. It has also been demonstrated that $NaHF_2$ $1\%_{wt/wt}$ treatment enabled to completely etch the SiO_x layer detected on double impacted areas after laser ablation on the rear polished side.

It would be interesting in a further work to investigate different PLA conditions to achieve a complete Si crystallinity recovering on the rear polished side. To better understand the results obtained on the front textured side, XPS measurements on bare n/p^+ textured Si wafer must be performed.

3.6 Proposition of an ablation mechanism

On the rear polished side of n-PERT precursors

To investigate the ablation mechanism, it is necessary to take into account dielectric layers properties. On the rear polished side, the SiO_xN_y bandgap has been determined by ellipsometry using Uvisel2 equipment from Horiba. Measurements have been carried out from 1 to 5 eV with a 0.02 eV step. A Tauc Lorentz model has been used to characterize the optical properties of SiO_xN_y layer and results have been successfully fitted (χ^2 = 1.9). The model gives expected thicknesses of SiO_x and SiO_xN_y layers (respectively around 10 and 70 nm) and a refractive index at 633 nm of 2.05. A Tauc diagram is subsequently obtained by plotting equation 3.3 which gives a SiO_xN_y bandgap of 3.6 eV, consistent with literature for this refractive index value [169].

$$(\alpha h\nu)^{\frac{1}{r}} = f(h\nu) \tag{3.3}$$

with α the absorption coefficient, h the Planck's constant, ν the frequency and r a coefficient equal to $\frac{1}{2}$ for a direct bandgap and 2 for an indirect bandgap.

The bandgap of SiO_x layer deposited by PECVD can not be determined precisely because the SiO_x layer is into a stack so ellipsometry is not suitable in this case. As the stoechiometry has been determined previously ($\approx$ 1.65 which corresponds to a refractive index of $\approx$ 1.5 [166]) we can estimate a bandgap $>$ 3.8 eV

according to literature [170]. However, as explained in section 2.6, the rear side dielectric stack has underwent an additional thermal treatment (used as boron diffusion barrier) which has probably modified the SiO_x layer optical properties [171]. As a reminder, at 300K, Si bandgap is 1.12 eV [172] and UV photons have an energy of 3.49 eV. If we consider a SiO_x bandgap $>$ 3.8 eV, that means it does not absorb directly the laser energy. In regards with the morphological and chemical composition analysis, this hypothesis is consistent.

Therefore, direct energy absorption is possible in underlying Si while multi-photon process is required for absorption in SiO_x and SiO_xN_y layers on the rear polished side. Laser pulse duration is 10 ps, which enables to bring high quantity of photons in a short time. In these conditions, matter thermalization is low and ablation can occur through sublimation without passing by melting and liquid phases [150]. Based on these considerations and previous characterization results, the following ablation mechanism have been proposed for the rear polished side. We consider three fluence threshold (F_{th1}, F_{th2}, F_{th3}) and the ablation process is based on partial lift-off as illustrated in Figure 3.27.

- In area n°3, $F \leq F_{th3}$ and dielectric layers have not been ablated. Contrary to SiO_xN_y and SiO_x, the Si underlying can absorb the laser energy. Underlying Si is sublimated/melted but not enough stress is created between Si and dielectric layers to lift-off these dielectric layers.

- In area n°2_{bis}, $F_{th3} \leq F \leq F_{th2}$. In these conditions, SiO_xN_y and SiO_x layers still can not absorb the laser energy because there are not enough photons to promote multi-photon absorption. Si underlying absorbs the laser energy but the higher quantity of photons in this case allows to create a sufficient mechanical stress, through sublimation/melting of Si underlying, to lift-off the dielectric layers. Si surface re-oxidation occurs slowly due to low fluence in this area.

- In area n°1 and n°2, fluence is high enough to promote multi-photon absorption in dielectric layers. Thus, both SiO_xN_y and SiO_x are sublimated/melted and Si surface re-oxydation can happen. For $F_{th3} \leq F \leq F_{th2}$, a gradient of remaining SiO_x appears along the laser opened spot, such as it is thicker in area n°2. It is worth mentioning that ablation in area n°1 and n°2 through direct absorption into dielectric layer occurs simultaneously to the lift-off in area 2_{bis}. That helps to remove dielectric layers in area 1 and 2.

In overlapped areas (not represented in Figure 3.27), the probable scenario is:

1. First, laser impact leads to the morphology represented in Figure 3.27.

2. As dielectric layers have been largely removed, the whole energy of the second impact is absorbed by the Si and/or SiO_x which is partially sublimated/melted. Meanwhile, as the laser ablation is performed under air atmosphere, Si surface is oxidized and finally, double impacted areas have a mix of remaining initial SiO_x layer and laser induced SiO_x.

During fast cooling, Si is probably amorphized in all observed areas.

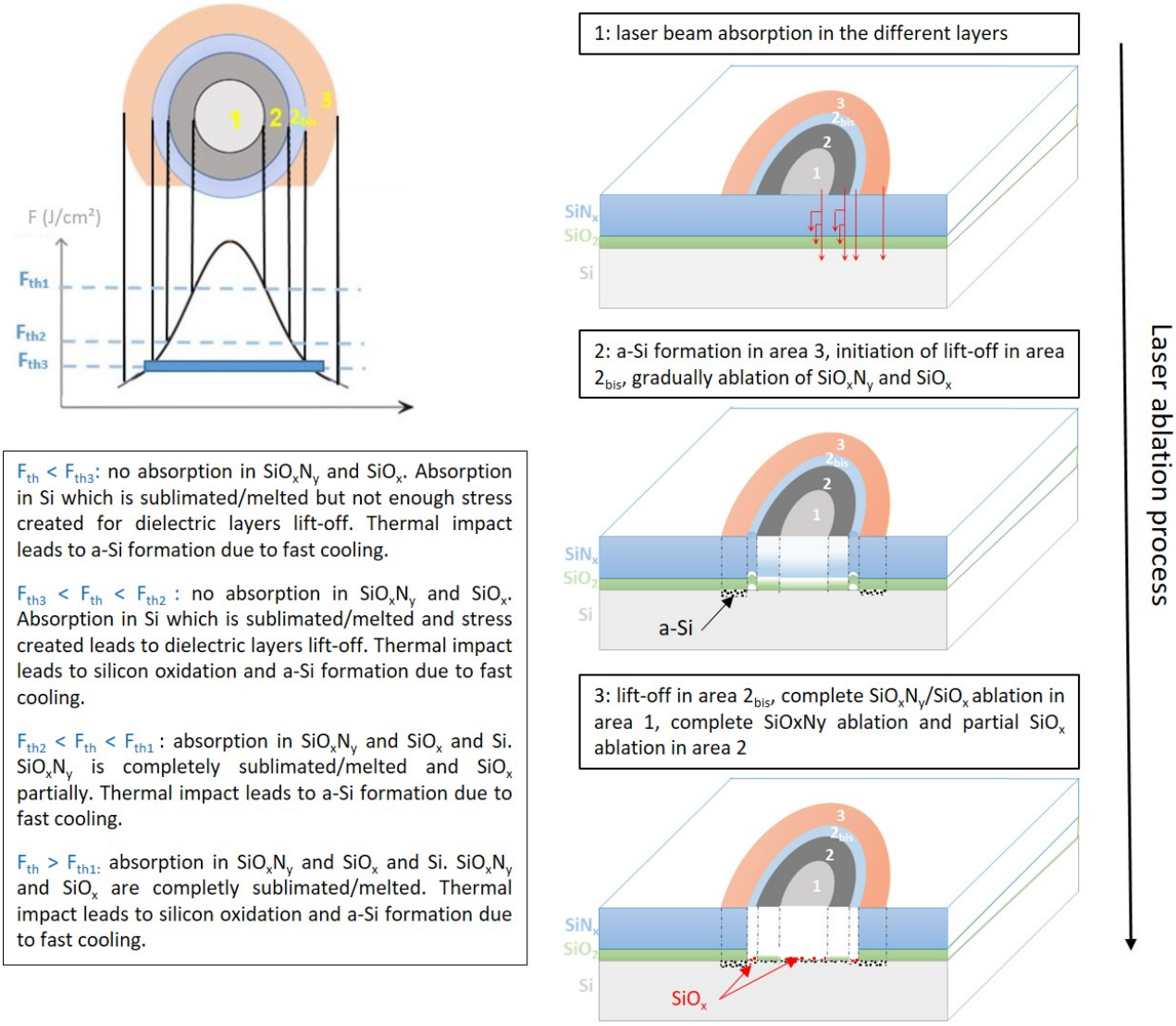

Figure 3.27: Proposed ablation mechanism based on partial lift-off of SiO_xN_y/SiO_x dielectric layers on the rear polished side with a UV-ps laser.

On the front textured side of n-PERT precursors

Since ellipsometry measurements are not suitable for highly textured surfaces, the SiO_xN_y refractive index and bandgap can not verified on front side of n-PERT precursors. However, according to the supplier, the refractive index at 630 nm should be around 2.03. The corresponding bandgap is thus $\approx$ 3.6 eV and SiO_xN_y can only absorb laser energy in case of high fluence through multi-photon process as for the rear side. In addition, residues observed by SEM on the front side after laser ablation are very sharp with thickness around 70 nm. Consequently, we can suggest that laser ablation process on the front textured side is also based on partial lift-off.

COMPLEMENTARY COMPARATIVE STUDY

For comparison with n-PERT precursors having a 70 nm thick SiO_xN_y dielectric layer which barely absorb the laser beam, we have also worked on Si samples with a 100 nm thick Si-rich SiO_xN_y dielectric layer deposited by PECVD and having better absorption properties. The refractive index obtained is 3.2, corresponding to a bandgap of 2.5 eV (Tauc plot determination method). The photon energy is higher than the material bandgap, providing direct absorption into SiO_xN_y layer. It results in a completely different morphology after ablation as visible on CLSM images in Figure 3.28. Much higher F_{peak} are necessary to completely remove the SiO_xN_y layer if we do not use overlapping (≈ 10 J/cm^2). The heat affect area is not observed which suggests that Si underlying is not amorphized. As laser beam energy is mainly absorbed in SiO_xN_y layer (direct ablation mechanism), Si underlying is much less impacted compared to partial lift-off mechanism described before on n-PERT precursors.

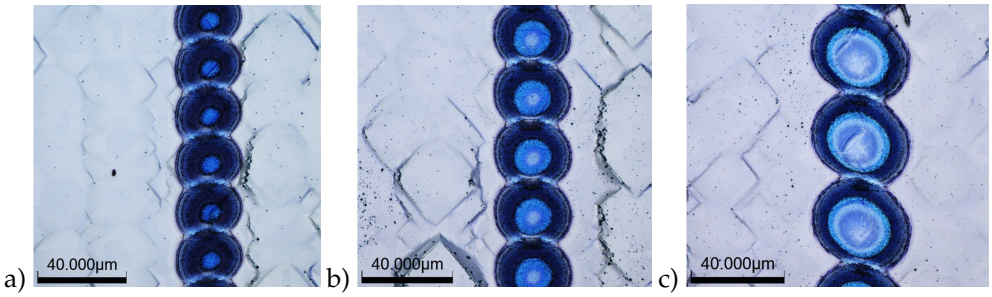

Figure 3.28: CLSM images after laser ablation on sample with Si-rich SiO_xN_y dielectric layer using F_{peak} = a) 1.35 J/cm^2, b) 3.34 J/cm^2 and c) 10.50 J/cm^2.

The color contrast reflects a SiO_xN_y thickness gradient such as laser opened area borders have thicker SiO_xN_y remaining layer. This is confirmed by EDS analysis depicted in Figure 3.29.

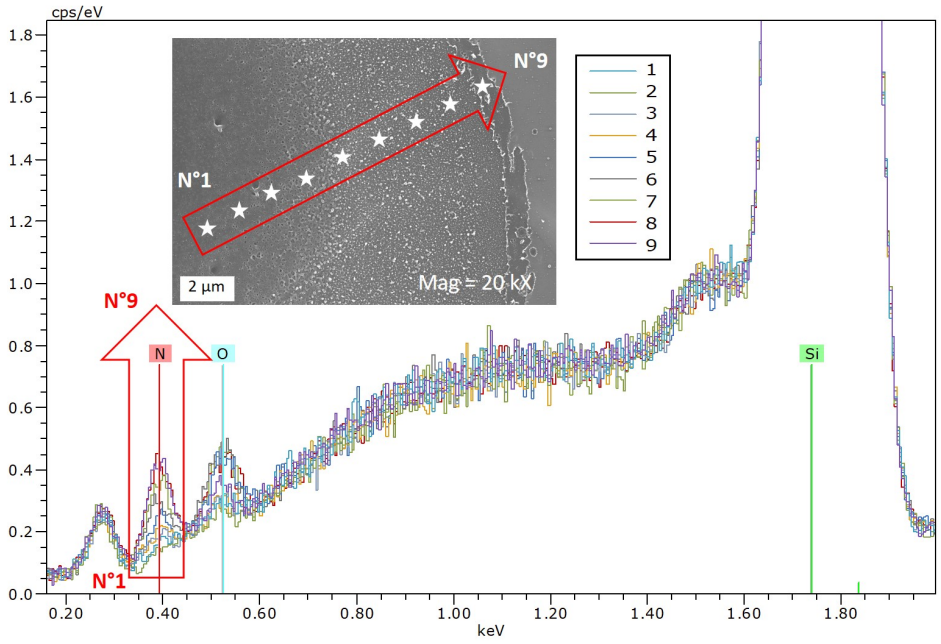

Figure 3.29: EDS spectra on laser ablated sample with Si-rich SiO_xN_y layer using F_{peak} = 10.50 J/cm^2.

3.7 Laser impact on electrical properties

3.7.1 Evolution of R_{sheet}

To evaluate the laser impact on Si surface sheet resistance, four-probe measurements have been performed on the 90 patterns represented in Figure 3.5 after laser ablation, after PLA and after fluoride treatment ($NaHF_2$ $1\%_{wt/wt}$ 2 min). The measurements are realized under dark in the center of 1 x 1 cm^2 ablated squares. On the p^+ front side, R_{sheet} should be equal to 85 Ω/sq for a non damaged Si surface. On the n^+ rear side, as the bulk is also n-type, it must be taken into account on the R_{sheet} calculation as shown in equation 3.4. If Si surface is not damaged during laser ablation, R_{sheet} should be equal to 80 Ω/sq and so the $R_{sheet,meas}$ is given by equation 3.5.

$$R_{sheet} = \frac{R_{sheet,meas} \times R_{bulk}}{R_{bulk} - R_{sheet,meas}} \quad \text{with} \quad R_{bulk} = \frac{\rho_{bulk}}{e_{bulk}} = \frac{1}{0.018} = 55.55\Omega. \tag{3.4}$$

With $R_{sheet,meas}$ the measured sheet resistance, R_{bulk} the bulk resitance, ρ_{bulk} the bulk resistivity (= 1 Ω.cm) and e_{bulk} the bulk thickness (= 0.0180 cm).

$$R_{sheet,meas} = \frac{R_{bulk} \times R_{sheet}}{R_{bulk} + R_{sheet}} = \frac{55.55 \times 80}{55.55 + 80} = 32.78\Omega/sq \tag{3.5}$$

The impact of overlapping on R_{sheet} on both sides is presented for four F_{peak} in Figure 3.30. Without overlapping, R_{sheet} stays close to its initial value (85 Ω/sq on the front side and 33 Ω/sq on the rear side) even at high F_{peak}. However, R_{sheet} is increased when overlapping is used, especially on the front side with F_{peak} = 1.809 J/cm^2. The increased R_{sheet} with overlapping can be due to:

- Defects formation (dislocations, cracks…) caused by double impact on the surface;
- Doping profile modification or dopant activation/deactivation process under the thermal effect induced by overlapping. Other characterization techniques, such as Deep Level Transient Spectroscopy and Secondary Ion Mass Spectroscopy, would have been necessary to refine this study.
- Si surface oxidation. As silicon oxide is less conductive than silicon, R_{sheet} may be increased.
- Increased Si amorphization due to double impact leading to an higher thermal impact and thicker a-Si.

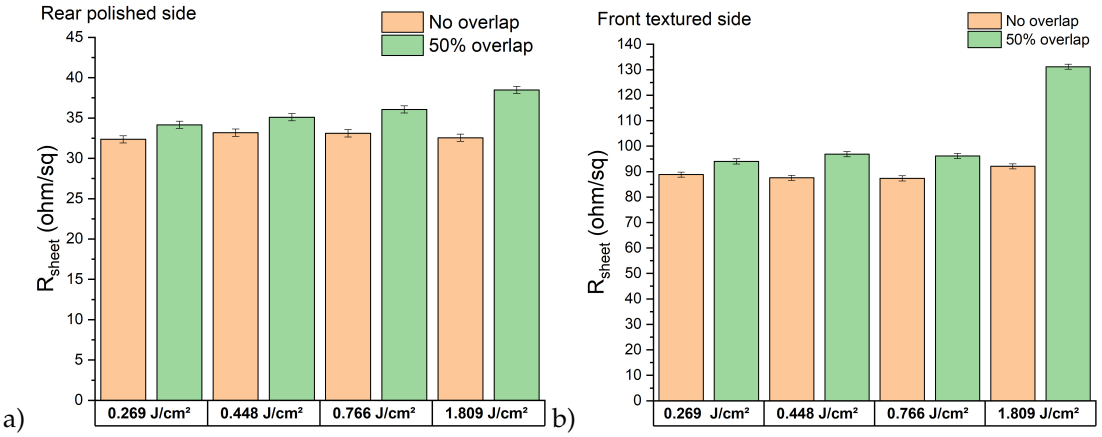

Figure 3.30: Four-probe measurements for various F_{peak} without or with 50% overlapping a) on the rear polished side, b) on the front textured side.

The effect of PLA and $NaHF_2$ treatments on R_{sheet} have been also investigated and results obtained with four F_{peak} are shown in Figure 3.31.

After PLA, the R_{sheet} value is reduced to its initial value and even lower. It is thus likely that increased R_{sheet} values after laser ablation come from a-Si formation and that PLA enables to improve Si electrical properties through a-Si recrystallization. Previous XPS measurements have evidenced the a-Si recrystallization after PLA on the rear polished side with the recovering of the spin-orbit splitting of Si2p peak (see section 3.5.3). Despite this phenomenon was not observed on the front side, four-probe measurements suggest that PLA has indeed a positive effect on Si electrical properties on the front textured side. Therefore, it is probable that PLA leads to a-Si recrystallization (at least partial) and that this phenomenon is not observed on XPS spectra due to pyramid texturing. Indeed, as explained previously, the spin-orbit splitting of $Si2p_{3/2}$ and $Si2p_{1/2}$ contributions can may not appear in any case (even on non impact surface) due to complication of XPS measurements on highly textured surfaces.

Fluoride treatment tends to slightly increase R_{sheet} values on the front side. This is not the expected effect because $NaHF_2$ etches the silicon oxide layer at the surface which is supposed to reduce the R_{sheet} values. However, if laser impact leads to increased dopant concentration at Si surface, the decrease of R_{sheet} values after $NaHF_2$ treatment could be due to the slow etching of Si surface observed in fluoride media.

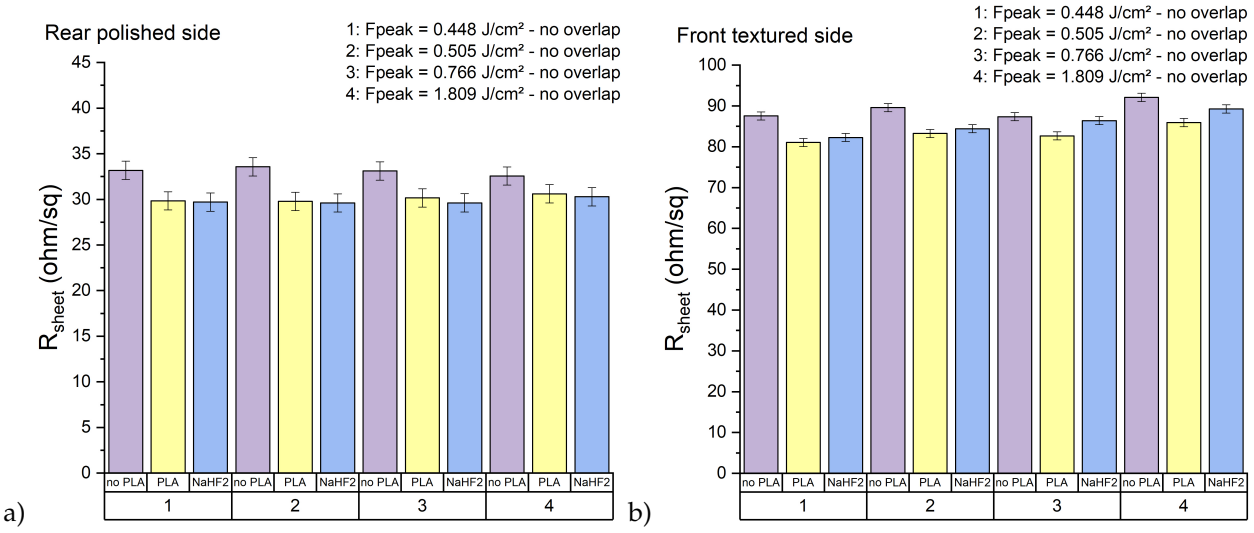

Figure 3.31: Four-probe measurements obtained for various F_{peak} without overlapping after laser ablation, PLA and $NaHF_2$ fluoride treatment a) on the rear polished side, b) on the front textured side.

Results obtained for two extreme cases, higher F_{peak} (2.159 J/cm^2) and important overlapping (d = 4 µm) are presented in Figure 3.32.

In Figure 3.32 a), the detrimental effect of overlapping is confirmed as when overlapping increases (d decreases), the R_{sheet} becomes higher. Overlapping on the front side is more critical because it is the emitter side (p-n junction) and the R_{sheet} achieves values up to 300 Ω/sq. However, when there is no overlapping, the R_{sheet} is barely impacted, even with the highest F_{peak} = 2.159 J/cm^2.

In Figure 3.32 b), an important overlapping (d = 4 µm) on the front side associated with high F_{peak} ($\geq$ 1 J/cm^2) leads to significantly reduced R_{sheet} values (32-33 Ω/sq). Here, damages are so deep that the p-n

junction is destroyed and we actually measure the R_{sheet} of n/n^+ stack, as for the rear side. R_{sheet} evolution using lowest distance d = 4 µm and various F_{peak} are shown in Figure 3.32 b). As expected, with high F_{peak} the n/p^+ junction on the front side is destroyed as R_{sheet} drastically decreases to 32-33 Ω/sq. However, R_{sheet} is not much impacted with important overlapping if lowest F_{peak} = 0.269 J/cm^2 is used.

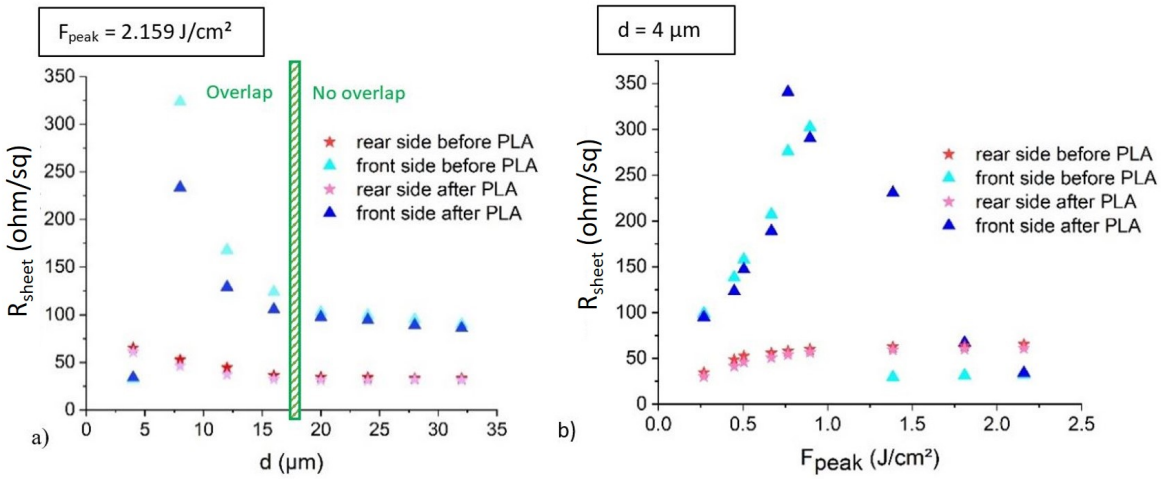

Figure 3.32: Four-probe measurements on the rear and front side before and after PLA. a) F_{peak} of 2.159 J/cm^2, variation of overlapping, b) d = 4 µm, important overlapping and variation of F_{peak}.

3.7.2 Charges carriers lifetime measurements

PL QSS-PC measurements have been carried out to investigate laser impact on the charges carriers lifetime. For this purpose, another pattern has been used with a reduced number of tested conditions to increase the square size and facilitate PL QSS-PC image analysis. With the aim to optimize laser parameters, F_{peak} close to the F_{th} identified previously (0.269 J/cm^2) have been tested with various overlapping. Two high F_{peak} have been also investigated for comparison (F_{peak} = 1.75 and 0.72 J/cm^2). A picture of ablated samples is given in Figure 3.33 and the details of the 30 laser parameters tested are reported in Figure 3.34.

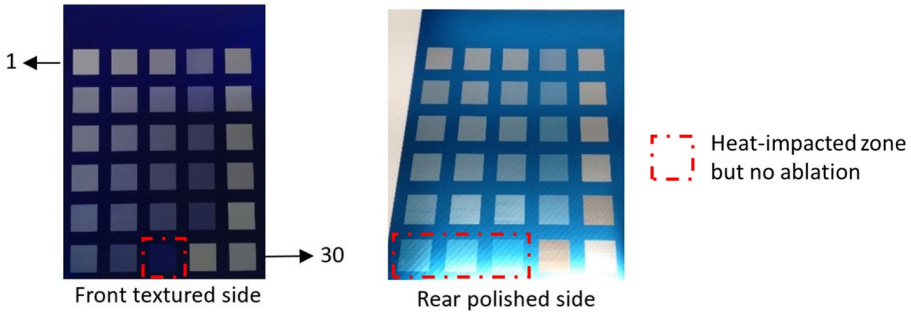

Figure 3.33: Pictures of ablated samples with various laser parameters (only one side is opened on each sample). Pattern surrounded in red are heat-impacted but not laser opened.

For this study, it is important to point out that spot overlapping is defined considering the light blue area (HAZ) and not only the opened area as it was the case until now. CLSM images are given in Figure 3.34 as for example. Pattern numbers in orange indicate that laser opened areas are not in contact (dielectric layers remaining). Due to the heat affected area, dielectric layers remain between opened lines. To achieve laser

contact opening with opened areas in contact along a line and from one line to another, laser parameters must be adjusted. These conditions have been used for patterns underlined in green in Figure 3.34.

1 1.75 J/cm² - 75%	**2** 1.75 J/cm² - 50%	**3** 1.75 J/cm² - 25%	**4** 1.75 J/cm² - 0%	**5** 1.75 J/cm² - 25%
6 0.72 J/cm² - 75%	**7** 0.72 J/cm² - 50%	**8** 0.72 J/cm² - 25%	**9** 0.72 J/cm² - 0%	**10** 0.72 J/cm² - 25%
11 0.56 J/cm² - 75%	**12** 0.56 J/cm² - 50%	**13** 0.56 J/cm² - 25%	**14** 0.56 J/cm² - 0%	**15** 0.56 J/cm² - 25%
16 0.40 J/cm² - 75%	**17** 0.40 J/cm² - 50%	**18** 0.40 J/cm² - 25%	**19** 0.40 J/cm² - 0%	**20** 0.40 J/cm² - 25%
21 0.32 J/cm² - 75%	**22** 0.32 J/cm² - 50%	**23** 0.32 J/cm² - 25%	**24** 0.32 J/cm² - 0%	**25** 0.32 J/cm² - 25%
26 0.24 J/cm² - 75%	**27** 0.24 J/cm² - 50%	**28** 0.24 J/cm² - 0%	**29** 0.24 J/cm² - 75%	**30** 0.24 J/cm² - 50%

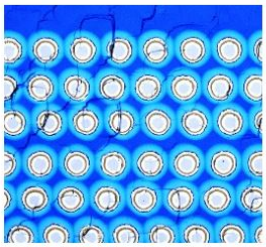

Pattern 9: opened areas not in contact

Pattern 10: opened areas in contact along a line and from one line to another

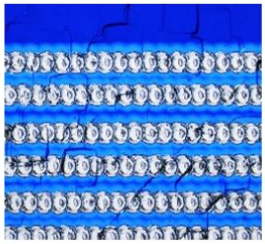

Pattern 12: overlapping of opened areas

Figure 3.34: Laser ablation parameters used for PL-QSS PC characterization and 3 examples of corresponding CLSM images: overlapping percentage takes into account the light blue area.

As explained in experimental part, samples are re-passivated with a-Si:H before PL QSS-PC to suppress the contribution of recombination due to dangling bonds at Si surface. Picture of re-passivated samples is shown in Figure 3.35. The effective surface reflectivity is an important parameter to consider for PL QSS-PC measurements, especially in this study because optical properties of samples after a-Si:H re-passivation are clearly modified. Reflectivity measurements have been carried out using a UV-Vis-NIR spectrophotometer from Agilent. Spectra have been obtained in the wavelength range 200 to 1100 nm with a 3 nm measure step. Effective reflectivities were measured at 3.6% (front side) and 17.3% (rear side) before a-Si:H re-passivation and at 30.3% (front side) and 59.2% (rear side) after re-passivation.

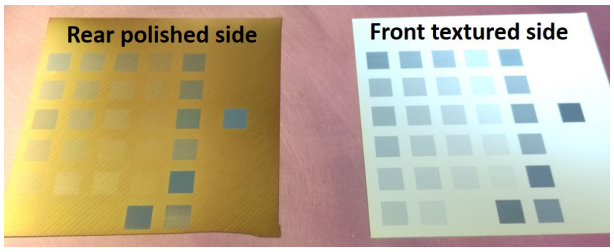

Figure 3.35: Picture of ablated samples using various F_{peak} and overlapping after a-Si:H re-passivation.

PL QSS-PC results are illustrated in Figure 3.36. Samples 1 and 1_{bis} have been re-passivated directly after laser ablation while samples 2 and 2_{bis} underwent a post laser annealing (750°C) before a-Si:H deposition. Differences between samples $1/1_{bis}$ and $2/2_{bis}$ can be mainly attributed to PLA effect.

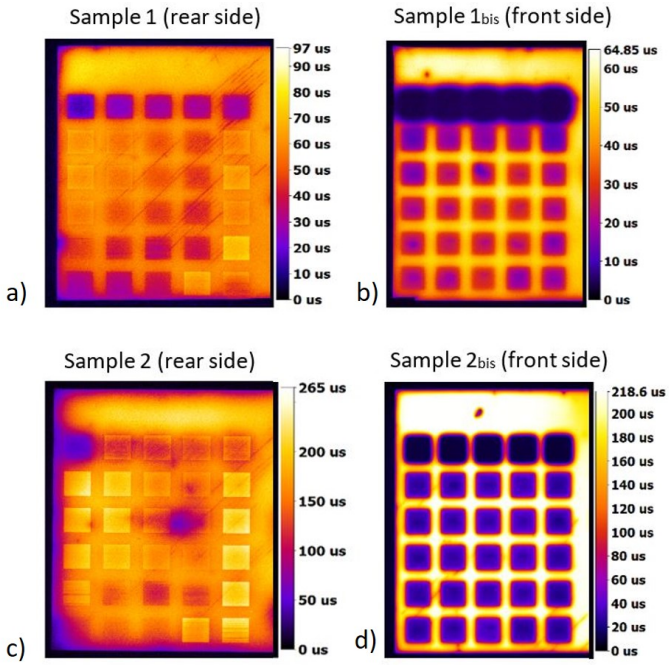

Figure 3.36: PL QSS-PC results on samples re-passivated directly after laser ablation (a) and b)) and re-passivated after laser ablation and PLA (c) and d)).

Laser impact on rear side charges carriers lifetime:

First, charges carriers lifetime into laser opened areas are almost three times higher for sample 2 (Figure 3.36 c)) where a PLA has been performed. This is consistent with a-Si recrystallization through PLA as there are less recombination centers when Si crystallinity increases. Yet, on amorphous material, localized states are present below the conduction band and above the valence band mobility edges as a consequence of lattice disorder. Geminate recombinations, consisting of immediate recombination of electron-hole pairs due to their proximity, [173], are more likely to occur which results in lower charges carriers mobility. In case of patterns underlined in green in Figure 3.34, improvement of charges carriers lifetime can be only due to a-Si re-crystallization as there are no more passivation layers. For all other patterns, effect of hydrogen diffusion from remaining passivation layers could also have a beneficial effect on charges carriers lifetime.

Patterns having less remaining dielectric layers thanks to overlapping (6, 7, 11, 12, 16, 17, 21), or even no passivation layers (patterns in green in Figure 3.34 except pattern 5), show better charges carriers lifetimes. Lower charge carriers lifetimes are obtained when dielectric layers remain (patterns in orange in Figure 3.34). This trend is visible for both samples 1 and 2 but is more significant after PLA. As a $NaHF_2$ treatment was performed before re-passivation, that enabled to etch SiO_x layer and probably also a part of damaged Si, which is beneficial for charges carriers lifetime. For patterns where few or no dielectric layers remain, the damaged Si is etched by $NaHF_2$ and charges carriers lifetimes $\geq$ 200 µs are obtained. Adversely, remaining dielectric layers hinder damaged Si surface from the $NaHF_2$ leading to lower charges carriers lifetimes.

For patterns 1 to 5, charges carriers lifetimes are $\leq$ 100 µs even after PLA and pattern 1 (75% overlapping) is clearly the most impacted. It suggests that high F_{peak} induces not only Si amorphization but also defects formation (cracks, dislocations...), which are more important when the surface is impacted several times.

Laser impact on front side charges carriers lifetime:

On the textured front side, charges carriers lifetimes values after laser ablation are much lower than on the rear polished side and no significant differences are observed between various laser parameters (except for pattern 1 to 5 where high F_{peak} leads to the worst charges carriers lifetime). Four probe measurements allowed to affirm that the p/n junction was not shunted for all laser parameters tested here (we do not observe a drastically diminution of R_{sheet} to $\approx 33\ \Omega$/sq). The front side is more sensitive to laser ablation due to optical diffusion mechanisms inducing an higher thermal impact. The lower charges carriers lifetimes observed in comparison with the rear polished side may be due to a thicker laser formed a-Si and/or an higher amount of defects such as cracks and dislocations. In addition, no significant improvements of charges carriers lifetimes are visible after the PLA (Figure 3.36 d)) which suggests that either a-Si recrystallization does not occur or is partial. PL-QSS PC results demonstrate that laser ablation has an important impact on charges carriers lifetime on the front textured side, even at low fluence and without overlapping.

3.7.3 Conclusions

On both sides, four probe measurements do not demonstrate a significant laser impact on R_{sheet} for all F_{peak} when no overlapping is used. In contrast, R_{sheet} increases with overlapping, especially on the front side where laser impact is enhanced by optical diffusion on pyramids. The p/n junction is likely to be destroyed when $F_{peak} \geq 1$ J/cm^2 with overlapping. Increased R_{sheet} with overlapping can be due to an higher thermal impact associated with a thicker a-Si layer. Impact of overlapping on R_{sheet} remains low when $F_{peak} \approx F_{th}$.

PLA enables to significantly reduce R_{sheet} values through a-Si re-crystallization on the rear side. On the front textured side, a-Si recrystallization after PLA has not been clearly evidenced by previous XPS measurements as for the rear polished side. Consequently, the positive effect of PLA on R_{sheet} values observed on the front side can not be attributed for sure to a-Si re-crystallization. Fluoride treatment has revealed to slightly increase R_{sheet} values which could be due to the etching of Si surface that may have an higher dopant concentration due to dopants diffusion during laser process.

PL-QSS PC measurements have demonstrated an important reduction of charges carriers lifetimes on the rear polished side for high F_{peak}, even without overlapping. Thermal impact is supposed to be low without overlapping so it is possible that cracks and dislocations are created. The importance of a-Si re-crystallization has been evidenced by improvement of charges carriers lifetime after PLA. As $NaHF_2$ cannot etch damaged Si surface in HAZ when dielectric layers remain between laser opened spots, that leads to reduced charges carriers lifetimes. On the front side, laser impact on charges carriers lifetime is more important even at low F_{peak} and without overlapping. This is consistent with an higher thermal impact (optical diffusion on pyramids), probably leading to a thicker a-Si layer and an higher amount of defects (cracks/dislocations). Charges carriers lifetimes are not improved after PLA which suggests that a-Si re-crystallization does not occur or is partial.

3.8 Optimized laser parameters

Based on these results, two sets of laser ablation parameters have been chosen as shown in Figure 3.37.

- **Parameters 1: F_{peak} = 0.56 J/cm^2, no spot overlapping** (laser ablation n°15 in Figure 3.34): F_{peak} is just above F_{th} such as a continuous ablation is obtained without overlapping of opened area. Low contact opening width ($\approx$ 14 µm) is obtained on both sides and the low thermal effect (thanks to low F_{peak}) limits the impact on R_{sheet} and charges carriers lifetimes.
- **Parameters 2: F_{peak} = 0.32 J/cm^2, 50% spot overlapping** (laser ablation n°21 in Figure 3.34): F_{peak} $\approx$ F_{th} and overlapping $\geq$ 50% is necessary to continuously open the dielectric layers on both sides. In this case, thermal impact caused by spot overlapping is limited by using F_{peak} as low as possible. Pyramids on the front side are not too damaged. Main advantage of parameters 2 is the induced roughness on the rear polished side. Continuous laser ablation has been also observed with F_{peak} = 0.269 J/cm^2, 50% spot overlapping in this study but further experiments have demonstrated some discontinuities to opened a entire cell (fingers + busbars), probably due to slightly variation of dielectric layers thicknesses on n-PERT precursors. Consequently, a slightly higher F_{peak} has been preferred.

For both optimized parameters, a PLA at 750°C is performed after laser ablation. Moreover, opened lines are just in contact from each others in busbars to limit HAZ proportion and promotes the etching of damaged Si surface by fluoride treatment to improve charges carriers lifetime.

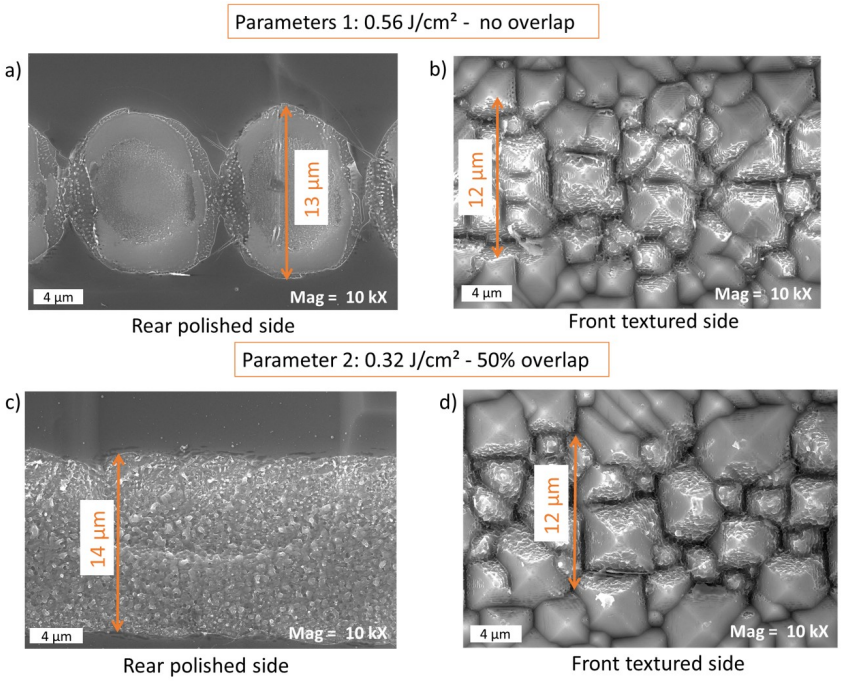

Figure 3.37: SEM images of laser ablated n-PERT precursors with optimized laser parameters (fingers).

It is possible to use parameter 1 on the front textured side and parameter 2 on the rear polished side. It enables to avoid overlapping on the front side while providing roughness on the rear one. A comparison of cell efficiencies with parameters 1, parameter 2 and non optimized parameters is performed in Chapter 5.

MEMENTO

Based on literature considerations, a UV-ps laser has been used for this study. Several F_{peak} and spot overlapping have been tested on both sides of n-PERT precursors and the morphology and chemical composition of ablated areas have been characterized. An ablation mechanism based on partial lift-off has been proposed and is summarized in Figure 3.38 for the rear polished side. This mechanism enables to understand the apparition of five concentric areas differently impacted related to laser fluence spatial distribution.

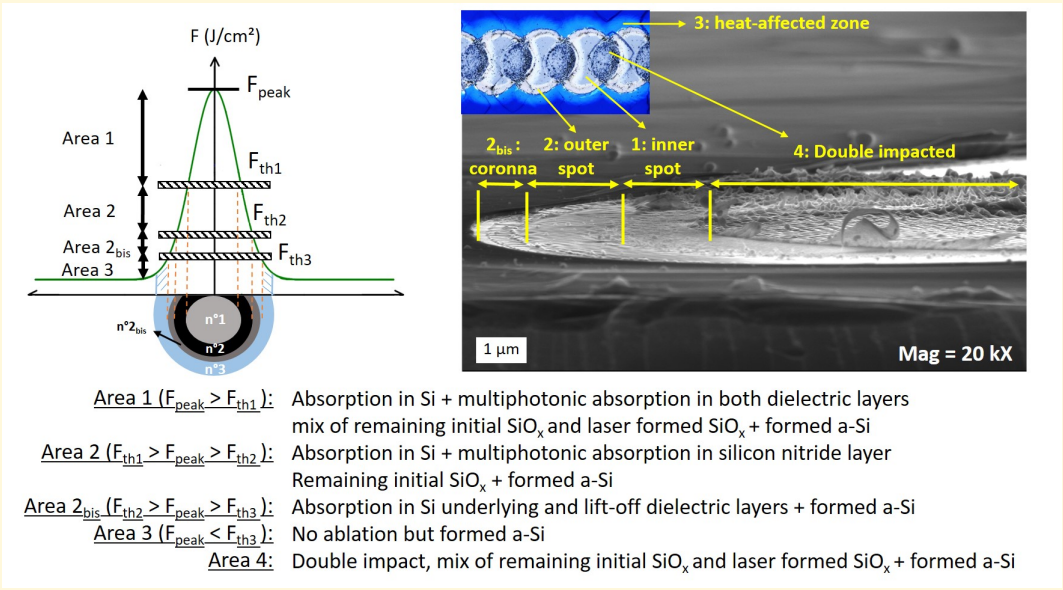

Area 1 ($F_{peak} > F_{th1}$): Absorption in Si + multiphotonic absorption in both dielectric layers
mix of remaining initial SiO_x and laser formed SiO_x + formed a-Si

Area 2 ($F_{th1} > F_{peak} > F_{th2}$): Absorption in Si + multiphotonic absorption in silicon nitride layer
Remaining initial SiO_x + formed a-Si

Area 2_{bis} ($F_{th2} > F_{peak} > F_{th3}$): Absorption in Si underlying and lift-off dielectric layers + formed a-Si

Area 3 ($F_{peak} < F_{th3}$): No ablation but formed a-Si

Area 4: Double impact, mix of remaining initial SiO_x and laser formed SiO_x + formed a-Si

Figure 3.38: Laser ablation mechanism based on partial lift-off on the rear polished side. Resulting concentric areas having different morphology and chemical surface compositions are represented on SEM and CLSM images (F_{peak} = 1.809 J/cm^2 with 10% overlapping, $F_{th3} \approx$ 0.269 J/cm^2).

Overlapping promotes surface roughness on the rear polished side which is beneficial for further metallization. Roughness is more important on the front textured side with the apparition of LIPSS even with no overlapping.

Characterization of electrical properties (R_{sheet} and charges carriers lifetimes) indicates that charges carriers lifetimes are impacted for all F_{peak} tested, even with no overlapping, due to a-Si formation and probably cracks and dislocations. Both parameters are highly impacted with overlapping due to higher thermal impact. Overlapping must be avoided, especially on the front side.

A PLA at 750°C enables to improve Si electrical properties. This is related to a partial a-Si recristallization on the rear polished side (phenomenon not clearly identified on the front side). When a fluoride treatment ($NaHF_2$ $1\%_{wt/wt}$ 2 min) is realized after PLA, charges carriers lifetimes are increased thanks to etching of the SiO_x layer observed after laser ablation as well the extreme damaged Si surface.

Finally, two optimized laser parameters have been proposed: F_{peak} = 0.56 J/cm^2 with no overlapping and F_{peak} = 0.32 J/cm^2 with 50% overlapping.

Chapter 4

Deoxidation and activation of silicon surface

CONTENTS

4.1 Introduction

As observed in Chapter 3, laser ablation leads to incomplete removal of SiO_x dielectric layer or laser formed SiO_x layer. A deoxidation step to etch this SiO_x layer is necessary and must be followed by Si surface Pd activation to prepare the Si surface before Ni/Cu plating steps. The quality of the metallic contacts highly depends on the effectiveness of these steps. Deoxidation and activation are both based on fluoride media, which are known to also etch silicon nitride layers. Yet, optical properties of the cell can be modified and parasitic plating is more likely to occur on damaged silicon nitride layers. The aim of this Chapter 4 is to optimize deoxidation and activation conditions to limit the etching of silicon nitride layers while removing SiO_x layer and providing efficient Pd activation of Si surface. The etching rates of n-PERT precursors SiO_xN_y layers is compared with the one of two SiO_x layers: a PECVD SiO_x layer and an anodic SiO_x layer (x $<$ 2 in both cases). Two fluoride media are investigated: the well-known hydrofluoric acid (HF) and the sodium difluoride ($NaHF_2$), less studied in literature. Etching mechanisms are investigated for both fluoride media and a better selectivity towards SiO_x and SiO_xN_y layers is highlighted for $NaHF_2$ which enables to optimize the deoxidation conditions. Activation in Pd-based solution is then studied in HF and $NaHF_2$. The aim is to achieve an homogeneous deposition of small Pd particles to activate the Si surface with a limited metal consumption. For that purpose, reaction mechanisms of Pd galvanic displacement on Si surface is investigated and bath composition as well as immersion time are optimized.

4.2 Study of silicon deoxidation in HF and $NaHF_2$

4.2.1 State of the art

SiO_x layers are commonly removed in fluoride-based solutions and various additives (acids, salts, alcohols) can be added to control etching rates, sensitivity, uniformity and solution stability [73]. Depending on the fluoride species involved in the etching mechanism, SiO_x dissolution can be expressed by equation 4.1, 4.2 or 4.3. Soluble silicon hexafluoride (SiF_6^{2-}) is found to be the dominant product of reaction [73], [174].

$$SiO_2 + 6HF \rightarrow SiF_6^{2-} + 2H_2O + 2H^+ \tag{4.1}$$

$$SiO_2 + 6F^- + 4H^+ \rightarrow SiF_6^{2-} + 2H_2O \tag{4.2}$$

$$SiO_2 + 3HF_2^- + H^+ \rightarrow SiF_6^{2-} + 2H_2O \tag{4.3}$$

SiO_x etching in hydrofluoric acid solutions has been studied intensively [175] but few of these works have isolated the kinetics or the reaction mechanisms. On the one hand, etching rates and mechanisms depend on the SiO_x properties such as density and stoechiometry [175]. On the other hand, the difficulty lies in the complexity of fluoride solutions which are not entirely understood [97], [176]. Nevertheless, some concordant elements found in literature [73], [97], [98], [175], [177], [178] are reported in this section.

According to Knotter M. [98], SiO_x is preferably etched by difluoride species (HF_2^-) and this opinion is shared by Judge et al. [178] and Monk et al. [175] who state that HF_2^- and HF are the two main species involved, with a faster etching rate with HF_2^-. Kikuyama et al. have also demonstrated that addition of NH_4F in HF solution (buffered HF solution) favors the formation of HF_2^- species and enables to increase

SiO_x etching rate [177]. It is suggested that HF and HF_2^- etch SiO_x layers faster compared to F^- ion thanks to their hydrogen atoms which are susceptible to create weak hydrogen bonds with the SiO_2 network. As a result, Si-O bond is easily broken thanks to stabilization of HF and HF_2^- species approaching the SiO_x surface and polarization of the Si-O bond. The possible mechanisms with HF are schematized in Figure 4.1 a). The higher etching rates observed with HF_2^- in literature are likely due to its better stabilization with the additional F atom, creating one more hydrogen bond compared to HF as represented in Figure 4.1 b).

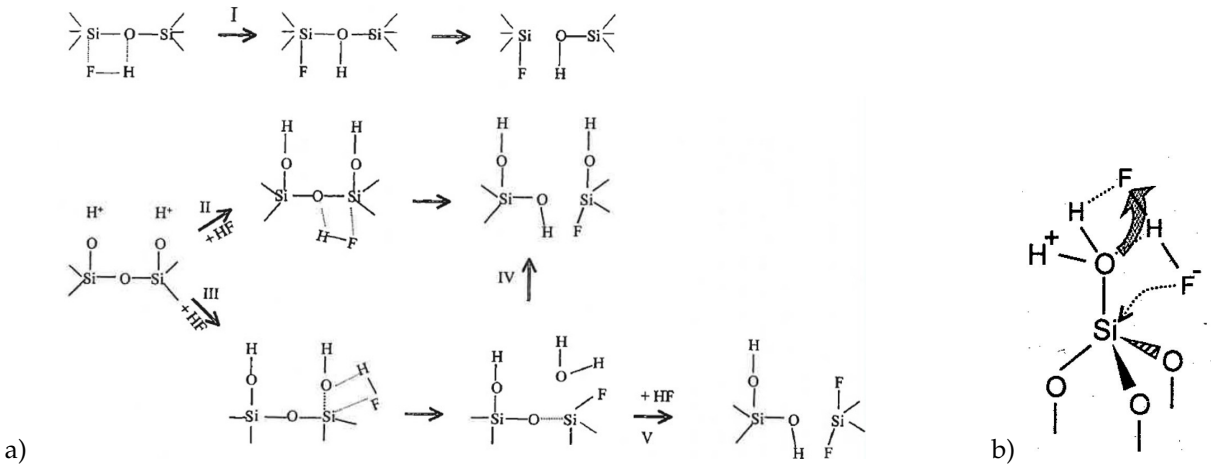

Figure 4.1: a) Possible reaction pathways resulting in the dissolution of SiO_x in HF solution [73] (from Monk et al. [175]), b) Stabilization of HF_2^- molecule on SiO_x surface according to Knotter et al. [98].

Silicon oxides have various origins and their etching rate in HF solutions are different as observed in Figure 4.2. The most common SiO_x layers are described below [73]:

- **Thermally grown SiO_x** is obtained between 900 and 1200 °C by using either water vapor (wet oxidation) or molecular oxygen (dry oxidation) as oxidant. Reactions are given in equation 4.4 and 4.5. Thermal oxide is amorphous with an exact stoechiometry composition (x = 2) and is the most difficult to etch.

$$Si + O_2(gas) \rightarrow SiO_2 \tag{4.4}$$

$$Si + 2H_2O(gas) \rightarrow SiO_2 + 2H_2(gas) \tag{4.5}$$

- **Chemical vapor deposited SiO_x** is obtained by reaction of silane with O_2 according to equation 4.6. The stoechiometry is not exact ($x < 2$) and depends on the deposition conditions (gaz flow, temperature, etc.)

$$SiH_4 + O_2 \rightarrow SiO_2 + 2H_2 \tag{4.6}$$

- **Anodic SiO_x** is formed electrochemically by monitoring the illumination onto a n-type Si surface or by applying a forward potential on n or p-type Si surface. Thus, holes are available to oxidize the Si surface according to the equation 4.7. Anodic SiO_x has a low density and is not stoechiometric due to incorporation of hydroxyl ions and water. Anodic SiO_x is etched faster than thermal and CVD SiO_x as shown in Figure 4.2.

$$Si + 2H_2O + 4h^+ \rightarrow SiO_2 + 4H^+ \tag{4.7}$$

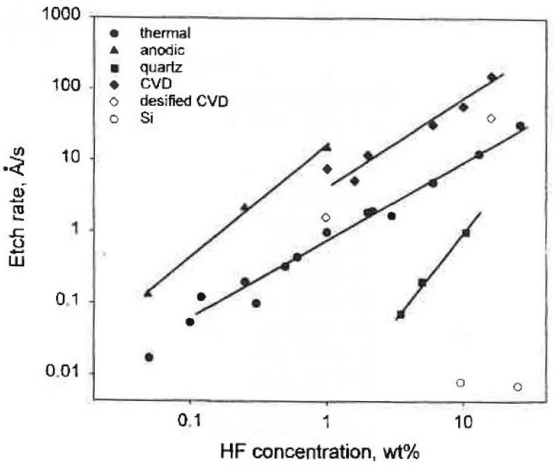

Trend curves equations:

Thermal: y = 0,87 x – 0,12
Anodic: y = 16 x – 1,87
Quartz: y = 0,11 x – 0,34
CVD: y = 8,77 x - 9,81
Densified CVD: y = 2,54 x – 1,04

Figure 4.2: Etching rates of different SiO_x layers as a function of HF concentration ($\%_{wt/wt}$) [73]. Equations of the trend curves have been extracted from the graph.

It has been demonstrated that Si is practically inert in fluoride media in dark and unbiased conditions with an etching rate of 5.10^{-3} Å.s^{-1} [97]. As a consequence, etching process in fluoride media affects the SiO_x but the Si underlying is little impacted. However, a long immersion in a fluoride solution can slowly etch the Si surface and increase its roughness. Si dissolution in fluoride media has been intensively studied, in particular by Allongue et al. [179] and the mechanisms are shown to comprise an electrochemical and a chemical part as detailed in reference [97]. It has also been proved that Si surface treated in fluoride media was covered with Si-H bond (and not Si-F bond as it was believed at first). This can be explained by kinetic considerations: despite that Si-F bond has a stronger dissociation energy ($\approx$ 7eV) than Si-H bond (3.2 eV), Si-F is more polarized and so more susceptible to chemical attacks [73], [97].

Si has a standard potential of - 0.85 V/SHE (see the Si-water system Pourbaix diagram in Appendix F.1) and its stability area is below the line (a) representing the equilibrium condition of solvent reduction into gaseous hydrogen (equation 2.37). Si is thus readily oxidized in aqueous solutions (wet oxidation) and under air atmosphere (dry oxidation). The oxide film formed is called "native oxide" and is not stoechiometric with a low density. As SiO_2 is placed above the line (a) in the Si-water system Pourbaix diagram (see Appendix F.1), the surface becomes inert as soon as around 1 or 2 nm of native SiO_x are formed. Growth rates are different under air atmosphere and in water and depend on whether Si surface has been pre-treated in fluoride media (passivation effect of Si-H bond formed after fluoride treatment). As shown in Table 4.1, a HF pre-treatment allows to reduce Si oxidation by a factor $\approx$ 6 and 3 for wet and dry oxidation respectively.

Table 4.1: Native SiO_x growth rates in water and under air atmosphere for cleaved and HF treated Si [73].

	Growth rate in water (0.6 ppm dissolved O_2) (wet oxidation)	**Growth rate under air (dry oxidation)**
Cleaved-Si (untreated with HF)	3-4 Å in 5-10 min	5-7 Å in 1 hour
Si after HF treatment	2-3 Å in 1 hour	2-3 Å in 1 hour

In order to compare both HF and HF_2^- etching rates, solutions having HF or HF_2^- as dominant species must be prepared. However, predominant HF_2^- species can not be obtained by dilution of HF solution,

as we can see on the graph in Figure 4.3 [96]. This graph provides the determination of the pH and respective concentration of HF, HF_2^- and F^- species for different concentration of HF solutions (log C). The red curve represents the pH as a function of log C and does not pass into HF_2^- predominance area. To achieve conditions where HF_2^- is predominant, NH_4F can be added into the HF solution to help shifting of fluoride equilibrium through difluorides. The resulting solution is called buffered HF solution because it also promotes pH solution stabilization. In this work, we have chosen to use solid $NaHF_2$, as it is easier to manipulate this solid species instead of manipulating two different harmful liquid fluoride media.

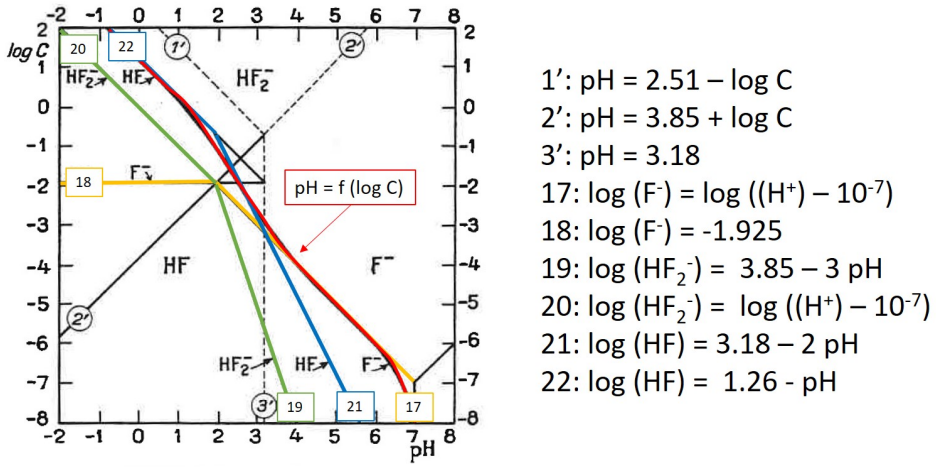

Figure 4.3: Predominance areas and respective concentrations of HF_2^-, HF and F^- species according to the pH and the global concentration of fluoride species (log(C)). [96].

4.2.2 Study of PECVD SiO_x etching rate by ellipsometry

The objective of this first study is to determine the etching rates of a PECVD SiO_x layer in HF and $NaHF_2$ to estimate the immersion times needed to remove the remaining SiO_x dielectric layer after laser ablation (deposited by PECVD too) and use the most suitable fluoride media.

Experimental details

SiO_x deposition has been performed on n-type polished mirror Si wafers (base resistivity $\approx 1.5\ \Omega$.cm) using an home-made 2.45 GHz ECR (Electron Cyclotron Resonance) HDP-CVD system (High-Density Plasma-Chemical Vapor Deposition). The deposition conditions to obtain a final thickness around 90-100 nm are:

- Gases flows: SiH_4 = 5 sccm / O_2 = 40 sccm;
- Pressure: 2 mTorr and Power: 1000 W;
- Temperature: Floating temperature, temperature does not rise above 50°C;
- Deposition time: 2 min 50.

The as-deposited SiO_x layers have been etched in HF and $NaHF_2$ at different concentrations as summarized in Table 4.2. Immersion times have been chosen empirically relying on etching rates reported in literature (see Figure 4.2). Ellipsometry measurements have been carried out to follow the SiO_x thickness with immer-

sion time and determine the corresponding etching rates (Uvisel2 equipment from Horiba, measure range is from 1 to 5 eV with a 0.02 eV step).

Table 4.2: Immersion times and [HF] and [$NaHF_2$] used for PECVD SiO_x layer etching.

Fluoride media	Concentration ($\%_{wt/wt}$)	Molar concentration (mol/L)	Immersion time (sec)
HF	1%	0.57	5, 10, 15, 20, 30, 40
	2.5%	1.43	5, 10, 15, 20, 30, 40
	5%	2.87	2, 5, 10, 20, 30, 40
$NaHF_2$	1%	0.16	15, 20, 25, 30, 40, 50
	2.5%	0.41	10, 15, 20, 25, 30, 40
	5%	0.84	2, 5, 10, 15, 20, 25, 30

Results

Results of ellipsometry have been analysed using a Bruggeman model (effective medium). Best fitting have been obtained by considering a two layers model:

- Layer 1: one superficial SiO_x layer having 50% of voids;
- Layer 2: an underlying SiO_x layer not etched by fluoride media and free of voids.

That suggests that PECVD SiO_x layers are not etched layer by layer in HF and $NaHF_2$ but rather in a random manner, leading to porous oxide layer. SEM images in Figure 4.4 enable to compare the initial SiO_x layer morphology with the one of SiO_x layer after etching in $NaHF_2$ 0.16 M during 20 and 30 seconds. A low porosity can be observed at initial state but after immersion in $NaHF_2$ 0.16 M the porosity is significantly increased. This is observed for all conditions tested in this work.

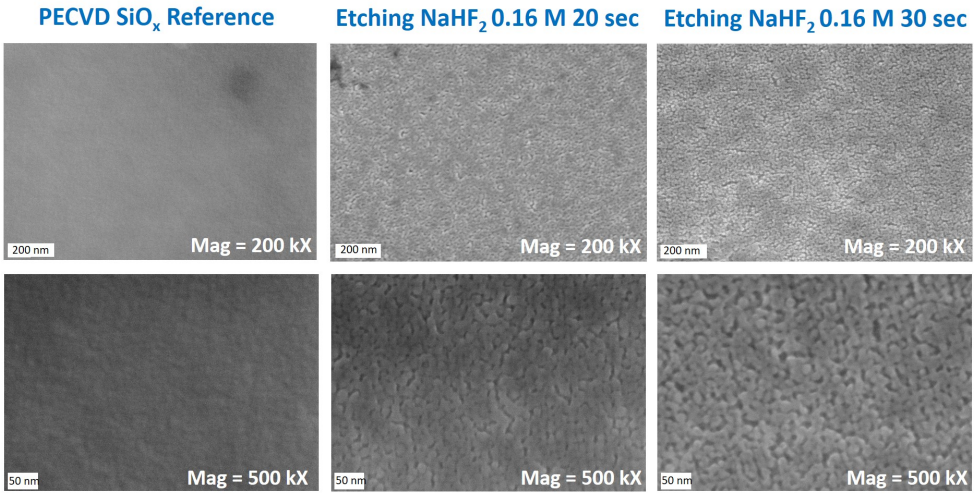

Figure 4.4: SEM images of SiO_x surface at initial state and after 20 and 30 seconds in $NaHF_2$ 0.16 M.

The remaining SiO_x thickness after fluoride treatments has been determined by taking into account layer 1 and 2 in the Bruggeman model. For instance, after 5 seconds in HF 0.57 M, fits indicate that layer 1 accounts

for 17.5 nm and layer 2 for 78.5 nm. Remaining SiO_x thickness is thus calculated as follow:

$$\begin{aligned} e(SiO_x)_{\text{after etching}} &= e(\text{layer 2}) + 0.5 \times e(\text{layer 1}) \\ e(SiO_x)_{\text{after 5 sec in HF 0.57 M}} &= 78.5 + 0.5 \times 17.5 = 87.25nm \end{aligned} \tag{4.8}$$

In this way, remaining SiO_x thicknesses have been determined on the six samples immersed different times for each fluoride media concentration. That allowed to determine the etching rates reported in Table 4.3. Figure 4.5 a) represents the etching rates as a function of fluoride media concentration for HF and $NaHF_2$ and Figure 4.5 b) shows the etching rate ratios for both fluoride media as function of the concentration.

Table 4.3: Calculated etching rates of PECVD SiO_x layer in HF and $NaHF_2$ solutions.

Fluoride media	Concentration ($\%_{wt/wt}$)	Molar concentration (mol/L)	Etching rate (nm/sec)
HF	1%	0.57	2.3 ± 0.2
	2.5%	1.43	7.3 ± 0.4
	5%	2.9	16.8 ± 0.9
$NaHF_2$	1%	0.16	1.9 ± 0.2
	2.5%	0.41	5.3 ± 1.0
	5%	0.84	8.5 ± 0.6

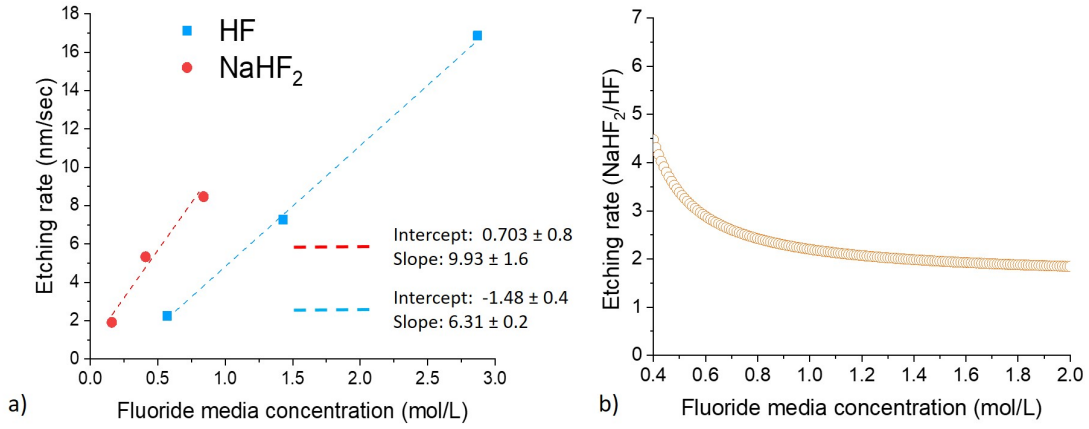

Figure 4.5: a) Etching rates of PECVD SiO_x layers in HF and $NaHF_2$ as a function of fluoride media concentrations, b) etching rate ratios between HF and $NaHF_2$ as a function of fluoride media concentrations.

According to Figure 4.5 a), SiO_x layers are etched faster in $NaHF_2$, which is consistent with literature. The etching rate ratios ($NaHF_2$/HF) reported in Figure 4.5 b) indicate two trends:

- For [fluoride media] < 0.8 M, the ratio increases when the fluoride media concentration decreases and SiO_x is etched until four times faster in $NaHF_2$;
- For [fluoride media] > 0.8 M, the ratio stabilizes such as SiO_x is etched 2 times faster in $NaHF_2$.

It also appears that curves in Figure 4.5 a) do not pass by zero but this is likely due to a change in etching mechanisms from a certain dilution of fluoride media. Indeed, by dissolving the solution, HF and HF_2^- dissociation are favored through equations 4.9 and 4.10 [96]. This leads to a shift to F^- predominance area and modification of the etching kinetic.

$$HF = F^- + H^+ \qquad \frac{[F^-]}{[HF]} = -3.18 + pH \tag{4.9}$$

$$HF_2^- = 2F^- + H^+ \qquad \frac{[F^-]^2}{[HF_2^-]} = -3.85 + pH \tag{4.10}$$

Etching rates of PECVD SiO_x from literature are presented in Figure 4.2 [73] and are found to be lower compared to our results. For instance, etching rate of CVD SiO_x in HF $1\%_{(wt/wt)}$ is found to be in the range [0.3 - 1] nm/sec (depending on SiO_x density) while our results indicate an etching rate of 2.3 nm/sec (Table 4.3). This deviation could originate from a lower density of PECVD SiO_x layers used in this work. Either way, results obtained are relevant in terms of comparison between HF and $NaHF_2$ fluoride media.

Finally, immersion time to etch SiO_x can be reduced by using $NaHF_2$ fluoride media instead of HF. As an example, 30 seconds immersion in HF 0.57 M removes 63.3 nm of SiO_x while the same thickness is removed in after only 10 seconds in $NaHF_2$ 0.57 M. Silicon nitride layers damaging can be limited provided that $NaHF_2$ is not more aggressive than HF towards them.

4.2.3 Study of anodic SiO_x etching rate by electrochemical impedance spectroscopy

The aim of this study is to determine the etching rate of a anodic SiO_x layer in $NaHF_2$ fluoride media (etching rates of anodic SiO_x layers in HF are well documented in literature [73] (see Figure 4.2) for comparison with previous results on PECVD SiO_x layer. The objective is also to develop a methodology that enables to determine precisely the SiO_x thickness on Si surface to adjust the immersion time in fluoride media.

Experimental details

Textured n-type Si wafers (base resistivity = 1 Ω.cm, corresponding to a low doping level N_D = $4.83.10^{15}$ at.cm^{-3} according to abacus) have been used for this study. A roughness factor defined by the developed surface divided by the planar surface has been determined with the Confocal Laser Scanning Microscope and an average value of 1.46 ± 0.03 has been obtained by analysing ten wafers. Anodic SiO_x layers have been grown by photo-oxidation using the experimental setup represented in Figure 4.6. The electrochemical cell contains an electrolyte (H_2SO_4 0.1 M, pH = 0.95), a platinum wire as counter electrode and an Ag/AgCl reference electrode. The electrolyte is concentrated so that the Gouy-Chapman layer is confounded with the Helmholtz layer (see section 2.3) and it can be considered that the potential drop mainly occurs in the semiconductor during experiments. The electrolyte is bubbled with N_2 15 min before and during experiments to remove dissolved O_2 and provide a soft solution agitation. This is recommended to limit spontaneous Si surface oxidation (native oxide) by oxygen contained in the electrolyte. Thus, we can approximate that grown SiO_x layers mainly originate from the photo-oxidation. Before experiments, Si wafers are cleaned in piranha solution (H_2O_2 (30%) : H_2SO_4 (96%), 1:3, 15 min) followed by HF $1\%_{wt}$ treatment (1 min).

The experimental setup is placed in a Faraday cage to avoid electromagnetic distortion of the electrochemical response. Anodic SiO_x layers are grown by photo-oxidation by applying a direct illumination and a forward bias potential (cyclic voltammetry under illumination, lamp power = 35 W). The photo-oxidation reaction is given in equation 4.11. The formed anodic SiO_x is stable and does not dissolve into silicates as experiments are performed in acidic solution (see Si-water system Pourbaix diagram in Appendix F.1).

$$Si + 2H_2O + 4h^+ \xrightarrow{h\nu} SiO_2 + 4H^+ \tag{4.11}$$

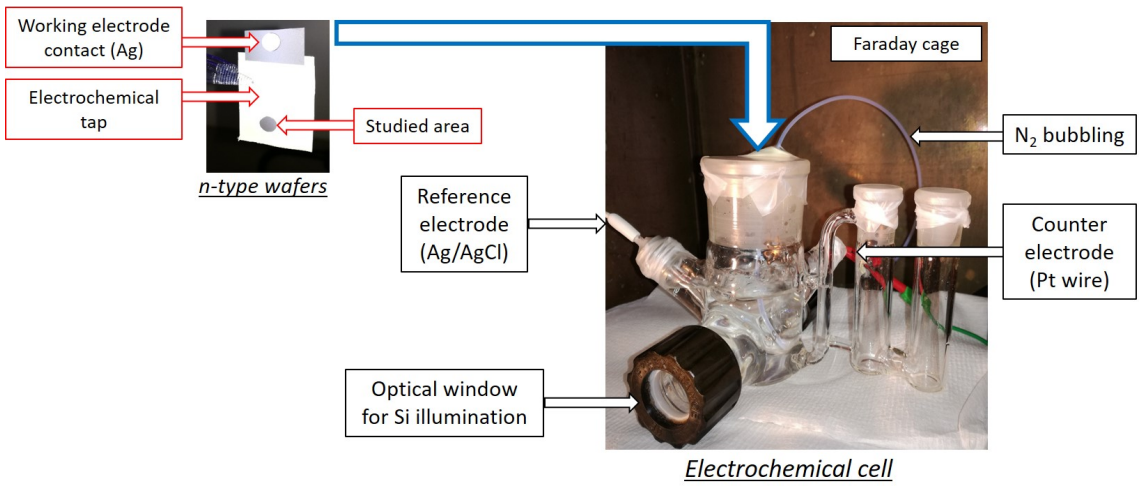

Figure 4.6: Electrochemical cell for photo-oxidation of textured n-type Si wafers.

In order to determine the anodic SiO_x thickness after various immersion times in fluoride media, a methodology has been established to draw a reference standard graph giving the anodic SiO_x thickness according to the measured flatband potential (V_{fb}). It is based on Electrochemical Impedance Spectroscopy (EIS) and illustrated in Figure 4.7. EIS measurements are performed in dark from 0.1 Hz to 500 kHz frequencies in a potential range where faradic current can be neglected (30 potential steps). EIS technique is detailed in Appendix G and enables to measure SiO_x thickness on textured surface at nanometer scale.

Firstly, anodic SiO_x is formed on n-type wafers by illumination of the sample into the electrochemical cell. The more the applied forward potential is increased, the thicker the SiO_x layer will be. SiO_x thickness can be also increased by successive cyclic voltammetry. The theoretical thickness of as-obtained anodic SiO_x e(SiO_x) can be determined using the charge formed during photo-oxidation experiment (Q_f) according to equation 4.12. As a first approximation, we consider that the whole current is used to grow the oxide layer (100% faradic yield). Different density values for anodic SiO_x are reported in reference [73] and a median value equal to 2 has been taken for calculations. In addition, the molar mass has been approximated to be equal to the one of SiO_2 ($M(SiO_2)$ = 60.08 g.mol^{-1}) and the studied area is multiplied by the roughness factor such as: A = $\Pi \times$ radius$^2 \times$ 1.46.

$$e(SiO_x) = \frac{M(SiO_x) \times Q_f}{d(SiO_x) \times z \times F \times A} \tag{4.12}$$

with M the molar mass, Q_f the formed charge, d the anodic oxide density, F the Faraday's constant, z the number of charges exchanged and A studied area.

Then, EIS measurements are performed on bare and oxidized n-type wafers with various SiO_x thicknesses and the Bode and Nyquist diagrams are used to determine the Si capacitance in the SCR (C_{SC}). The flatband potential is obtained by plotting the Mott-Schottky curve according to equation 4.13 and the reference standard graph (e(SiO_x) = f(V_{fb})) can be established.

$$\frac{1}{C_{SC}^2} = \frac{2}{\epsilon\epsilon_0 q N_D}((V - V_{fb}) - \frac{k_B T}{q}) = \frac{2}{\epsilon\epsilon_0 q N_D}(V_{SC} - \frac{k_B T}{q}) \tag{4.13}$$

With ϵ the material permittivity, ϵ_0 the vacuum permittivity, q the electron elementary charge, N_D the density of

donors, V the applied voltage, V_{fb} the flatband potential, V_{SC} the potential drop in the semiconductor, k_B the Boltzmann's constant and T the temperature.

Finally, EIS measurements are realized on oxidized samples after various immersion times in $NaHF_2$ to determine the corresponding V_{fb}. By reporting, this value on the reference standard graph, the SiO_x thickness at various immersion times can be determined as well as the dissolution kinetic.

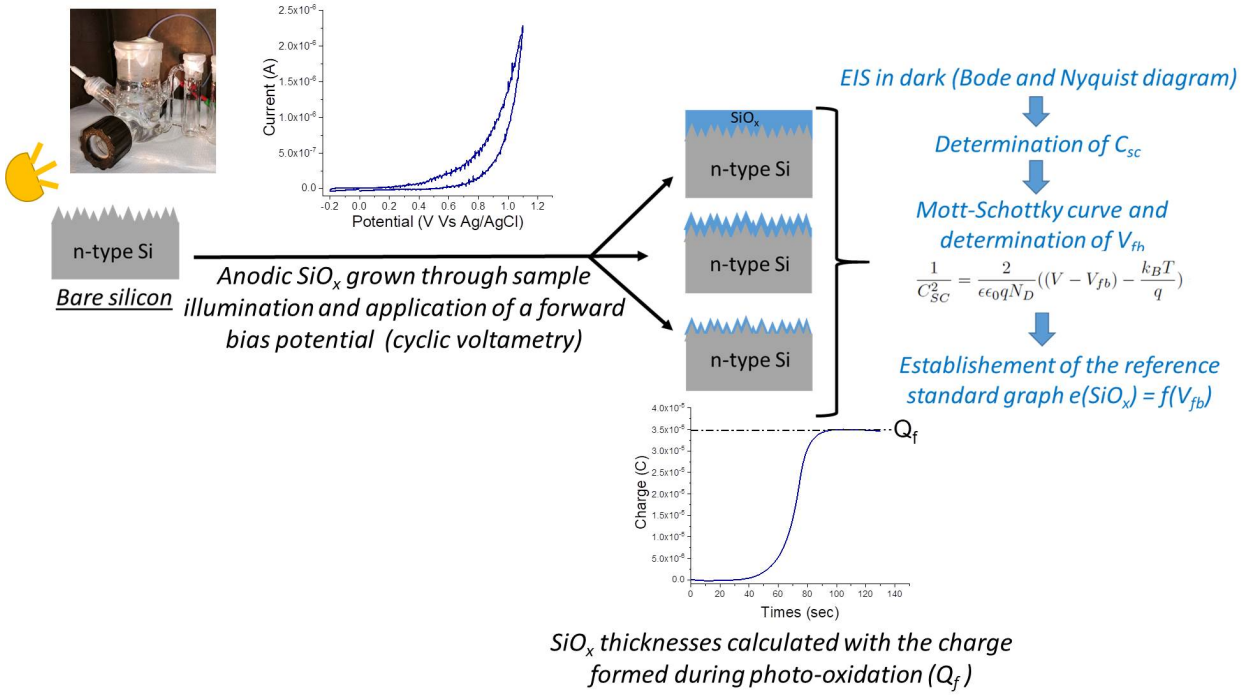

Figure 4.7: EIS-based methodology for establishment of the reference standard graph e(SiO_x) = f(V_{fb}).

In order to facilitate results analysis, the expected band diagram of n-Si/electrolyte interface at initial state (bare Si) is represented in Figure 4.8 respectively to Ag/AgCl reference electrode. Before contact, Si band diagram is determined as explained in section 2.3. In literature [71], the OCP of Si immersed in a fluoride media is experimentally found near to the redox potential of H^+/H_2 couple at all pH values. Consequently, the redox couple of interest is H^+/H_2 on electrolyte side. Despite that this work is not performed in fluoride media, there is no other redox couple in the electrolyte and a same behavior can be expected. $E_{(H^+/H_2)}$ can be determined at all pH values using equation 4.14 (no H_2 relative pressure) [96]. In this way, $E_{(H^+/H_2)}$ at pH = 0.95 is equal to - 0.246 V respectively to Ag/AgCl reference electrode (equation 4.15). As represented in Figure 4.8, a potential drop of 0.330 V/Ag/AgCl is expected (V_{SC}).

$$E_{(H^+/H_2)} = E^0_{(H^+/H_2)} - 0.059 \ \ \text{pH} \tag{4.14}$$

$$E_{(H^+/H_2)} = -0.190 - 0.059 \times 0.95 = -0.246V \ \ (\text{V/Ag/AgCl}) \tag{4.15}$$

In addition, acido-basic surface interactions induce a non negligible potential drop in the Helmholtz layer (V_H) which varies with the pH solution according to equation 4.16 [70]. That results in the sliding of Si CB and VB borders from - 0.056 V.

$$\Delta V_H = Constant - \frac{2.3RT}{F} \ \ \text{pH} \approx -0.059 \ \ \text{pH} \tag{4.16}$$

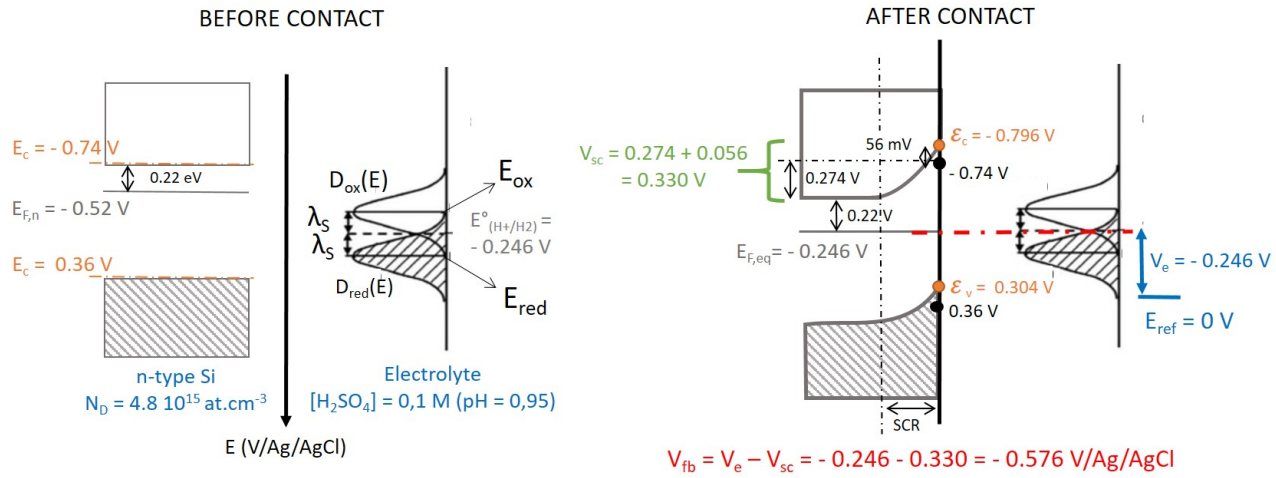

Figure 4.8: Predicted band diagram of Si/electrolyte interface in our experimental conditions: n-type Si, N_D = 4.83.10^{15} at.cm^{-3}, [H_2SO_4] = 0.1 M, pH = 0.95.

Initial state: characterization of bare Si surface

Samples have been first characterized after cleaning and HF treatment (bare Si represents the initial state without SiO_x on Si surface). The evolution of E_{OCP} with time is reported in Figure 4.9 a). This experiment is directly followed by cyclic voltammetry to observe anodic and cathodic behaviors and resulting graphs are shown in Figure 4.9 b). Both methods are performed in dark conditions. The experiment was reproduced three times at 3 different days by using new samples and new electrolytes. As the E_{OCP} in experiment 2 stayed stable, experiment has been stopped after 300 seconds.

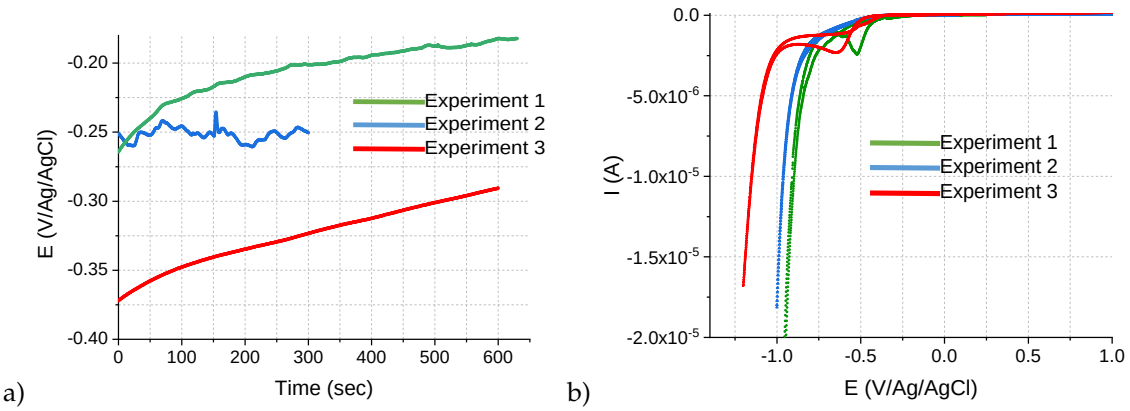

Figure 4.9: a) Evolution of E_{OCP} with time, b) Cyclic voltammetry on bare n-type Si (cleaning + HF treatment). Experiments are performed in dark conditions.

In Figure 4.9 a), the initial E_{OCP} in experiments 1 and 2 is close to the expected value of - 0.246 V/Ag/AgCl (see Figure 4.8). However, experiment 3 shows a different initial E_{OCP} value which can be due to the presence of surface states on Si surface. Moreover, the E_{OCP} is not stable with time for experiments 1 and 3. Considering that experiments are performed in aqueous electrolyte free of fluoride media, it can be supposed that E_{OCP} is not stable due to slow Si surface oxidation, enhanced with dissolved O_2 content. It is therefore probable that electrolyte desaeration was less efficient for experiments 1 and 3 in comparison with

experiment 2.

Cyclic voltamperogram of the three experiments in Figure 4.9 b) are similar. In the anodic part, current is very low, as expected for a n-type Si, and does not overpass 200 nA. Indeed, as described in equation 4.11, silicon oxidation requires holes which are the minority carriers in n-type Si. Consequently, Si oxidation is very slow and anodic current can be neglected. A sharp increase of cathodic current appears at ≈ - 1 V/Ag/AgCl and can be attributed to H^+ reduction. It does not happen at the same potential valuefor the three experiments but this is due to the different E_{OCP}. In Table 4.4, E_{OCP} and the potential E for which the current starts to drop are reported and it appears that the difference between these two values (η' = E - E_{OCP}) is similar for the three experiments. It is worth to mention that E_{OCP} at the beginning of cyclic voltammetry experiments corresponds to E_{OCP} at the end of experiments in Figure 4.9 a) as cyclic voltammetry has been performed on the same samples.

To promote H^+ reduction, Si must be in accumulation which necessitates to apply a potential difference of at least 0.330 V relatively to E_{OCP} towards negative potentials (see V_{SC} in Figure 4.8). Thus, η' = 0.334 ± 0.043 V found in Table 4.4 is consistent with the expected band diagram in Figure 4.8 and supports the validity of measurements. Moreover, a bump appears at around - 0.5 and - 0.6 V/Ag/AgCl for experiment 1 and 3 respectively. As mentioned above, dissolved O_2 was probably still present during these experiments so these bumps can be attributed to O_2 reduction according to equation 4.17.

$$O_2 + 2H^+ + 2e^- = H_2O_2 \qquad E = 0.682\text{–}0.0591 \ \text{pH} + 0.0295 \ log\frac{P_{O_2}}{[H_2O_2]} \tag{4.17}$$

Table 4.4: Difference between E_{OCP} and the potential at the beginning of protons reduction on voltamperogram in Figure 4.9 b).

Experiments	E_{OCP} (V/Ag/AgCl)	E at I = - 1 × 10^{-6} A (V/Ag/AgCl) (beginning of H^+ reduction)	η' = E - E_{OCP}
1	- 0.150	- 0.465	0.315
2	- 0.250	- 0.674	0.384
3	-0.290	- 0.553	0.303
Average and standard deviation	- 0.23 ± 0.072	- 0.564 ± 0.104	0.334 ± 0.043

EIS measurements have been then performed on bare n-type Si samples. The electrolyte/Si interface can be simulated by the equivalent circuit represented in Figure 4.10 a) where R_{SOL} is the electrolyte resistance, R_{CT} the charge transfer resistance (due to electrochemical discharge of the species at the interface) and C_{SC} is the Si capacitance. Corresponding Nyquist and Bode diagrams are schematized in Figure 4.10 b) and c).

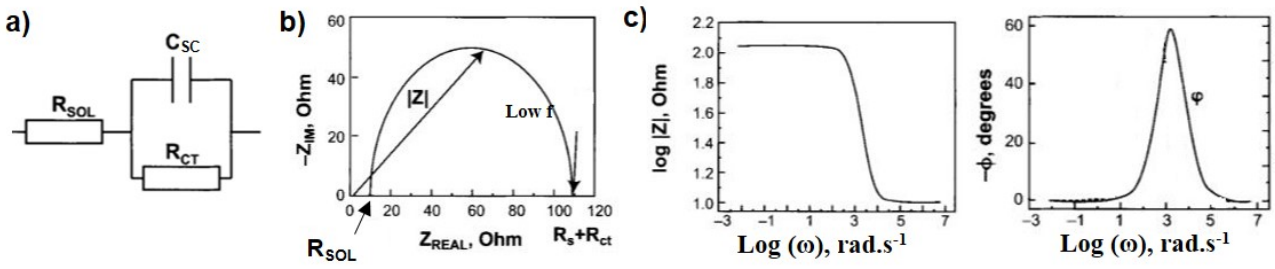

Figure 4.10: a) Equivalent circuit for bare n-type Si in contact with an electrolyte,b) Corresponding Nyquist diagram, c) Corresponding Bode diagram [180].

EIS measurements have been performed in dark in the potential range [-0.3, - 1] V/Ag/AgCl with 30 potential steps. In this potential range, faradic current is negligible on the voltamperogram, which is a necessary condition to plot the Mott-Schottky curve and perform EIS measurements. Five bare Si wafers have been characterized and the obtained Nyquist and Bode diagrams look similar. For better readability, results obtained for one sample at only four potential steps are given in Figure 4.11. The appearance of Nyquist and Bode diagrams is consistent with a R_{SOL} + R_{CT}/C_{SC} equivalent circuit which suggests the absence of SiO_x layer. Even after curves fitting with various equivalent circuits (EClab software), best fits are obtained with R_{SOL} + R_{CT}/C_{SC} circuit.

Fit results enable to determine R_{SOL} for the five experiments and values are shown in Table 4.5. R_{SOL} is supposed to be constant during measurements which is confirmed by the low standard deviations. R_{SOL} is also supposed to be similar from one experiment to another but the slight variations observed in Table 4.5 are likely due to the distance between working and counter electrodes which can little differ for each experiment. R_{CT} values are not reported but are always above 10^6 Ω/cm^2 which confirms that no current exchange occurs during measurements, except the exchange current at equilibrium. R_{SOL} and R_{CT} values are in the same order of magnitude compared to literature for same type of experiments [181].

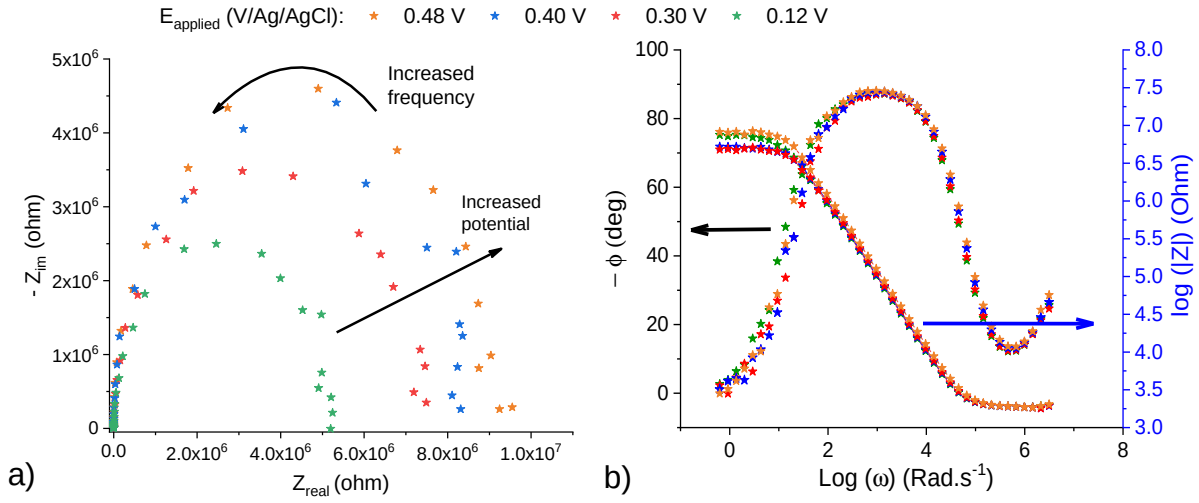

Figure 4.11: EIS measurements on bare n-type Si: a) Nyquist diagram, b) Bode diagram.

Table 4.5: R_{SOL} values for bare Si after fitting of EIS results with R_{SOL} + R_{CT}/C_{SC} equivalent circuit.

Experiments	Studied area (cm^2)	R_{SOL} ($\Omega.cm^2$)
1	0.288	248.51 ± 11.38
2	0.194	62.12 ± 3.80
3	0.247	74.78 ± 14.45
4	0.401	277.26 ± 45.77
5	0.487	60.52 ± 5.12

In addition, C_{SC} is determined at each potential step and the corresponding Mott-Schottky curve is plotted using equation 4.13 for each experiment. Results are displayed in Figure 4.12. Globally, C_{SC} values vary from $1.5.10^{-2}$ to 3.10^{-2} $\mu F/cm^2$ which is consistent with literature [70].

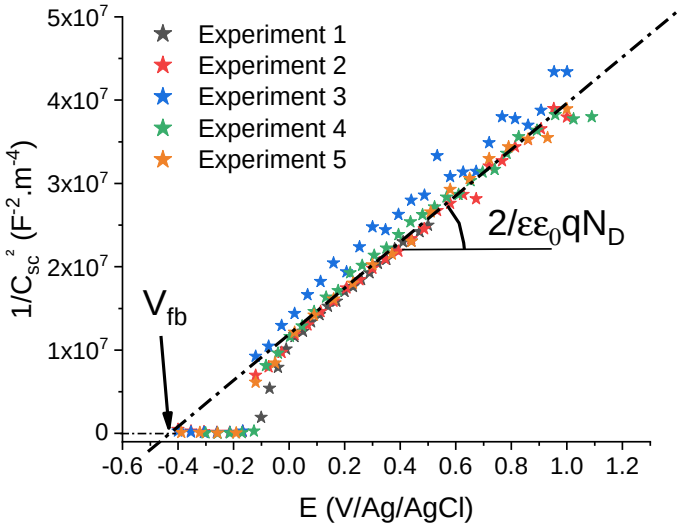

Figure 4.12: Mott-Schottky curves obtained by EIS measurements for five experiments on bare n-type Si.

Table 4.6: Determination V_{fb} and N_D from Mott-Schottky curves in Figure 4.12.

Experiments	V_{fb} (V/Ag/AgCl)	N_D (at.cm^{-3})($\times 10^{15}$)
1	- 0.397	4.31 $\pm$ 0.19
2	- 0.401	4.32 $\pm$ 0.28
3	- 0.505	4.21 $\pm$ 0.28
4	- 0.440	4.37 $\pm$ 0.18
5	- 0.400	4.28 $\pm$ 0.17
Average and standard deviation	- 0.429 $\pm$ 0.046	4.30 $\pm$ 0.058

Mott-Schottky curves in Figure 4.12 are similar for the five experiments which means that measurements are reproducible. The flatband potential is determined by extrapolating the straight line in [0 - 1.2] V/Ag/AgCl potential range to x-axis intersection and the dopant concentration is calculated with the corresponding slope. Results are summarized in Table 4.6. Our results are nearby expected value of $4.83.10^{15}$ at/cm^{-2}, confirming the validity of measurements. The V_{fb} is found to be equal to - 0.429 $\pm$ 0.046 V/Ag/AgCl which is close to the expected value of - 0.576 V/Ag/AgCl (see Figure 4.8). The gap of $\approx$ 150 mV could be explained by the presence of Si surface states. For instance, the formation of a native oxide during experiments will shift the CB and VB anchoring levels ($\mathcal{E}_C$ and $\mathcal{E}_V$) to more positive potential values due to apparition of positives charges on semiconductor side. Consequently, V_{fb} will be also shifted towards more positive values which could explain why the V_{fb} is little less negative than expected. Finally, electrochemical characterization enables to retrieve the parameters on the expected band diagram described in Figure 4.8.

Oxidized states: Si surface characterization with various anodic SiO_x thicknesses

As described in Figure 4.8, bare n-type Si is in depletion at equilibrium with the electrolyte. To promote Si surface oxidation according to equation 4.11, holes are necessary which necessitates illumination of n-type Si surface. The behavior of the device under illumination is illustrated in Figure 4.13.

Under illumination, electron holes pairs are generated and a photo-potential (V_{ind}) is induced such as the potential barrier is lowered (V'_{SC} = V_{SC} - V_{ind}). Therefore, band bending is lowered as well as the SCR thickness. Thanks to the electric field in the SCR, photo-generated holes diffuse towards the Si surface, leading to its oxidation, while photo-generated electrons diffuses towards the external circuit (cathodic photo-current). In order to separate all the photo-generated charges carriers and achieve the maximum photo-current, a forward bias must be applied to increase the band bending (and so the electrical field in the SCR).

A cyclic voltammetry has been realized by alternating illumination/dark conditions at various potential steps. Graph is displayed in Figure 4.14 and it can be observed that the photo-current increases with the applied potential and achieves a maximum value at $E_{applied} \approx 1.2$ V/Ag/AgCl.

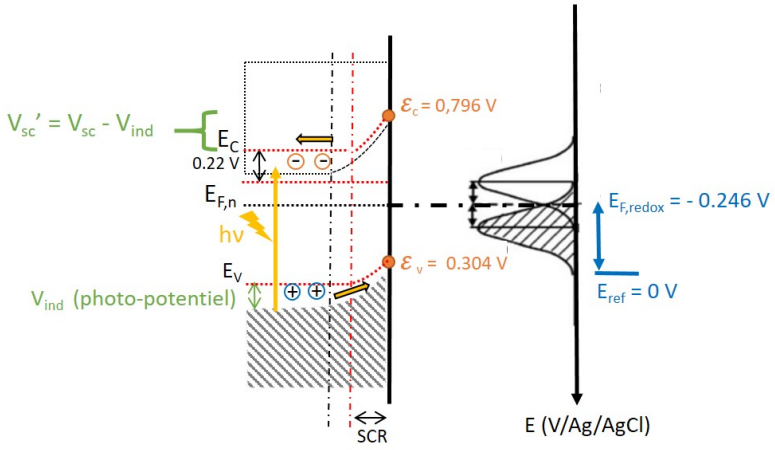

Figure 4.13: Illustration of Si band diagram under illumination. V_{ind} represents the induced photo-potential and V'_{SC} is the resulting potential barrier when band bending is lowered.

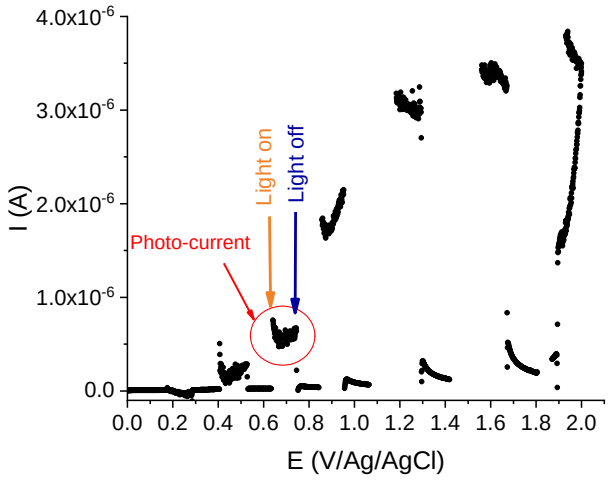

Figure 4.14: Evolution of the photo-current with the applied potential on n-type bare Si.

By following the protocol in Figure 4.7, anodic SiO_x layers have been grown by photo-oxidation to obtain samples with various SiO_x thicknesses determined by equation 4.12. Oxidized samples are then analyzed by EIS in dark conditions, in the frequency range from 0.1 Hz to 500 kHz. Potential range is adjusted for each

sample by looking on cyclic voltamperogram obtained during photo-oxidation and identify the potential range where faradic current can be neglected.

Five voltamperograms obtained after successive photo-oxidations have been superimposed in Figure 4.15. The apparition of anodic current occurs at higher potential values when e(SiO_x) increases. This is related to the blocking effect of the oxide (potential drop into the oxide layer). The same effect is observed on cathodic side (not shown here) such as the H^+ reduction starts at potential values more and more negative when e(SiO_x) increases.

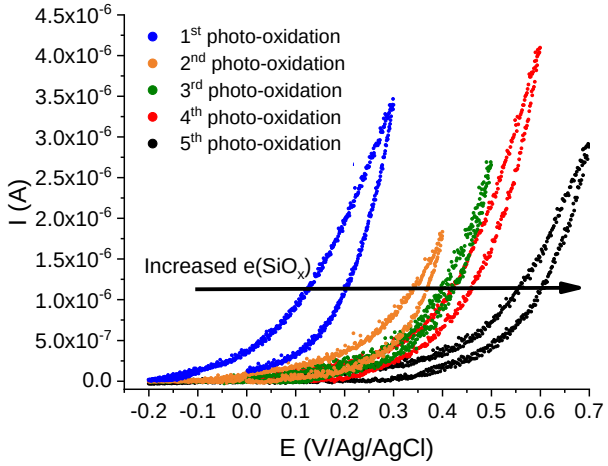

Figure 4.15: Voltamperogram obtained after five successive photo-oxydations (20 mV scan rate).

Nyquist and Bode diagrams have been fitted with several equivalent circuits: $R_{SOL} + R_{OX}/C_{OX} + R_{CT}/C_{SC}$, $R_{SOL} + R_{OX}/Q_{OX} + R_{CT}/Q_{SC}$, $R_{SOL} + C_{OX} + R_{CT}/C_{SC}$ and $R_{SOL} + C_{OX} + R_{CT}/Q_{SC}$. Best results (lower coefficient of determination (χ^2)) have been obtained with $R_{SOL}+C_{OX}+R_{CT}/C_{SC}$ equivalent circuit represented in Figure 4.16, where there is no contribution of oxide layer resistance. That could be explained by the very thin SiO_x layers studied (e(SiO_x) < 4 nm). C_{OX} represents the capacitance of the formed SiO_x layer such as:

$$C_{OX} = \frac{\epsilon_{(SiO_x)} \times \epsilon_0}{d_{OX}} \tag{4.18}$$

where $\epsilon_{(SiO_x)}$ and ϵ_0 are the relative permittivity of SiO_x layer and vacuum permittivity respectively and d_{ox} represents the oxide thickness.

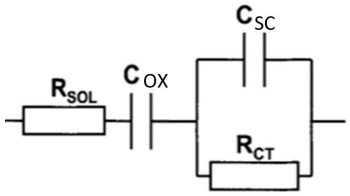

Figure 4.16: Representation of the equivalent circuit for Si/SiO_x/electrolyte device.

An example of Nyquist and Bode diagrams obtained in these experiments is given in Figure 4.17. In the potential ranges studied, three different shapes of the curves have been observed. For a better readability, results at only three potential steps, corresponding to each particular shape of Nyquist and Bode diagrams, have been represented. The behavior of the device is explained below.

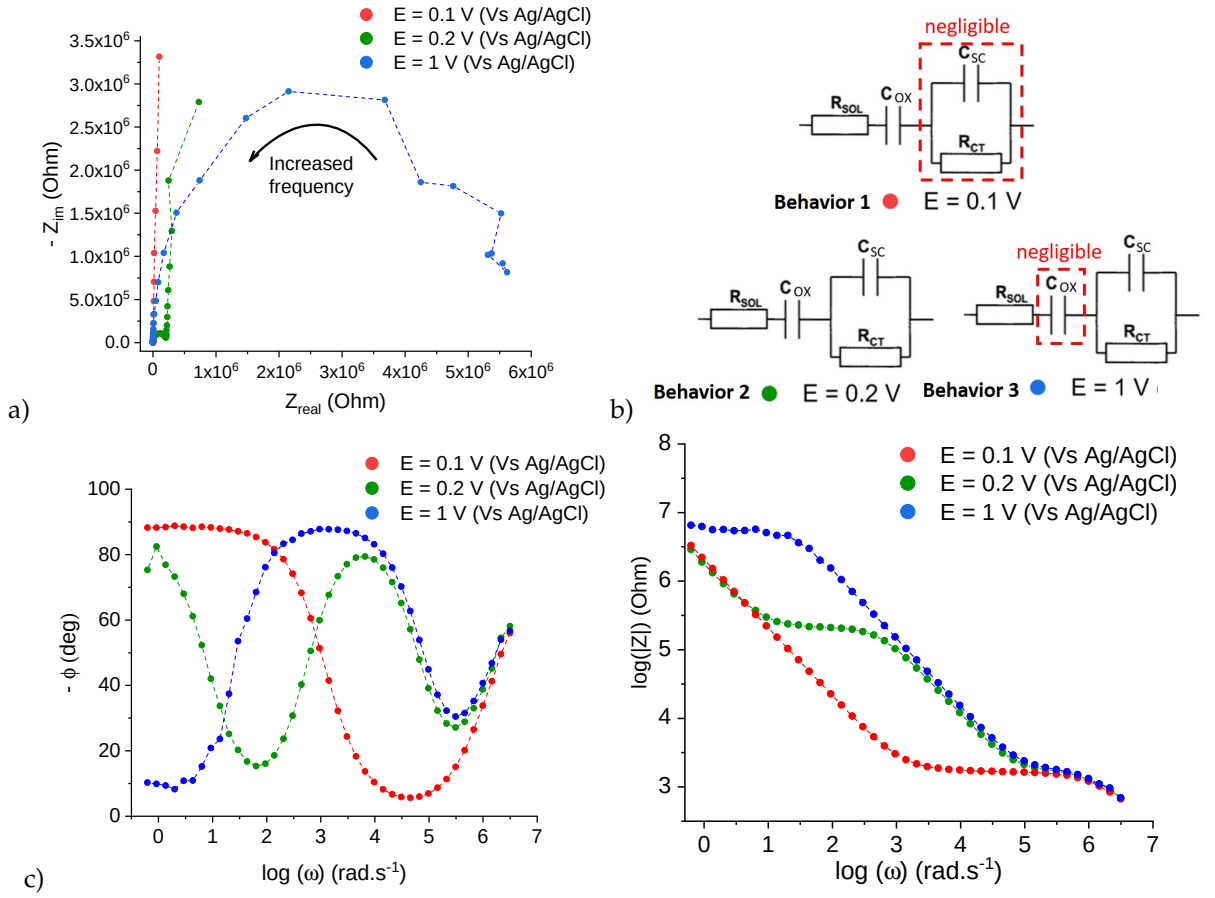

Figure 4.17: Results of EIS measurements on photo-oxidized samples: a) Nyquist diagram, b) respective equivalent circuits, c) Bode diagrams. Only three potential steps illustrating the three behaviors identified are represented for better readability.

- **Behavior 1**: At potential 0.1 V/Ag/AgCl, Nyquist and Bode diagrams are typical of a R_{SOL}-C_{SC} equivalent circuit (see Figure 4.16). The following hypothesis can be proposed: the potential drop is mainly supported by the SiO_x layer so that the semiconductor is not impacted and its contribution (R_{CT}/C_{SC}) in the equivalent circuit represented in Figure 4.16 can be neglected.
- **Behavior 2**: At potential 0.2 V/Ag/AgCl, Nyquist and Bode diagrams are such as both contributions C_{OX} and C_{SC} are involved. This is particularly visible on the representation of - ϕ (Z) in the Bode diagram where two contributions can be noticed. The following hypothesis can be proposed: potential is high enough to modify Si band bending but C_{OX} is not yet negligible with respect to C_{SC} leading to this shape of Nyquist and Bode diagrams.
- **Behavior 3**: At potential 1 V/Ag/AgCl, Nyquist and Bode diagrams are typical of R_{SOL}-R_{CT}/C_{SC} equivalent circuit (see Appendix G). By looking at the representation of - ϕ (Z) in the Bode diagram, only one contribution is visible and likely corresponds to C_{SC} contribution. Thus, it seems that C_{OX} contribution becomes negligible in the impedance response. The following hypothesis can be proposed: the oxide layer already supports the higher potential drop it can and additional potential drop only occurs in the semiconductor. Variation observed on Nyquist and Bode diagrams are only caused by phenomena related to the semiconductor.

More than twenty samples have been studied and results obtained for eight of them are shown here. By fitting Nyquist and Bode diagrams, C_{OX} and R_{SOL} have been determined and reported in Table 4.7. Theoretical values of $C_{OX,theo}$ is also calculated using equation 4.18 with $\epsilon_{(SiO_x)} = \epsilon_{(SiO_2)} = 3.9$ as a first approximation.

Table 4.7: C_{OX} and R_{SOL} values for 8 oxidized samples determined by Nyquist and Bode diagrams fitted with equivalent circuit in Figure 4.16. Theoretical values of C_{OX} are also reported.

Sample	Area (cm^2) ($\times 10^{-5}$)	**Charge Q_f (C) ($\times 10^{-4}$)**	**e(SiO_x) (nm)**	**$C_{OX,theo}$ (F/cm^2) ($\times 10^{-5}$)**	**$C_{OX,exp}$ (F/cm^2) ($\times 10^{-5}$)**	**R_{SOL} ($\Omega.cm^2$)**
1	2.88	4.29	1.16	2.9	1.7 ± 0.4	299.86 ± 97.14
2	2.88	4.74	1.28	2.6	2.9 ± 1.7	442.38 ± 57.26
3	2.88	8.86	2.39	1.4	1.9 ± 0.3	382.12 ± 162.72
4	1.93	8.42	3.38	0.99	1.5 ± 0.2	67.25 ± 11.02
5	1.93	9.08	3.64	0.92	1.8 ± 0.5	111.11 ± 16.25
6	1.93	12.1	4.85	0.69	1.7 ± 0.2	79.96 ± 3.45
7	2.46	5.28	1.66	2.0	1.9 ± 0.3	73.95 ± 8.23
8	2.46	5.61	1.80	1.9	1.9 ± 0.4	73.21 ± 5.66

For all samples, $C_{OX,theo} \approx C_{OX,exp}$ which supports the accuracy of measurements. As for the initial state (bare Si), R_{CT} values (not shown here) are in the range of 10^6 Ω/cm^2 and R_{SOL} values remain the same (same electrolyte used for all experiments). By fitting the Nyquist and Bode diagrams, C_{SC} have been also determined at each potential step to plot the Mott-Schottky curves and obtain the V_{fb} value associated to each SiO_x thickness. C_{SC} values are also in the order of magnitude of 10^{-2} $\mu F/cm^2$ which is consistent with literature [70].

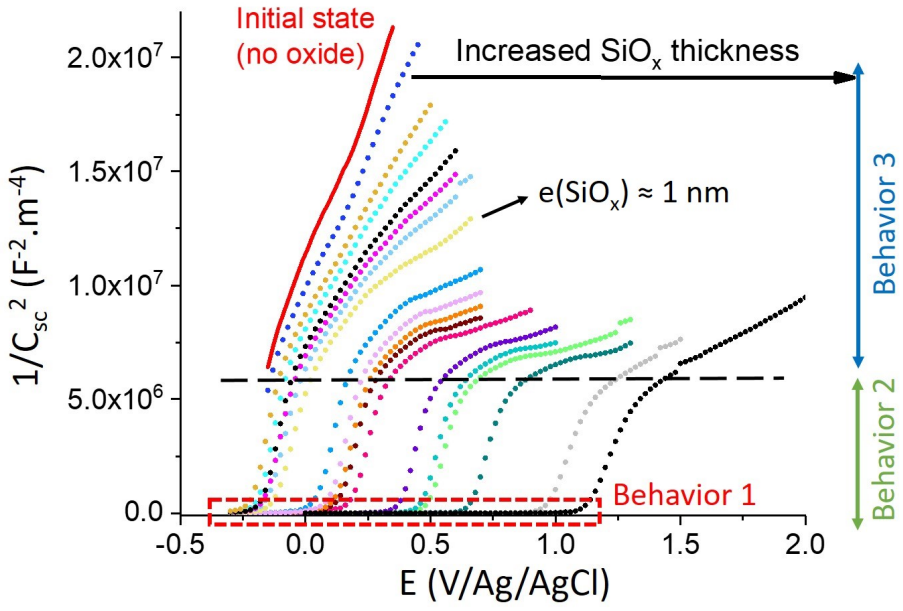

Figure 4.18: Evolution of Mott-Schottky curves with anodic SiO_x thickness on n-type Si surface.

It appears that Mott-Schottky curves are shifted towards high potential values when SiO_x thickness increases. Interestingly, three different areas can be distinguished and they correspond to the three behaviors

identified before on Nyquist and Bode diagrams:

- **Behavior 1:** Firstly, the Mott-Schottky curves are flat which is due to the blocking effect of the oxide layer. The potential drop is supported by the oxide layer so that Si band bending is not modified. The thickness of the SCR stays constant when the potential increases and so C_{SC} value is constant too. When the anodic SiO_x thickness increases, it can support an higher potential drop and the potential range associated with this behavior 1 is larger.
- **Behavior 2:** Then, $1/C_{SC}^2$ value increases with the potential and a specific slope, identical for all measured samples, is observed. This slope enables to find the Si dopant density ($\approx 4.10^{15}$ at.cm^{-3}) which indicates that this part of Mott-Schottky curve is relevant to determine V_{fb}. In this part, Mott-Schottky relation is verified and the Si material is in depletion regime. The flatband potential associated with each anodic SiO_x thickness has been determined by extrapolation of the curve in this area and that allowed to plot the graph in Figure 4.19 (Experiment A).

  It can also be noticed that V_{fb} are shifted towards higher potential values. This is related to the positive surface charges induced at the Si surface when an oxide layer is grown [73]. Indeed, the CB and VB anchoring levels ($\mathcal{E}_C$ and $\mathcal{E}_V$) will slide to higher potential values and V_{fb} will be observed at higher potentials. Therefore, the variation of the V_{fb} is proportional to the charge at the surface (which increases with SiO_x thickness) according to equation 4.19 [70].

$$\Delta V_{fb} = \frac{\Delta Q_S}{C_H} = \Delta V_H \tag{4.19}$$

  with Q_S the charge of surface states (C), C_H the Helmholtz's layer capacitance (F) and $\Delta\ V_H$ the potential drop in the Helmholtz's layer (V).

  Interestingly, the behavior 2 is confined in a potential range of about 200-300 mV from a certain oxide thickness ($\approx$ 1 nm). To explain this, we have to remind that minority carriers (holes in the present case) start to accumulate at the Si surface as soon as the Fermi potential $E_{F,n}$ is below the intrinsic Fermi level $E_{F,i}$. That corresponds to the middle of the Si bandgap positioned at 560 mV below the CB level (1.12/2 = 0.56 V). As represented in Figure 4.8, μ_c = 0.220 mV so only + 0.340 mV potential drop is needed for $E_{F,n}$ cross $E_{F,i}$ value. From this value, minority carriers start accumulating slowly at Si surface and the Mott-Schottky conditions are not anymore completely fulfilled. The slope of the curve starts to change and this is the beginning of behavior 3.
- **Behavior 3:** In this part, the slope of the Mott-Schottky curves declines with increased SiO_x thickness. When the SiO_x layer is still thin ($<$ 1 nm, which corresponds to the six first Mott-Schottky curves), minority carriers which start to be accumulated at the Si surface are not blocked by the oxide. Therefore, the depletion regime can continue (non equilibrium depletion regime) and the behavior 2 is prolonged over higher potential values. However, for thicker SiO_x layers, minority carriers are progressively blocked by the oxide layer, leading to an inversion regime (see section 2.3). Mott-Schottky conditions are not verified anymore and the curve is not related to dopants concentration and V_{fb}.

These three parts of Mott-Schottky curves have been already described in literature [182] and authors have highlighted that V_{fb} determination is not relevant in some papers in which the wrong part of Mott-Schottky curve has been used. The whole protocol to draw the reference graph e(SiO_x) = f(V_{fb}) has been

performed three times at three different days to assess the reproducibility of this work. Results are depicted in Figure 4.19. The three experiments give similar results and a linear evolution of V_{fb} with e(SiO_x) is observed such as:

$$e(SiO_x)(nm) = 2.47 \times V_{fb}(\mathrm{V/Ag/AgCl}) + 0.83. \tag{4.20}$$

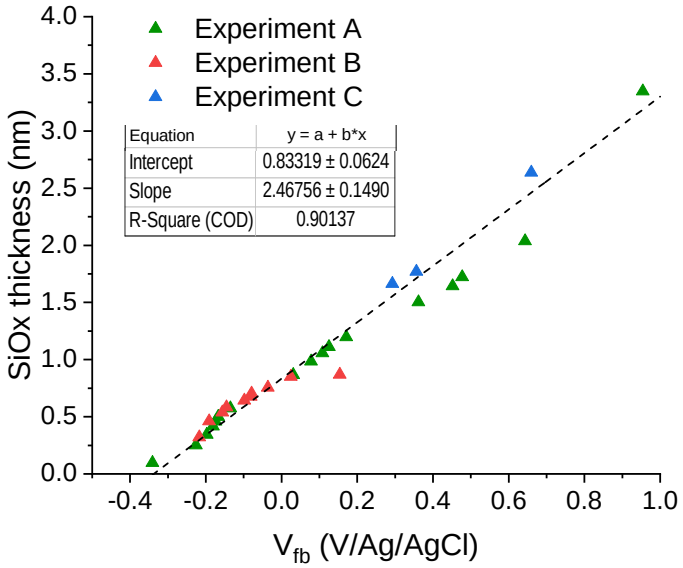

Figure 4.19: Established reference graph e(SiO_x) = f(V_{fb}). Experiment A is related to Mott-Schottky curves in Figure 4.18.

Etching rate of anodic SiO_x in $NaHF_2$

Finally, the etching rates of anodic SiO_x layer in $NaHF_2$ $1\%_{wt/wt}$ (0.16 M) have been investigated. Two samples have been photo-oxidized to achieve anodic SiO_x thickness of 6.2 and 2.9 nm. Then, these samples are immersed in $NaHF_2$ 0.16 M for few seconds and EIS measurements are performed to determine the corresponding flatband potential. This latter is reported on the reference graph in Figure 4.19 to determine the remaining SiO_x thickness and calculate the etching rates displayed in Figure 4.20.

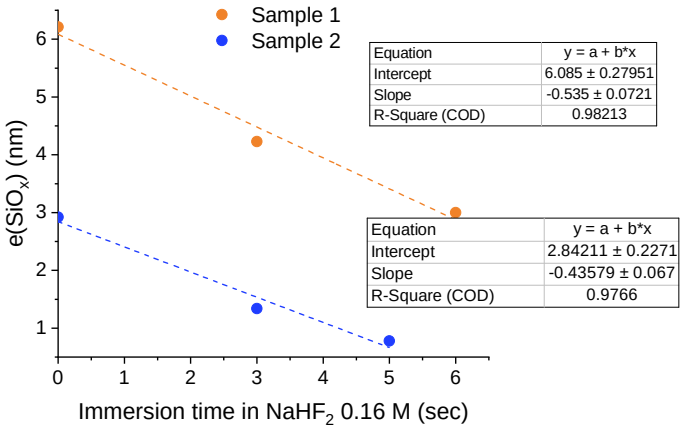

Figure 4.20: Evolution of anodic SiO_x thickness as a function of immersion time in $NaHF_2$ 0.16 M.

Etching rates appear to be so fast that no more oxide is present after less than 10 seconds immersion.

That explains the low number of measurement points in Figure 4.20. The average value of etching rate in $NaHF_2$ 0.16 M is found to be equal to 0.48 nm/sec. Etching rates of anodic oxide in HF reported in Figure 4.2 indicate a value of 0.26 nm/sec for HF 0.28%$_{wt/wt}$ (0.16 M) ((1.6 $\times$ 0.28) - 0.187). That represents an etching rate of anodic SiO_x two times faster in $NaHF_2$ compared to HF as observed for PECVD SiO_x studied before. These results are consistent with literature and represent strong arguments to use $NaHF_2$ instead of HF, provided that silicon nitride layers are not more damaged in $NaHF_2$.

4.2.4 Conclusions and perspectives

Etching rates of PECVD and anodic SiO_x layers in HF and $NaHF_2$ have been studied. For both SiO_x layers, it appears that $NaHF_2$ is more involved in the etching mechanism. A relationship between the etching rate of PECVD SiO_x layer and the concentration of fluoride media has been established for HF and $NaHF_2$ (see Table 4.8). PECVD SiO_x layers are etched more than 2 times faster in $NaHF_2$ compared to HF for a same molar concentration. In both fluoride media, the PECVD SiO_x layer porosity increases during the etching process. For anodic SiO_x, a methodology based on EIS has been established to follow the evolution of anodic SiO_x thickness with immersion times in $NaHF_2$ 0.16 M. In comparison with etching rate in HF 0.16 M reported in literature, anodic SiO_x layer is etched $\approx$ 2 times faster in $NaHF_2$ (see Table 4.8).

Table 4.8: PECVD and anodic SiO_x etching rates (y) as a function of HF and $NaHF_2$ concentrations (x).

etching rate equation: y = ax + b	**HF**	**$NaHF_2$**
PECVD SiO_x	y = 6.31 x - 1.48 For 0.5 M: 1.67 nm/s	y = 9.93 x + 0.71 For 0.5 M: 5.67 nm/sec
Anodic SiO_x	For 0.16 M: 0.26 nm/s	For 0.16 M: 0.48 nm/s

These results confirm the interest of using $NaHF_2$ instead of HF for deoxidation treatment. Indeed, shorter immersion times can be used to etch SiO_x layers which limits the impact on silicon nitride layers. However, that is only true if $NaHF_2$ does not etch silicon nitride layer faster than HF does. It is thus necessary to investigate the etching rate of SiO_xN_y layers in $NaHF_2$ and HF to determine which one has the best selectivity.

4.3 Study of SiO_xN_y layers etching rate in HF and $NaHF_2$

In this section, etching rate of n-PERT precursors SiO_xN_y layers is studied in both HF and $NaHF_2$ fluoride media. The objective is to determine a relationship between the etching rate and the concentration of fluoride media to compare these results with the one obtained on SiO_x layers and identify the most selective fluoride media.

4.3.1 State of the art

Etching kinetics of silicon nitride materials in fluoride media have been studied by few authors [98], [183]–[186] and it emerges that material properties, such as density and hydrogen content, highly impact the etching rate. The specific case of ARC silicon nitride layer deposited by PECVD is barely investigated, and

most of the time, only HF species is considered in the etching mechanism. HF-based solutions contain free fluoride ions (F^-), un-ionized HF and partially ionized difluoride (HF_2^-) ions with respective proportions depending on the solution concentration. The determination of each fluoride species role in the etching mechanisms is not simple and authors do not agree when deciding which one is the most involved.

Knotter et al. have investigated the etching rate and mechanism of three silicon nitride layers in HF [98]:

- a low-pressure vapor deposited nitride (SiN), quasi-stoechiometric, with 3.6% hydrogen content;
- a PECVD nitride (SiNH) with a Si/N ratio of 0.81 and an hydrogen content of 19.5%;
- a PECVD antireflective coating (SiNARC) with a Si/N ratio of 1.5 and an hydrogen content of 21.8%.

A statistical analysis of the results has been performed and equation 4.21 has been established to calculate the etching rate. Constants of reaction obtained for the three silicon nitride layers are reported in Table 4.9.

$$R = k_0 \frac{[HF_2^-]}{1 + K_3[H^+]} + \frac{(k_1[HF] + k_2[F^-])K_3[H^+]}{(1 + K_3[H^+])} \tag{4.21}$$

With k_i the etching rate constants and K_3 the equilibrium constant of $[SiNH_3^+]/([SiNH_2][H^+])$

Table 4.9: Parameters of equation 4.21 for the silicon nitride layers investigated by Knotter et al. [98].

	k_0 (HF_2^-) ($Å.L.mol^{-1}.s^{-1}$)	k_1 (HF) ($Å.L.mol^{-1}.s^{-1}$)	k_2 (F^-) ($Å.L.mol^{-1}.s^{-1}$)	K_3 ($L.mol^{-1}$)
SiNARC	8.3	2.8	120	25
SiNH	10	9.1	820	25
SiN (quasi-stoechiometric)	0.29	0.21	28	25

It appears that F^- is the main etching species for the three silicon nitrides studied ($k_2 >> k_1$ and k_0) but some authors do not agree with this statement. Deckert et al. have worked on chemical vapor deposited Si_3N_4 and claim that F^- species is not involved in the etching mechanism [186]. Rathi et al. have studied Si_3N_4 layers with various compositions deposited by chemical vapor deposition and they propose that HF_2^- is the main etching species [185].

Whatever the main etching species, similar etching mechanisms have been proposed by Liu et al. (see Figure 4.21) and Knotter et al. (see Figure 4.22) for a quasi-stoechiometric silicon nitride (Si_3N_4). In both cases, the rate limiting step involves a first step, which consists of the conversion of the superficial Si-NH_2 site into a Si-F one. Knotter et al. give more details on the elementary reactions and suggest that nucleophilic substitution (SN2) is not possible because the opposite site on Si atom in respect to Si-N bond is blocked and the approach of the fluoride species onto the $SiNH_2$ is hampered. Consequently, the replacement of the NH_2 group by a F atom is likely to happen through the breaking of Si-N bond and subsequent filling of the vacant site by a fluoride species (F^- is the most probable one as it is the best nucleophilic). Due to the high pKa value of amino-terminated groups, NH_2 group is easily protonated, which favors the breaking of Si-N bond (see Figure 4.22 a)). Then, the mechanism continues by successive breaking of Si-N bonds (see Figure 4.21). According to Knotter et al., once the first Si-N bond is replaced by a Si-F site, subsequent reactions can take place according to the SN2 mechanism, which is also favored by first protonation of the N atom (see Figure 4.22 b)). Here again, F^- species is more likely to be involved due to its higher nucleoplilic ability.

Concerning the SiNARC nitride, Knotter et al. have found an etching rate constant related to HF (k_1) about three times smaller than the HF_2^- one (k_0). They suggest that the etching mechanism is slightly different due to the presence of hydrogen. As Si-H bonds can be oxidized, and given that the breaking of Si-O bond is favored with HF_2^-, this latter would be more involved in the etching mechanism.

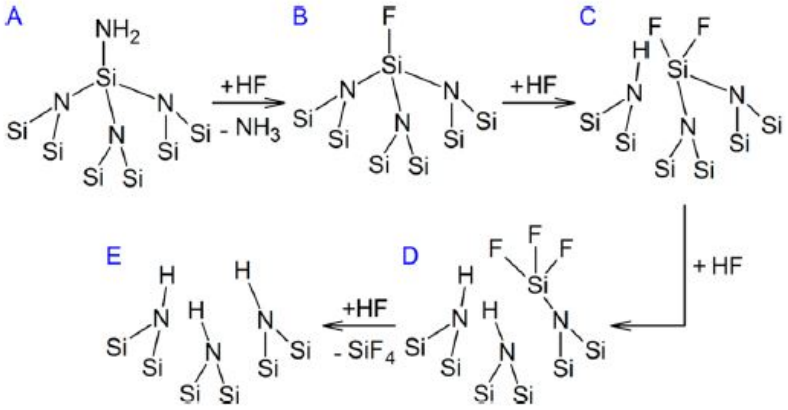

Figure 4.21: Reaction mechanism for the etching of Si_3N_4 in HF proposed by Liu et al. [187], [188].

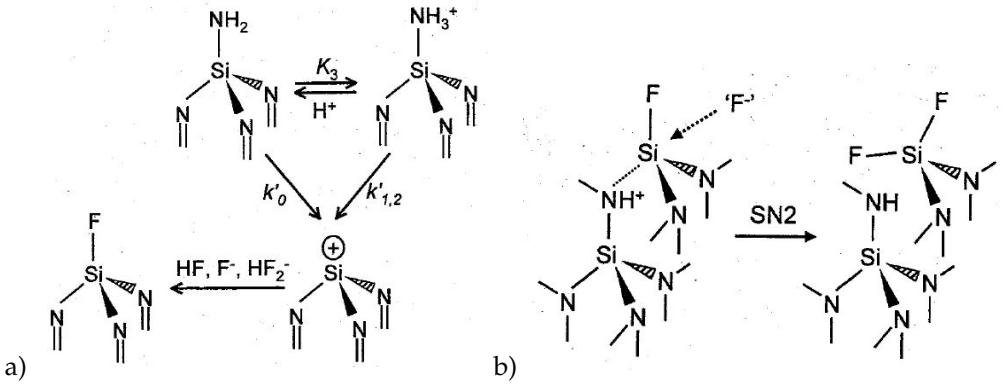

Figure 4.22: Elementary reactions proposed by Knotter et al. to decompose the steps described in Figure 4.21 a) transition from step A to B, b) transition from step B to C [98].

In this section, the etching rate and mechanism of n-PERT precursors SiO_xN_y (ARC layers) is investigated but results will be specific to the deposition technique and properties of these SiO_xN_y layers. However, some similarities with the different opinions found in the literature will be highlighted.

4.3.2 Experimental part

The etching rates of n-PERT precursors SiO_xN_y ARC layers have been investigated as a function of HF and $NaHF_2$ concentrations. 20 x 20 mm^2 samples have been immersed in HF or $NaHF_2$ solutions at various concentrations (ambient temperature, no stirring). Immersion times have been chosen empirically and experimental conditions are summarized in Table 4.10.

Table 4.10: Immersion times and concentrations of HF and $NaHF_2$ solutions used to etch n-PERT precursors SiO_xN_y layers

Fluoride media	Concentration ($\%_{wt/wt}$)	Molar concentration (mol/L)	Immersion time (min)
HF	1%	0.57	4, 10, 20, 30, 45
	2.5%	1.43	4, 8, 11, 30, 40
	5%	2.87	2, 4, 10, 20, 30
$NaHF_2$	1%	0.16	10, 20, 40, 60, 90
	2.5%	0.41	8, 11, 20, 40, 60
	5%	0.84	4, 10, 15, 40, 50

Concentration of commercial HF solutions are given in weight percentage ($\%_{wt/wt}$) and $NaHF_2$ is a solid. Thus, molar concentrations of HF and $NaHF_2$ have been calculated using equation 4.22 and 4.23 respectively.

$$[HF] = \frac{\frac{\%_{wt/wt}}{100} \times d_{HF}}{M(HF)} = \frac{\frac{\%_{wt/wt}}{100} \times 1150}{20.01} \tag{4.22}$$

$$[NaHF_2] = \frac{m(NaHF_2)\text{for 1 L of solution}}{M(NaHF_2)} = \frac{m(NaHF_2)\text{for 1 L of solution}}{62} \tag{4.23}$$

Reflectivity measurements have been carried out on each etched sample using a UV-Vis-NIR spectrophotometer from Agilent (Cary 5000) to measure accurately SiO_xN_y layers thicknesses on both sides. Spectra have been obtained in the wavelength range 200 to 1100 nm with a 3 nm measure step. As mentioned in Chapter 1, equation 1.6 enables to calculate the ARC thickness for the λ associated with the minimum reflectivity coefficient (λ_{min}). SiO_xN_y thickness is thus given by equation 4.24 according to λ_{min} and SiO_xN_y refractive coefficient $n_{SiO_xN_y}$, which is equal to 2.03 on the front textured side according to the supplier and 2.05 on the rear polished side (see section 3.6).

$$e(SiO_xN_y) = \frac{\lambda_{min}}{4 \times n_{SiO_xN_y}} \tag{4.24}$$

To assess the evolution of anti-reflection properties, we have also calculated the effective reflectivity (R_{eff}) of SiO_xN_y layers in regards to standard AM 1.5 spectrum [189] by using equation 4.25.

$$R_{eff} = \frac{\int_{\lambda_i}^{\lambda_f} RJ'_0 d\lambda}{\int_{\lambda_i}^{\lambda_f} J'_0 d\lambda} \tag{4.25}$$

with J'$_0$ the standard AM 1.5 spectrum irradiance, λ the wavelength and R the reflectivity. The range of measurement is λ_i = 280 nm and λ_f = 1100 nm.

4.3.3 Results

Evolution of SiO_xN_y thickness with immersion time in HF and $NaHF_2$ is visible to the naked eye through color changing until the layer is completely removed and underlying Si appears in grey. An example is given in Figure 4.23 for etching in HF 0.57 M and $NaHF_2$ 0.41 M. We clearly observe a difference between both sides, such as the rear one is slowly etched.

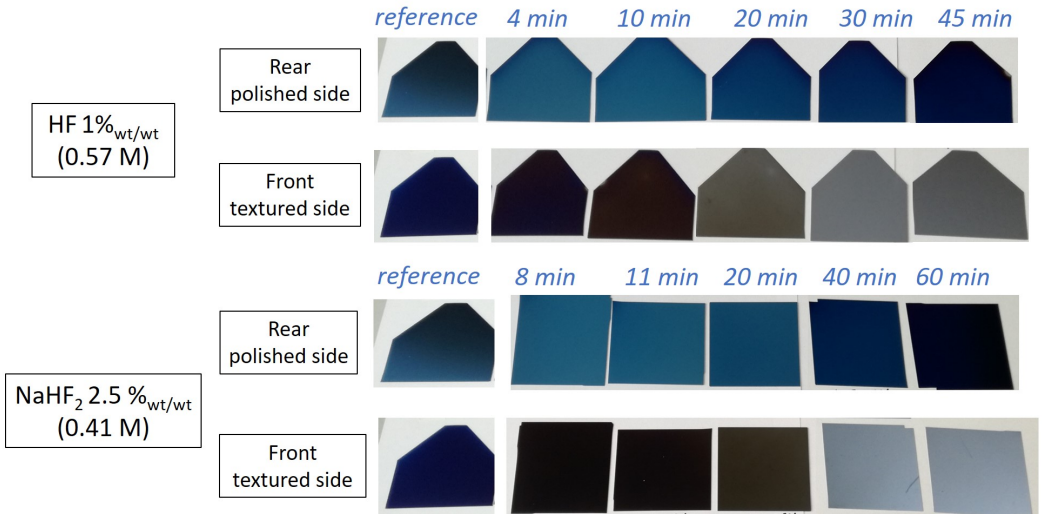

Figure 4.23: Pictures of SiO_xN_y layers after various immersion times in HF 0.57 M and $NaHF_2$ 0.41 M.

The reflectivity spectrum of each sample has been used to determine the corresponding λ_{min}. For instance, spectra obtained in case of HF 0.57 M are displayed in Figure 4.24 and 4.25. On both sides, λ_{min} is reduced with immersion time, which is consistent with a diminution of SiO_xN_y thickness. The etching rate appears to be faster on the front side, where curves do not show a minimum wavelength value after 30 and 45 minutes immersion. This is related to a complete SiO_xN_y removal as visible in Figure 4.23.

Using equation 4.24, the evolution of SiO_xN_y layers thickness with immersion time has been determined for each fluoride media concentration which enables to calculate the etching rates summarized in Table 4.11. Etching rates as a function of both fluoride media molar concentrations are plotted in Figure 4.26. Etching rate ratios on front and rear side are displayed in Figure 4.27.

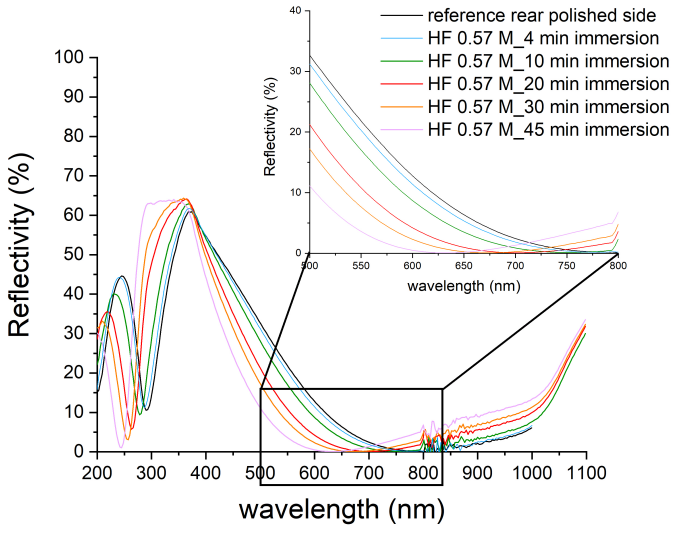

Figure 4.24: Reflectivity spectra obtained on the rear polished side after various immersion times in HF 0.57 mol/L.

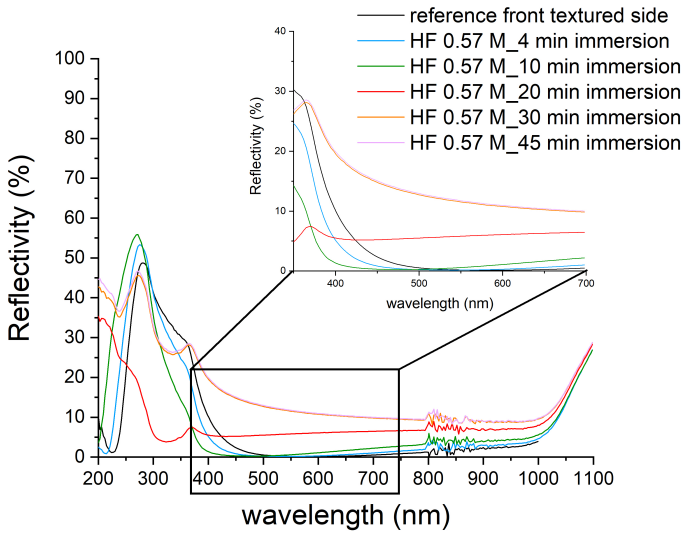

Figure 4.25: Reflectivity spectra obtained on the front textured side after various immersion times in HF 0.57 mol/L.

Table 4.11: Etching rates of front and rear side SiO_xN_y layer in HF and $NaHF_2$ solutions.

	Concentration ($\%_{wt/wt}$)	Concentration (mol/L)	Etching rate (nm/sec) on front side (n = 2.03)	Etching rate (nm/sec) on rear side (n = 2.05)
HF	1%	0.57	$2.73 \pm 0.15 \times 10^{-2}$	$0.75 \pm 0.04 \times 10^{-2}$
	2.5%	1.43	$4.62 \pm 1.48 \times 10^{-2}$	$1.66 \pm 0.11 \times 10^{-2}$
	5%	2.87	$10.7 \pm 0.90 \times 10^{-2}$	$2.57 \pm 0.05 \times 10^{-2}$
$NaHF_2$	1%	0.16	$0.95 \pm 0.05 \times 10^{-2}$	$0.33 \pm 0.03 \times 10^{-2}$
	2.5%	0.41	$1.92 \pm 0.18 \times 10^{-2}$	$0.58 \pm 0.04 \times 10^{-2}$
	5%	0.84	$3.46 \pm 0.32 \times 10^{-2}$	$0.88 \pm 0.04 \times 10^{-2}$

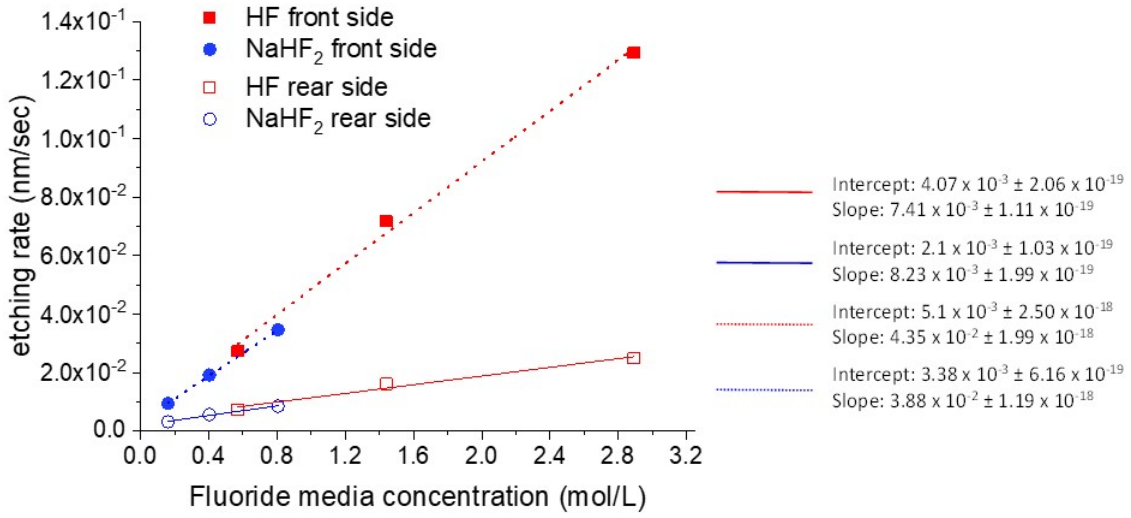

Figure 4.26: SiO_xN_y etching rates as a function of HF and $NaHF_2$ concentrations on both sides of n-PERT precursors.

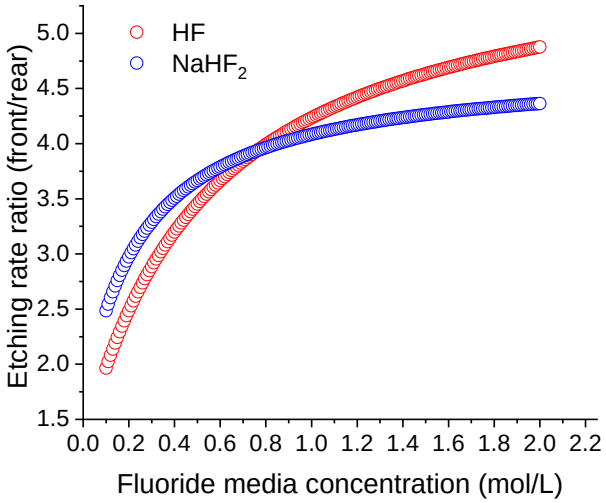

Figure 4.27: Front and rear side SiO_xN_y etching rate ratios with HF and $NaHF_2$ concentrations.

Results confirm that SiO_xN_y layer on the front textured side is etched faster than the one on the rear polished side. By looking in Figure 4.27 the ratio of etching rate on the front side to the rear side varies from $\approx$ 2 to 5 in the fluoride media concentration range 0.1 M to 2 M. This behavior is likely to come from a difference of SiO_xN_y layer density, which has been observed in literature [184], [185]. Indeed, on the rear side, the dielectric stack has been used as diffusion barrier during the emitter formation (see section 2.6). This additional thermal treatment at around 1000°C for 1 hour has certainly made the SiO_xN_y layer denser through loss of hydrogen content. As chemical bonds are less accessible in a denser material due to steric considerations, SiO_xN_y layer is more difficult to etch. This SiO_xN_y layer is also etched slowly due to its higher refractive index compared to the front textured side SiO_xN_y layer. Indeed, it has been demonstrated in literature that silicon nitride layers having lower refractive index were etched faster in fluoride media [190]. In term of etching mechanism, an higher refractive index is related to an higher Si content and so more Si-Si bonds. As the etching mechanism is based on Si-N bonds breakage, it is consistent to observe a lower etching rate in this case. Difference of etching rates between the front textured side and the rear polished side can be also due to the difference of roughness.

As explained before, the etching rate of a silicon nitride layer highly depends on deposition conditions and resulting layer properties. Thus, the comparison of our results with literature is delicate. Nevertheless, in case of HF in the concentration range commonly used ($1\%_{wt/wt}$ - $5\%_{wt/wt}$), we obtain etching rates in the range [1-10] nm/min which is in the same order of magnitude than values observed in literature [183], [186].

No significant difference of etching rates in HF and $NaHF_2$ is observed contrary to some results reported in literature. Indeed, Rathi et al. have proposed that HF_2^- is the main etching species [185] but they have studied a quasi-stoechiometric Si_3N_4 layer, different from the ARC silicon nitride studied in this work. Knotter et al. have observed an etching rate for SiNARC $\approx$ 3 times lower with HF compared to HF_2^- [98] (see Table 4.9). They also suggest that F^- is the main etching species, which is unlikely in our case by considering the Figure 4.3. Indeed, [F^-] is constant in pH range [0-2], which corresponds to 0.1 mol.L^{-1} < [HF]

< 10 mol.L^{-1} according to the red curve (pH = f(log C)). If F^- was the main etching species in this work, the etching rate of SiO_xN_y layer should be similar in this HF concentration range which is not the case (see Figure 4.26). The presence of oxygen into the silicon nitride layers studied in this work could explain the differences obtained compared to literature. By stabilizing HF and HF_2^- through weak hydrogen bond with oxygen non-binding electron pairs, HF and HF_2^- are more involved into the etching process than F^- ions.

Etching of SiO_xN_y layers can have two major impacts on n-PERT precursors:

1. Some cell areas can have no more or too thin SiO_xN_y layer, favoring further parasitic plating. An illustration of Ni parasitic plating is given in Figure 4.28.

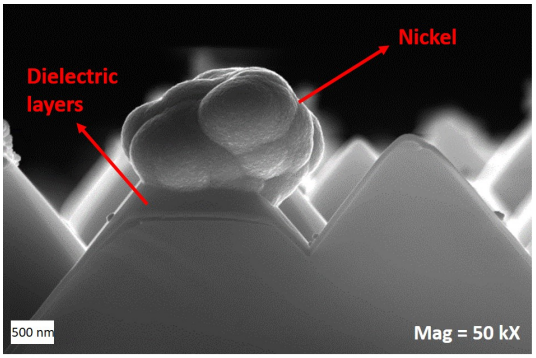

Figure 4.28: Example of Ni parasitic plating on textured front side. A pyramid has a too thin dielectric layer or crack on its top leading to nickel deposition.

2. Effective cell reflectivity can be modified due to the etching of SiO_xN_y layers modifying their optical properties. For instance, R_{eff} has been measured on the front textured side after various immersion times in HF 0.57 M, 1.43 M, $NaHF_2$ 0.16 M and 0.41 M using equation 4.25. This side is of particular interest because it receives more photons and it is the most impacted side by fluoride media. Results are depicted in Figure 4.29. The linear fits for the four conditions tested are similar which supports the accuracy of previous thickness measurements. The following relationship is established: R_{eff} = -0.14 e(SiO_xN_y) + 12.5, which allows to estimate R_{eff} value by measuring the remaining SiO_xN_y thickness after fluoride treatment using Figure 4.26.

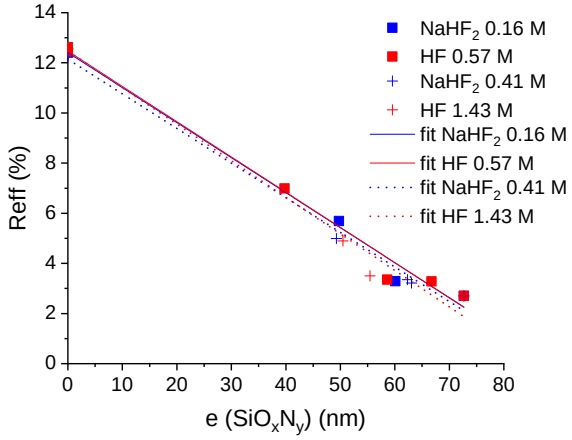

Figure 4.29: Evolution of effective reflectivity (R_{eff}) with thickness of front side SiO_xN_y ARC layer.

4.3.4 Conclusions and perspectives

Etching rates of n-PERT SiO_xN_y layers have been investigated in HF and $NaHF_2$ at various concentrations. A relationship between the etching rate and the concentration of fluoride media has been determined for both sides in HF and $NaHF_2$ as reported in Table 4.12. For both fluoride media, SiO_xN_y layer on the front textured side is etched 3-4 times faster compared to the rear polished side. This behavior is mainly attributed to higher density and refractive index of SiO_xN_y layer on the rear side but differences of roughness could be also involved. No significant differences have been observed by comparing both fluoride media suggesting a similar etching mechanism. Impact of SiO_xN_y layer etching on R_{eff} has been investigated for the front side and a linear relationship has been established between R_{eff} and e(SiO_xN_y).

Table 4.12: Etching rates of SiO_xN_y layers on both sides of n-PERT precursors in HF and $NaHF_2$.

etching equation y = ax + b	HF	$NaHF_2$
SiO_xN_y (front textured side)	y = $4.35.10^{-2}$ x + $5.1.10^{-3}$ For 0.5 M: $2.68.10^{-2}$ nm/s	y = $3.88.10^{-2}$ x + $3.4.10^{-3}$ For 0.5 M: $2.28.10^{-2}$ nm/s
SiO_xN_y (rear polished side)	y = $7.41.10^{-3}$ x + $4.1.10^{-3}$ For 0.5 M: $7.77.10^{-3}$ nm/s	y = $8.23.10^{-2}$ x + $2.1.10^{-3}$ For 0.5 M: $6.21.10^{-3}$ nm/s

Finally, etching rates of SiO_xN_y layers are similar in HF and $NaHF_2$ while it has been demonstrated that PECVD and anodic SiO_x layers are etched faster in $NaHF_2$. $NaHF_2$ is therefore more selective than HF and its use has a great advantage to remove SiO_x layers with limited SiO_xN_y layers damaging.

4.4 Optimization of Si surface activation with palladium

Deoxidation is followed by Si surface activation by Pd galvanic displacement. In this section, a first study is realized on n-type mirror polished Si samples to understand the Pd deposition mechanism and optimize the bath composition. A second study is then performed to implement the optimized conditions on n-PERT samples opened after laser ablation with the parameters optimized in chapter 3.

4.4.1 State of the art

As explained in section 2.5.2, the deposition of Pd particles on Si surface is needed to activate the further nickel electroless deposition. Activation solution contains Pd ions and fluoride media and the process is based on Pd galvanic displacement. Pd^{2+} ions are reduced into metallic Pd on Si surface and meanwhile the Si surface is dissolved. Depending on the relative energy level positions, Pd ions are reduced through electrons capture from the Si CB (reaction 1 in Figure 2.10 a)) or by injection of holes into the Si VB (reaction 4 in Figure 2.10 a)). Gorostiza et al., have studied the Pt deposition on Si in HF and have proposed a mechanism based on holes injection into the Si VB in regards with the energy diagram of the interface at equilibrium (the Nernst's potential of the solution lies close to the Si VB) [71], [191]. Such as platinum, palladium is a transition metal and is a strong oxidant ($E^0_{(Pd^{2+}/Pd)}$ = 0.915 V/SHE and $E^0_{(Pt^{2+}/Pt)}$ = 1.188 V/SHE) so it is likely to observe the same behavior in this study.

To verify this point, the energy band diagram of Si/activation solution interface has been drawn for the experimental conditions used (detailed in the experimental part) in Figure 4.30. The energy band diagram

depends on solution pH and $PdSO_4$ concentration. HF and $NaHF_2$ solutions used in this work have a pH around 1 and 3 respectively but the case of pH = 14 is also presented for comparison. To calculate the Nernst's potential of the solution, the medium $PdSO_4$ concentration tested in this work ($2.5.10^{-4}$ M) has been considered which gives a value of 0.88 V/SHE according to Nernst's relation (equation 2.5). The energy level in Si has been calculated as for the band diagram drawn in Figure 4.8. It can be noticed that $E_{F,n}$ does not equalize with $E_{(Pd^{2+}/Pd)}$ but at an intermediate value between $E_{(Pd^{2+}/Pd)}$ and $E_{(H^+/H_2)}$. As $E_{(Pd^{2+}/Pd)}$ lies close to Si VB, the Pd galvanic displacement is mainly based on holes injection into Si VB.

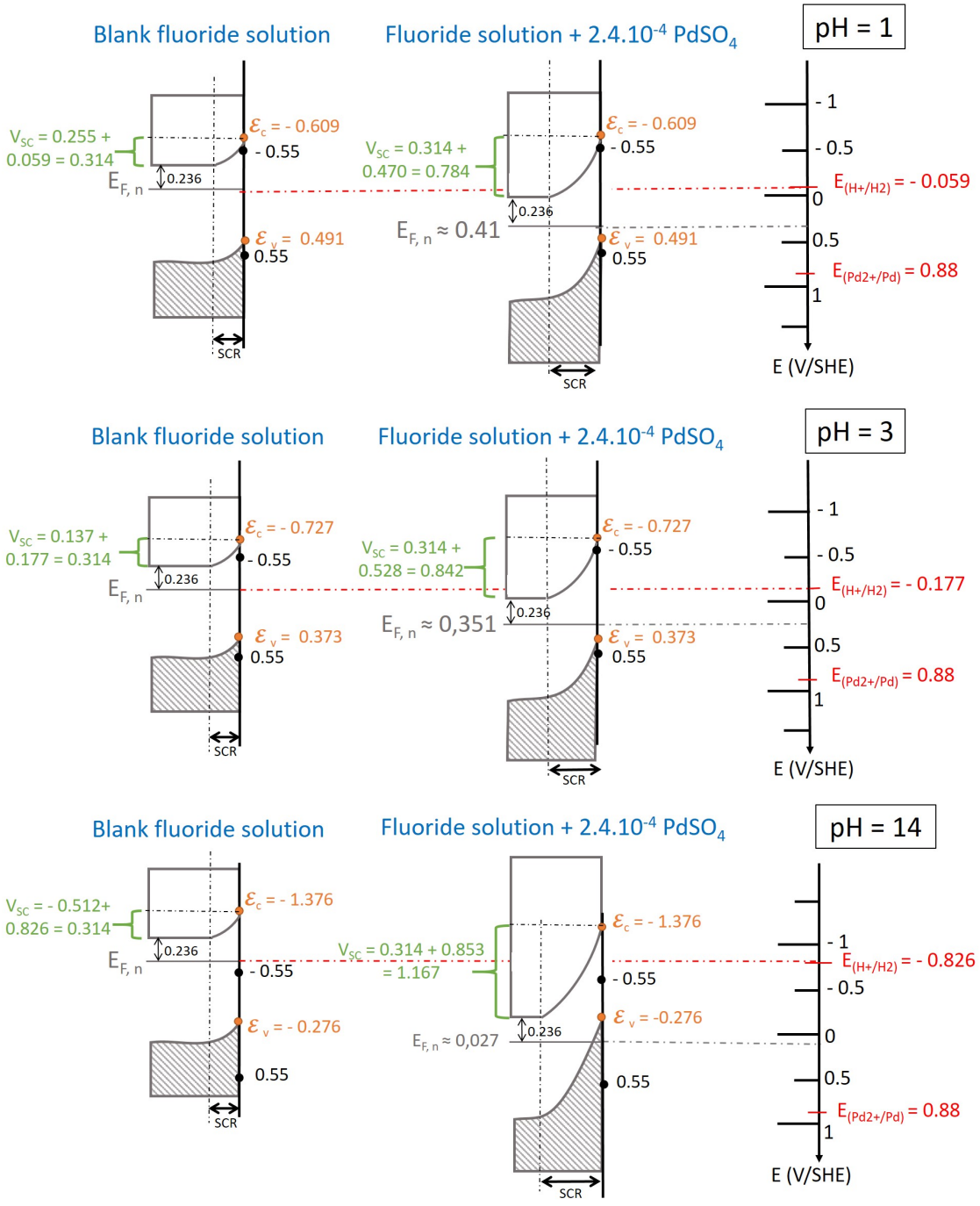

Figure 4.30: Energy band diagram relatively to SHE energy scale for n-type Si in fluoride media at pH = 1,3 or 14 before and after addition of $PdSO_4$. N_D = 3.10^{15} at/cm^{-3}, T = 300 K, [$PdSO_4$] = $2.5.10^{-4}$ M.

In that respect, Pd^{2+} ions are reduced through injection of holes into the VB of Si according to equation 4.26. That leads to Si surface oxidation according to equation 4.29. Between injection and capture, holes can travel through Si and Pd deposition can occur at different surface locations. Not only Si surface must be free of oxide layers to make a good contact with Pd, but activation solution also has to contain a fluoride media to sustain the reaction by etching of the native oxide formed during the process (equation 4.30).

Pd^{2+} ions reduction [96]:

$$2Pd^{2+} = 2Pd^{0} + 4h^{+}_{VB} \quad \text{(E = 0.987 + 0.0295 log([Pd}^{2+}\text{]) (V/SHE)} \tag{4.26}$$

Si surface oxidation [96]:

$$\text{Semi-equation 1:} \quad Si^{0} + 4h^{+}_{VB} = Si^{IV} \tag{4.27}$$

$$\text{Semi-equation 2:} \quad Si^{IV} + 2H_2O = SiO_2 + 4H^{+} \tag{4.28}$$

$$\text{Global equation:} \quad Si^{0} + 4h^{+}_{VB} + 2H_2O = SiO_2 + 4H^{+} \quad \text{(E = - 0.85 - 0.0591 pH (V/SHE)} \tag{4.29}$$

SiO_2 dissolution [73]:

$$SiO_2 + 6HF = SiF^{2-}_{6} + 2H^{+} + 2H_2O \tag{4.30}$$

Three models have been described in literature for the nucleation and growth of metallic films: 1) Frank-van der Merwe (layer by layer growth) 2) Volmer-Weber (growth by islands) 3) Stransky-Krastanov (layer by layer + islands growth) [192]. A Volmer-Weber growth mode is observed when the interaction between metallic adatoms is stronger than the interactions between adatoms and the surface. In contrast, a Frank-van der Merwe model is preferred when interaction between adatoms and the surface is stronger. The growth mode depends on lattice mismatches between metallic atoms to be deposited and surface atoms. For instance, nucleation and growth behavior of Pd on Cu surface have been studied by Huh et al. [193] and a Volmer-Weber model has been demonstrated. Pd particles are first nucleated on the Cu surface and grow by islands due to the mismatch between Pd and Cu (7.6% mismatch). A critical size is then achieved so that an additional grow requires time to generate a misfit dislocation. With a lattice parameter of 3.88 Å for Pd and 5.43 Å for Si, the mismatch is about 30% [194] so it is likely to observe a Volmer-Weber growth mode. In addition, Carraro et al. have raised the following characteristics for the galvanic displacement of metallic films on semiconductors [93]:

- High surface states density enhances the deposition rate by facilitating nucleation on kinks or steps;
- The doping type of the semiconductor impacts the deposition rate due to transfer of charges carriers through the substrate. p-type Si is favoured compared to n-type;
- Deposition rate increases with temperature;
- Stirring can be beneficial by improving film homogeneity;
- Thickness is limited to hundred of nanometers: as soon as the surface is completely covered by the metallic film, it can not be dissolved anymore so the galvanic displacement reactions are stopped;
- The reaction is thermodynamically more favourable for metals with higher redox potentials;
- Efficiency of metal deposition varies according to the solution composition and pH;

- Poor film adherence can be observed due to hydrogen evolution followed by hydrogen incorporation into the film. This is explained by the standard redox potential of silicon oxidation (reaction 4.29) which is more negative than the one of H^+ reduction (equation 4.14).

The quality of further Ni seed layer deposition highly depends on Pd particles size and density. Bajpai et al. have worked on Pd activation in HF-based solutions and have obtained a conformal Ni layer, with no interfacial voids, good adherence ($>$ 23 MPa) and no junction shunting after annealing, which are the major issues raised during the Ni electroless deposition on Si [13]. They have highlighted that too long activation leads to non-uniform Ni seed layer. The higher amount of Pd particles also implies increased costs (considering the high price of Pd) and affects the effectiveness of Ni barrier towards Cu diffusion. Small Pd particles with high nucleation density help to control hydrogen evolution during Ni electroless deposition and limit formation of pinholes like structures. They have also raised that Pd nucleation could be suppressed in case of high surface hydrophobicity. Finally, their pre-requisites for a suitable Pd activation are: short activation time ($\approx$ 30 sec), high nucleation density, small Pd particles size and high surface wetting.

To optimize the Pd activation step, the influence of different parameters on the size, number and morphology of Pd particles has been investigated. For that purpose, samples have been immersed different times in activation solutions containing Pd^{2+} ions ($PdSO_4$ solution) and either HF or $NaHF_2$. The concentration of components is varied and the impact of stirring is also investigated. So far, no study has been carried out on Pd activation in $NaHF_2$ fluoride media so a comparison with Pd activation in HF will be realized. Two studies have been conducted:

1. A quantitative study on n-type mirror polished Si samples to easily analyse Pd particles number, size and morphology. Thus, a statistical analysis for the different experimental conditions can be performed to determine the best activation conditions;
2. A qualitative study on laser opened n-PERT precursors to define if optimized conditions identified in the first study are suitable or need to be adjusted.

4.4.2 Study 1: Pd galvanic displacement on n-type mirror polished Si wafers

Experimental approach

This study is performed on n-type (1.5 Ω.cm, N_D = 3.10^{15} at/cm^{-3}) mirror polished Si wafers. At different immersion times in activation solutions, SEM analysis is performed and images are processed using a Python code to calculate the number of particles, the dispersion and the average radius, the dispersion and the average distance between particles (see Figure 4.31). For each sample, five SEM images are realized at various sample locations to obtain mean values. The influence of the following parameters has been studied:

- Immersion time: samples are immersed from minimum 5 seconds to maximum 5 minutes;
- Concentration of Palladium ions is varied such as [$PdSO_4$] = 5.10^{-5} M, $2.5.10^{-4}$ M or 5.10^{-4} M;
- Solutions are either agitated with a magnetic stir (200 rpm) or not;
- A comparison between HF and $NaHF_2$ fluoride media is realized;

- Different fluoride media concentrations have been tested for HF and $NaHF_2$: [HF] = 0.5 M or 1.5 M and [$NaHF_2$] = 0.16 M or 0.5 M.

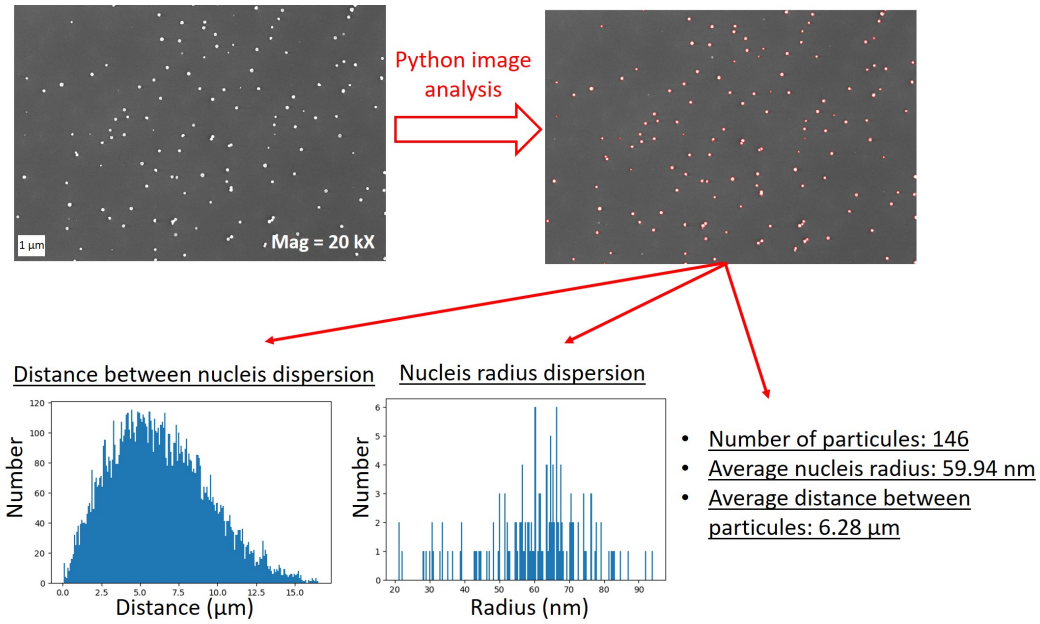

Figure 4.31: Example of SEM images analysis with Python code on activated n-type mirror polished Si.

Results

IMPACT OF IMMERSION TIME

CONDITIONS TESTED

- HF 0.5 M
- $PdSO_4$ 5.10^{-4} M
- No solution stirring
- Immersion time: 5, 10, 15, 20, 25, 30, 35, 40, 45 and 50 seconds

Samples have been immersed in activation solution and the evolution of Pd particles number and size with immersion time are plotted in Figure 4.32. Two parts can be distinguished on the graph: 1) before 30 seconds immersion, Pd particles mean radius increases but the particles number increases slowly 2) after 30 seconds immersion, Pd particles mean radius decreases drastically which is associated with an important increase of particles number.

Complementary information are obtained by looking at particles radius dispersion and corresponding SEM images displayed in Figure 4.33 for 5, 20, 30, and 45 seconds immersion. At 5 and 20 seconds immersion, dispersion of particles radius is centered around one value (35 nm and 60 nm respectively). That suggests a first nucleation step followed by particle growth. Then, at 30 and 45 seconds immersion, two radius populations are observed: a first one centered around 40 nm and 50 nm respectively and the other centered around 100 nm in both cases. That suggests a second nucleation step with the apparition of small particles as visible on SEM images.

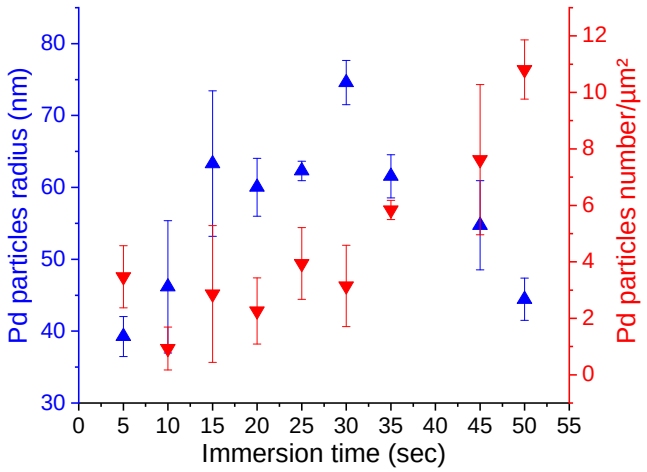

Figure 4.32: Evolution of Pd particles number and mean radius with immersion time in HF 0.5 M + $PdSO_4$ 5.10^{-4} M (no stirring).

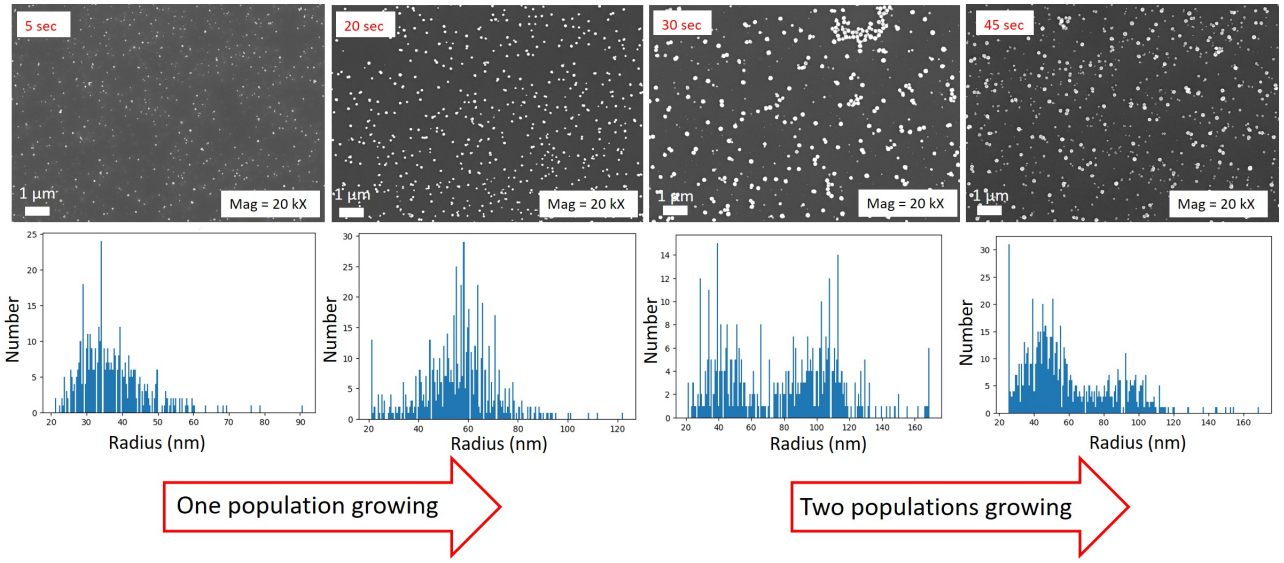

Figure 4.33: SEM images and Pd particles radius dispersion after 5, 20, 30, 45 seconds immersion in HF 0.5 M + $PdSO_4$ 5.10^{-4} M (no stirring).

Regarding these results, the following scenario can be proposed. At the beginning, a first nucleation step occurs and a certain number of Pd particles are deposited on Si surface (Figure 4.33, 5 seconds). Until 30 seconds, particles are preferably deposited on existing particles rather than on Si surface (growth is favored towards nucleation, Volmer-Weber growth model) and Pd particles size is thus increased (Figure 4.33, 20 seconds). At around 30 seconds immersion, a critical size (radius $\approx$ 75 nm) is reached due to constraints between Pd and Si surface (lattice mismatch). Nucleation is more favorable at this moment and a second nucleation step occurs, associated with a significant increase of particles number. As a result, two radius populations can be observed and the average particles radius is reduced due to second nucleation step (Figure 4.33, 30 seconds). Finally, Pd particles deposited during the second nucleation step are grown as visible on radius dispersion graphs in which the particles populations are shifted towards higher radius values (Figure 4.33, 45 seconds).

These two particles radius populations are also observed with HF 1.5 M and for other $PdSO_4$ concentrations, whether with or without solution stirring. An example is given in Figure 4.34 after 30 seconds immersion. It suggests that this behavior is independent of [HF], [$PdSO_4$]and solution stirring.

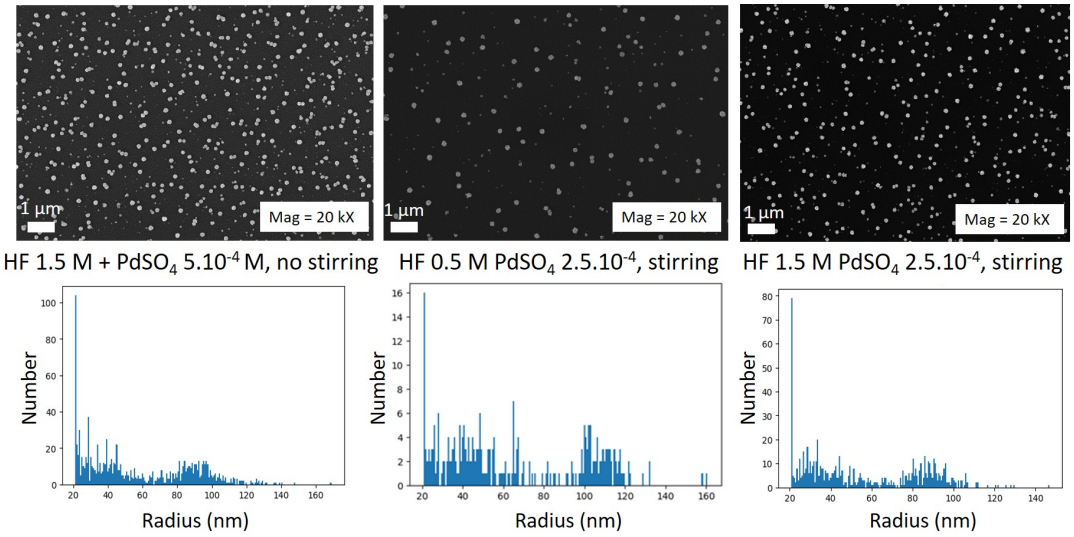

Figure 4.34: SEM images and Pd particles radius dispersion after 30 seconds immersion in various HF-based activation solutions.

On the contrary, in case of $NaHF_2$ based activation solution, only one Pd particles size population is most of the time observed as illustrated in Figure 4.35. Some smaller particles are visible but after longer immersion times ≥ 1 min (not shown here) and the contrast of two particles sizes populations is much less pronounced than with HF. A more detailed comparison between both fluoride media is presented further.

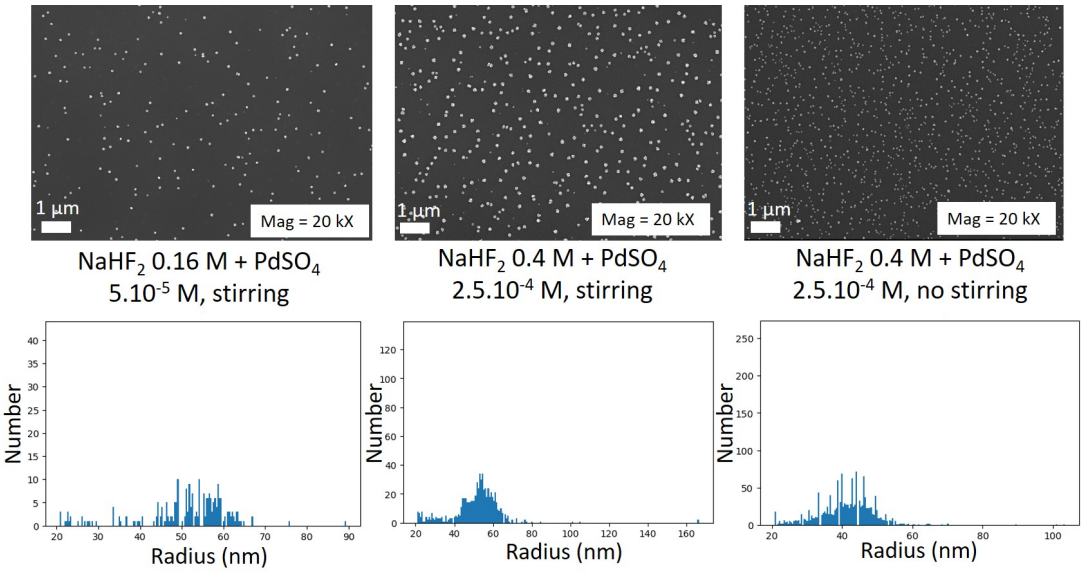

Figure 4.35: SEM images and Pd particles radius dispersion after 30 seconds immersion in various $NaHF_2$-based activation solutions.

In regards with this first analysis, it seems to us that a satisfying Si surface activation is achieved for a density > 3 particles/µm^2 with a good particles dispersion and a radius as small as possible (< 50 nm).

An example is given in Figure 4.36. For most of the conditions tested, 30 seconds immersion time were sufficient to deposit enough particles while limiting particles growth.

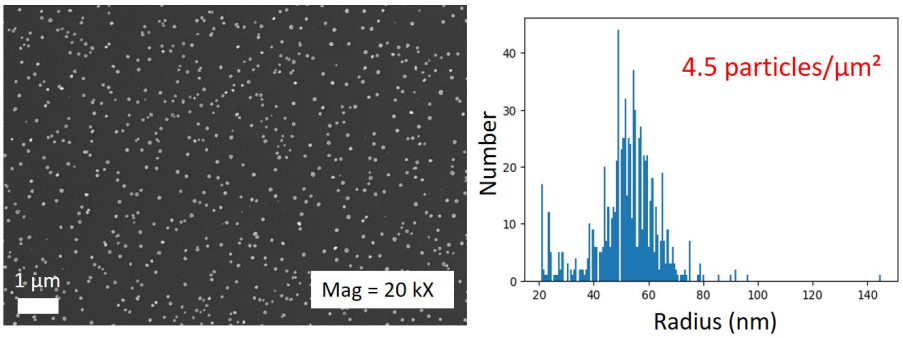

Figure 4.36: SEM images and Pd particles radius dispersion after 30 seconds in $NaHF_2$ 0.16 M + $PdSO_4$ $2.5.10^{-4}$ M (stirring).

IMPACT OF $PdSO_4$ CONCENTRATION

CONDITIONS TESTED

- HF 0.5 M or $NaHF_2$ 0.16 M
- $PdSO_4$ $2.5.10^{-4}$ M and 5.10^{-5} M
- Solution stirring
- Immersion time: 10, 30, 60, 300 seconds

Pd particles number and mean radius after 10, 30 and 60 seconds immersion are displayed in Figure 4.37 for HF 0.5 M with both $PdSO_4$ concentration tested. Results obtained in $NaHF_2$ 0.16 M fluoride media are presented in Figure 4.38. After 5 minutes immersion, statistical analysis is not possible due to the high density of particles but SEM images are presented in Figure 4.39.

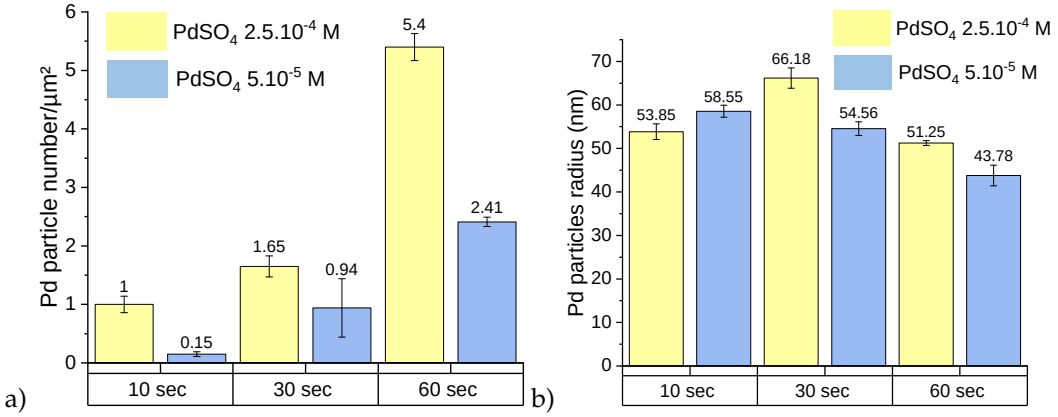

Figure 4.37: Pd particles number and mean radius after 10, 30 and 60 seconds in HF 0.5 M + $PdSO_4$ $2.5.10^{-4}$ or 5.10^{-5} M (with stirring).

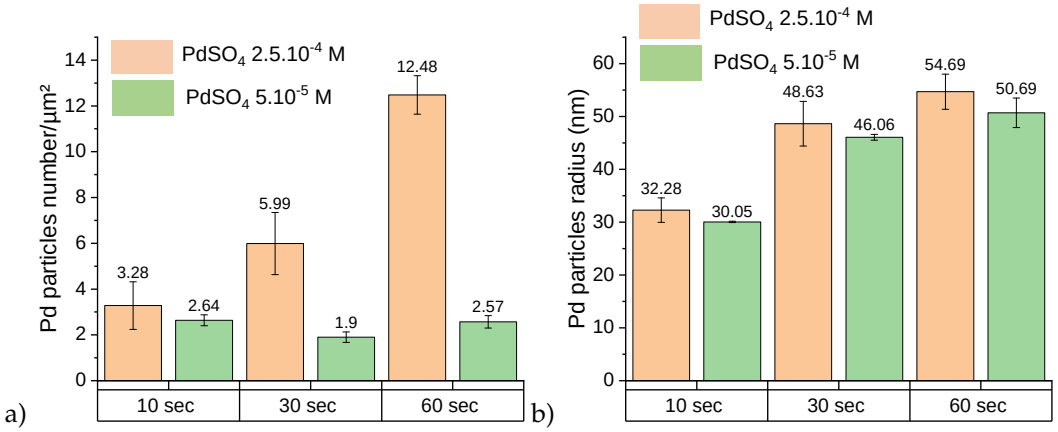

Figure 4.38: Pd particles number and mean radius after 10, 30 and 60 seconds in $NaHF_2$ 0.16 M + $PdSO_4$ $2.5.10^{-4}$ or 5.10^{-5} M (with stirring).

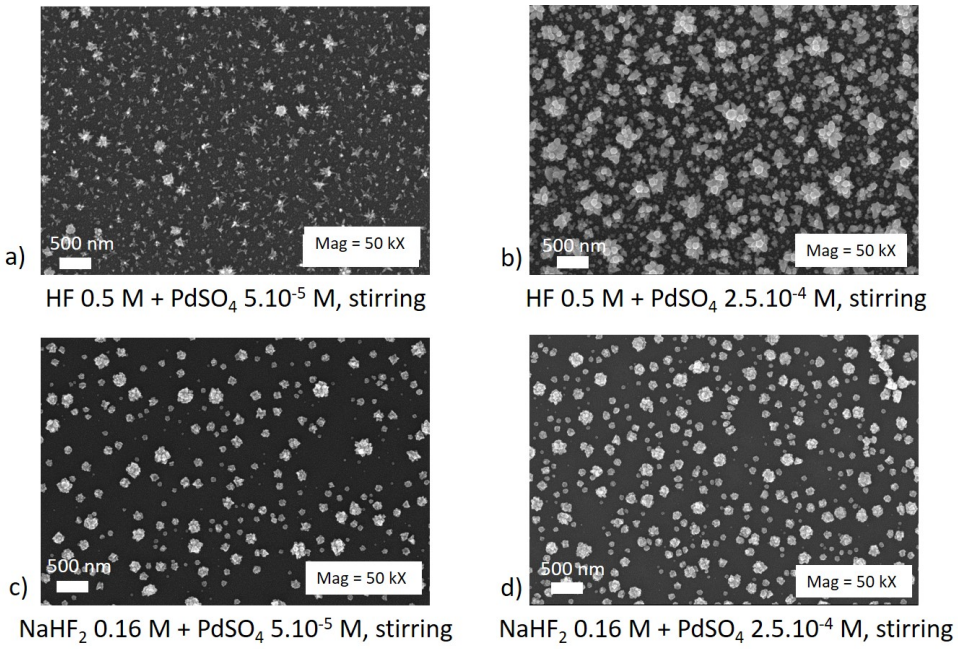

Figure 4.39: SEM images after 5 min immersion in the four activation solutions tested.

For both fluoride media, the density of Pd particles and the mean radius are increased with $PdSO_4$ concentration, indicating that nucleation and particles growth are both favoured. This is particularly visible by comparing SEM images after 5 min immersion in HF 0.5 M with $PdSO_4$ $2.5.10^{-4}$ or 5.10^{-5} M (Figure 4.39 a) and 4.39 b)). Long immersion times promote the formation of branched dendritic structures on Pd particles, even with the low $PdSO_4$ concentration. A colored SEM pictures showing these dendritic structures is presented in Figure 4.40. This latter has been obtained after 5 minutes immersion in HF 0.5 M with a high $PdSO_4$ concentration (5.10^{-4} M)). This specific shapes have been already observed [93] and are not desirable in this study. For both fluoride media, it is preferable to use the lowest $PdSO_4$ concentration (5.10^{-5} M) to obtain small particles. At this $PdSO_4$ concentration, only 10 seconds immersion are sufficient for $NaHF_2$ 0.16 M (Pd particles number $\approx$ 2) but HF 0.5 M fluoride media requires 60 seconds immersion time to reach sufficient particles density.

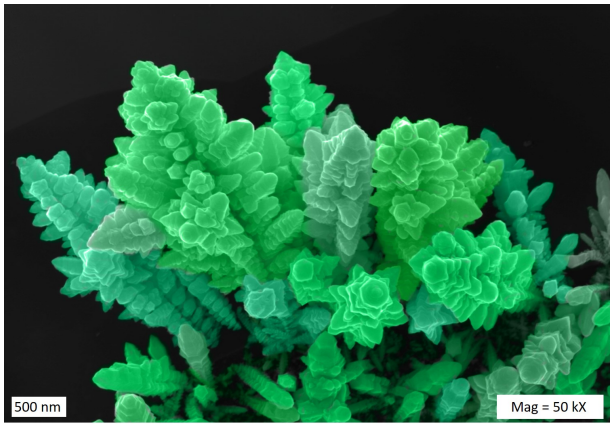

Figure 4.40: SEM image representing the branched dendritic structures of Pd particles after a long immersion time (5 minutes) in HF-based activation solution with an high $PdSO_4$ concentration (5.10^{-4} M).

IMPACT OF STIRRING

CONDITIONS TESTED

- HF 0.5 M and $NaHF_2$ 0.5 M
- $PdSO_4$ $2.5.10^{-4}$ M
- Stirring and no stirring
- Immersion time: 30 seconds

Pd particles number and mean radius after 30 seconds immersion are displayed in Figure 4.41 and the corresponding SEM images are shown in Figure 4.42. More homogeneous Pd deposition is observed with stirring, as attested by the lower standard deviations in Figure 4.41. Pd particles are also bigger as the solution is continuously regenerated at Si surface, avoiding depletion of species needed for Pd ions reduction (equation 4.26), surface oxidation (equation 4.29) and desoxydation (equation 4.30). However, there are less particles with stirring due to the mechanical effect removing some particles from the surface. Even if Pd particles deposition is more homogeneous with stirring, it is preferable to not agitate the solution to obtain smaller Pd particles with an higher surface density.

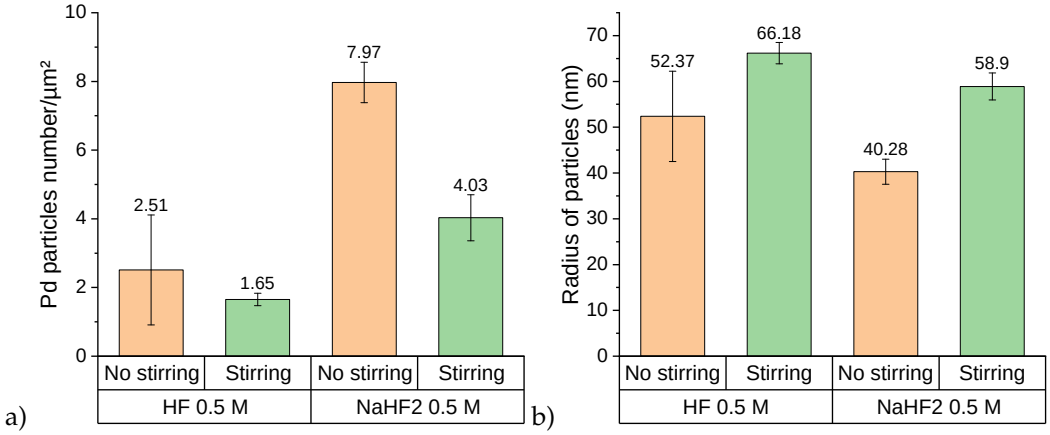

Figure 4.41: Pd particles number and mean radius after 30 seconds in $NaHF_2$ 0.5 M + $PdSO_4$ $2.5.10^{-4}$ and HF 0.5 M + $PdSO_4$ $2.5.10^{-4}$ with or without solution stirring.

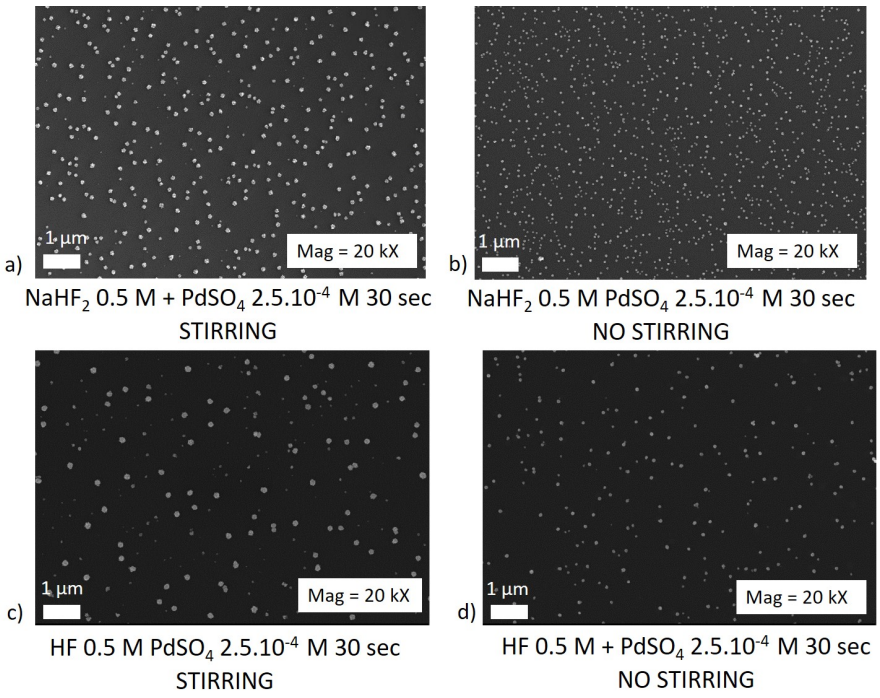

Figure 4.42: SEM images after 30 seconds in $NaHF_2$ 0.5 M + $PdSO_4$ 2.5.10^{-4} and HF 0.5 M + $PdSO_4$ 2.5.10^{-4} M with or without solution stirring

IMPACT OF FLUORIDE MEDIA CONCENTRATION

CONDITIONS TESTED

- HF 0.5 M, HF 1.5 M, $NaHF_2$ 0.16 M and $NaHF_2$ 0.5 M
- $PdSO_4$ 2.5.10^{-4} M
- Solution stirring
- Immersion time: 10, 30 and 60 seconds

Results obtained after immersion in HF solutions are presented in Figure 4.43. Pd particles are bigger with a lower surface density in case of HF 0.5 M compared to HF 1.5 M but in both cases, the mean radius increases until 30 seconds immersion and then decreases. This is due to the second nucleation step occurring after 30 seconds immersion as highlighted before. To explain the differences observed with different HF concentrations, it is necessary to report on Pd galvanic displacement reactions. Assuming that:

- Pd ions reduction (equation 4.26) has a constant k_1;
- Si oxidation (equation 4.29) has a constant k_2;
- deoxidation reaction (equation 4.30) has a constant k_3.

A non optimized fluoride media concentration induces a disequilibrium between Si surface oxidation and deoxidation. For instance, when $k_3 \ll k_2$ Si surface deoxidation is not efficient enough to properly remove native oxide formed during the process. Consequently, native oxide can hinder the Pd ions reduction on Si surface (holes injection into Si VB). As Si oxidation can still occur through electrons injection into the electrolyte, formed electrons reach the existing Pd particles and reduce Pd ions. In this way, growth

is favored towards nucleation which reduces the particles surface density but increases their sizes. This is exactly the behavior observed in case of HF 0.5 M. With an higher HF concentration (HF 1.5 M), a best equilibrium between k_3 and k_2 leads to smaller Pd particles with an higher density which is more suitable in this work.

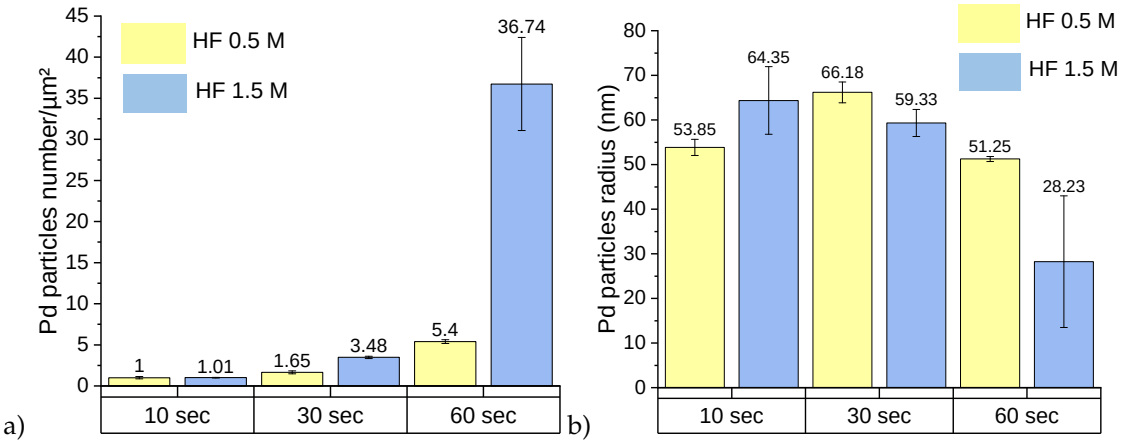

Figure 4.43: Pd particles number and mean radius after 10, 30 and 60 seconds in $PdSO_4$ $2.5.10^{-4}$ M + HF 0.5 M or HF 1.5 M (with stirring).

In the opposite situation ($k_3 \gg k_2$), the native oxide is removed as soon as it is formed and it can be hypothesized that Si surface dissolution leads to removal of Pd nucleus through surface etching below the particles. Therefore, particles are preferably deposited on existing ones rather than on Si surface. The density is reduced but the mean radius is increased and this behavior is observed for $NaHF_2$ 0.5 M (Figure 4.44). A better Si oxidation/deoxidation equilibrium is obtained for lower $NaHF_2$ concentration (0.16 M) and smaller particles with higher surface density are observed. As shown in section 4.2.4, SiO_x is etched at least 2 times faster with $NaHF_2$. Lower $NaHF_2$ concentrations are thus needed compared to HF to achieve a good oxidation/deoxidation and deposit smaller Pd particles with an higher surface density.

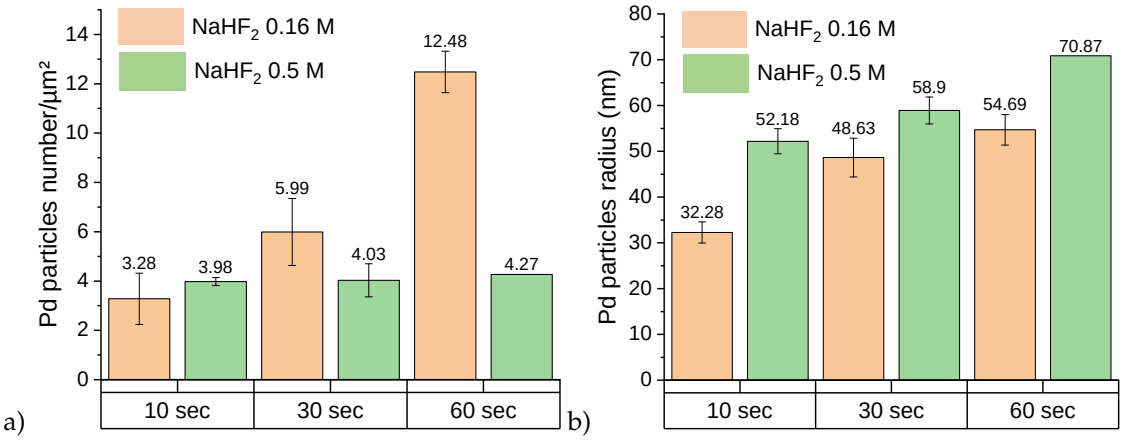

Figure 4.44: Pd particles number and mean radius after 10, 30 and 60 seconds in $PdSO_4$ $2.5.10^{-4}$ M + $NaHF_2$ 0.16 M or $NaHF_2$ 0.5 M (with stirring).

Comparison of HF and $NaHF_2$ fluoride media

Differences between both fluoride media have been already raised but a closer comparison is presented

in this part. Conditions tested are the same as for the study on the impact of fluoride media concentration but results are shown in a different manner for better readability. Pd particles number and mean radius after 10 and 30 seconds in $NaHF_2$ 0.16 M, $NaHF_2$ 0.5 M, HF 0.5 M and HF 1.5 M solutions + $2.5.10^{-4}$ M $PdSO_4$ are reported in Figure 4.45 and 4.46. SEM images after 30 seconds immersion are presented in Figure 4.46.

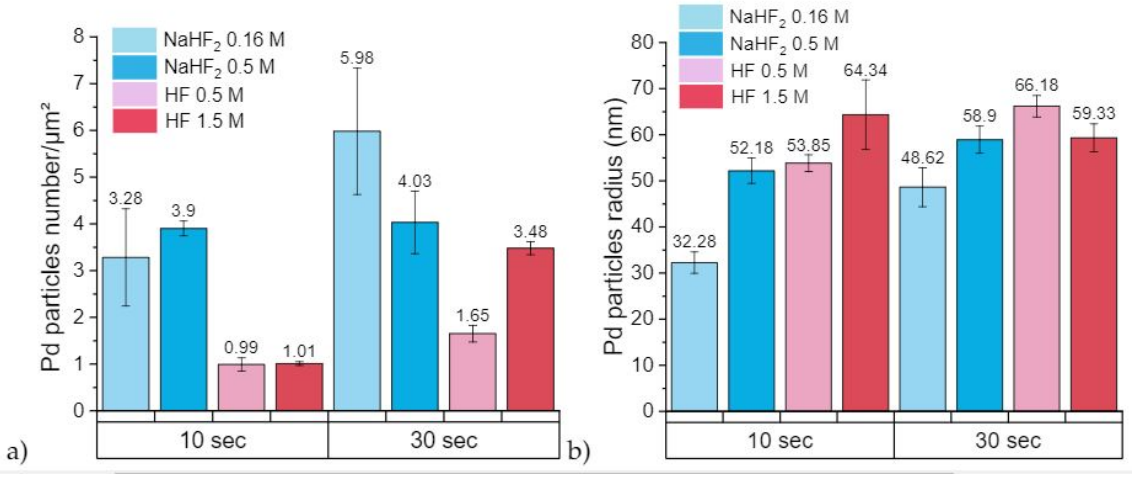

Figure 4.45: Pd particles number and mean radius after 10 and 30 seconds in $NaHF_2$ 0.16 M, $NaHF_2$ 0.5 M, HF 0.5 M and HF 1.5 M + $PdSO_4$ $2.5.10^{-4}$ M (with stirring).

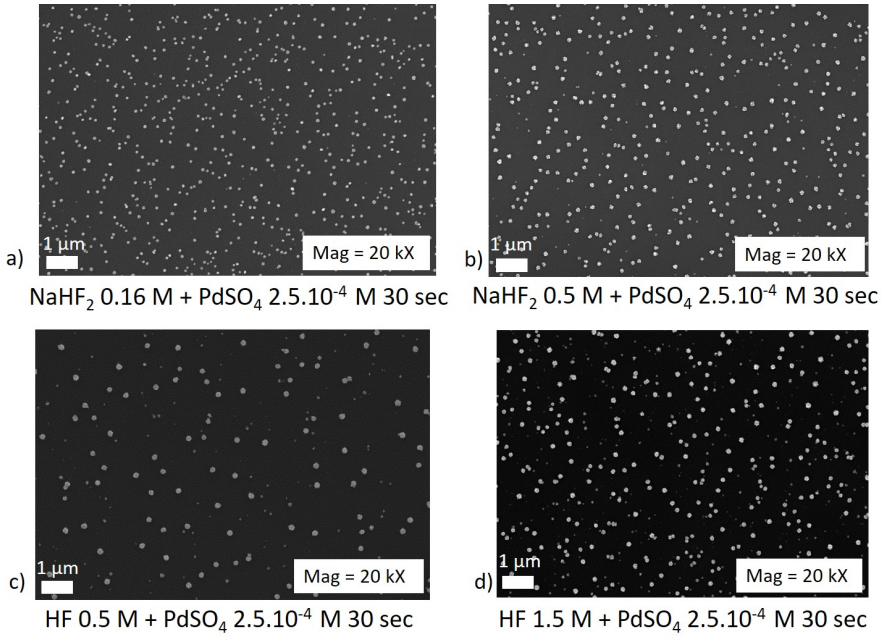

Figure 4.46: SEM images after 30 seconds in $PdSO_4$ $2.5.10^{-4}$ M + a) $NaHF_2$ 0.16 M, b) $NaHF_2$ 0.5 M, c) HF 0.5 M, d) HF 1.5 M (with stirring).

The higher surface density of particles after immersion in $NaHF_2$ suggests that nucleation is favoured compared to HF fluoride media. By looking at the energy band diagrams in Figure 4.30, the difference between $\mathcal{E}_V$ and $E_{(Pd^{2+}/Pd)}$ is greater at high pH values. Thus, the electromotive force is greater at high pH and holes injection from the $E_{(Pd^{2+}/Pd)}$ to the Si valence band to reduce Pd^{2+} ions is facilitated. Nucleation is therefore favoured in $NaHF_2$ solution (pH $\approx$ 3) compared to HF solution (pH $\approx$ 1). In addition, it appears

that $NaHF_2$ fluoride media leads to smaller Pd particles with an higher density for both concentrations tested. The mean radius in case of HF (Figure 4.45 b)) represents a mean value (particles from the first nucleation step + smaller ones from the second nucleation step). SEM images are thus more suitable to compare the particles size. After immersion in HF (Figure 4.46 c) and d), two sizes populations are visible, as already demonstrated earlier, while size is more homogeneous for $NaHF_2$ (Figure 4.46 a) and b)). The first particles deposited in case of HF are bigger than the particles observed after immersion in $NaHF_2$. Globally, Pd particles are grown slowly in $NaHF_2$ solution and the critical size is reached later. Two particles size population are visible after 30 seconds immersion (and sometimes before) in HF solutions but this effect is observed only after 1 minute in $NaHF_2$ solutions as shown in Figure 4.47.

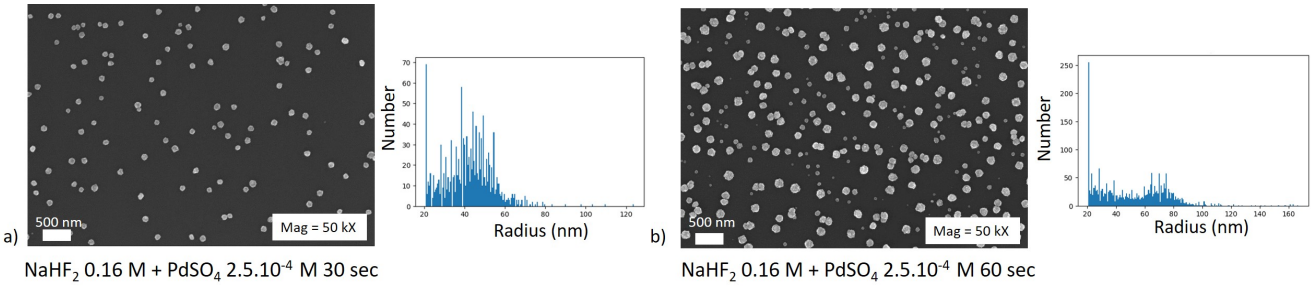

Figure 4.47: SEM images and corresponding Pd particles radius dispersion graph after immersion in $NaHF_2$ 0.16 M + $PdSO_4$ 2.5.10^{-4} M during a) 30 sec, b) 1 min (with stirring).

4.4.3 Conclusions and perspectives

In regards with these results, several conclusions have been deduced and are summarized in Table 4.13. Best activation conditions are also reported by keeping in mind that the aim is to achieve high surface density of small Pd particles.

Table 4.13: Impact of various parameters on Pd activation on n-type mirror polished Si wafers.

PARAMETERS	OBSERVATIONS	BEST CONDITIONS
Immersion time	• Successive nucleation/growth cycles occur during Pd galvanic displacement deposition (Volmer-Weber model). Second nucleation happens when the critical size (radius ≈ 75 nm) is reached and two particle size populations are then observed • It is preferable to have only one particle size populations • Branched dendritic structures appear for long immersion	30 sec immersion times
[$PdSO_4$]	• Bigger Pd particles with an higher surface density when [$PdSO_4$] increases. Low concentration is better to have small particles but higher concentration is needed if surface density is not high enough	5.10^{-5} M or 2.5.10^{-4} M
Stirring	• Pd particles dispersion is slightly better with stirring but detrimental mechanical effect is observed • Pd Particles are smaller with an higher density without stirring	No stirring
[Fluoride media]	• Fluoride media concentration must provide a suitable equilibrium between Si surface oxidation and deoxidation • Lower $NaHF_2$ concentrations are needed to achieve this equilibrium thanks to faster SiO_x etching rate (section 4.4.1)	HF 1.5 M $NaHF_2$ 0.16 M
HF or $NaHF_2$	• Smaller particles and higher surface density in $NaHF_2$ thanks to a better energy band diagram configuration for holes transfer	$NaHF_2$

In this study, most experiments have been realized with stirring and best results have been obtained with $NaHF_2$ 0.16 M + $PdSO_4$ $2.5.10^{-4}$ M 30 seconds immersion (Pd radius = 48.7 nm and density = 5.99 particles/µm^2). A lower $PdSO_4$ concentration (5.10^{-5} M) with the same conditions enables to limit metal consumption and mean radius is reduced (46.1 nm). The particles surface density in these conditions is lower (2 particles/µm^2) but still satisfying. It has been observed that no solution stirring is preferable so a perspective would be to perform these both optimized conditions without stirring.

Another perspective would be to directly deposit Ni particles on the Si surface. By considering equation 4.31, $E_{(Ni^{2+}/Ni)}$ is around - 0.25 V/SHE and does not lie to Si VB, except for high pH value (for instance pH = 14 in the energy diagram in Figure 4.30). Consequently, galvanic displacement of nickel on Si surface may be possible in alkaline fluoride media such as NH_4F.

$$Ni^{2+} + 2e^- = Ni \quad (\text{E = - 0.25 + 0.0295 log(Ni}^{2+}\text{) (V/SHE)}) \tag{4.31}$$

4.4.4 Study 2: Pd galvanic displacement on laser opened n-PERT samples

Experimental approach

N-PERT precursors have been laser opened with laser parameters optimized in the Chapter 3:

1. Laser parameters 1: 0.56 J/cm^2, no spot overlapping
2. Laser parameters 2: 0.32 J/cm^2, 50% spot overlapping

Then, samples have been deoxidized before immersion in different activation solutions. The best activation conditions identified in the study 1 are first implemented and SEM characterization is performed to analyse the surface morphology. The aim is to determine if activation conditions optimized before are suitable for laser opened n-PERT precursors and adjust these conditions accordingly. As deoxidation and Pd activation are both performed in fluoride media, it is also interesting to investigate Si surface activation without prior deoxidation step.

Results

Laser opened samples have been first immersed in the following activation solution: $NaHF_2$ 0.16 M + $PdSO_4$ $2.5.10^{-4}$ M 30 seconds without solution stirring (no prior deoxidation). SEM images are displayed in Figure 4.48.

White particles correspond to metallic Pd particles as confirmed by EDS analysis. On the rear polished side opened with laser parameters 1 (no overlaping) (see Figure 4.48 a)) the activation is not homogeneous and Pd particles deposition depends on the location in laser opened areas identified in Chapter 3: inner spot: area n°1, outer spot: area n°2, corona: area n°2_{bis} and double impacted area: area n°4. Thus, the morphology and chemical composition of the surface after laser ablation impact the deposition of Pd particles.

Results in Chapter 3 have revealed a lower oxygen content in area n°2_{bis} where dielectric layers have been completely removed by lift-off. In this area, native oxide is removed during immersion in activation solution containing $NaHF_2$ and Pd particles are properly deposited. However, it has been proposed that areas 1 and 2 are still covered by SiO_x layers (from remaining initial SiO_x dielectric layer and/or laser formed SiO_x). In these areas, SiO_x layers have not been removed during activation step and hinder the

Pd particles deposition. In double impacted area, significant amount of Oxygen has been also detected but Pd particles are deposited in this area. It confirms that laser spot overlapping provides the removal of remaining SiO_x layers and so SiO_x detected in this area mostly corresponds to laser formed SiO_x easily removed in fluoride media. This layer is removed by $NaHF_2$ during immersion in activation solution and Pd particles deposition is also facilitated by the surface roughness. Therefore, Pd particles deposition is homogeneous when 50% overlapping is used as observed in Figure 4.48 b)). Pd particles in area 2_{bis} and 4 will provide Ni electroless deposition but it is expected that Ni seed layer shows a poor adherence below areas 1 and 2.

On the front textured side, the presence of LIPSS structures is favourable for Pd particles deposition and Si surface activation is homogeneous for both laser parameters tested (see figure 4.48 c) and 4.48 d)).

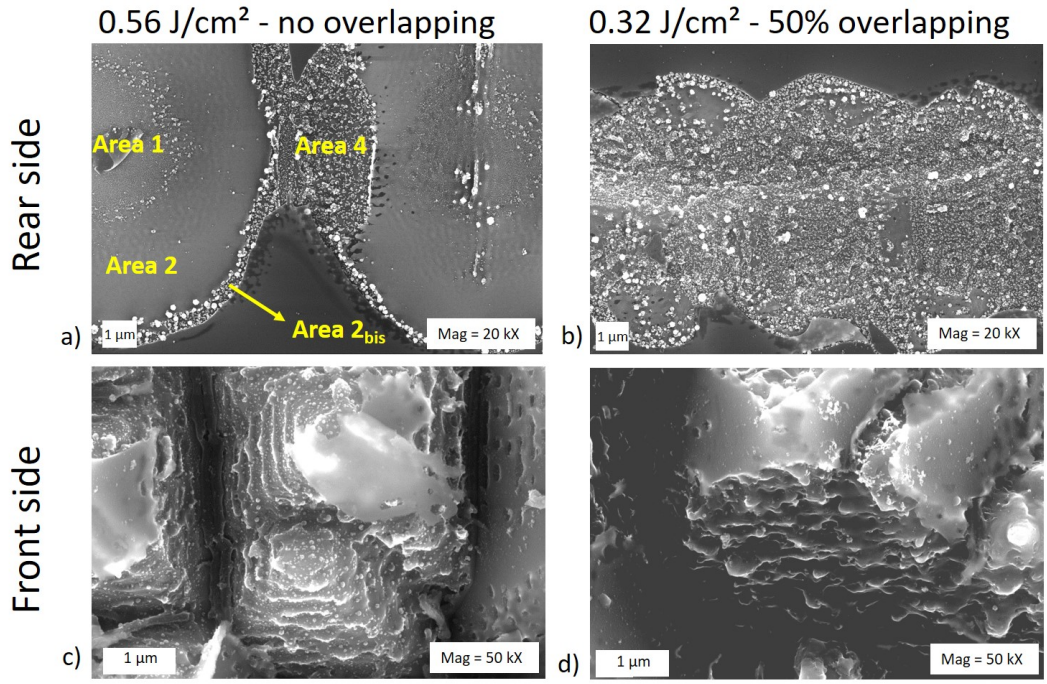

Figure 4.48: SEM images after immersion of ablated n-PERT precursors in $NaHF_2$ 0.16 M + $PdSO_4$ $2.5.10^{-4}$ M during 30 seconds (no stirring).

Then, a prior deoxidation has been performed in $NaHF_2$ 0.5 M to remove SiO_x layers hindering Pd deposition in area 1 and 2 on the rear side opened with laser parameters 1. SEM images are displayed in Figure 4.49 for two magnifications. Figure 4.49 a) and b) have been obtained after 30 seconds prior deoxidation while Figure 4.49 c) and d) have been obtained after 1 minute prior deoxidation. A prior deoxidation in $NaHF_2$ 0.5 M during 30 seconds is not sufficient to remove efficiently SiO_x layers in area 1 and 2 and Pd particles deposition is not homogeneous. Some isolated Pd particles are however visible in area 2, suggesting that SiO_x layer has been randomly etched. It is consistent with results in section 4.2.2 in which PECVD SiO_x exhibits a random etching leading to increased layer porosity.

For deoxidation longer than 1 minute, an higher surface density of Pd particles is observed in all opened spot areas. It is however difficult to determine if SiO_x layers have been completely removed in area 1 and 2 or whether they are still present with an important porosity allowing more particles deposition.

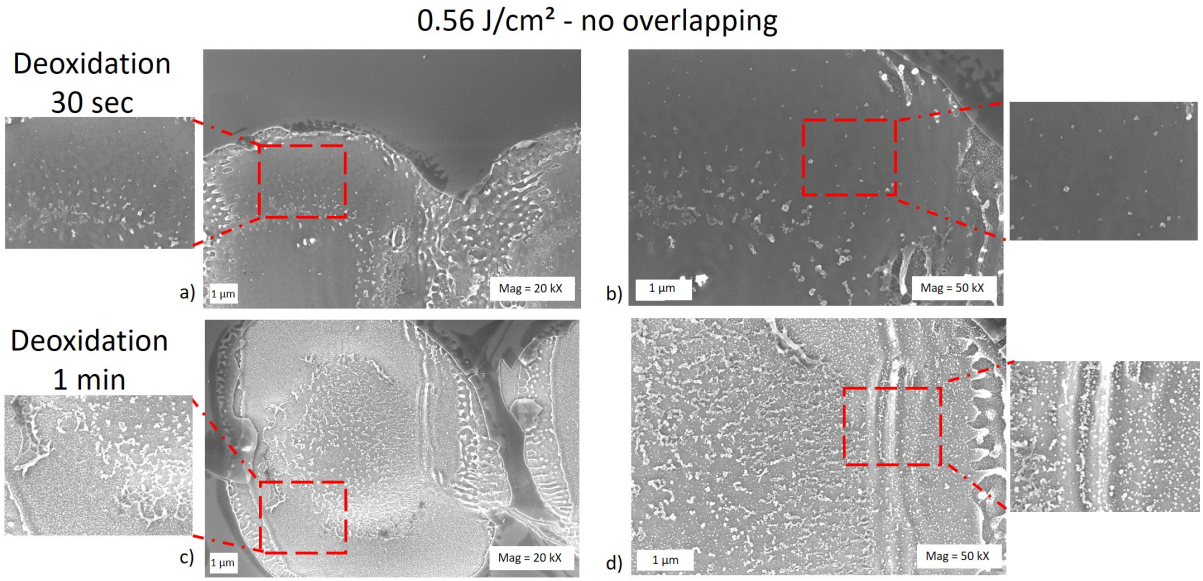

Figure 4.49: SEM images on rear side opened with laser 1 after deoxidation in $NaHF_2$ 0.5 M 30 seconds (a and b) or 1 minute (c and d) followed by immersion in $NaHF_2$ 0.16 M + $PdSO_4$ $2.5.10^{-4}$ M during 30 sec.

A comparison of Figures 4.48 and 4.49 indicates that Pd particles are smaller with more homogeneous size when a prior deoxidation is performed. This is particularly visible in area 2_{bis} (see Figure 4.48 a) and Figure 4.49 a)). This behavior is also observed on double impacted areas on the rear side and on the front side (not shown here). The following explanation is proposed: SiO_x thickness is not homogeneous and can be etched at different speed depending on surface roughness. Underlying Si is therefore exposed more or less quickly to the activation solution and nucleation steps are delayed at different sample locations. The first particles deposited will grow as long as other Si surface locations are exposed to the solution and Pd particles deposition is concentrated on few areas, leading to bigger particles with different sizes. Finally, a prior deoxidation is preferable to achieve a more homogeneous and dispersed Pd particles deposition.

On the activated samples represented in Figure 4.49 c) and d), Ni electroless deposition has been realized after a prior deoxidation in $NaHF_2$ 0.5 M during 1 minute. Important parasitic plating (PP) has been observed (not shown here) which means that 1 minute deoxidation in $NaHF_2$ 0.5 M is too aggressive towards SiO_xN_y layers. With a lower $NaHF_2$ concentration (0.16 M), it appears after several experiments that a total immersion time (deoxidation + activation) must not exceed 3 minutes to preserve the dielectric layers and limit PP. $NaHF_2$ 0.16 M is preferred to obtain smaller Pd particles size with higher surface density as demonstrated in the first study (see section 4.4.2) but 3 minutes exposition to $NaHF_2$ does not enable a uniform removal of SiO_x layers in area 1 and 2.

On this basis, this work has been pursued using $NaHF_2$ 0.16 M and $PdSO_4$ concentration has been reduced to 5.10^{-5} M to reduce Pd particles size and metal consumption. Various deoxidation times in $NaHF_2$ 0.16 M and activation times in $NaHF_2$ 0.16 M + $PdSO_4$ 5.10^{-5} M have been tested such as the total exposition to fluoride media does not exceed 3 minutes. A satisfying Pd particles deposition is obtained in the two following cases and SEM images in Figure 4.50 show the surface morphology obtained for case 1.

- Case 1: Deoxidation in $NaHF_2$ 0.16 M 1 min 30 and activation in $NaHF_2$ 0.16 M + $PdSO_4$ 5.10^{-5} M 30 seconds: Pd activation is satisfying on both sides for laser parameters 1 and 2.
- Case 2: Deoxidation in $NaHF_2$ 0.16 M 30 seconds and activation in $NaHF_2$ 0.16 M + $PdSO_4$ 5.10^{-5} M 30 seconds: Pd activation satisfying on front side for laser parameters 1 and 2 and on the rear side for laser parameters 2 (thanks to spot overlapping).

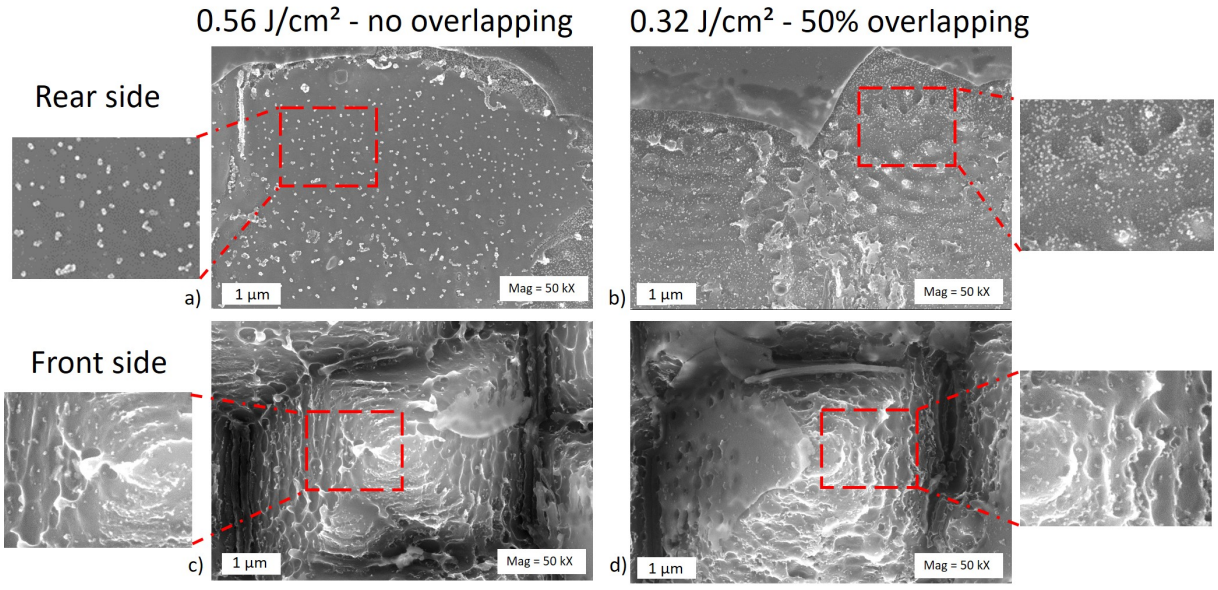

Figure 4.50: SEM images after deoxidation in $NaHF_2$ 0.16 M 1 min 30 and activation in $NaHF_2$ 0.16M + $PdSO_4$ 5.10^{-5}M 30 sec on rear and front sides for both optimized laser parameters.

In Figure 4.51, the rear side opened with laser parameters 1 and 2 has been deoxidized and activated with conditions described in case 1 but $NaHF_2$ 0.16 M has been replaced by HF 0.16 M. For laser parameters 1 (no overlapping), no Pd particles are observed in area 1 and 2 as it can be observed in Figure 4.51 a)). It indicates that 1 min 30 of deoxidation does not enable to etch sufficiently the SiO_x layer in these areas to expose the Si underlying and provide Pd deposition when NaH_2 0.16 M is replaced by HF 0.16 M. It confirms that $NaHF_2$ has an higher SiO_x etching rate which is consistent with conclusions in section 4.4.1. Furthermore, Pd particles are slightly smaller when $NaHF_2$ is used. It is easily remarkable by comparing Figure 4.50 b) and Figure 4.51 b). This is consistent with previous observations in section 4.4.2.

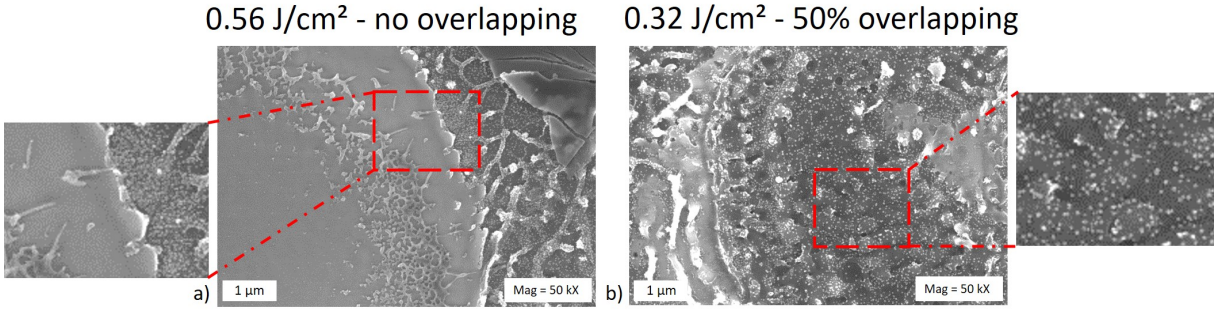

Figure 4.51: SEM images after deoxidation in HF 0.16 M 1 min 30 min and activation in HF 0.16 M + $PdSO_4$ 5.10^{-5} M 30 sec on the rear side polished side opened with laser parameters 1 a) and 2 b)

4.4.5 Conclusions

In this part, n-PERT precursors have been opened on both sides using optimized laser parameters identified in Chapter 3. Based on the results obtained in the study 1 on activation of n-type mirror polished Si wafers, various deoxidation/activation conditions have been tested on laser opened n-PERT precursors.

SEM characterization has revealed that Pd particles deposition depends on the surface morphology and composition after laser ablation. In particular, when laser spots do not overlap for ablation on the rear polished side, Pd activation is non-homogeneous in the different areas identified in Chapter 3 (area 1, 2 and 2_{bis}). The presence of remaining initial SiO_x dielectric layer in area 1 and 2, hinders the deposition of Pd particles if a suitable deoxidation is not performed. On the contrary, activation is homogeneous in area 2_{bis} as dielectric layers have been lifted-off. A non-homogeneous Pd deposition is expected to cause poor adherence of the further Ni seed layer. The deoxidation treatment to remove the SiO_x layer in areas 1 and 2 and provide homogeneous Pd particles deposition is too aggressive for SiO_xN_y layers and leads to significant parasitic plating. It appears that remaining SiO_x layers (deposited by PECVD) are etched in a randomly manner in fluoride media which is consistent with results in section 4.2.2. Thus, some Pd particles are deposited at some locations in areas 1 and 2 when a prior deoxidation treatment is performed which is expected to improve the adherence of further deposited Ni seed layer. In addition, Pd particles are smaller when a prior deoxidation is performed. Finally, deoxidation/activation have been optimized to be suitable for both sides surface morphology and composition obtained with laser parameters 1 and 2 (see Figure 4.50):

- Deoxidation: $NaHF_2$ 0.16 M 1 min 30
- Activation: $NaHF_2$ 0.16 M + $PdSO_4$ 5.10^{-5} M 30 seconds

On the front textured side and on the rear polished side laser opened with 50% overlapping, shorter deoxidation conditions are sufficient to obtain a satisfying Si surface activation. LIPSS on the front side and roughness on overlapped areas favored Pd particles deposition. The homogeneous activation on double impacted areas also confirms that dielectric layers have been efficiently removed. In these cases, the following conditions are suitable:

- Deoxidation: $NaHF_2$ 0.16 M 30 seconds
- Activation: $NaHF_2$ 0.16 M + $PdSO_4$ 5.10^{-5} M 30 seconds

Finally, the same optimized conditions using HF 0.16 M based solutions instead of $NaHF_2$ 0.16 M have been tested. The results confirm that SiO_x is etched slowly in HF fluoride media and that Pd particles are smaller when $NaHF_2$ solutions are used.

MEMENTO

PECVD SiO_x etching rate has been studied through ellipsometry measurements and a linear relationship has been highlighted between the etching rate and HF and $NaHF_2$ concentrations. To study the etching rate of anodic SiO_x layer, a methodology based on EIS has been established to obtain a standard reference graph which gives the anodic SiO_x thickness as a function of V_{fb}. The following observations have been made:

1. In both HF and $NaHF_2$, PECVD SiO_x layer is etched randomly, leading to porous material.
2. Etching rates of both PECVD and anodic SiO_x layers are found to be $\gg 2$ times faster in $NaHF_2$.

Etching rates of n-PERT precursors SiO_xN_y layers have been investigated in both HF and $NaHF_2$ through reflectivity measurements. A linear relationship has been established between etching rate and HF and $NaHF_2$ concentrations. Two major conclusions have been settled:

1. The SiO_xN_y layer on the front textured side is etched 3-4 times faster than on the rear polished side. This is mainly related to the higher density and refractive index of SiO_xN_y layer on the rear side.
2. At same fluoride media concentration, SiO_xN_y layers are etched at the same rates in HF and $NaHF_2$.

These results indicate a better selectivity of $NaHF_2$ towards SiO_x and SiO_xN_y layers. $NaHF_2$ is preferred to HF as immersion time can be reduced to etch SiO_x layer and limit SiO_xN_y layers damaging.

A statistical study of Pd galvanic displacement has been carried out. The influence of various parameters on Pd particles number and size has been highlighted such as immersion time, [$PdSO_4$], solution stirring, [HF] and [$NaHF_2$]. $NaHF_2$ provides smaller and more numerous particles compared to HF fluoride media. Among the conditions tested, the best ones are: $NaHF_2$ 0.16 M + $PdSO_4$ $2.5.10^{-4}$ M or 5.10^{-5} M 30 seconds, no solution stirring. Finally, deoxidation and activation on n-PERT samples opened with laser parameters optimized in Chapter 3 have been investigated. The non-homogeneous surface morphology and composition observed on the rear side when no spot overlapping is used highly impacts the Pd particles deposition. Remaining SiO_x layer in area 1 and 2 hinders the deposition of Pd particles. Unfortunately, the deoxidation step needed to completly remove this SiO_x layer is too aggressive towards SiO_xN_y and leads to important parasitic plating. However, deoxidation conditions have been found such as dielectric layers are preserved while some Pd particles are deposited randomly in area 1 and 2. Once again, $NaHF_2$ gives the best results with higher SiO_x etching rate and smaller Pd particles.

DEOXIDATION

- $NaHF_2$ 0.16 M 30 sec for front textured side and rear polished side laser opened with 50% overlapping
- $NaHF_2$ 0.16 M 1 min 30 for rear polished side laser opened with no overlapping

PD ACTIVATION

- $NaHF_2$ 0.16 M + $PdSO_4$ 5.10^{-5} M 30 sec, no solution stirring

Chapter 5

Nickel/Copper plating and n-PERT solar cells efficiencies

CONTENTS

5.1 Introduction

In the present Chapter, the impact of laser contact opening width and illumination conditions on the homogeneity of Ni electroless deposition on n-PERT precursors is highlighted. The adherence of Ni layers obtained using different electroless deposition conditions is also studied through Acoustic Picosecond Colored (APiC) technique. To assess the quality of the metallic contact between Si and Ni layer after annealing step, Transmission Line Measurements (TLM) are performed to determine the contact and line resistivities. Various annealing conditions are investigated with the purpose to achieve lowest contact resistivities. Concerning the Cu electrolytic deposition, the main purpose is to improve the experimental setup to contact efficiently the cells to the external circuit. Important adherence issues observed on the rear polished side after Ni/Cu plating and final annealing will lead to shift this work on double textured n-PERT precursors instead of textured/polished precursors used until now. That enables to obtain non delaminated Ni/Cu contacts and measure solar cells conversion efficiencies. Finally, optimized conditions for each plating process step determined in this thesis are implemented and the conversion efficiency of as-obtained cells is measured and compared to reference screen-printed cells. The impact of non-optimized laser ablation parameters and annealing conditions is also investigated.

5.2 State of the art

The different components of Ni electroless bath and the reactions involved have been introduced in the section 2.5.2. In this work, the Ni electroless bath used has a pH $\approx$ 10, so the reactions involved are:

Reduction of Ni ions [96]

$$Ni^{2+} + 2e^- = Ni \quad \text{(E = - 0.25 + 0.0295 log([Ni}^{2+}\text{]) (V/SHE)} \tag{5.1}$$

Oxidation of hypophosphite ions [96]

$$H_2PO_2^- + H_2O = HPO_3^{2-} + 2e^- + 3H^+ \quad \text{(E = - 0.323 - 0.0886 pH + 0.0295 log } (\frac{[HPO_3^{2-}]}{[H_2PO_2^-]}) \text{ (V/SHE))} \tag{5.2}$$

$$HPO_3^{2-} + H_2O = HPO_4^{2-} + 2e^- + 2H^+ \quad \text{(E = - 0.234 - 0.0591 pH + 0.0295 log } (\frac{[HPO_4^{2-}]}{[HPO_3^{2-}]}) \text{ (V/SHE))} \tag{5.3}$$

Parasitic reactions: hydrogen evolution and phosphorus incorporation [96])

$$2H^+ + 2e^- = H_2 \quad \text{(E = 0 - 0.0591 pH - 0.0295 log(P}_{H_2}\text{) (V/SHE))} \tag{5.4}$$

$$H_2PO_2^- + 2H^+ + e^- = P + 2H_2O \quad \text{(E = - 0.391 - 0.1182 pH + 0.0591 log ([H}_2PO_2^-\text{]) (V/SHE)} \tag{5.5}$$

Four main mechanisms have been proposed in literature to explain the elementary step behind the reduction of Ni ions and oxidation of hypophosphite ions [105]. First one is proposed by Brenner and Riddel [105] who postulate that reducting agent acts as atomic hydrogen. A second mechanism, named hydride transfer mechanism, is proposed by Hersh [105] who suggests that hypophosphite acts as a donor of hydride ions. The third mechanism, called electrochemical mechanism, has also been proposed by Brenner and Riddel [105]. The fourth mechanism established by Cavallotti and Salvago [105] is based on the coordination of hydroxyl ions with hexaquonickel ion.

Ni electroless deposition without prior Pd activation is possible on Si if the galvanic displacement reaction is allowed and initiates the deposition. That requires to work in alkaline bath [195], [196] to have a favorable position of $E_{(Ni^{2+}/Ni)}$ relatively to VB and CB of Si. In case of Ni bath having pH ≥ 10, native SiO_x film tends to be dissolved into soluble silicates H_2SiO_3, $HSiO_3^-$ and SiO_3^{2-} [92] and a displacement reaction between Si surface and Ni ions can occurs leading to spontaneous initiation of Ni deposition. This specific case can only occur on n-type Si, where mobile electrons are the majority carriers and can be transferred to the solution [197]. It is also possible to add a fluoride species (NH_4F) to the bath to continuously etch the native oxide formed at Si surface.

However, Ni seed layers obtained without prior Pd activation are less adherent [103] and deposition rates are significantly lower. Oxidation of hypophosphite ions can be enhanced by catalytic activity of Pd particles, increasing Ni electroless deposition rate. Some authors have found lower deposition rates on p-type surfaces compared to n-type ones [198]. Ni electroless deposition can be performed either in acidic or alkaline bath but alkaline baths are generally preferred for the following reasons:

- Ni electroless deposition rate is increased with pH [199]
- Smaller Ni nuclei are observed thanks to a better hypophosphite oxidation leading to an higher nucleation rate [200]. Smaller Ni particles are desirable to improve Ni film adherence.
- Higher pH decreases the phosphorus incorporation into the Ni layer which reduces the Ni film resistivity [106], [199]. It has also been demonstrated that P atoms could segregate at the nickel silicide/Si interface during annealing process and act as donor impurities which reduces the contact resistivity [201]. However, an increased phosphorus incorporation improves the barrier property towards Cu diffusion [202] and reduces the internal stress into Ni layer. Consequently, an appropriate balance of the phosphorus content is needed to promote low Ni film resistivity while maintaining good Cu diffusion barrier properties.

A schematic representation of the Ni deposition mechanism is given in Figure 5.1.

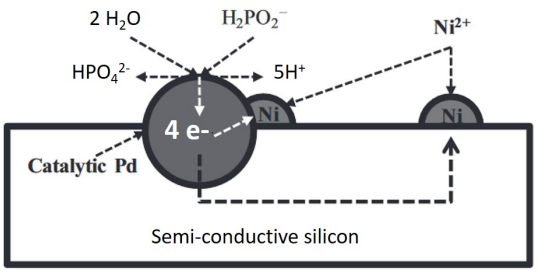

Figure 5.1: Schematic representation of nucleation and growth process of Ni layer electrolessly deposited on Pd-activated Si surface (from [203]).

The catalytic activity of Pd particles provides the oxidation of hypophosphite ions according to reactions 5.2 and 5.3 which releases four electrons. As silicon is a semiconductive material, electrons can flow on the surface and reduce the Ni^{2+} ions at various surface locations according to reaction 5.1. However, at the initial stages of the process, Ni nucleation is more likely to occur at the vicinity of Pd particles. As a result, a

high density of dispersed Pd particles will lead to a Ni layer growth similar to a layer-by-layer model rather than a island model, which improves Ni film adherence.

Philipsen et al. have worked on electrodeposition of Ni layer on Si surface and have demonstrated that hemispherical nuclei are formed on Si-H terminated surfaces while spherical nuclei are formed on oxidized surfaces [204]. Spherical nuclei are not advantageous for Ni film adherence due to less contact between Ni and Si surface compared to hemispherical shape. As a consequence, the formation of native SiO_x on Si surface during the Ni electroless deposition is a significant issue as it will block the Ni deposition [114] in the worst case or lead to spherical Ni nuclei in the best case.

Ni electroless films are amorphous when phosphorus proportion is higher than $6.5\%_{(wt/wt)}$ [201] but a thermal treatment above $330°C$ leads to semi-crystalline face centered cubic Ni interspersed with intermetallic compounds such as Ni_3P [106]. Ni seed layer acts as a barrier for Cu diffusion into Si and Ni-P allow electrolessly deposited is a most effective barrier to prevent Cu diffusion compared to electrolytically deposited Ni layer. It can be explained by the formation of intermetallic NiP compound able to block the Cu diffusion path through Ni layer [202]. In contact with Si surface, heat treatment leads to Ni/Si interdiffusion and formation of nickel silicides Ni_xSi_y. Silicide formation on solar cells from plated Ni layers is still not completely understood. Based on references [13], [92], [114], the following temperature ranges can be proposed: Ni_2Si is formed between 200 and $350°C$, NiSi between 400 and $530°C$ and $NiSi_2$ above $650°C$. The objectives of the annealing step are the following:

- Obtain the NiSi phase which demonstrates the lower contact resistivity [114];
- The nickel silicide layer formed should be preferably less than 0.1 µm to avoid shunt formation [198]. It has been demonstrated that the diffusion length of Ni depends on the initial Ni layer thickness [205];
- Obtain an uniform nickel silicide layer to reduce the contact resistivity and improve the metallic contact adherence. Unfortunately, SiO_x presence at Ni/Si interface is critical as it blocks the Ni/Si interdiffusion, leading to unbalanced Ni/Si interdiffusion velocities. As a result, unexpected Ni_xSi_y phases can be observed and several phases can be formed at the same time. Kirkendall voids can be also formed between Ni and Ni_xSi_y layer leading to adherence issues [133].

After Ni seed layer deposition, a suitable thick conductive layer is needed to reduced line resistance of the metallized grid. Copper is a good candidate due to its high conductivity and low price. The main issue is the Cu ability to easily diffuse into Si as a positively charged ion Cu^+. Cu diffusion coefficient in Si increases with the temperature and depends on the Si dopant type. Indeed, diffusion in p-type Si is reduced due to the attraction between positively charged Cu^+ and negatively charged B^- ions [202].

5.3 Ni electroless deposition: homogeneity issues.

5.3.1 Impact of laser opened area geometry on Ni thickness.

This study has been realized early in this thesis. At that moment, only a UV-ns laser was available to open the dielectric layers and deoxidation and Pd activation conditions were not optimized. However, this part deals with the impact of

line width on Ni homogeneity and it is reasonable to consider that results will be applicable to optimized conditions determined in previous Chapters (identical kinetic ratios for Ni electroless deposition between the different line width).

The dielectric layers of n-PERT precursors have been laser opened on both sides with a UV-ns laser at INL (Institut de Nanotechnologies de Lyon) using a F_{peak} = 1.6 J/cm^2 and 50% overlapping. As represented in Figure 5.2, a pattern has been designed with four different line widths. One of them is related to finger width and another one to busbar width typically used.

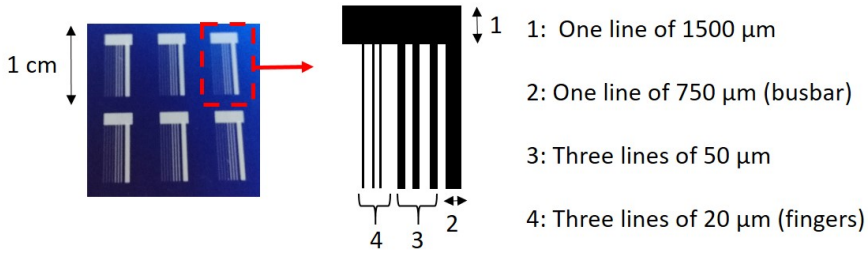

Figure 5.2: Picture of pattern for laser ablation: the different line widths are detailed next to the picture.

Samples are then immersed 30 seconds in activation solution HF 1%$_{wt}$ + 1.25.10^{-4} M $PdSO_4$ without stirring before 3, 5, 7 or 9 minutes immersion in the Ni electroless bath detailed below.

NICKEL ELECTROLESS BATH

Nickel electroless deposition is performed using the Enthone commercial bath "Enplate Al-100". As this bath is dedicated to Ni deposition on aluminum (indeed there is no commercial bath for Ni electroless deposition on Si), the quantities of each component have been adapted for our application. Consequently, 3 components are mixed in water according to the quantities depicted in Table 5.1. The bath is alkaline (pH $\approx$ 10) and is agitated during the make up and experiments (200 rpm). Once the components mixed up, the solution is heated at 40°C in a water bath. The pH solution is controlled regularly to verify that it does not fall below 9.5. The bath is kept maximum two days to ensure good Ni electroless deposition conditions for all experiments. **The conditions detailed above remained unchanged in this thesis work.**

Table 5.1: Made up of Enplate Al 100 Ni electroless bath from Enthone

Name	Quantity	Chemical species
Enplate Al-100 A	70 mL/L	Complexing agent (tetrapotassium pyrophosphate) + Nickel ions (nickel bi(sulfamidate)) + ammoniac
Enplate Al-100 C	150 mL/L	Reducing agent (sodium hypophosphite)
Enplate Al-100 Stabilizer	0.8 mL/L	Stabilizing agent (lead di(acetate))

On both sides, sectional SEM characterization has been performed to measure the Ni thickness after various immersion times in Ni electroless bath and results are reported in Table 5.2. For each sample, four SEM images are realized and Ni thickness is measured at 3 or 4 locations on each image to calculate the deposition rates. SEM images after 7 minutes immersion are shown in Figure 5.3 as an example.

Table 5.2: Ni thicknesses on both sides for different line widths and calculated deposition rates.

	Line width (µm)	Nickel thickness (nm)				Deposition rates ($nm.min^{-1}$)
		3 min	5 min	7 min	9 min	
4*Rear side	20	146 ± 20	287 ± 47	436 ± 41	509 ± 64	57.9
	50	151 ± 8	245 ± 8	336 ± 22	431 ± 32	48.0
	750	123 ± 7	209 ± 6	306 ± 18	369 ± 20	41.6
	1500	95 ± 4	187 ± 8	284 ± 11	332 ± 14	37.8
4*Front side	20	122 ± 18	241 ± 21	345 ± 30	453 ± 45	49.6
	50	104 ± 14	192 ± 9	295 ± 10	386 ± 12	40.2
	750	69 ± 5	139 ± 7	200 ± 8	262 ± 12	27.7
	1500	62 ± 4	113 ± 6	159 ± 18	208 ±18	22.9

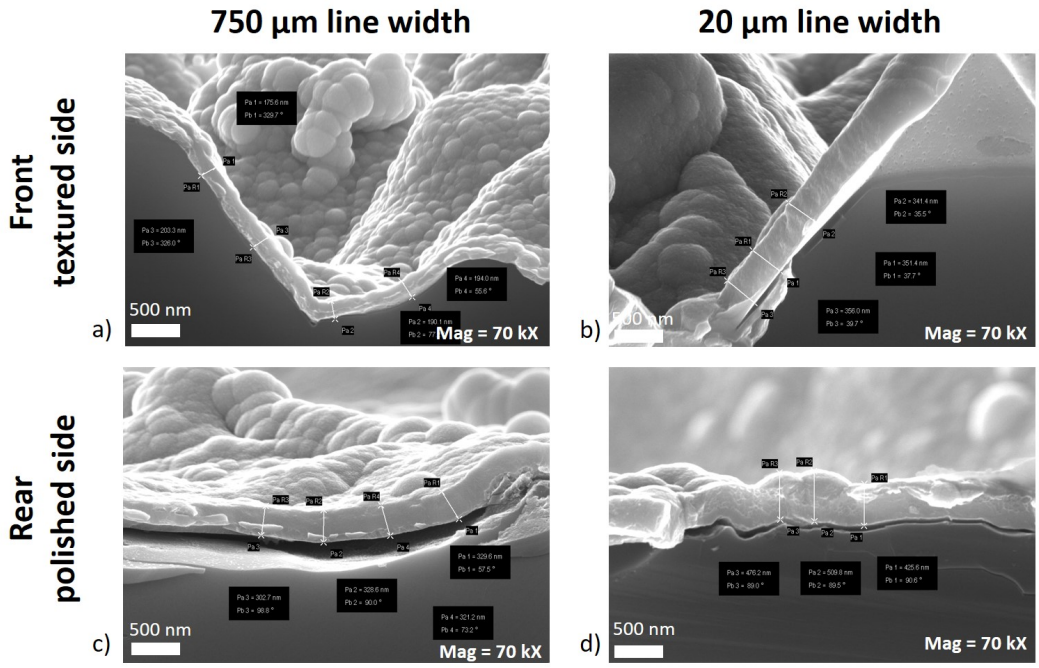

Figure 5.3: Sectional SEM images after 7 minutes Ni electroless deposition on both sides for 750 µm line width (a) and c)) and 20 µm line width (b) and d)).

According to the results in Table 5.2, two main observations can be made:

- On both sides, the wider the line width, the lower the Ni deposition rate is (comparison of Figure 5.3 a)-b) or c)-d)). This is consistent with literature [118] and can be explained by the geometry of narrow line width, enabling the mass transfer of species in a semi-cylindrical volume. The ratio of deposition rate on fingers (20 µm line width) to the one on busbars (750 µm line width) is equal to 1.8 for the front side and 1.4 for the rear side. To limit Ni thickness difference between fingers and busbars and reduce the risk of junction shunting during annealing, a busbarless metallization pattern seems more suitable. Another alternative could be to performe laser ablation of busbars with several fingers not in contact from each other but close enough to provide coalescence of nickel clusters from each finger during the deposition process.

- Ni deposition rate is slower on the front textured side than on the rear polished side (comparison of Figure 5.3 a)-c) or b)-d)). Deposition rate ratios of rear side on front side are equal to 1.2, 1.2, 1.5 and 1.6 for 20 µm, 50 µm, 750 µm and 1500 µm line width respectively. As nickel ions require electrons to be reduced on Si surface, the p^+ front side may be disfavoured compared to the n^+ rear side. However, subsequent experiments on Ni deposition have brought out reproducibility issues. With same process conditions before Ni deposition, significant Ni thickness variations are observed on the front textured side (sometimes no Ni is deposited at all). These issues have not been observed on the rear side. As already mentioned, holes are majority carriers on the front side and can disfavour Ni deposition so it is probable that fume-hood and lab light enhance this behavior thought photogeneration of holes. This point is investigated in the next part.

5.3.2 Effect of illumination conditions on Ni electroless deposition.

These experiments have been realized before optimization of laser parameters and deoxidation/activation conditions.

Twelve 10 × 5 mm^2 n-PERT samples have been used in this work. A laser ablation using a UV-ps laser with F_{peak} = 0.72 J/cm^2 and 50 % overlapping has been performed on both sides in order to obtain a 1 cm line with 750 µm width (busbar geometry). 9 samples have been immersed 30 seconds in HF $1\%_{wt}$ + $PdSO_4$ 5.10^{-5} M and 3 samples have only been deoxidized 30 seconds in HF $1\%_{wt}$ (no activation). Samples have been finally immersed 5 minutes in the Ni bath under various illumination conditions as reported in Table 5.3. Illumination was performed either on rear n^+ or front p^+ side using a lamp (power 20 or 35 W, 30 cm distance). The impact of various solution agitation conditions has also been investigated (if not mentioned, stirring conditions are equal to 200 rpm). Pictures of the experimental setup are shown in Figure 5.4.

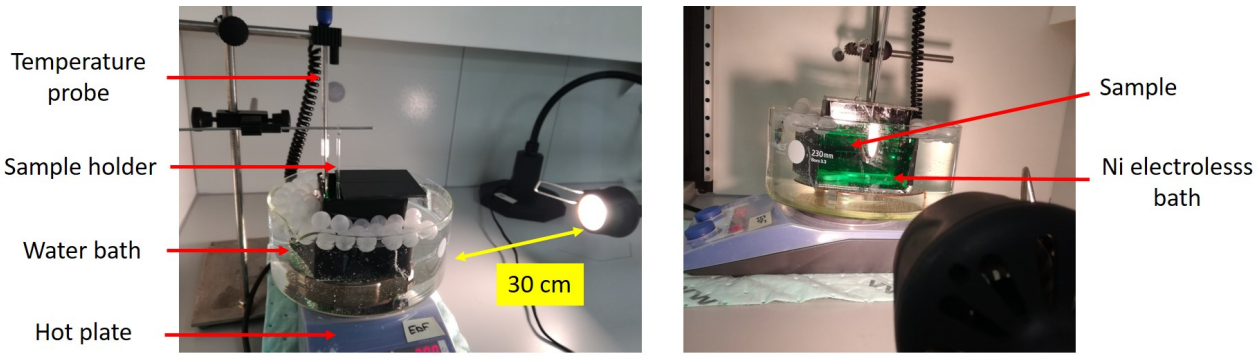

Figure 5.4: Experimental setup used to assess the impact of illumination on Ni electroless deposition.

For each sample, Ni thickness has been measured on both sides using X-ray fluorescence (XRF) (simpler and faster than SEM). XRF tool has been calibrated using samples in section 5.3.1 for which the Ni thicknesses have been accurately determined with SEM. Therefore, the twelve samples have been analysed by XRF after Ni deposition to determined the Ni thickness displayed in Table 5.3. On each sample, 4 measurements are performed at various locations to evaluate the homogeneity along the busbar. SEM images of samples 1, 3 and 10 are given in Figure 5.5 to illustrate the results analysis.

Table 5.3: Ni layers thicknesses after 5 minutes deposition under various illumination conditions.

	Sample	Illumination conditions	Front side (p^+) Ni thickness (nm)	Rear side (n^+) Ni thickness (nm)
Pd activation	1	Dark	262 ± 40	290 ± 16
	2	Fume-hood	few Ni clusters	309 ± 5
	3	20 W (n^+ side)	0	313 ± 8
	4	20 W (p^+ side)	0	287 ± 15
	5	35 W (n^+ side)	0	300 ± 6
	6	35 W (p^+ side)	0	281 ± 38
	7	Dark - no stirring	185 ± 32	282 ± 38
	8	Dark - 300 rpm	80 ± 35	110 ± 126
	9	Dark - 400 rpm	0	0
No Pd activation	10	Dark	0	0
	11	35 W (n^+ side)	0	19.7 ± 20.6
	12	35 W (p^+ side)	0	55.6 ± 65.0

Analysis of activated samples (1 to 9):

In dark conditions, results in Table 5.3 indicate that Ni is properly deposited on both sides with similar thicknesses (sample 1, see Figure 5.5 a), b), c) and d)). Ni seed layer completely covers the Si surface and no cracks are observed. This is important to prevent further Cu diffusion into Si. The doping type does not seem to impact the Ni deposition rate in dark conditions. However, it appears that the speed of solution stirring must be carefully chosen. When the solution is not agitated, Ni layer is thinner on both sides (sample 7) than with 200 rpm stirring (sample 1), which is probably due to the depletion of reducing agent and nickel ions at the surface without stirring. Ni deposition rate is thus decreased due to limited species diffusion. When solution stirring is too fast, Ni layers are thinner on both sides (samples 8). No nickel is observed for 400 rpm on sample 9. In these cases, Ni deposition is not limited by species diffusion but by the mechanical effect of stirring which removes Ni clusters during deposition. A soft stirring at 200 rpm is the most suitable.

When samples are illuminated, Ni deposition only occurs on the rear side (n^+) (samples 2 to 6, Figure 5.5 e) and f)). Photogenerated charges carriers are separated by the p/n junction and holes diffuse towards p^+ area (front side). Illumination also reduces the band bending in the semiconductor which favors the charges transfers. Two phenomena avoiding Ni deposition can be proposed:

1. Holes on the p^+ side recombine with electrons released by the oxidation of the reducing agent. These electrons are thus not available anymore for Ni^{2+} ions reduction;
2. Holes on the p^+ side serve for Ni or Pd particles dissolution. Indeed, in Figure 5.5 e) Pd is not detected in EDS. However, Pd is sometimes not detected in EDS when particles are very small (limit of detection). It would be interesting in a further work to perform an analytical analysis of Ni bath for samples 2 to 6 in order to investigate the presence of Pd ions.

For their part, photogenerated electrons diffuse towards the n^+ side (rear side) where they can potentially by involved into Ni ions reduction. However, Ni thicknesses on the rear side are very similar whatever the illumination conditions used. It suggests that Ni deposition is limited by the mass transfer on this side. It can also be noticed that no differences are observed when samples are illuminated on the n^+ or p^+ side.

Some Ni clusters are observed on sample 2 suggesting that fume-hood light disfavours Ni deposition but does not completely prevent it. That could explain the reproducibility issues observed on previous experiments as well as the differences of Ni thicknesses on front and rear sides.

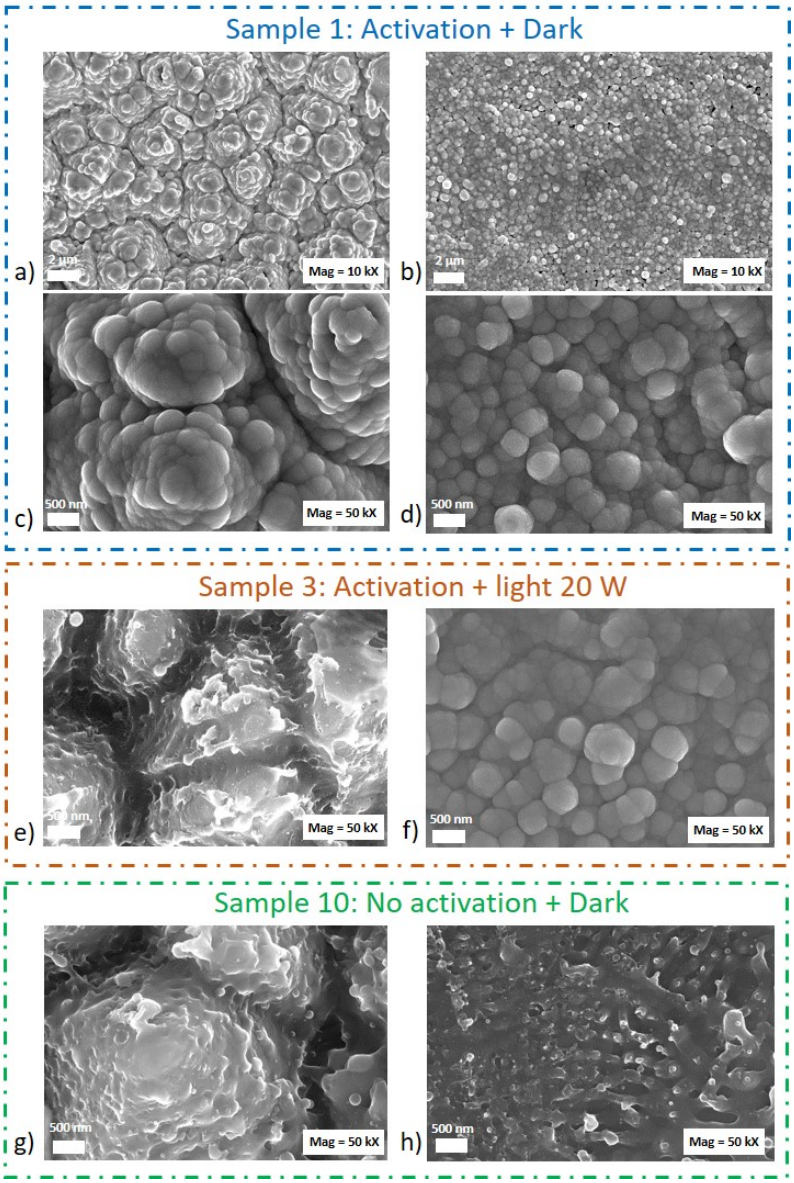

Figure 5.5: SEM images on front and rear side of sample 1, 3 and 10 after Ni deposition.

Analysis of non activated samples (10 to 12):

Without Pd activation, thee is no Ni deposition on both sides in dark (sample 10, Figure 5.5 g) and h)) which confirms the necessity to activate the Si surface with Pd particles. It is not surprising to observe that illumination does not promote Ni deposition on the p^+ front side. On the contrary, Ni is detected by XRF measurements on the rear n^+ side of illuminated samples (samples 11 and 12). However, Ni deposition is thin and not homogeneous, as attested by the important standard deviations for these both samples in Table 5.3. On SEM images (not shown here), some parts of the samples are not metallized.

5.3.3 Conclusions and perspectives

Ni electroless deposition rate is impacted by the geometry of laser opened area. Narrow opened areas are metallized faster than larger ones. Therefore, the deposition rate (nm/min) is around 1.6 times higher on fingers (20 µm width) than on busbars (750 µm width). To tackle this homogeneity issue between fingers and busbars, busbarless metallization pattern could be a great alternative. Laser ablation of busbars with several fingers having a suitable spacing from each other could be also considered.

Ni electroless deposition on the p^+ doped Si surface (front textured side) is highly affected by illumination conditions. This is due to the diffusion of photogenerated holes to p^+ side of the cell. A reproducible deposition on the front textured side p^+ with a similar Ni thickness than on the rear polished side n^+ requires to perform Ni electroless deposition in dark. Stirring must be carefully chosen to provide constant regeneration of solution species at the surface without inducing a detrimental mechanical effect.

In the following of this work, it would be interesting to investigate the impact of bath components concentrations, pH and temperature on the Ni electroless deposition rate, the morphology of Ni clusters and phosphorus incorporation.

5.4 Ni electroless deposition: adherence issues.

5.4.1 Experimental part

This study has been carried out before optimization of laser parameters and deoxidation/activation conditions. Moreover, the necessity to perform Ni electroless deposition in dark conditions has not yet been highlighted.

This work has been realized in collaboration with the Fraunhofer ISE in order to compare the adherence and homogeneity of three different Ni electroless deposition processes. Five 156 $\times$ 156 mm^2 textured/polished n-PERT precursors have been laser opened on both sides at Fraunhofer ISE using a UV-ps laser with a F_{peak} = 0.448 J/cm^2 and without spot overlapping (H-pattern: 5 busbars of 500 µm + 120 fingers, see Figure 5.6). It appears that dielectric layers have not been properly removed at some sample locations, indicating that a slightly higher F_{peak} should have been used as demonstrated in the Chapter 3 (see optimized laser parameters in the section 3.7.3). Ni seed layers have been then deposited on both sides, with the aim to obtain a thickness $\approx$ 500 nm, with one of the electroless processes below:

- Ni electroless deposition performed at IPVF (2 samples)
- Ni electroless deposition performed at Fraunhofer ISE (2 samples)
- Ni LIP deposition performed at Frauhofer ISE (1 sample)

For concerns of confidentiality, details of processes performed at Fraunhofer ISE were not communicated. At IPVF, samples have been immersed 1 minute in HF $1\%_{(wt/wt)}$ + $PdSO_4$ $1.25.10^{-4}$ M before 7 minutes immersion in Ni electroless bath detailed above (see Table 5.1). Solution is not agitated and illumination is not controlled (fume-hood light). For Ni electroless deposition at IPVF and Fraunhofer ISE, two samples have been metallized: one is not annealed and the other is annealed during 3 minutes at 230°C either at IPVF or Fraunhofer ISE. The experimental procedure is summarized in Table 5.4.

Table 5.4: Experimental procedure for metallization of 156 × 156 mm^2 textured/polished n-PERT precursors using three different Ni deposition processes.

Sample name	Step 1: Laser ablation	Step 2: Ni deposition	Step 3: Annealing
IPVF el1	F_{peak} = 0.448 J/cm^2 No overlapping Both sides opened	Electroless deposition at IPVF	No
IPVF el2		Electroless deposition at IPVF	Yes
ISE el1		Electroless deposition at ISE	No
ISE el2		Electroless deposition at ISE	Yes
LIP		LIP deposition at ISE	No

A picture of front and rear sides for IPVF sample el1 is given in Figure 5.6. Adherence issues are already visible at naked eye on the rear polished side.

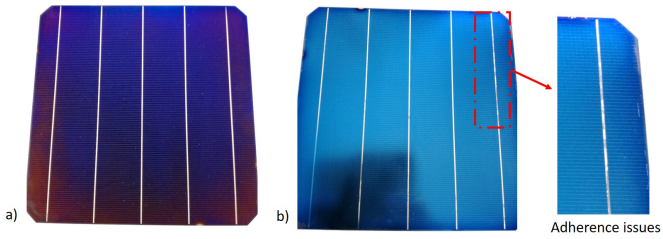

Figure 5.6: Picture of sample IPVF el1 after Ni deposition: a) front textured side, b) rear polished side.

Non annealed samples have been characterized by XRF and APiC measurements to assess the homogeneity of Ni layers and the adherence at Ni/Si interface respectively. 13 XRF measurements have been performed along each busbar on both sides as schematized in Figure 5.7 a). 3 APiC measurements have been performed in the central busbar as shown in Figure 5.7 b). CLSM images have been also realized to observe the surface morphology. For their poart, annealed samples have been characterized by APiC measurements to compare the adherence of Ni layers for both Ni electroless processes. Measurements are performed at various locations on the samples as schematized in Figure 5.7 c).

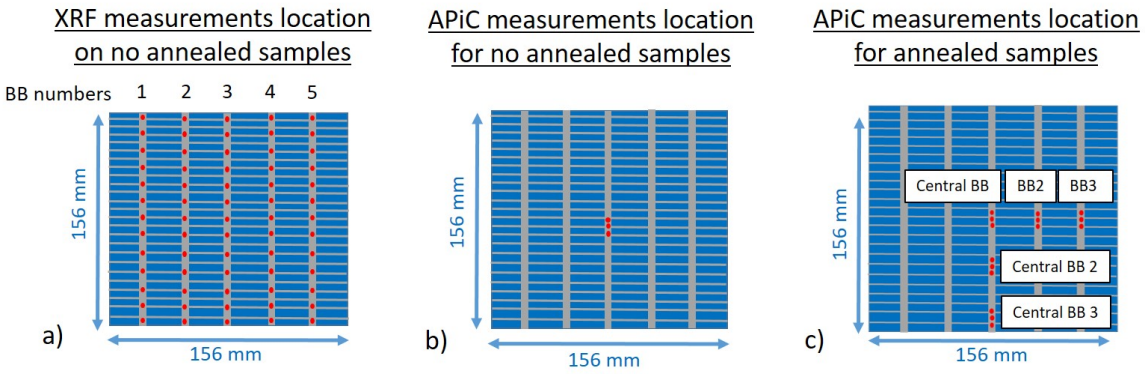

Figure 5.7: Location of a) XRF measurements on non annealed samples, b) APiC measurements on non annealed samples, c) APiC measurements on annealed samples.

Most techniques to measure the adherence of thin metallic films are destructive as they imply the mechanical removal of the film. The APiC method is a contactless and non destructive technique enabling to compare adherence of a thin film relatively to a reference (semi-quantitative). Acoustic waves are generated

with a picosecond laser beam and their reflections at thin film/substrate interface are analysed which gives information on the interface quality. The method is detailed in Appendix H.

5.4.2 Results on non annealed samples

CLSM characterization

Images have been realized on the rear side of samples IPVF el1, ISE el1 and LIP in the center of the wafer and at a BB-finger intersection. Images are displayed in Figure 5.8.

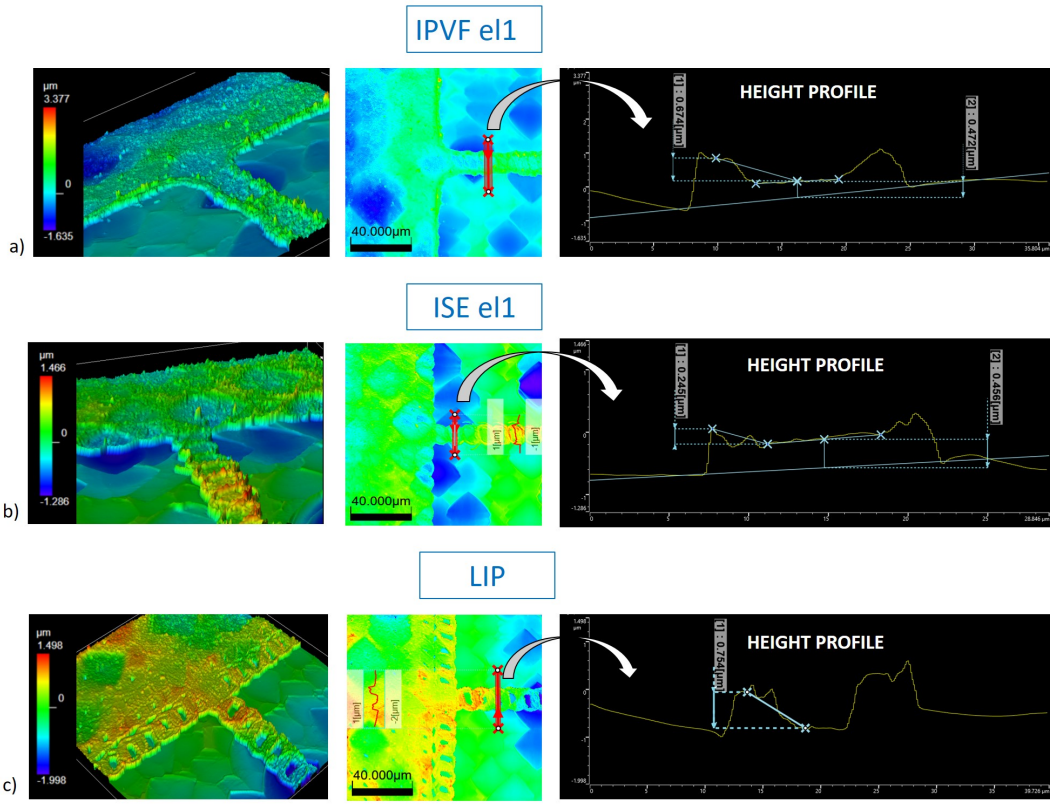

Figure 5.8: CLSM images on the rear side of non annealed samples a) IPVF el1, b) ISE el1, c) LIP. For each sample, 3D and 2D height intensity images are shown as well the height profile for a finger is displayed.

On the three samples, Ni deposition is thicker on the border of fingers (border effect). This effect is more significant for LIP sample, while ISE el1 sample shows the less important border effect. These differences are probably due to different operating conditions between the three processes.

As demonstrated in the Chapter 3, laser ablation with F_{peak} = 0.448 J/cm^2 and no spot overlapping leads to different areas (1, 2 and 2_{bis}). It has been demonstrated that during the activation step, Pd particles are preferably deposited on area 2_{bis} (external corona of laser opened area). In area 1 and 2 (center of laser spot), remaining SiO_x layers are not easily removed in fluoride media and Pd particles deposition is hindered. As Ni electroless deposition is promoted by the catalytic activity of Pd particles, this specific morphology after laser ablation and Pd activation can explain the morphology of Ni seed layers on fingers. Even if Ni could be deposited in the center of laser opened areas, it is likely to observe adherence issues.

XRF characterization

Ni thicknesses are reported in the Table 5.5 and 5.6 for the rear and front side respectively. The higher standard deviations observed for LIP sample indicate that Ni thickness homogeneity along a busbar and from one busbar to another is worst with this process in comparison with both electroless processes. With LIP process, Ni deposition is enhanced by sample illumination so the non homogeneity observed could be due to uneven light power dispersion on the sample during experiments.

Both IPVF el1 and LIP samples demonstrate Ni thicknesses about 2 times higher on the rear side than on the front side. As a reminder, Ni electroless deposition at IPVF has not been performed in dark conditions and as explained in section 5.3.2, light tends to inhibit Ni deposition. The detrimental effect of light on the p^+ front side could therefore explain the higher Ni thicknesses observed on the n^+ rear side. These results confirm the importance to realize Ni electroless deposition in dark conditions. Ni electroless deposition realized at Fraunhofer ISE leads to the best thicknesses homogeneity between front and rear side.

Table 5.5: Results of XRF measurements on the rear side of IPVF el1, ISE el1 and LIP metallized samples.

Samples	**Ni average thicknesses (nm) for each busbar (rear side)**					**Average**
	Busbar n°1	*Busbar n°2*	*Busbar n°3*	*Busbar n°4*	*Busbar n°5*	
IPVF el 1	473 ± 35	407 ± 26	431 ± 43	421 ± 33	433 ± 22	433 ± 32
ISE el1	514 ± 25	542 ± 21	541 ± 14	540 ± 14	534 ± 16	534 ± 18
LIP	496 ± 36	649 ± 128	482 ± 66	670 ± 158	598 ± 46	579 ± 87

Table 5.6: Results of XRF measurements on the front side of IPVF el1, ISE el1 and LIP metallized samples.

Samples	**Ni average thicknesses (nm) for each busbar (front side)**					**Average**
	Busbar n°1	*Busbar n°2*	*Busbar n°3*	*Busbar n°4*	*Busbar n°5*	
IPVF el 1	231 ± 102	224 ± 36	227 ± 36	182 ± 30	168 ± 32	206 ± 47
ISE el1	624 ± 46	655 ± 16	669 ± 15	655 ± 17	656 ± 18	652 ± 23
LIP	282 ± 54	252 ± 38	345 ± 41	298 ± 72	266 ± 51	289 ± 51

APiC characterization

APiC spectra obtained on the rear side for IPVF el1, ISE el1 and LIP samples are displayed in Figure 5.9. The corresponding echo amplitudes and shapes are summarized in Table 5.7.

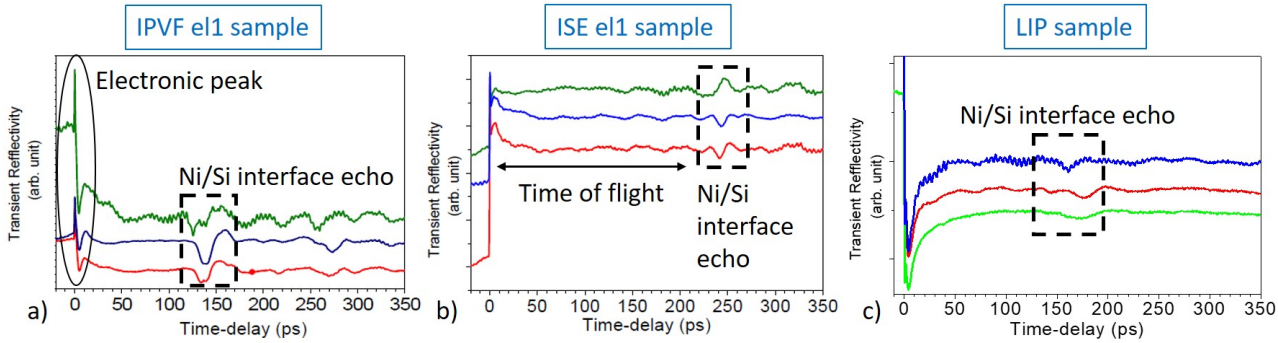

Figure 5.9: APiC spectra on rear polished side for non annealed samples a) IPVF el1, b) ISE el1, c) LIP.

Table 5.7: Echoes amplitudes and shapes on the rear side of IPVF el1, ISE el1 and LIP samples.

	IPVF el1			ISE el1			LIP		
Echo amplitude	85	100	130	64	74	46	23.2	16.8	25
Echo shape	bipolar	down	bipolar	down	up	down	down	down	down

Electronic peaks are difficult to interpret but their sign is generally related to the surface chemistry. Therefore, the opposite electronic peak signs observed for the three samples suggest different surface chemistry of the Ni layers. It is maybe related to various components in Ni electroless baths used, leading to different chemical bonds at Ni surface. Time of flight for echoes observed in Figure 5.9 have been analysed and the corresponding Ni thicknesses (not shown here) determined by equation H.1 are similar to the ones measured by XRF. It supports that these echos correspond to acoustic wave reflection at Ni/Si interface. In Table 5.7, the lowest echoes amplitudes are observed for LIP sample, meaning that this process gives the best adherence at Ni/Si interface. On the contrary, Ni electroless deposition process at IPVF leads to the poorest adherence as echoes amplitude are the highest observed. The asymmetric bipolar echo shape for IPVF el1 sample suggests the presence of an interfacial layer between which could correspond to the presence of Pd particles between Ni layer and Si surface. Indeed, a numerical modelling introducing a 40 nm thick layer having a 12 g.cm^{-3} density (Pd density) gives a great agreement with experiments as shown in Figure 5.10.

	Simulation parameters		
Layer	**Thickness (nm)**	**Mass density (g.cm-3)**	**Sound velocity (m/s)**
Ni	390	5,00	6050
Pd	40	12,00	5000
Si	infinite	2,33	8430

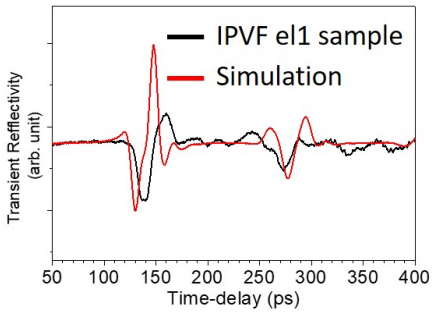

Figure 5.10: Simulation of echo shape with an interfacial Pd layer at Ni/Si interface.

Results on the front textured sides have not been presented here but observations are similar except that echoes amplitude are lower, indicating a better adherence in comparison to the rear polished side. This is consistent as pyramids and LIPSS observed after laser ablation are beneficial for adherence of the deposited nickel layer.

5.4.3 Results on annealed samples

APiC measurements have been then performed on annealed samples IPVF el2 and ISE el2. Spectra obtained for measurements on the central busbars are displayed in Figure 5.11 and the corresponding echoes shapes and amplitudes are summarized in the Table 5.8. Results on the front side are more difficult to analyse due to signal noise induced by optical diffusion on pyramids but identified echoes have been framed in Figure 5.11 b) and d) to not be confounded with the signal noise.

During annealing, the interdiffusion of nickel and silicon leads to the formation of a nickel silicide layer

Ni_xSi_y. As a result, it is expected to observe two echoes on APiC spectra: one corresponding to the reflection at Ni/Ni_xSi_y interface and the other one to the reflection at Ni_xSi_y/Si interface. However, a single echo for each measurement has been identified on both sides as shown in Figure 5.11. Even for measurements at longer time delays (not shown here), a second echo has not been detected. Two hypothesis can be raised to explain the absence of the second echo corresponding to Ni_xSi_y/Si interface:

- HYPOTHESIS 1: The adherence at Ni_xSi_y/Si is good, implying a low amplitude of the corresponding echo. Thus, the second echo can not be discerned from signal noise;
- HYPOTHESIS 2: The formed Ni_xSi_y layer is very thin so that the second echo related to Ni_xSi_y/Si interface appears at similar time delays than the first echo related to Ni/Ni_xSi_y interface. Both echoes are "mixed" and a single echo is observed.

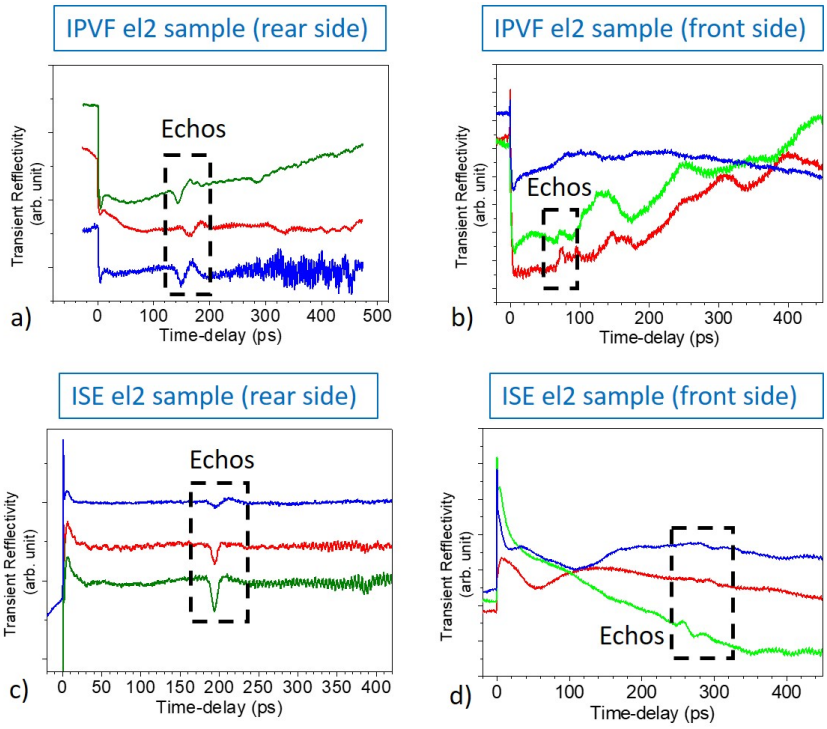

Figure 5.11: APiC spectra obtained on the central busbars of annealed samples a) IPVF el2 rear side, b) IPVF el2 front side, c) ISE el2 rear side, d) ISE el2 front side.

Table 5.8: Echoes amplitudes and shapes for annealed samples IPVF el2 and ISE el2.

	IPVF el2			ISE el2		
Echo amplitude (rear side)	39	66	103	23	36	11.5
Echo shape (rear side)	bipolar	bipolar	bipolar	down	down	bipolar
Echo amplitude (front side)	14	7	n.a	6	16	7
Echo shape (front side)	up	up	n.a	up	bipolar	bipolar

Comparison of non annealed and annealed samples:

For sample IPVF el2, echoes amplitudes on the rear side are lower compared to non annealed sample IPVF el1 (comparison of Table 5.7 and 5.8). The same observation is realized for ISE samples. The reduction

of echo amplitude is linked to the reduction of acoustic waves at the encountered interface and suggests a better adherence. By providing Ni/Si interdiffusion and formation of Ni_xSi_y layer, annealing is supposed to improve adherence at the Ni_xSi_y/Si interface. As echoes amplitudes are reduced after annealing, it is likely that they correspond to reflection at Ni_xSi_y/Si interface and thus hypothesis 2 is the most probable.

For ISE el2 (annealed sample) echoes are observed at lower time delays than ISE el1 (non annealed samples) which is consistent with smaller Ni thicknesses after annealing due to interdiffusion process. However, echoes for IPVF el1 and IPVF el2 samples appear at similar times delays suggesting that interdiffusion process is less efficient. It could be related to the poor adherence at Ni/Si interface observed before annealing as lack of contact between Ni and Si surface will hinder atoms interdiffusion.

Comparison between ISE el2 and IPVF el2 samples:

The lower echoes amplitudes observed for sample ISE el2 compared to sample IPVF el2 indicate a better adherence with Ni electroless deposition process performed at Fraunhofer ISE. Echoes shapes are also thinner for ISE el2 sample which suggests a more abrupt interface. The poor adherence observed on IPVF samples likely comes from inefficient Ni/Si interdiffusion. Some measurements on sample IPVF el2 (not shown here) even show very high echo amplitude (> 300 for instance) which could correspond to locations where Ni or Ni/Ni_xSi_y stack have been delaminated.

Despite the complexity of the signal on textured surfaces, lower echoes amplitudes have been observed compared to the rear side which indicates a better adherence. As already mentioned, this is not surprising as pyramids and LIPSS on the front side are beneficial for Ni layer adherence. Amplitudes are similar for both electroless processes at IPVF and ISE suggesting that adherence properties are similar on the front textured side with both processes.

Measurements along the busbsars:

The comparison of results obtained at different parts of samples (see Figure 5.7 c)) is not shown here but revealed a large dispersion of echoes amplitudes and times of flight, in particular for IPVF el2 sample. This indicates that Ni/Si interdiffusion process is not uniform along a busbar.

5.4.4 Conclusions and perspectives

The specific surface morphology and composition observed after laser ablation on the rear polished side with no overlapping (area 1, 2 and 2_{bis}) leads to non homogeneous Ni electroless deposition. A border effect is observed due to higher Pd particles density in laser opened area 2_{bis} identified previously. In laser opened area 1 and 2, remaining SiO_x layers can hinder Ni deposition and probably leads to poor adherence of Ni seed layer.

LIP and Ni electroless deposition performed at IPVF have demonstrated Ni thicknesses about 2 times lower on the p^+ front side probably due to detrimental effect of light identified before. Ni electroless deposition process performed at Fraunhofer ISE is the best one in terms of Ni thickness homogeneity between

rear and front side and LIP process shows the best adherence at Ni/Si interface before annealing. After annealing at 230°C during 3 minutes, Ni electroless deposition at Fraunhofer shows better adherence than samples metallized at IPVF. However, Ni/Si interdiffusion is not uniform on the samples. For all samples, adherence has been found to be better on the front textured side compared to the rear polished one thanks to higher roughness (pyramids and LIPSS). To better explain these results, it would have been necessary to know the details of deposition processes at Fraunhofer ISE. Nevertheless, it indicates that Ni electroless process performed at IPVF can be improved.

APiC technique has enabled to compare different Ni electroless deposition processes in term of Ni thickness homogeneity and adherence. However, this technique must be improved for highly textured surface (important signal noise). On the rear polished side, the complexity of interfaces (presence of Pd particles, non homogeneous Ni_xSi_y layers, remaining silicon oxide layers after laser ablation etc.) leads to complex echoes shapes not completely understood. Moreover, it has not been possible to analyse separately the echo from Ni/Ni_xSi_y interface and the one from Ni_xSi_y/Si interface, probably due to too thin Ni_xSi_y layer. It would be interesting to further perform measurements in other conditions to investigate adherence at Ni/Ni_xSi_y and Ni_xSi_y/Si interfaces independently. For instance, nickel layer could be directly deposited on a flat Si surface (no laser ablation needed, no roughness, no palladium interlayer) and a longer annealing could be used to increase Ni_xSi_y thickness and observe the echoes related to each interface.

Some authors have proposed alternatives to improve the adherence of Ni electroless layer on Si. The Ni layer can be first annealed, followed by the removal of the unreacted Ni before redeposition of Ni to act as Cu diffusion barrier. Moreover, addition of fluoride species in the Ni bath (NH_4F for an alkaline Ni bath) enables to avoid the formation of native oxide (causing voids formation during annealing and poor adherence) between Si an Ni layer. These alternatives require additional process steps and have therefore not been investigated at first. However, they could be promising for an upcoming study.

5.5 Contact resistivity at nickel silicide/Si interface: impact of annealing conditions.

5.5.1 Experimental details

In this part, the impact of annealing conditions on the metallic contact quality is investigated. This study is focused on the front textured side (emitter) for two reasons: 1) adherence issues observed previously on the rear polished side can complicate the study 2) unsuitable annealing conditions have more impact on the emitter side due to risks of junction shunting so this side is more important to investigate.

10×40 mm^2 n-PERT precursors samples have been used and dielectric layers have been opened using a UV-ps laser with one of the parameters optimized in the Chapter 3: F_{peak} = 0.56 J/cm^2 without spot overlapping. Laser ablation has been performed according to the TLM pattern represented in Figure 5.12 a). The TLM technique is detailed in Appendix A and the pattern geometry has been chosen under the light of reference [69]. A picture of the measuring bench is given in Figure 5.12 b).

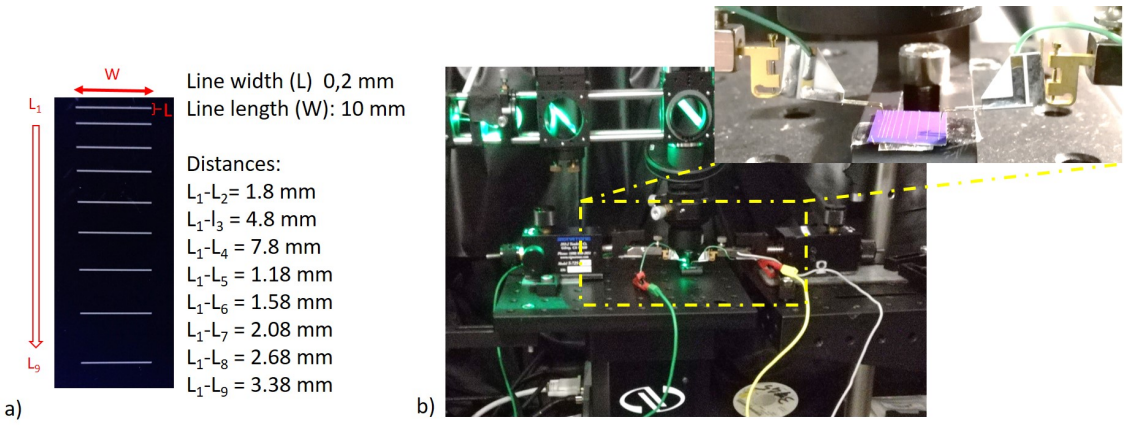

Figure 5.12: a) TLM pattern geometry, b) Picture of the TLM measurement bench.

After laser ablation, deoxidation and Pd activation have been performed with optimized conditions deduced in the Chapter 4. On the front side, 30 seconds deoxidation in $NaHF_2$ 0.16 M are sufficient and activation is performed by 30 seconds immersion in $NaHF_2$ 0.16 M + $PdSO_4$ 5.10^{-5} M. Ni deposition is then realized in dark in the bath described in section 5.3.1. A designed experiment to study the impact of initial Ni layer thickness and annealing conditions on the quality of metallic contact has been established using the JMP software. 3 input and 2 output parameters have been chosen and lead to the various experimental conditions detailed in Table 5.9.

- Input parameter 1: Ni deposition time (1, 3.5 or 6 min)
- Input parameter 2: Annealing plateau temperature (230, 340 or 450°C)
- Input parameter 3: Annealing plateau duration (3, 6 or 9 min)
- Output parameter 1: Contact resistivity
- Output parameter 2: Line resistivity

Table 5.9: Parameters of the designed experiment for the 11 samples. Annealing is performed in a RTA furnace with a heating up at 115°C/min.

Sample	Ni deposition time (min)	Ni thickness (nm)	Temperature plateau (°C)	Plateau duration (min)
1	3.5	236 ± 8	230	9
2	6	346 ± 2	450	3
3	1	52 ± 5	450	9
4	3.5	209 ± 6	450	3
5	1	58 ± 1	450	6
6	6	311 ± 49	450	9
7	1	52 ± 1	340	3
8	6	314 ± 6	230	3
9	1	46 ± 8	230	9
10	3.5	229 ± 6	340	6
11	3	49 ± 3	230	3

TLM measurements have been performed for a non annealed sample (NA) and for each sample after annealing with the methodology described in Appendix A. The line resistivity and resistance of the Ni layer have been also measured by placing the probes on both edges of a 1 cm metallized line.

5.5.2 Results

TLM measurements allowed to determine the contact resistivity (ρ_c), the contact resistance (R_C), the sheet resistance R_{sheet}, the transfer length (L_T), the line resisitivity (ρ_L) and the line resistance (R_L). Results are summarized in Table 5.10. It can be noticed that transfer lengths (L_T) are higher than metallized line widths (L) such as $L \leq 0.5\ L_T$. As described in Appendix A, the equation needed to calculate ρ_c in this case is the following:

$$\rho_c = \frac{R_c}{2} \times L \times W \tag{5.6}$$

Good contact quality of Ni seed layer is expected to give ρ_c around 1 mΩ.cm^2 before annealing and around 0.1 mΩ.cm^2 after a suitable annealing (see Figure 2.24). The values obtained in this work are higher with an order of magnitude of 100, even for the non annealed sample. It is unlikely that such a difference only comes from a poor contact quality. Experiments have been realized using other TLM patterns and values appeared to significantly vary depending on the pattern used. It indicates that the issue does not come from a non suitable TLM pattern but rather from the measurement procedure. According to reference [69], the voltage distribution along the lines is not homogeneous when the metallization is too resistive. In this case, a voltage drop is induced and leads to wrong contact resisitivity values (overestimation). Ni line resistivities in Table 5.10 are ten times higher compared to the standard Ni resistivity in literature (7.10^{-6} Ω.cm). That could be due to phosphorus incorporation during Ni electroless deposition. These high line resistances are likely to induce an important voltage drop during TLM measurements, leading to overestimation of ρ_c values. Moreover, Ni layers are few hundred nanometers thick and follow the pyramids shape so the measurement probes will not be properly in contact with Ni layer at some locations. To tackle these issues, it would have been better to deposit the conductive Cu layer before TLM measurements.

Nevertheless, some trends can be observed by comparing the different samples. A global view of the results is given in Figure 5.13.

Table 5.10: Values of contact resistivity ρ_c, contact resistance R_C, sheet resistance R_{sheet}, transfer length L_T, line resistivity ρ_L and line resistance R_L determined by TLM measurements.

Sample	ρ_c (mΩ.cm^2)	R_C (Ω)	$Rsheet$ (Ω/sq)	L_T (cm)	ρ_L (Ω.cm).10^{-5}	R_L (Ω/cm)
1	177.1 $\pm$ 11.0	8.85	43.76	0.202	4.3	24.04
2	96.1 $\pm$ 5.3	4.80	55.02	0.087	2.1	8.05
3	250.8 $\pm$ 10.4	12.54	51.53	0.243	2.4	65.22
4	148.9 $\pm$ 22.2	7.44	39.42	0.189	2.0	12.77
5	276.1 $\pm$ 19.3	13.81	45.11	0.306	2.9	68.76
6	126.6 $\pm$ 4.5	6.33	52.35	0.121	1.6	6.59
7	291.2 $\pm$ 14.7	14.56	57.29	0.254	3.0	77.21
8	145.8 $\pm$ 8.9	7.29	46.22	0.158	4.0	17.28
9	316.2 $\pm$ 12.1	15.81	54.40	0.291	3.2	96.11
10	524.4 $\pm$ 9.0	26.22	39.69	0.715	3.7	21.54
11	122.5 $\pm$ 4.4	6.13	41.90	0.411	1.7	44.7
NA	158.5 $\pm$ 10.0	7.92	44.94	0.176	4.9	19.94

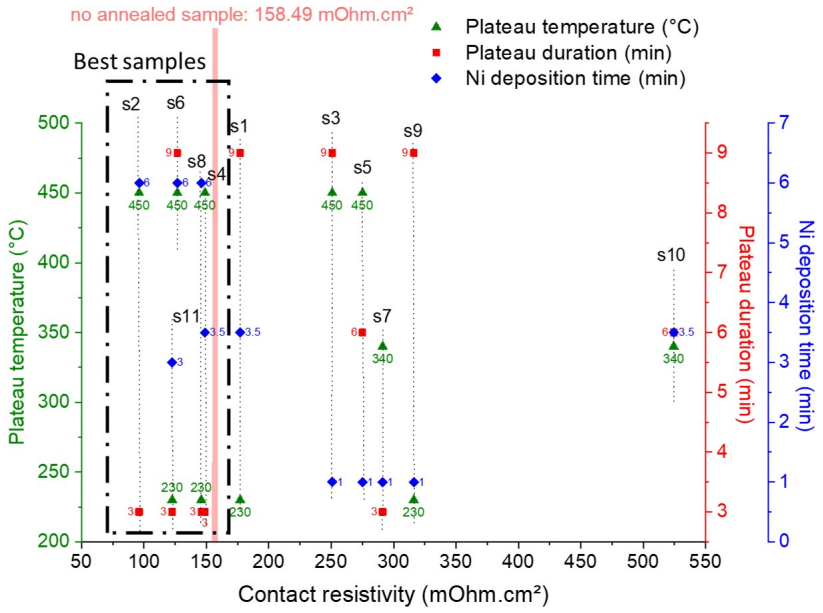

Figure 5.13: Measured contact resistivity for each sample (from s1 to s11) depending on Ni deposition time, annealing plateau temperature and annealing plateau duration.

Best contact resistivities have been obtained for samples 2, 1, 6, 8 and 4 as visible in Figure 5.13. Thus, a short annealing plateau duration (3 min) at either 230 or 450 °C with the longer Ni deposition times tested (6 min) seem to be preferable to achieve the lowest contact resistivity. As described in section 5.2, the Ni_2Si phase is formed between 200 and 350°C while NiSi phase is formed between 400 and 530°C. Sectional SEM image of a non annealed sample is shown in Figure 5.14 a) in comparison with sample 2 in which the NiSi phase formed during annealing at 450°C during 3 minutes is visible.The formation of NiSi layer is not uniform on the surface as suggested by APiC results in section 5.4.2.

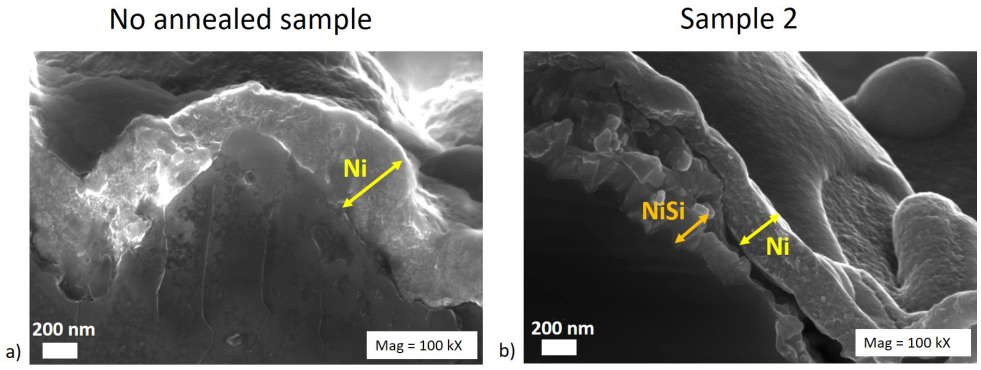

Figure 5.14: Sectional SEM images of a) non annealed sample, b) sample 2 after annealing.

As the NiSi phase has the lowest resistivity and Schottky barrier with Si, it was expected to obtain best results at 450°C rather than 230°C which is not the case. Additional X-ray Diffraction (DRX) measurements would have been necessary to investigated the Ni_xSi_y phases formed and complete this analysis.

All samples annealed after 1 minute Ni electroless deposition have demonstrated high ρ_c values. For these samples, thin Ni layers ($\approx$ 50 nm) seem to have completely reacted with underlying Si. The SEM

images of sample 9 and 3 are presented in Figure 5.15 b) and c) respectively in comparison with a non annealed sample (Figure 5.15 a)) to illustrate this phenomenon. The complete interdiffusion of Ni layer with underlying Si could explain high ρ_c values thought an increased voltage drop for instance. Moreover, it is preferable to keep some Ni above Ni_xSi_y layer to provide Cu diffusion barrier properties. Not only short annealing plateau duration (3 minutes) gives the lowest ρ_c values but it enables to limit the risk of too deep Ni/Si interdiffusion and junction shunting. The thermal budget is also reduced.

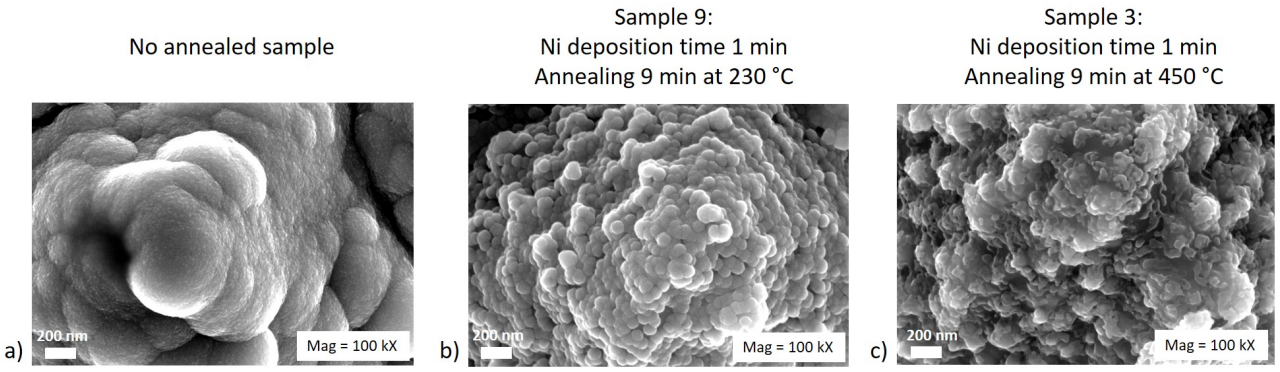

Figure 5.15: SEM images of a) non annealed sample, b) sample 9 after annealing, c) sample 3 after annealing.

5.5.3 Conclusions and perspectives

This preliminary study to optimize annealing conditions has consisted of varying the Ni deposition time, the annealing temperature and the duration of annealing plateau. TLM measurements have been performed to determine the contact and line resistivities. Line resistivities of Ni layers appeared to be ten times higher compared to standard values reported in literature, leading to voltage drop and overestimation of ρ_c values. The deposition of a thick Cu layer (around 8-10 µm), more conductive than Ni layer, would have been necessary before TLM measurements to avoid this phenomenon. However, it has been possible to highlight a trend for the best conditions to obtain lower ρ_c values.

Annealing at 230 and 450°C both lead to lower ρ_c values in comparison with 340°C. Short annealing plateau ($\leq$ 3 minutes) must be preferred to avoid a deep Ni/Si interdiffusion and risks of junction shunting. This is particularly the case at 450°C where a $\geq$ 200 nm thick NiSi layer has been observed on SEM images after 3 minutes annealing. In addition, thick enough Ni layer must be deposited such as unreacted Ni remains after annealing and acts as Cu diffusion barrier.

In a further work, it would be useful to identify the different Ni_xSi_y phases present after the various annealing conditions through DRX measurements. Palladium silicides can also be formed during annealing step [206] and impact the quality of metallic contact so identification of these phases should also be performed. Moreover, the impact of annealing temperature built-up rate and Ni layer phosphorus content on ρ_c values could be studied. In addition, laser parameters as well as deoxidation and activation parameters could affect ρ_c values so this point could be investigated too.

5.6 Cu electrolytic deposition and measurement of cell efficiencies

After the Ni electroless deposition, the Cu layer is deposited electrolytically before performing the final annealing. The Ni layer could be annealed before Cu deposition but it is more practical to deposit the Ni/Cu stack without interrupting the metallization process.

On the rear polished side, adherence issues of the nickel seed layer ($\approx$ 500 nm) have been identified and are enhanced after the deposition of thicker Cu layer ($\approx$ 10 µm) due to induced internal stress. Consequently, important fingers delamination have been observed on the rear polished side and sometimes on the front textured side too. A sectional SEM image of delamination on the front textured side is given in Figure 5.16 to illustrate that delamination of metallic contacts seems to occur at Ni/NiSi interface. Accordingly, the photo-generated charges can not be properly collected by the metallic contacts which affects severely the measured cell efficiency. Improvement of adherence on rear polished side would have required more experiments so **it has been decided to work on double textured n-PERT precursors presented in section 2.6**.

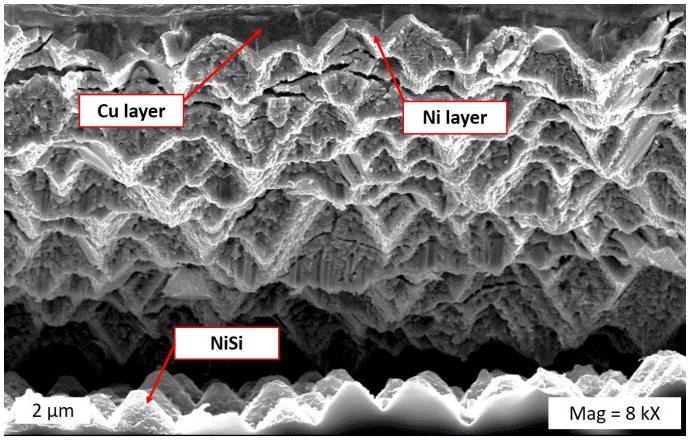

Figure 5.16: Sectional SEM image of a delaminated finger on the front textured side after Ni/Cu plating and final annealing at 380°C during 3 min.

5.6.1 Experimental details

The overall Ni/Cu plating process has been performed on 50 $\times$ 50 mm^2 pre-cells having one busbar (40 $\times$ 0.75 mm^2) and 38 fingers with a pitch of 1 mm. Therefore, nine pre-cells can be laser opened and pre-cutted in a 156 $\times$ 156 mm^2 double textured n-PERT precursor. Pre-cutting of the cells is needed because n-PERT precursors have a clivage orientation at 45°. This step is performed on the rear side to avoid junction shunting and the laser parameters used are: F_{peak} = 10 J/cm^2, scan speed = 1 m/s and number of repetition = 100.

For each Ni/Cu plating process step, optimized conditions determined previously have been implemented and I-V measurements have been performed to determine cells conversion efficiencies before and after final annealing. Before the final annealing, pre-cells borders must be laser cutted to avoid copper diffusion during annealing. The Cu thickness homogeneity at different sample locations have been also investigated by Confocal microscopy (CLSM). The different process steps are schematized in Figure 5.17 and reminded below.

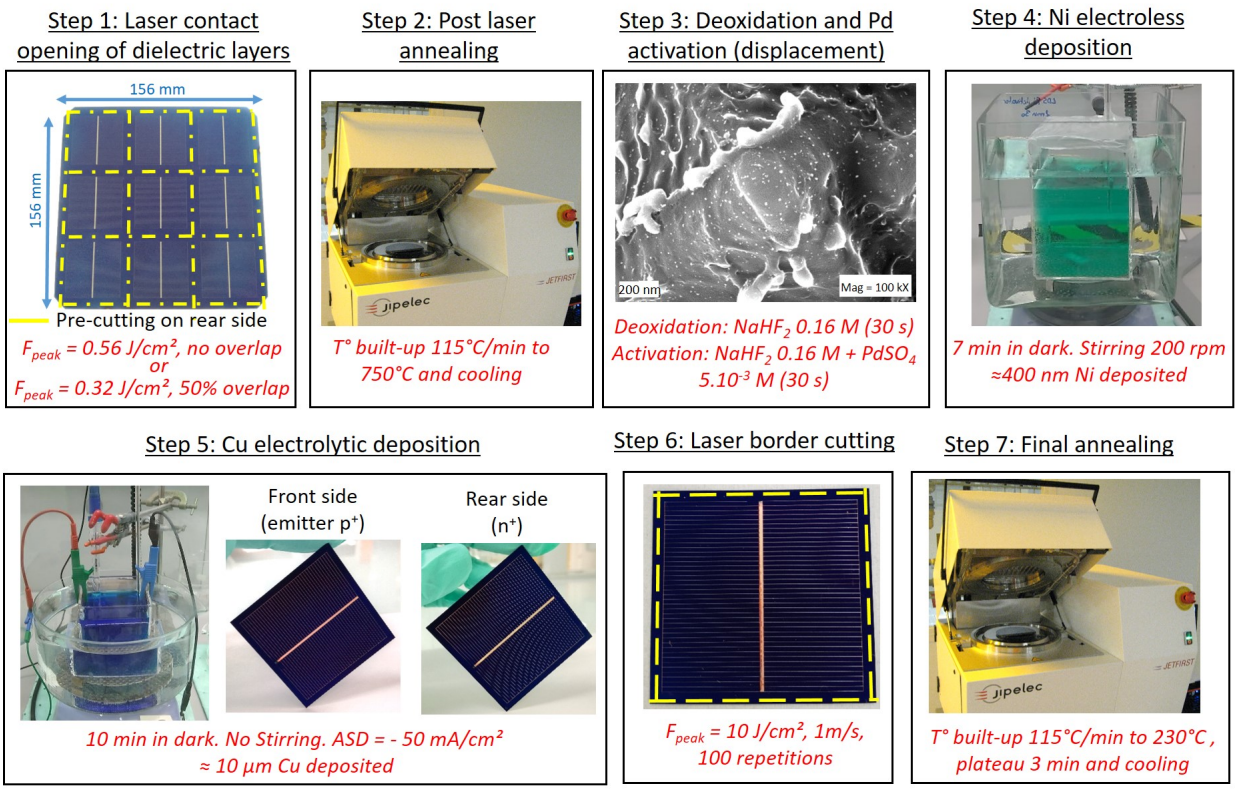

Figure 5.17: Optimized Ni/Cu plating process steps to metallize bifacial double textured n-PERT cells.

- **Step 1: Laser contact opening.** Optimized laser parameters determined in Chapter 3 have been implemented. Pre-cells have been therefore laser opened using either F_{peak} = 0.56 J/cm^2 without spot overlapping, or F_{peak} = 0.32 J/cm^2 with 50% overlapping. Pre-cells are also pre-cutted.

- **Step 2: Post laser annealing (PLA).** This step is needed to promote hydrogen diffusion from dielectric layers (SiO_xN_y layers) and promote passivation properties. As explained in Chapter 3, it is advantageous to perform the PLA after laser ablation as it improves electrical properties through recrystallization of the a-Si formed during laser ablation. PLA is performed in a RTA furnace (SEMCO Jipelec Jetfirst) under N_2 flow. Temperature is built up at 750°C (115°C/min) and directly cooled down.

- **Step 3: deoxidation and activation of Si surface.** Pre-cells are clived to be individually deoxidized and activated with Pd particles. Optimized conditions identified in Chapter 4 have been used: 30 seconds in $NaHF_2$ 0.16 M followed by 30 seconds in $NaHF_2$ 0.16 M + $PdSO_4$ 5.10^{-5} M.

- **Step 4: Ni electroless deposition.** Pre-cells are immersed 7 min into the Enthone Ni electroless bath (see bath description in section 5.3.1) to deposit ≈ 400-500 nm of Ni seed layer. This step is realized in dark conditions with solution stirring at 200 rpm.

- **Step 5: Cu electrolytic deposition.** Samples are then immersed in the Cu bath described in Table 5.11. Based on the calculation in reference [92] to optimize the grid geometry, the height of Cu layer must be ≈ 10 µm. According to equation 2.19 and considering as a first approximation that the current

efficiency β is equal to 1, the time necessary to deposit 10 µm of Cu can be estimated such as:

$$t = \frac{h \times F \times z \times \rho_{Cu}}{M(Cu) \times j} = \frac{10.10^{-3} \times 96485 \times 2 \times 8.96}{63.54 \times 50.10^{-3}} = 544 \text{ seconds} \approx 9 \text{ minutes}$$

with t the deposition time, h the height of Cu layer, F the Faraday's constant, z the number of electrons exchanged, ρ_{Cu} the Cu density, M(Cu) the molar mass of Cu and j the density of current applied.

COPPER ELECTROLYTIC BATH

Cu electrolytic deposition is performed using a commercial bath from KMG. This bath is made of 4 components given in Table 5.11. The bath is acidic (pH $\approx$ 0.6) and is agitated during the make up but not during the deposition process. The solution is kept in a water bath at 22°C and the pH is regularly controlled. This bath can be kept one week.

Table 5.11: Made up of TSV Fill copper bath from KMG

Name	Quantity	Chemical species
OmniCu HC electrolyte	Electrolyte	Copper sulfate , Sulfuric acid
TSV Fill Leveler	1.5 mL/L	Copper sulfate, sulfuric acid
TSV Fill Accelerator	2 mL/L	Copper sulfate, sulfuric acid
TSV Fill Suppressor	5 mL/L	Sulfuric acid

A setup with 3 electrodes is connected to the potentiostat:

- The working electrode (solar cell). The ASD current must be comprised between - 20 and - 50 mA/cm^2 according to the technical data sheet and the ASD of - 50 mA/cm^2 has been used in this work. The pre-cells surface is equal to 2.765 cm^2 which necessitates to apply a current of - 138.25 mA.
- A counter electrode: two Cu plates placed on both sides of the solar cell (bifacial metallization).
- A saturated calomel electrode as reference electrode.

The difficulty has been to connect the solar cells without breaking them. As for Ni electroless deposition, experiments are performed in dark conditions to avoid a detrimental light effect on the p^+ side. **The conditions detailed above remained unchanged in this thesis work.**

- **Step 6: Laser cutting of cell borders.** This step is needed as the borders of pre-cells is also metallized. Laser cutting is performed at 5 mm distance from cell borders.
- **Step 7: Final annealing.** Regarding the results obtained in section 5.5, pre-cells have been annealed at 230°C during 3 minutes (temperature built-up = 115 °C/min) under N_2 flow in the same RTA furnace than for PLA. I-V measurements are then performed before and after this final annealing.

The conversion efficiency of as-obtained metallized bifacial double textured n-PERT precursors is compared to screen-printed references. Meanwhile, the impact of non optimized laser parameters and annealing temperatures have been also investigated. For that purpose, pre-cells laser opened with strong laser parameters (F_{peak} = 1.8 J/cm^2, no spot overlapping) have been metallized. In addition, pre-cells opened with one of the optimized laser parameters (F_{peak} = 0.56 J/cm^2, no spot overlapping) have been annealed at 300°C or 380°C instead of 230°C.

5.6.2 Results: impact of non-optimized laser ablation parameters on cell efficiency

Three 156 × 156 mm^2 double textured n-PERT precursors cells have been laser processed to obtain nine pre-cells opened with different laser parameters as shown in Figure 5.18 a). It seemed interesting to investigate not only the impact of laser parameters on carriers lifetime through PL QSS-PC measurements, but also to determine if the ablation process affects both sides similarly. For that purpose, one cell has been laser opened on both sides (Figure 5.18 b)) and the two others have been laser opened only on the front (Figure 5.18 c)) or the rear side (Figure 5.18 d)). The pre-cells used for further Ni/Cu plating are framed in green (optimized laser parameters) and red (non optimized laser parameters).

As observed in Figure 5.18, few differences are visible for the different parameters tested except for the high F_{peak} = 1.8 J/cm^2 where carriers lifetime is significantly reduced. Regarding the study in section 3.7, the use of high F_{peak} = 1.8 J/cm^2 with 50% overlapping or no overlapping is likely to lead to cracks/dislocations formation. Moreover, by looking at Figure 5.18 c) and d), the laser ablation seems to be more critical on the front side (emitter p$^+$) than on the rear side (n$^+$). It is particularly visible at F_{peak} = 1.8 J/cm^2 with 50% and no overlapping. Considering that the junction is not supposed to be shunted for these laser parameters (see results in Figure 3.30 b) in Chapter 3), the differences observed on both sides may be due to different initial dopant concentration profiles, a different sensitivity of doped layers depending on dopant type (phosphorus or boron) or a slightly different pyramids texturation.

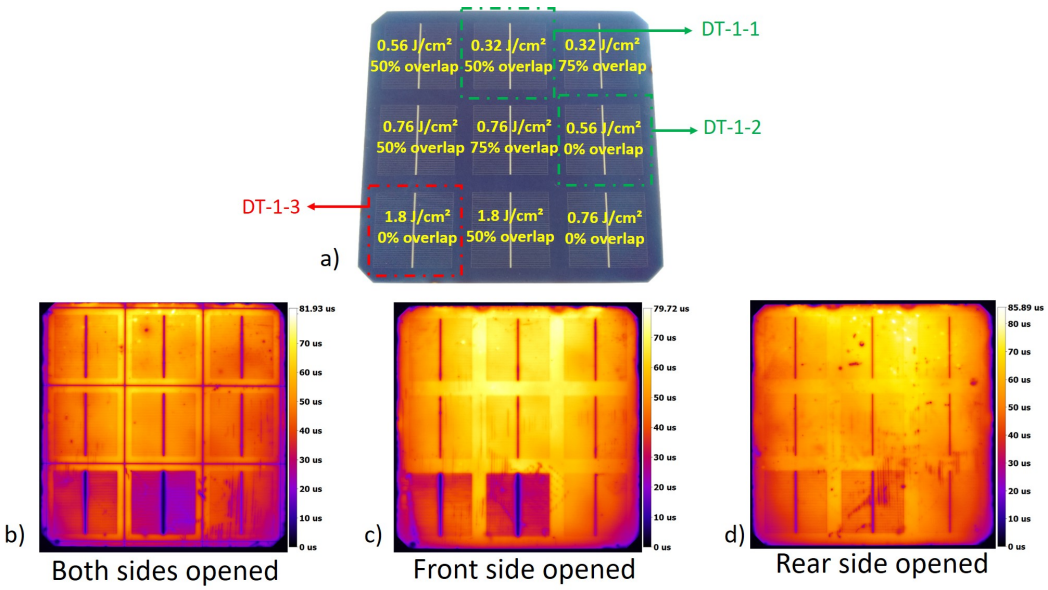

Figure 5.18: PL QSS-PC results using various laser parameters (represented in picture a) b) on both n-PERT precursors sides, c) on the front side only (emitter p$^+$), d) on the rear side only. Measurements have been performed after PLA. Framed laser opened pre-cells are named and then metallized.

Morphology of nickel and copper plated layers and investigation of thickness homogeneity.

Then, the three pre-cells framed in Figure 5.18 a) have been metallized according to the process described in Figure 5.17. For sample DT-1-1, SEM images after Ni/Cu plating are given in Figure 5.19 to show the layers morphologies. In Figure 5.19 a), the Ni seed layer is ≈ 22 µm width and two regions can be discerned:

- Region 1: In the center of the finger, Ni has been deposited on the laser opened area of about 12 µm width and various sizes of Ni clusters are visible.
- Region 2: On the borders, Ni layer appears less rough and has been deposited directly on the dielectric layers due to overflow of Ni layer deposited on laser opened area.

In Figure 5.19 b), Cu layer is ≈ 25 µm width which is slightly broader than Ni layer observed before. Thus, overplating is mainly due to Ni deposition rather than Cu deposition. Finally, the total metallized width is about two times larger than laser opened width.

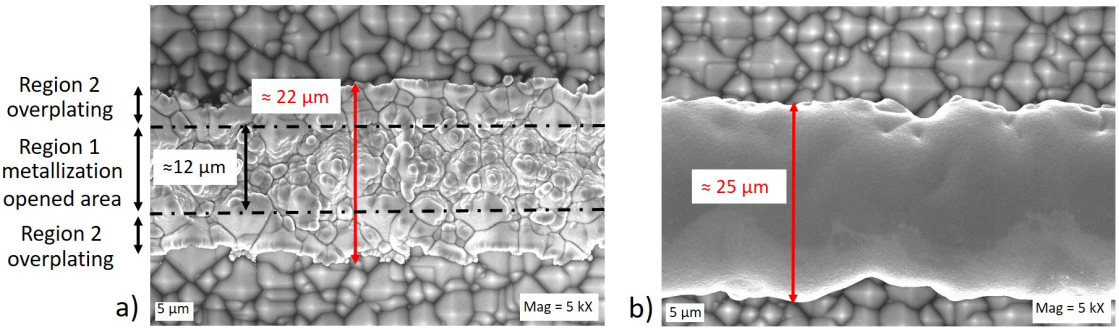

Figure 5.19: SEM images on DT-1-1 pre-cell after a) Ni electroless and b) Cu electrolytic depositions.

CLSM images have been realized on the front side of DT-1-1 cell to measure thickness and width of Ni/Cu metallic contacts. As represented in Figure 5.20 a), measurements have been performed at various locations to investigate the homogeneity of the metallic contact geometry. An example is displayed in Figure 5.20 b). For each location, five measurements have been realized and results are given in Table 5.12.

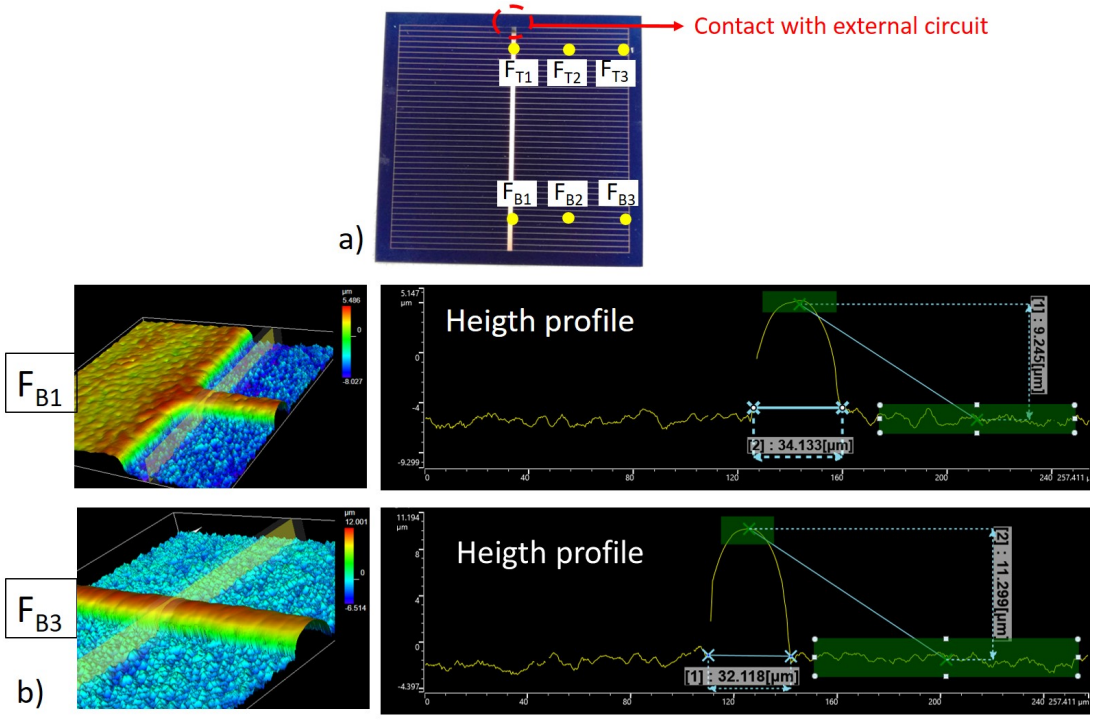

Figure 5.20: a) Location of CLSM measurements on the front side of Ni/Cu plated DT-1-1 cell (five measurements performed at each location), b) example of CLMS image processing.

Table 5.12: Ni/Cu metallic contact thickness on fingers and busbars at various DT-1-1 cell locations (average values have been obtained with five measurements at each location).

Location	Busbar height (µm)	Finger height (µm)	Finger width (µm)	Ratio height/width
$\mathbf{F}_{T1}$	8.29 ± 0.19	8.22 ± 0.21	30.87 ± 3.25	0.26 ± 0.02
$\mathbf{F}_{T2}$	-	9.67 ± 0.23	34.18 ± 1.19	0.28 ± 0.01
$\mathbf{F}_{T3}$	-	11.71 ± 0.21	33.32 ± 1.25	0.35 ± 0.01
$\mathbf{F}_{B1}$	8.42 ± 0.28	9.67 ± 0.29	34.54 ± 3.39	0.28 ± 0.02
$\mathbf{F}_{B2}$	-	10.61 ± 0.56	32.11 ± 0.27	0.33 ± 0.01
$\mathbf{F}_{B3}$	-	11.88 ± 0.32	31.06 ± 5.27	0.39 ± 0.08

First, results for location F_{T1}, F_{T2} and F_{T3} have been compared each other and same comparison has been realized for F_{B1}, F_{B2} and F_{B3} location. It can be observed that the height and width of Ni/Cu stack depends on the finger distance relatively to the busbar. Indeed, fingers tend to be higher and narrower when they are far from the busbar. That gives an indication of the current dispersion on the cell during Cu electrolytic deposition. The current density reaching the external part of fingers is thus higher and decreases by approaching the busbar. As a result, fingers on the borders of the cell have a better aspect/ratio, limiting shadowing effect and collecting more efficiently the photogenerated charges carriers.

Then, results for location F_{T1}, F_{T2} and F_{T3} have been compared with results for locations F_{B1}, F_{B2} and F_{B3} respectively to determine if the distance from the contact area with external circuit affects the Cu deposition rate. Fingers seem to be globally higher and narrower (better aspect ratios) when they are far away the contact area with external circuit. This suggests an higher current density for locations far away the contact area with external circuit. However, the differences are small and in the range of standard deviations so these results must be taken with precaution. Busbars are globally thinner than the fingers which can be related to the larger area to be metallized as observed for Ni electroless deposition in section 5.3.1.

I-V measurements:

I-V measurements have been carried out on DT-1-1, DT-1-2 and DT-1-3 metallized cells, before and after the final annealing at 230°C during 3 minutes. It is not possible to implement I-V measurement technique explained in section 1.5.2 for bifacial solar cells so measurements have been performed on front side and rear side successively. Results are given in Table 5.13 and Table 5.14 respectively. I-V and SunsV_{OC} curves have been plotted for the front side in Figure 5.21 and a comparison of I-V before and after annealing for each cell is given in Figure 5.22. Results have raised the following points:

1. Cells parameters are globally better on the front side rather than on the rear side. On double textured n-PERT cells, more parasitic plating (PP) has been observed on the rear side which could be due to worse quality of the dielectric layers. This additional PP could explain the systematically higher R_S and lower J_{SC} observed for the rear side.

2. For both sides of the three cells, R_s is reduced after the final annealing, which is related to the formation of nickel silicide layer at Ni/Si interface. However, the cells parameters J_{SC}, V_{OC}, FF and η are reduced after the final annealing. This behavior is likely due to Cu diffusion during the final annealing because

the R_{sh} is also significantly reduced.

3. The laser parameters have an impact on the cell efficiency as attest by the different I-V curve shape in Figure 5.22. Best parameters have been obtained with DT-1-1 cell, closely followed by DT-1-2 cell which are both cells opened with optimized laser parameters. DT-1-3 cell demonstrates the worst parameters related to higher impact of the laser observed on PL QSS-PC images.

4. DT-1-1 cell demonstrates a better efficiency η, J_{SC}, V_{OC} and R_{sh} before annealing than reference SP cells which is a promising result. However, efficiency is reduced after the final annealing and to address this issue the final annealing should be performed just after Ni electroless deposition to suppress the risk of Cu diffusion.

5. FF and R_s are lower compared to SP reference cells. The higher R_s values for Ni/Cu plated cells indicates a worse quality of contact between Ni and Si. This could be due to adherence issues at Ni/Si interface and/or formation of a thin native oxide before Ni deposition which hinders the Ni/Si interdiffusion process and the formation of voids.

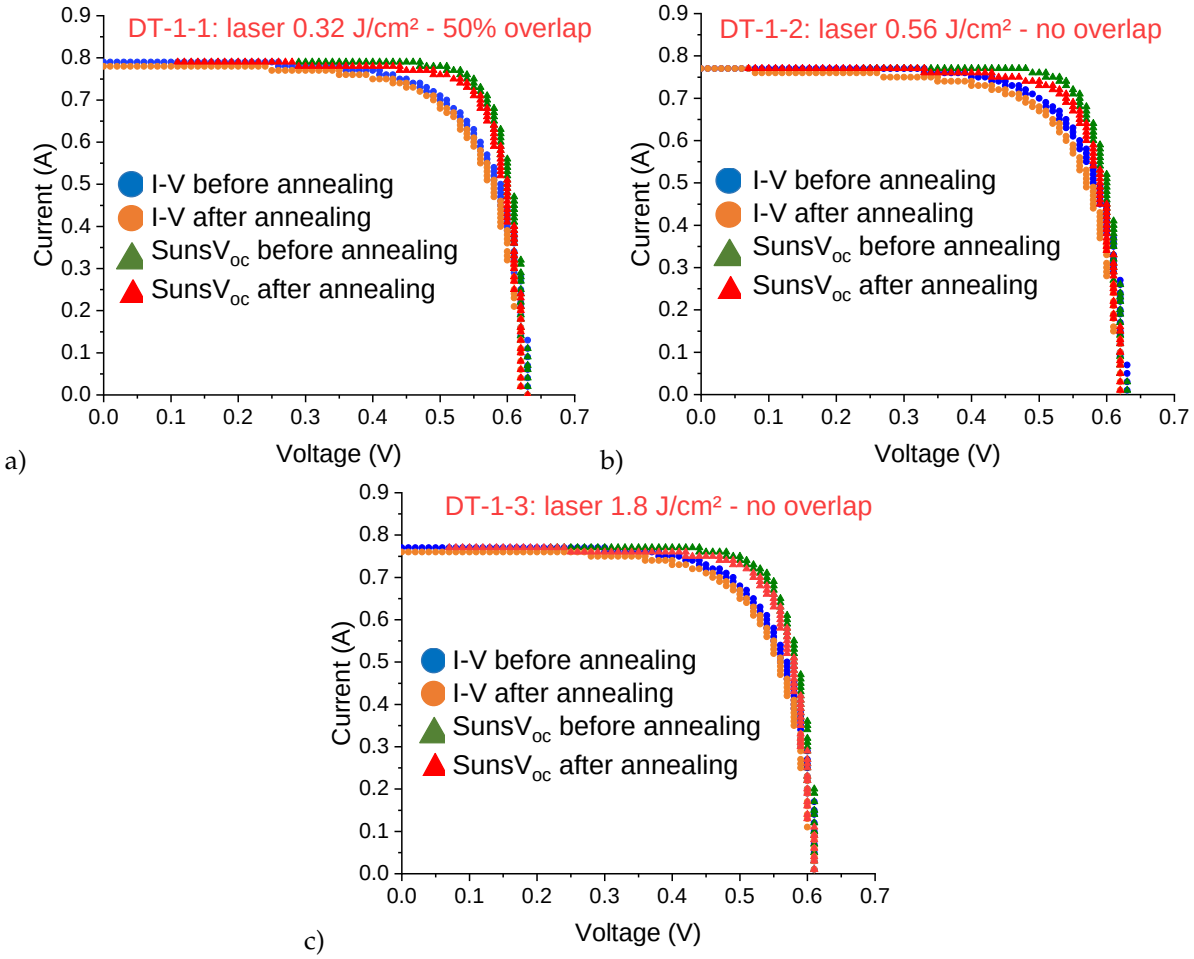

Figure 5.21: I-V and SunsV_{OC} curves before and after annealing on the front side of a) DT-1-1, b) DT-1-2, c) DT-1-3 cells.

Table 5.13: Results of I-V measurements on the front side of DT-1-1, DT-1-2 and DT-1-3 cells. A: Annealed cells, NA: Non annealed cells.

Cells	J_{SC} (mA/cm^2)	V_{OC} (mV)	FF (%)	η (%)	R_s (Ω.cm^2) (from Suns-V_{OC})	R_{sh} (Ω.cm^2)
DT-1-1 NA	38.99	629.25	71.07	17.44	1.77	35855.99
DT-1-1 A	38.87	625.87	70.06	17.04	1.63	2006.41
DT-1-2 NA	38.24	626.91	72.17	17.30	1.58	13314.05
DT-1-2 A	38.02	622.26	70.40	16.66	1.42	1711.00
DT-1-3 NA	38.08	614.23	71.53	16.73	1.40	7957.53
DT-1-3 A	37.86	610.14	70.59	16.30	1.47	1964.84
SP reference	35.94	618	78.11	17.35	0.75	25408

Table 5.14: Results of I-V measurements on the rear side of DT-1-1, DT-1-2 and DT-1-3 cells. A: Annealed cells, NA: Non annealed cells.

Cells	J_{SC} (mA/cm^2)	V_{OC} (mV)	FF (%)	η (%)	R_s (Ω.cm^2) (from Suns-V_{OC})	R_{sh} (Ω.cm^2)
DT-1-1 NA	36.95	628.17	72.02	16.71	1.72	34916.87
DT-1-1 A	37.00	625.16	70.27	16.25	1.71	1978.10
DT-1-2 NA	37.10	626.43	72.72	16.90	1.50	13657.01
DT-1-2 A	37.01	621.90	70.76	16.29	1.57	1741.98
DT-1-3 NA	35.79	612.60	71.16	15.60	1.65	7715.91
DT-1-3 A	35.80	608.89	70.72	15.41	1.50	2077.83

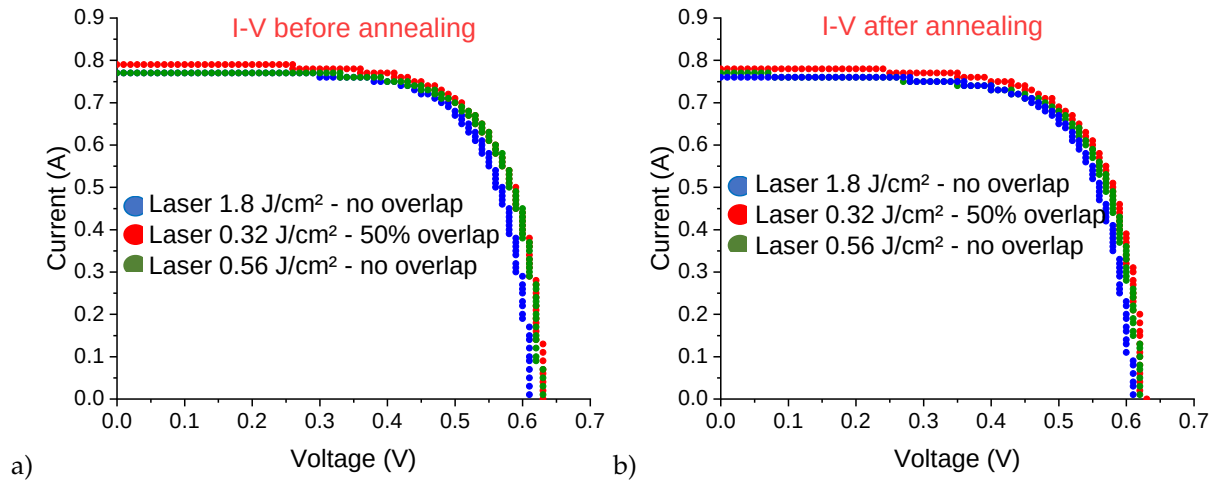

Figure 5.22: Comparison of I-V curves obtained on the front side for the three laser parameters tested a) before final annealing and b) after final annealing.

In a previous work, TLM measurements have been realized after Ni/Cu plating on samples with various laser ablation parameters (2 parameters optimized in Chapter 3 and 2 parameters non optimized). The metallization was not optimized at this moment neither the final annealing so results can not be related to this study. The TLM pattern was also slightly different than the one represented in Figure 5.12 a) such as distances between lines were smaller. Results are displayed in Appendix I. Contact and line resistivities have been measured and it appears that ρ_c is lower with optimized laser parameters which highlights the impact of non optimized laser parameters on metallic contact quality. Best contact resistivity is obtained with F_{peak} = 0.32 J/cm^2, 50% overlapping (ρ_c = 10.47 mΩ.cm^2) and line resistivity is equal to 3.7.10^{-6} Ω.cm.

5.6.3 Results: impact of non-optimized annealing conditions on cell efficiency

In this part, we have investigated the impact of final annealing conditions (temperature and plateau duration) on cell efficiency. First, it has been evidenced that a too long annealing at 380°C during 20 minutes lead to the shunting of the cell due to nickel silicide spiking. This phenomenon is illustrated on SEM images in Figure 5.23. EDS analysis indicates that Ni and Si are the two major elements in the spikes observed which suggests that spiking originates from a too long Ni/Si interdiffusion.

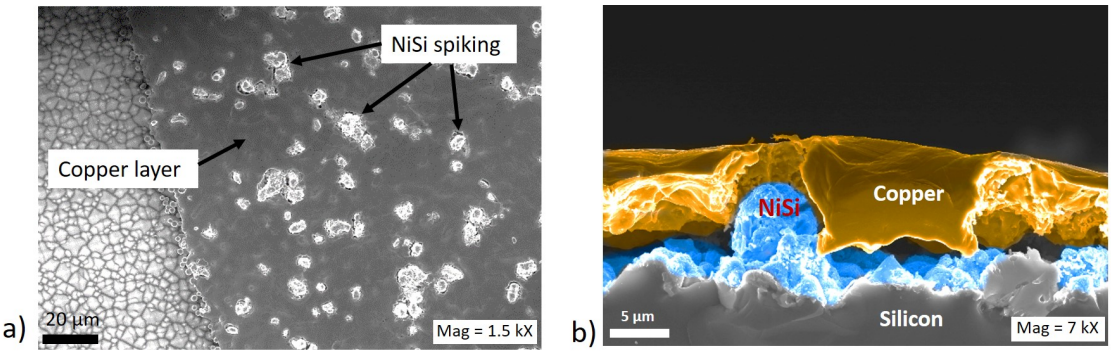

Figure 5.23: SEM images of Ni/Cu plated contacts after annealing at 380°C during 20 minutes: illustration of nickel silicide spiking: a) planar SEM images b) colored sectional SEM image.

Then, three pre-cells laser opened with F_{peak} = 0.56 J/cm^2 with no overlapping have been metallized according to the process described in Figure 5.17. One cell has been annealed at 230°C (DT-1-2 cell), another at 300°C (DT-2-2 cell) and the third at 380°C (DT-3-2 cell). Built-up temperature is performed at 115°C/min and the temperature plateau is 3 minutes for the three cells. Cells parameters determined by I-V measurements before and after the final annealing are reported in Table 5.15 and 5.16 for the front and rear side respectively. I-V and SunsV_{OC} curves before and after final annealing are also displayed in Figure 5.24 and a comparison between the three cells is given in Figure 5.25.

The detrimental effect of too high annealing temperatures is clearly visible in Figure 5.25 b) with the modification of I-V curve shape when annealing temperature is increased. In Table 5.15 and 5.16, it can be noticed that cell parameters are reduced after annealing at 300 and 380°C. R_{sh} drastically falls down at these both temperatures which suggests that cells are shunted. This is likely due to Cu diffusion during the final annealing and this phenomenon is enhanced by increased the annealing temperature.

Before annealing, J_{SC} and V_{OC} are better than SP reference cells and conversion efficiency η is similar and even better for DT-2-2 cell. It means that the Ni/Cu plating process developed has the potential to improve cell efficiency compared to standard SP process. However, the annealing step must be improved to avoid Cu diffusion and cell shunting. As already mentionned, an alternative could be to perform the annealing step before Cu deposition but this implies to interrupt the wet chemical process steps.

Table 5.15: Results of I-V measurement on the front side of DT-1-2, DT-2-2 and DT-3-2 cells. A: Annealed cells, NA: Non annealed cells.

Cells	J_{SC} (mA/cm^2)	V_{OC} (mV)	FF (%)	η (%)	R_s (Ω.cm^2) (from Suns-V_{OC})	R_{sh} (Ω.cm^2)
DT-1-2 NA	38.24	626.91	72.17	17.30	1.58	13314.05
DT-1-2 A 230°C	38.02	622.26	70.40	16.66	1.42	1711.00
DT-2-2 NA	38.63	629.33	71.95	17.49	1.62	17721.80
DT-2-2 A 300°C	38.45	614.90	62.15	14.69	1.52	301.88
DT-3-2 NA	38.12	627.85	71.72	17.16	1.62	16745.45
DT-3-2 A 380°C	37.88	224.39	54.84	4.66	0.26	9.63
SP reference	35.94	618	78.11	17.35	0.75	25408

Table 5.16: Results of I-V measurement on the rear side of DT-1-2, DT-2-2 and DT-3-2 cells. A: Annealed cells, NA: Non annealed cells.

Cells	J_{SC} (mA/cm^2)	V_{OC} (mV)	FF (%)	η (%)	R_s (Ω.cm^2) (from Suns-V_{OC})	R_{sh} (Ω.cm^2)
DT-1-2 NA	37.10	626.43	72.72	16.90	1.50	13657.01
DT-1-2 A 230°C	37.01	621.90	70.76	16.29	1.57	1741.98
DT-2-2 NA	36.97	627.59	72.66	16.86	1.56	20189.24
DT-2-2 A 300°C	36.55	612.83	62.16	13.92	1.49	302.29
DT-3-2 NA	36.68	626.51	72.62	16.69	1.60	15706.59
DT-3-2 A 380°C	34.46	221.24	54.54	4.15	0.28	10.39

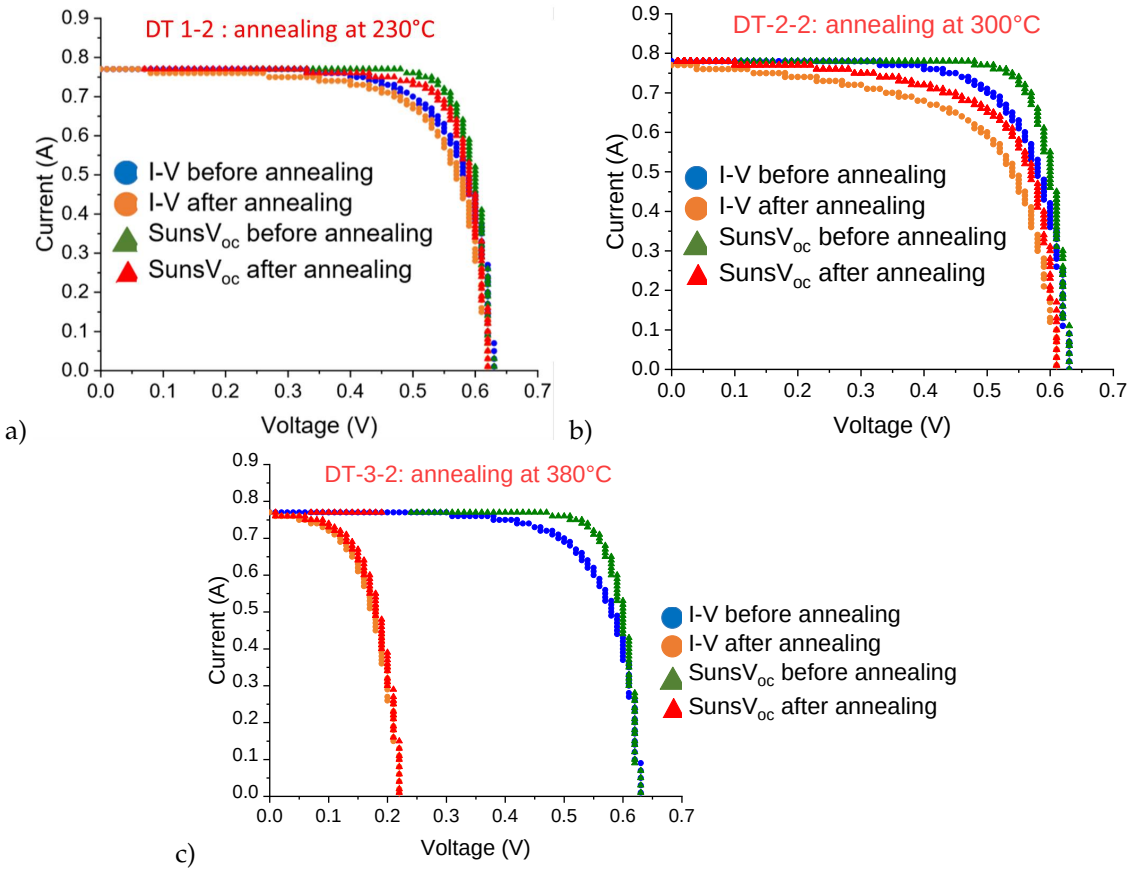

Figure 5.24: I-V and SunsV_{OC} curves before and after annealing for the front side of a) DT-1-2, b) DT-2-2, c) DT-3-2 cells.

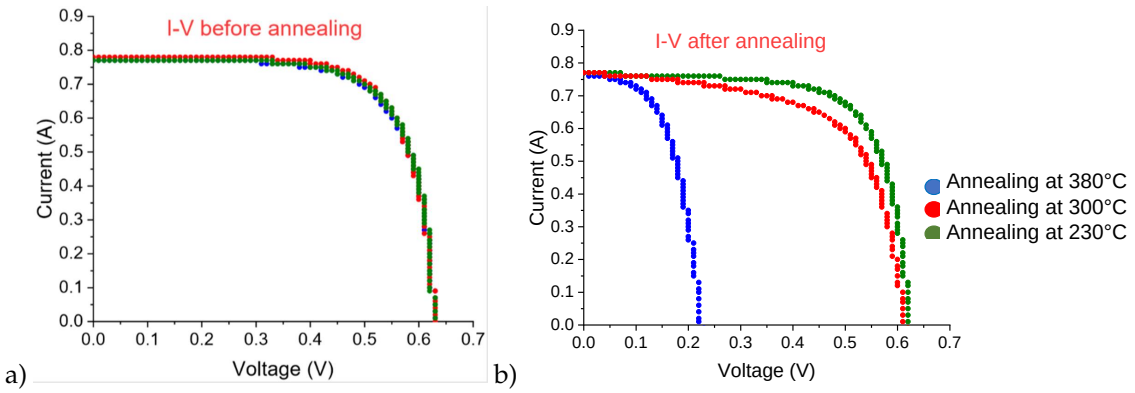

Figure 5.25: Comparison of I-V curves on the front side for the three annealing temperatures tested a) before final annealing and b) after final annealing.

5.6.4 Conclusions and perspectives

In this study, an optimized Ni/Cu plating process has been implemented and the morphology of Ni/Cu plated contacts has been observed. 400 nm of Ni seed layer were deposited in ≈ 7 min and 8 µm of Cu were deposited in ≈ 10 min in our experimental conditions. Overflow of the metallization is about two times the laser opened area width on fingers and Ni/Cu stack thickness is not homogeneous on the cell. Current density dispersion during Cu deposition leads to better aspect ratios on fingers far away from the busbar.

Moreover, I-V measurements have been carried out to determine the cell parameters: J_{SC}, V_{OC}, FF, η, R_s and R_{sh}. Among both laser parameters optimized in the Chapter 3, best cell has been obtained with F_{peak} = 0.32 J/cm^2 and optimized Ni/Cu plating process steps in Figure 5.17. Cell parameters are reported in Table 5.17 in comparison with parameters of SP reference cell. Better J_{SC} and V_{OC} have been obtained and for non annealed best cell, R_{sh} are also higher in comparison with SP reference. Conversion efficiencies are very close to the one of SP references and even better for the front side of best cell non annealed (+0.09%$_{abs}$). However, R_s are higher compared to SP references and R_{sh} are significantly reduced after the final annealing, suggesting Cu diffusion into Si. These higher R_s values may be due to the presence of native SiO_x layer between Si and Ni layer, affecting the Ni/Si interdiffusion. In a further work, a fluoride media could be added in the Ni bath (NH_4F for alkaline bath) to avoid the formation of this native SiO_x at Ni/Si interface.

Table 5.17: Best cell parameters (DT-1-1 cell) for the front and rear side, before and after annealing in comparison with parameters of SP reference cells.

Cells	J_{SC} (mA/cm^2)	V_{OC} (mV)	FF (%)	η (%)	R_s (Ω.cm^2) (from Suns-V_{OC})	R_{sh} (Ω.cm^2)
Best cell non annealed (front side)	38.99	629.25	71.07	17.44	1.77	35855.99
Best cell annealed 230°C (front side)	38.87	625.87	70.06	17.04	1.63	2006.41
Best cell non annealed (rear side)	36.95	628.17	72.02	16.71	1.72	34916.87
Best cell annealed 230°C (rear side)	37.00	625.16	70.27	16.25	1.71	1978.10
SP reference	35.94 ± 0.053	618 ± 0.3	78.11 ± 1	17.35 ± 0.3	0.75 ± 0.13	25408 ± 20400

Furthermore, annealing conditions must be optimized to prevent Cu diffusion into Si. In particular, the annealing should be performed just after the Ni deposition to suppress the risk of Cu diffusion.

Sectional SEM images of the best cell DT-1-1 after annealing are given in Figure 5.26. At this temperature, Ni_2Si phase is formed and can be observed on the SEM images. Poor adherence at Ni/Ni_2Si interface is visible and still need to be tackeled.

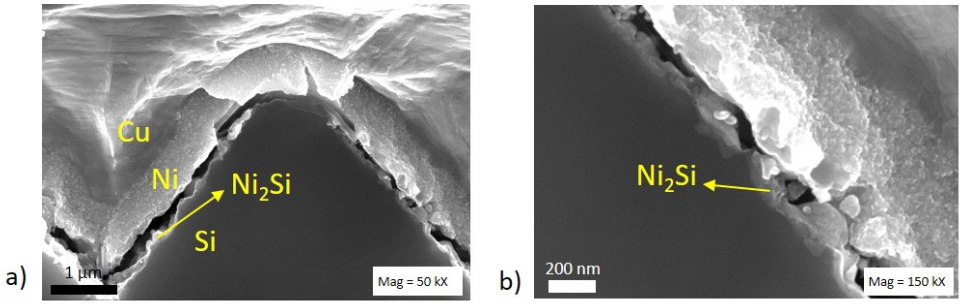

Figure 5.26: Sectional SEM images on front side of the best cell (DT-1-1) after the final annealing at 230°C during 3 minutes.

The impact of non optimized laser ablation parameters and annealing temperature on cell parameters have been investigated. Non optimized laser parameter F_{peak} = 1.8 J/cm^2 with no overlapping leads to significantly lower conversion efficiency in comparison with the cell opened with F_{peak} = 0.32 J/cm^2 with 50% overlapping (-0.74%$_{abs}$ on the front side after final annealing). It has been also demonstrated by PL QSS-PC measurements that laser is more critical on the front side rather than on the rear side. The more the annealing temperature is increased, the more the cell parameters are affected. It is likely that Cu diffusion in enhanced at 300°C and 380°C, explaining the significantly worse cell parameters obtained compared to the one obtained with annealing at 230°C.

In the following of this work, the impact of deoxidation and activation conditions on cell efficiency could be studied. In addition, the importance of the PLA could be investigated by comparing cells with and without PLA. Grid design could be also improved using Quokka software to optimize the pitch between fingers, the width of busbars or the height of Ni and Cu layers.

MEMENTO

Ni electroless deposition rate is higher on narrow laser opened areas (fingers) compared to large ones (busbars). Under illumination, the photogenerated holes diffuse to the p^+ side (front side of n-PERT precursors) which prevents the reduction of Ni^{2+} ions on Si surface. Ni electroless deposition must therefore be performed under dark conditions. In addition, the surface morphology and composition observed after laser ablation on the rear polished side with no overlapping (area 1, 2 and 2_{bis}) lead to non homogeneous Ni electroless deposition with a border effect and probably a poor adherence in the center due to remaining SiO_x. Among the two laser parameters optimized previously, F_{peak} = 0.32 J/cm^2 with 50% overlapping must be preferred than F_{peak} = 0.56 J/cm^2, no overlapping to avoid this phenomenon.

APiC technique enabled to compare the adherence of different Ni electrolessly deposited seed layers (Fraunhofer ISE and IPVF processes). For all samples, adherence is better on the front textured side thanks to higher surface roughness. Ni/Si interdiffusion is not uniform along the samples but this is more significant on samples metallized at IPVF. That may be related to the presence of native SiO_x at Ni/Si interface, leading also to poor adherence on the rear polished side (delamination) of Ni seed layer deposited at IPVF. These results led to shift this work on double textured n-PERT precursors.

TLM have been performed to determine the contacts and line resistivities of Ni plated contact depending on Ni layer thickness, annealing temperature and duration of annealing plateau. Despite an overestimation of ρ_c values, due to voltage drop in the Ni layer, a trend has been identified. Among the conditions tested, lower ρ_c values are obtained for short annealing plateau (3 min) and annealing at 230 and 450°C in comparison with 340°C.

Based on optimized Ni/Cu plating process step conditions determined in previous Chapters, double textured n-PERT pre-cells (50 × 50 mm^2) have been metallized. I-V measurements have been carried out and best cell has been obtained with F_{peak} = 0.32 J/cm^2 and final annealing at 230°C during 3 minutes. Results are promising as cell parameters are found to be similar to reference SP cells, and even better for non annealed (NA) cells.

	J_{SC} (mA/cm^2)	**V_{OC} (mV)**	**FF (%)**	**η (%)**	**R_s (Ω.cm^2) (from Suns-V_{OC})**	**R_{sh} (Ω.cm^2)**
Best cell NA (front side)	38.99	629.25	71.07	17.44	1.77	35855.99
Best cell A (front side)	38.87	625.87	70.06	17.04	1.63	2006.41
Best cell NA (rear side)	36.95	628.17	72.02	16.71	1.72	34916.87
Best cell A (rear side)	37.00	625.16	70.27	16.25	1.71	1978.10
SP reference	35.94 ± 0.053	618 ± 0.3	78.11 ± 1	17.35 ± 0.3	0.75 ± 0.13	25408 ± 20400

The impact of non optimized laser parameters and annealing temperature on solar cell parameters have been demonstrated. For instance, at 380°C cell parameters are severely impacted and this is related to Cu diffusion into Si. An alternative could be to perform the annealing step just after Ni electroless deposition.

Main conclusions and perspectives

In this doctoral research project, Ni/Cu electrochemical metallization (also called "plating") for c-Si solar cells has been studied as an alternative to standard screen-printing (SP). The aim was to address the issues related to Ni/Cu plating and develop an optimized process in order to achieve same or better conversion efficiencies than reference SP cells. For that purpose, the methodology has been to understand the involved reaction mechanisms to improve the Ni/Cu plating process accordingly. This work has been mainly carried out on n-PERT precursors and metallization has been performed on both sides to obtain bifacial cells. The front side is boron doped (p^+) and textured while the rear side is phosphorus doped (n^+) and polished. SiO_x/SiO_xN_y dielectric stack on the rear polished side is denser and has a lower refractive index than the BSG/SiO_xN_y stack on the front textured side. For the different Ni/Cu plating process steps investigated, main conclusions are detailed and some perspectives are proposed.

Selective laser ablation of dielectric layers

The first step of Ni/Cu plating process consists of selectively ablate the dielectric layers on both sides. The difficulty is to efficiently remove the dielectric layers while limiting the laser impact on underlying Si. Laser ablation has been performed with a UV-ps laser by varying the F_{peak} and spots overlapping.

On the rear polished side, five concentric areas having a different surface morphology and chemical composition have been observed after laser ablation with no spots overlapping. This is related to the Gaussian shape of the laser beam and an ablation mechanism based on partial lift-off has been proposed to explain these observations. The presence of SiO_x layers in the center of laser opened areas has been detected and probably originates from remaining initial SiO_x layer and/or laser formed SiO_x.

Overlapping promotes surface roughness on the rear polished side which is beneficial for further metallization steps. On the front textured side, Laser Induced Periodic Surface Structures (LIPSS) have been observed and increase the surface roughness even with no spots overlapping. Due to optical diffusion mechanisms on pyramids, thermal impact is more important on the front textured side and overlapping must be preferably avoided to limit the impact on electrical properties (R_{sheet} and carriers lifetime). Laser ablation on the front textured side is more critical because of the risk to shunt the p/n junction.

A heat-affected area has been observed next to the laser opened areas and Si surface amorphization has been evidenced on both sides for all laser parameters investigated. Carriers lifetime is impacted for all F_{peak} tested, even with no overlapping. This is due to Si amorphization and probably the formation of cracks and dislocations. Laser impact on R_{sheet} is low provided that no spots overlapping is used. With overlapping, higher R_{sheet} values are observed, especially on the front textured side, due to the higher thermal impact. A

post-laser annealing at 750°C allows to partially recrystallize the amorphous Si and improves the electrical properties. Moreover, a fluoride treatment enables to etch the SiO_x layers and the damaged Si surface which improves the carrier's lifetimes.

Finally, two optimized laser parameters have been proposed: F_{peak} = 0.56 J/cm^2 with no overlapping and F_{peak} = 0.32 J/cm^2 with 50% overlapping.

Perspectives: To better understand the laser impact on electrical properties, it would be interesting to perform Secondary Ion Mass Spectroscopy (SIMS) analysis to determine the dopant profiles after laser ablation. Moreover, other post-laser annealing conditions could be tested (higher temperature, longer annealing time etc.) with the aim to achieve a complete recrystallization of amorphous Si.

SI SURFACE DEOXIDATION

Deoxidation in a fluoride media is needed to remove native oxide layer and remaining SiO_x observed after laser ablation. The aim is to completely remove the SiO_x layers without damaging the SiO_xN_y dielectric layers to limit the risk of parasitic plating. Two fluoride media (HF and $NaHF_2$) have been investigated and etching rates of PECVD and anodic SiO_x have been determined and compared to the ones of SiO_xN_y layers on both sides of n-PERT precursors.

Etching rates of both PECVD and anodic SiO_x layers are $\gg$ 2 times faster in $NaHF_2$ while SiO_xN_y layers are etched at the same rate in both fluoride media. Therefore, $NaHF_2$ has a better selectivity compared to HF and SiO_xN_y layers damaging can be limited as shorter immersion times are needed to etch SiO_x layers. In both fluoride media, the SiO_xN_y layer on the front side is etched 3-4 times faster than the one on the rear side. This is mainly related to the higher density and refractive index of SiO_xN_y layer on the rear side.

Perspectives: In a future work, the etching rates of SiO_x layers present on Si surface after laser ablation could be investigated in $NaHF_2$. The methodology based on EIS measurements and established to study the etching rate of anodic SiO_x could be used. That will allow to determine the exact immersion time necessary to completely remove SiO_x layers on both sides after laser ablation.

SI SURFACE ACTIVATION THROUGH PD GALVANIC DISPLACEMENT

Pd particles have a catalytic activity for the further Ni electroless deposition. The Pd galvanic displacement deposition has been studied in both HF and $NaHF_2$ and the aim was to achieve an homogeneous deposition of small Pd particles to activate the Si surface with a limited metal consumption.

A statistical study has been first carried out on n-type mirror polished wafers and the influence of several parameters (immersion time, [$PdSO_4$], solution stirring, [HF] and [$NaHF_2$]) on Pd particles size and density has been understood. $NaHF_2$ fluoride media provides smaller Pd particles with an higher density compared to HF. This behavior has been explained regarding the Si energy band diagram configuration in both fluoride media. Among the conditions tested the best ones are the following: 30 seconds immersion in $NaHF_2$ 0.16 M + $PdSO_4$ 2.5.10^{-4} M (or 5.10^{-5} M), no solution stirring.

These activation conditions have been implemented on n-PERT precursors after ablation with optimized laser parameters. On the rear side opened with no spots overlapping, Pd particles deposition is not uniform

on the different concentric areas observed previously. Remaining SiO_x layers in the center of laser opened areas hinder the activation process but the fluoride treatment needed to obtain a uniform Pd particles deposition ($NaHF_2$ 0.5 M, 1 min) is too aggressive towards the dielectric layers and leads to important parasitic plating. Nevertheless, a good compromise has been found to start depositing some Pd particles in the center of laser opened areas (random etching of SiO_x layer) while preserving the SiO_xN_y dielectric layers. It consists of: a prior deoxidation in $NaHF_2$ 0.16 M during 1 m 30 followed by Pd activation in $NaHF_2$ 0.16 M + $PdSO_4$ 5.10^{-5} M 30 seconds (no stirring). Prior deoxidation is not mandatory for Pd activation on the front textured side and the rear polished side opened with laser spot overlapping. Nevertheless, this treatment is recommended as it enables to obtain smaller Pd particles. Best conditions are summarized in Table 5.18.

Table 5.18: Best deoxidation and Pd activation conditions on both n-PERT precursors sides after laser ablation using optimized parameters.

	F_{peak} = 0.56 J/cm^2, no overlapping	**F_{peak} = 0.32 J/cm^2, 50% overlapping**
Rear polished side	Deoxidation: $NaHF_2$ 0.16 M 1m30 Activation: $NaHF_2$ 0.16 M + $PdSO_4$ 5.10^{-5} M 30s, no stirring	$NaHF_2$ 0.16 M 30s Activation: $NaHF_2$ 0.16 M + $PdSO_4$ 5.10^{-5} M 30s, no stirring
Front textured side	$NaHF_2$ 0.16 M 30s Activation: $NaHF_2$ 0.16 M + $PdSO_4$ 5.10^{-5} M 30s, no solution stirring	$NaHF_2$ 0.16 M 30s Activation: $NaHF_2$ 0.16 M + $PdSO_4$ 5.10^{-5} M 30s, no stirring

Perspectives: A perspective of this work would be to avoid the use of expensive Pd material. In alkaline fluoride media (NH_4F), the Si band diagram configuration is theoretically favourable for the galvanic displacement of Ni^{2+} ions. Therefore, a thin layer of nickel could be deposited and further thickened by Ni electroless deposition process.

Ni electroless deposition

Ni electroless deposition has been then investigated and homogeneity as well as adherence issues have been evidenced. The geometry of laser opened areas affects the Ni electroless deposition rate such as the fingers are metallized faster than busbars.

Moreover, both sides are not metallized at the same rate if illumination conditions are not controlled (front p^+ side is not metallized at all in some cases). This can be explained by the photogeneration of charges carriers, leading to an increased holes concentration on the front p^+ side and a diminution of band bending in the semiconductor. Thus, holes on the p^+ side can recombine with the electrons resulting from oxidation of the reducing agent which are not available anymore to reduce the Ni^{2+} ions. It has also been proposed that holes may dissolve the catalytic Pd particles and/or the Ni nuclei as soon as they are deposited. Ni electroless deposition must therefore be performed in dark conditions. Stirring must also be carefully chosen to regenerate the solution at Si surface without removing mechanically the Ni clusters from the Si surface (200 rpm was suitable for our experiments).

The adherence of Ni layers deposited with 3 different electroless processes (Fraunhofer collaboration) have been investigated with APiC method. Poor adherence at Ni/Si interface has evidenced on the rear polished side for samples metallized at IPVF. Consequently, Ni/Si interdiffusion during annealing was not uniform and adherence issues remained. SEM images suggested that delamination mainly happens at Ni/Ni_xSi_y interface. In any case, adherence is better on the front side thanks to higher roughness. Due to ad-

herence issues on the rear polished side, this work has been pursued on double textured n-PERT precursors.

Perspectives: To address homogeneity issues, a further work could be performed on busbarless cells and it would be interesting to laser open the busbar with several fingers closed to each other but not in contact. A better control of Ni deposition requires additional experiments to understand the influence of different bath components, temperature and pH. The formation of a native oxide at Ni/Si interface is believed to lead to high contact resistivity and poor adherence so it should be considered to add a fluoride media (NH_4F) into the Ni electroless bath. To tackle adherence issues at Ni/Ni_xSi_y interface, the following alternative, proposed in literature, could be implemented: the Ni layer is first annealed and unreacted Ni is chemically removed before the redeposition of a Ni layer acting as Cu diffusion barrier.

CU ELECTROLYTIC DEPOSITION AND FINAL ANNEALING

Transmission Line Measurements (TLM) were performed after Ni electroless deposition and annealing by varying the annealing temperature, annealing plateau duration and Ni layer thickness. The contact resistivities appeared to be overestimated due to potential drop into Ni layer during TLM, indicating that Cu layer should have been deposited before measurements. Some trends have been nevertheless observed: lower contact resistivities have been observed with short annealing times (3 min) at 230 or 450°C in comparison with longer annealing times (6 and 9 min) and other annealing temperature tested (340°C).

The main difficulty of Cu electrolytic deposition is to contact both sides of the cell without breaking it. Globally, the width of metallized fingers is about 2 times larger than laser opened area and this is mainly due to overflow of Ni electroless deposition. Regarding the results obtained in this work, 50×50 mm^2 double textured n-PERT precursors have been metallized with the optimized Ni/Cu plating process in Figure 5.17 (best laser parameters = F_{peak} = 0.32 J/cm^2, 50% overlapping). I-V measurements have been carried out and similar cell parameters than reference SP cells have been obtained. The best cell non annealed has even better parameters than SP reference with: η = 17.44 % (+ 0.09 %), V_{OC} = 629.25 mV (+ 11.25 mV), I_{SC} = 38.99 mA.cm^{-2} (+ 3.05 mA.cm^{-2}), FF = 71.07 % (- 7.04 %) (I-V performed on the front side). The impact of non optimized laser parameters and annealing temperature on cell parameters have been demonstrated. For instance, after an annealing at 380°C during 3 min, cell parameters are severely impacted which is probably related to Cu diffusion into Si.

Perspectives: It would be useful to study in more details the impact of annealing conditions on nickel silicides (and palladium silicides) phases formation through DRX measurements (in-situ DRX). With the aim to suppress the risk of Cu diffusion during annealing, an alternative could be to perform the annealing step just after Ni deposition. The impact of deoxidation and activation conditions on cell efficiency could also be studied and cell efficiency with and without a PLA could be compared. Finally, the pitch between fingers as well the width of busbars and the height of Ni and Cu layers should be optimized (grid design with Quokka software for instance).

Appendices

Appendix A

Contact resistance determination by Transmission Line Measurements (TLM)

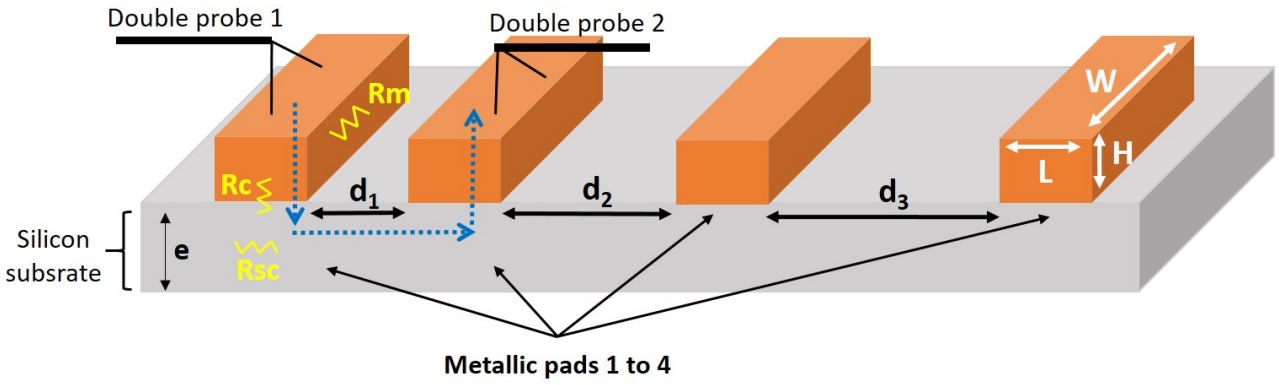

Figure A.1: Schematic representation of typical TLM structure.

Transmission Line Measurements consists of measuring the resistance between two metallic pads by means of two probes, as represented in Figure A.1, and repeating this at different distances d_i between probes. For each measurement, the current passes through 1) the metallic contact of pad 1 having a resistance R_m 2) the metal/Semiconductor interface of pad 1 having a contact resistance R_c 3) the semiconductor having a resistance R_{sc} 4) the interface Semiconductor/metal of pad 2 5) and finally through the metallic contact of pad 2 (blue arrow in Figure A.1). In a first approximation, we consider that R_c, R_{sc} and R_m are homogeneous along the TLM structure. The total resistance R_T for each measure is given by equation A.1 and R_{sc} depends on the distance d_i as shown is equation A.2.

$$R_T = 2R_m + 2R_c + R_{sc} \tag{A.1}$$

$$R_{sc} = \frac{\rho_{sc} \times d_i}{e \times W} = R_{sheet} \times \frac{d_i}{W} \tag{A.2}$$

with R_m the metallic pad resistance (Ω), R_C the contact resistance (Ω), R_{SC} the semiconductor resistance (Ω), ρ_{sc} the semiconductor resistivity (Ω.cm), e the semiconductor thickness (cm), d_i the distance between the two pads (cm), W the pad length (cm), L the pad width (cm) and R_{sheet} the semiconductor sheet resistance (Ω/sq).

In Si solar cells, doped areas such as the emitter are not homogeneous and dopant atoms are mainly present close to the surface. The thickness is thus complex to determine and the parameter R_{sheet} is used to

evaluate Si doping such as $R_{sheet} = \frac{\rho_{sc}}{e}$.

Finally R_T is given by equation A.3 and can be plotted as a function of distance d_i as represented in Figure A.2 a). On the as-obtained curve, the slope gives R_{sheet}/W, y-intercept is equal to $2(R_c + R_m)$ and x-intercept allows to determine the transfer length parameter (L_T).

$$R_T = 2R_m + 2R_c + R_{sheet} \times \frac{d_i}{W} \tag{A.3}$$

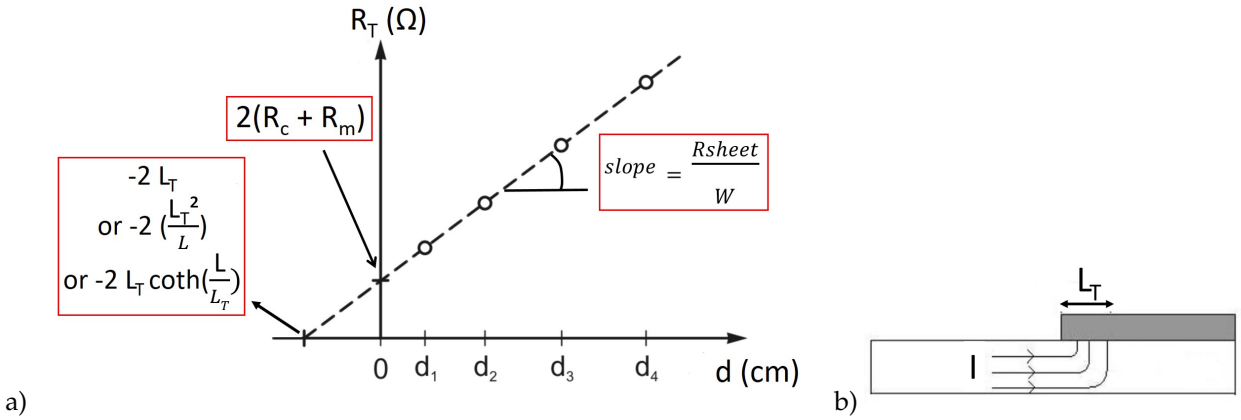

Figure A.2: a) Curve obtained by plotting total resistance as a function of pads spacing d_i b) Illustration of transfer length (L_T) concept.

L_T corresponds to the average distance travelled by charges in the semiconductor beneath the contact, before passing into the contact (Figure A.2 b)). It is defined as:

$$L_T = \sqrt{\frac{\rho_c}{R_{sheet}}} \tag{A.4}$$

with L_T the transfer length, ρ_c the contact resistance and R_{sheet} the semiconductor sheet resistance.

Most of the time, R_m contribution can be neglected (or easily determined by measuring the pad line resistance) and R_c is given by y-intercept (O.O). It can be expressed according to the contact resistance ρ_c in three different ways depending on L_T value against L:

$$\text{for } 0.5\,L_T \leq L \leq 1.5\,L_T \qquad R_c = \frac{\rho_c}{L_T \times W} \times \coth\left(\frac{L}{L_T}\right) \tag{A.5}$$

$$\text{for } L \geq 1.5\,L_T \qquad R_c = \frac{\rho_c}{L_T \times W} \tag{A.6}$$

$$\text{for } L \leq 0.5\,L_T \qquad R_c = \frac{\rho_c}{L \times W} \tag{A.7}$$

Using equations A.3, A.4, A.5, A.6 and A.7, L_T can be determined with the x-intercept (A.O) such as:

for 0.5 $L_T \leq L \leq 1.5\ L_T$	for $L \geq 1.5\ L_T$	for $L \leq 0.5\ L_T$
$2R_c + R_{sheet} \times \frac{A.O}{W} = 0$	$2R_c + R_{sheet} \times \frac{A.O}{W} = 0$	$2R_c + R_{sheet} \times \frac{A.O}{W} = 0$
$2\frac{\rho_c}{L_T \times W} \times \coth\left(\frac{L}{L_T}\right) + R_{sheet} \times \frac{A.O}{W} = 0$	$2\frac{\rho_c}{L_T \times W} + R_{sheet} \times \frac{A.O}{W} = 0$	$2\frac{\rho_c}{L \times W} + R_{sheet} \times \frac{A.O}{W} = 0$
$2\frac{R_{sheet} \times L_T^2}{L_T \times W} \times \coth\left(\frac{L}{L_T}\right) + R_{sheet} \times \frac{A.O}{W} = 0$	$2\frac{R_{sheet} \times L_T^2}{L_T \times W} + R_{sheet} \times \frac{A.O}{W} = 0$	$2\frac{R_{sheet} \times L_T^2}{L \times W} + R_{sheet} \times \frac{A.O}{W} = 0$
$A.O = -2L_T \coth\left(\frac{L}{L_T}\right)$	$A.O = -2L_T$	$A.O = -2\frac{L_T^2}{L}$

Finally, the contact resistance can be expressed as follow:

for 0.5 $L_T \leq L \leq 1.5\ L_T$	for $L \geq 1.5\ L_T$	for $L \leq 0.5\ L_T$
$\rho_c = R_c \times L_T \times W$	$\rho_c = R_c \times L_T \times W$	$\rho_c = R_c \times L \times W$
ρ_c can be calculated by defining L_T as solution of equation $A.O = -2L_T \coth\left(\frac{L}{L_T}\right)$	$\rho_c = \frac{O.O}{2} \times \frac{-A.O}{2} \times W$	$\rho_c = \frac{O.O}{2} \times L \times W$

We have described the ideal case but different factors can influence the accuracy of TLM measurement: pad length (possible drop voltage), edge shunting, current flow through intermediate pads, non-uniform contact resistance, non uniform sheet resistance. Some methods to take into account these parameters and optimize TLM structure geometry for accurate measurements are described in reference [69].

Appendix B

Laser ablation parameters

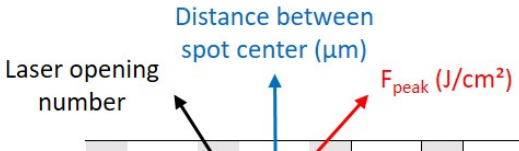

1	4 2.159	2	8 2.159	3	12 2.159	4	16 2.159	5	20 2.159	6	24 2.159	7	28 2.159	8	32 2.159	9	36 2.159
10	4 1.809	11	8 1.809	12	12 1.809	13	16 1.809	14	20 1.809	15	24 1.809	16	28 1.809	17	32 1.809	18	36 1.809
19	4 1.385	20	8 1.385	21	12 1.385	22	16 1.385	23	20 1.385	24	24 1.385	25	28 1.385	26	32 1.385	27	36 1.385
28	4 0.896	29	8 0.896	30	12 0.896	31	16 0.896	32	20 0.896	33	24 0.896	34	28 0.896	35	32 0.896	36	36 0.896
37	4 0.766	38	8 0.766	39	12 0.766	40	16 0.766	41	20 0.766	42	24 0.766	43	28 0.766	44	32 0.766	45	36 0.766
46	4 0.668	47	8 0.668	48	12 0.668	49	16 0.668	50	20 0.668	51	24 0.668	52	28 0.668	53	32 0.668	54	36 0.668
55	4 0.505	56	8 0.505	57	12 0.505	58	16 0.505	59	20 0.505	60	24 0.505	61	28 0.505	62	32 0.505	63	36 0.505
64	4 0.448	65	8 0.448	66	12 0.448	67	16 0.448	68	20 0.448	69	24 0.448	70	28 0.448	71	32 0.448	72	36 0.448
73	4 0.269	74	8 0.269	75	12 0.269	76	16 0.269	77	20 0.269	78	24 0.269	79	28 0.269	80	32 0.269	81	36 0.269
82	4 0.130	83	8 0.130	84	12 0.130	85	16 0.130	86	20 0.130	87	24 0.130	88	28 0.130	89	32 0.130	90	36 0.130

Appendix C

Morphological characterization techniques

C.1 Scanning electron microscopy (SEM)

The scanning electron microscope produces images by scanning the sample with a focused electron beam. This latter penetrates to a depth of a few microns, depending on the accelerating voltage and the sample density. Interactions between electrons and matter produce secondary electrons (SE), backscattered electrons (BSE) and X-rays (Figure C.1 b)) collected by different detectors (Figure C.1 a). As represented in Figure C.1 c), they are extracted more or less deeply from the analysed material and the interaction volume between the incident beam and the material has a peer-like shape. These signals allow to display an image of the analyzed surface with topography and/or chemical composition contrast.

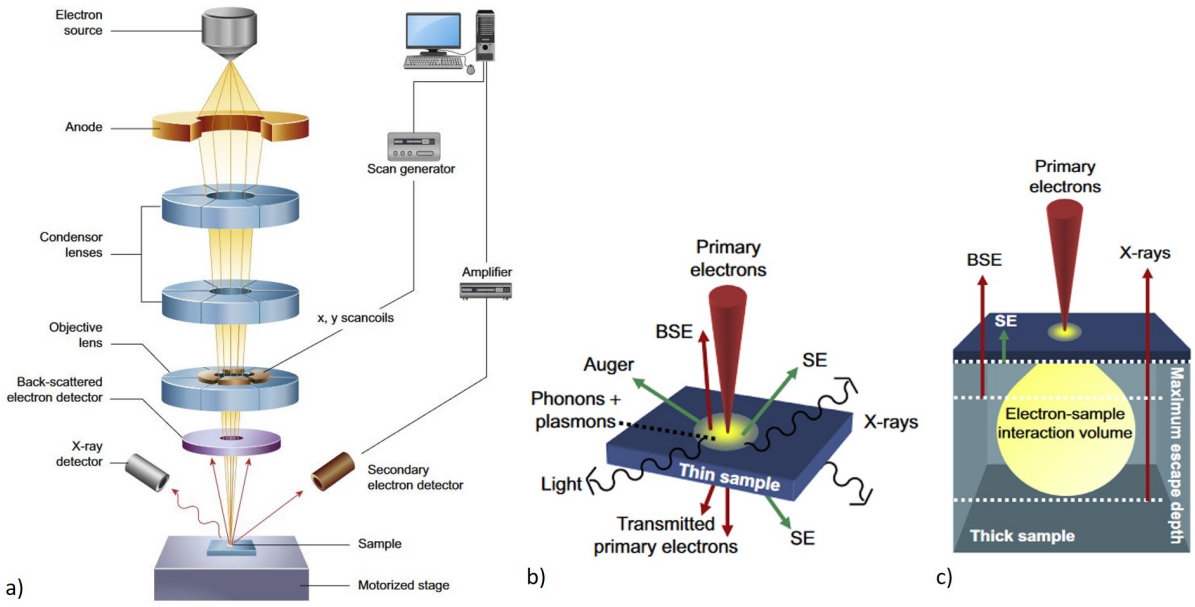

Figure C.1: a) Representation of the different components of a SEM b) interaction between the sample and the incident electron beam c) peer-like shape interaction volume. [207]

The BSE come from the incident electron beam deviated after interaction with atoms nuclei. Their energies are close to the incident electron beam one but vary depending on atomic number of elements analyzed.

Typically, heavier elements appear more brightly on SEM images than lighter ones. BSE give mainly information on chemical composition contrast while SE are more suitable to obtain topography contrast. SE come from the analyzed sample: incident electrons beam transfers a part of its energy to extract an electron low-energy electrons emission. SE come from superficial layers of the sample due to their low energy and their intensities depend on sample inclination. Topography information are thus obtained. Finally, the incident electrons beam can knocked-off electrons from sample atoms and create a subsequent transition occurs; an electron from an higher-energy shell fills the hole created. The energy difference of this transition is released in the form of a characteristic X-ray and the corresponding energy can be directly attributed to a specific element. This analysis is called Energy Dispersive Spectrocopy (EDS).

In this work, images have been realized with a Zeiss Merlin VP compact SEM. Unless otherwise, images are obtained at 15 keV as operating voltage, 3.8 mm working distance and by detection of BSE. EDS analysis are obtained using Bruckers silicon Drift Detectors and 10.5 mm working distance. Unless otherwise, operating voltage is 15 keV.

C.2 Confocal Laser Scanning Microscopy

In conventional microscopy, the whole sample is illuminated and image is not completely clear due to emitted light from non focal plans. To tackle this, Confocal Laser Scanning Microscope (CLSM) uses laser light focused onto a defined spot at a specific depth within the sample. The sample is scanned in x-y directions and then along z-axis to re-construct a clear three dimension image. The different components of a CLSM are schematized in Figure C.2. In this work, we used LEXT OLS 5000 CLSM equipment from Olympus (405 nm laser source). The equipment analysis software enables to analyse the surface morphology and in particular the roughness of the samples.

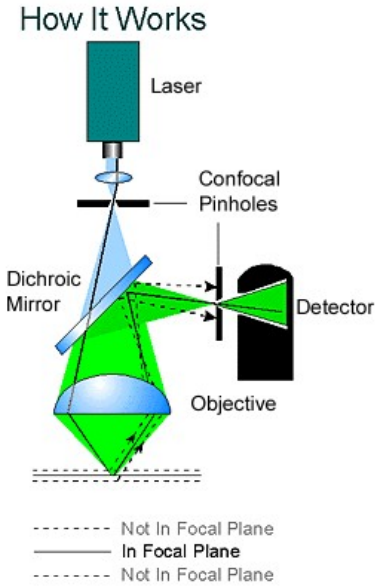

Figure C.2: Working principle of a Confocal Laser Scanning Microscope [208].

Appendix D

Surface and bulk composition analysis techniques

D.1 X-ray Photoelectron Spectroscopy (XPS)

XPS consists of using an X-ray source (AlKα and MgKα are the main sources available in laboratory) to bombard the analyzed surface and ionise atoms. Emitted electrons are collected by a detector which determines their kinetic energy (E_{KE}). Then, binding energy of each electron (E_{BE}) is calculated according to equation D.1. As a result, an XPS spectrum represents the number of electrons detected as a function of their binding energy (Figure D.1).

$$E_{KE} = h\nu - KE_{BE} \tag{D.1}$$

with E_{KE} and E_{BE} the electron kinetic and binding energies, h the Planck's constant, ν the X-Ray frequency and K a constant.

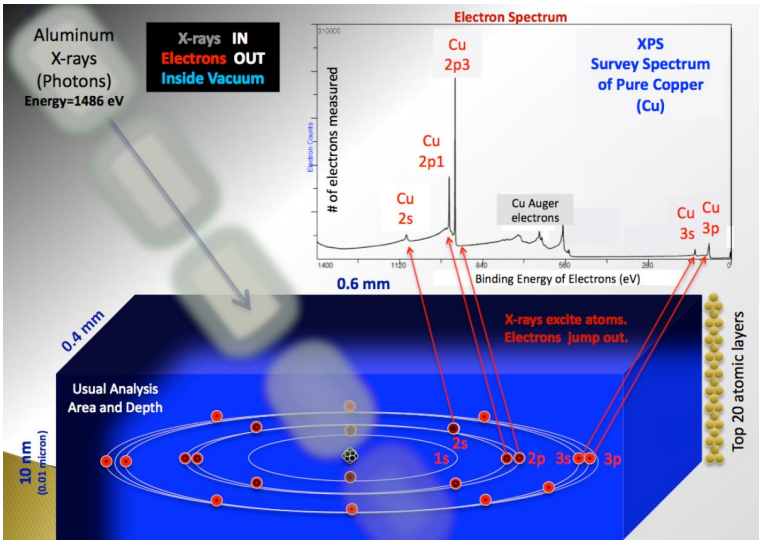

Figure D.1: Working principle of XPS and typical obtained spectrum [209].

The E_{BE} calculated are specific to atoms present in the material so the elemental composition of the surface can be determined. As the number of collected electrons is related to the atomic concentration of

each element identified, XPS is a also a quantitative technique. XPS is also sensitive to chemical states of elements and chemical environment. The analyzed depth is ≈ 10 nm but it is possible to etch the surface with an inert gas ion gun (Argon) to investigate sample composition in its depth (profiling).

In this work, analyses have been carried out with a Thermo Electron K-Alpha$^+$ spectrometer using a monochromatic Al-Kα X-Ray source (1486.6 eV). The Thermo Electron K-Alpha$^+$ spectrometer procedure is used to calibrate the spectrometer and verified using Cu and Au samples following the ASTM-E-902-94 standard procedure. Acquisition parameters of high energy resolution photopeaks are: 400 µm spot size, 12 kV primary energy, 6.0 mA emission intensity, Constant Analyser Energy mode (CAE) 10 eV and 0.05 eV energy step size. Data are processed using the Thermo Fisher scientific Avantage data system with the sensitivity factors of AlThermo1 library. The background is calculated using the Shirley method. The peaks modeling is performed using Gaussian/Loretzian mix (30%).

D.2 Scanning Auger electron Microscopy (SAM)

Like XPS, SAM measures the kinetic energy (E_{KE}) of an emitted electron to determine its binding energy (E_{BE}) and identify the elements present in the sample and their chemical state. However there are two main differences with XPS:

- Firstly, XPS uses an X-ray beam to eject an electron while SAM uses an electron beam.
- Secondly, XPS analyzes electron directly ejected from inner-shell (typically K shell) while SAM analysed emitted electron created by an Auger process and coming from higher shell (typically L or M).

An Auger electron comes from a cascade of events described in Figure D.2. SAM spectrum displays the number of collected Auger electrons as a function of electron kinetic energy and peaks intensity is related to each elements concentration. SAM analyses the extreme surface of sample with a depth limited to 1-5 nm and an analysis spot size ≈ 10 nm.

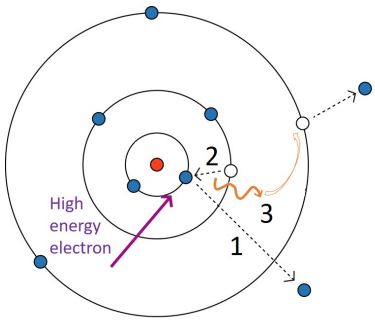

1: High energy electron beam ejects a core electron (typically from K shell) creating a vacancy;

2: A electron from an higher shell (typically from L shell) drops down to fill the vacancy;

3: The photon energy released by process 2 enables to eject another electron from an higher shell (from L or M shell). This electron is called « Auger electron »

Figure D.2: Illustration of electron Auger emission process.

JEOL JAMP 9500 F equipment have been used for SAM analysis with a 12-15 nm spot size and a depth probe < 4 nm. Acquisition is performed at 20 kV, 10 nA without tilt and quantification has been realized with derivative spectra (diff9) and JEOL RSF factors.

Appendix E

Opto-electronical characterization techniques

E.1 Four-probe measurements

The four-probe method is often used to measure thin film sheet resistance. Four equally-spaced, co-linear probes are put into the surface material and a direct current is applied between the outer two probes. Meanwhile, the voltage drop is measured between the inner two probes (Figure E.1). Separation of current and voltage electrodes eliminates the lead and contact resistances from the measurement.

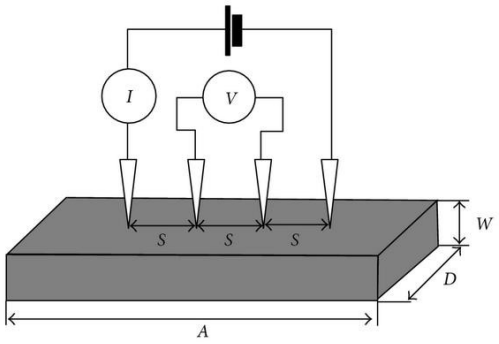

Figure E.1: Working principle of 4-probe measurement.

The sheet resistance can be calculated using equation E.1 with a correcting factor generally equal to $\frac{\pi}{\ln 2}$ = 4.532. However, this is only valid when the distance between probes is small compared to sample size. Most accurate values are obtained when measurement are performed in the center of the sample. If the thickness (e) of the material is known, R_{sheet} can be used to calculate the material resistivity (equation E.2).

$$R_{sheet} = F' \times \frac{\Delta V}{I} \tag{E.1}$$

$$\rho = 4.532 \times \frac{\Delta V}{I} \times e \tag{E.2}$$

with R_{sheet} the sheet resistance (Ω/sq), ΔV the voltage drop (V), I the applied current (A), F' the correcting factor, e the material thickness (cm) and ρ the material resistivity (Ω.cm)

Appendix F

Potential-pH equilibrium diagrams

This appendix is based on reference [96]

F.1 System silicon-water at 25°C

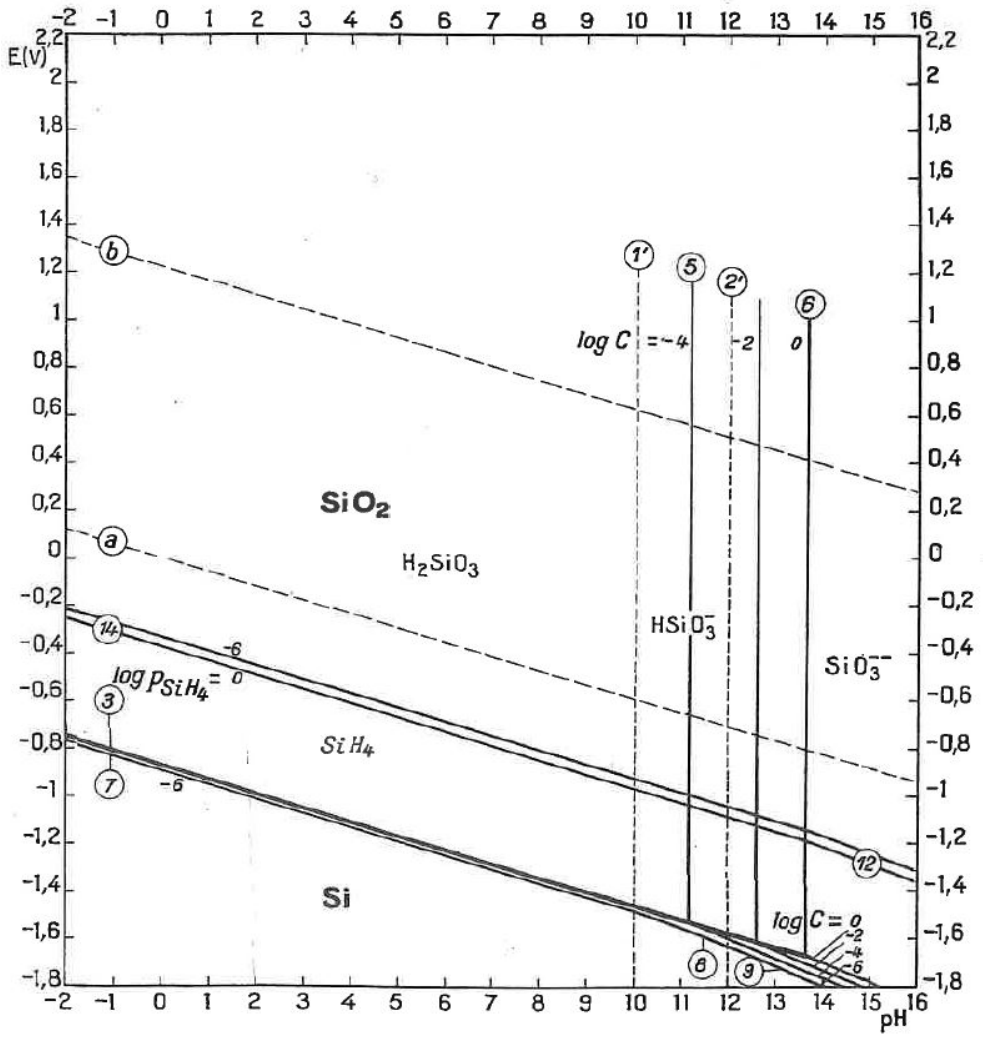

F.2 System phosphorus-water at 25°C

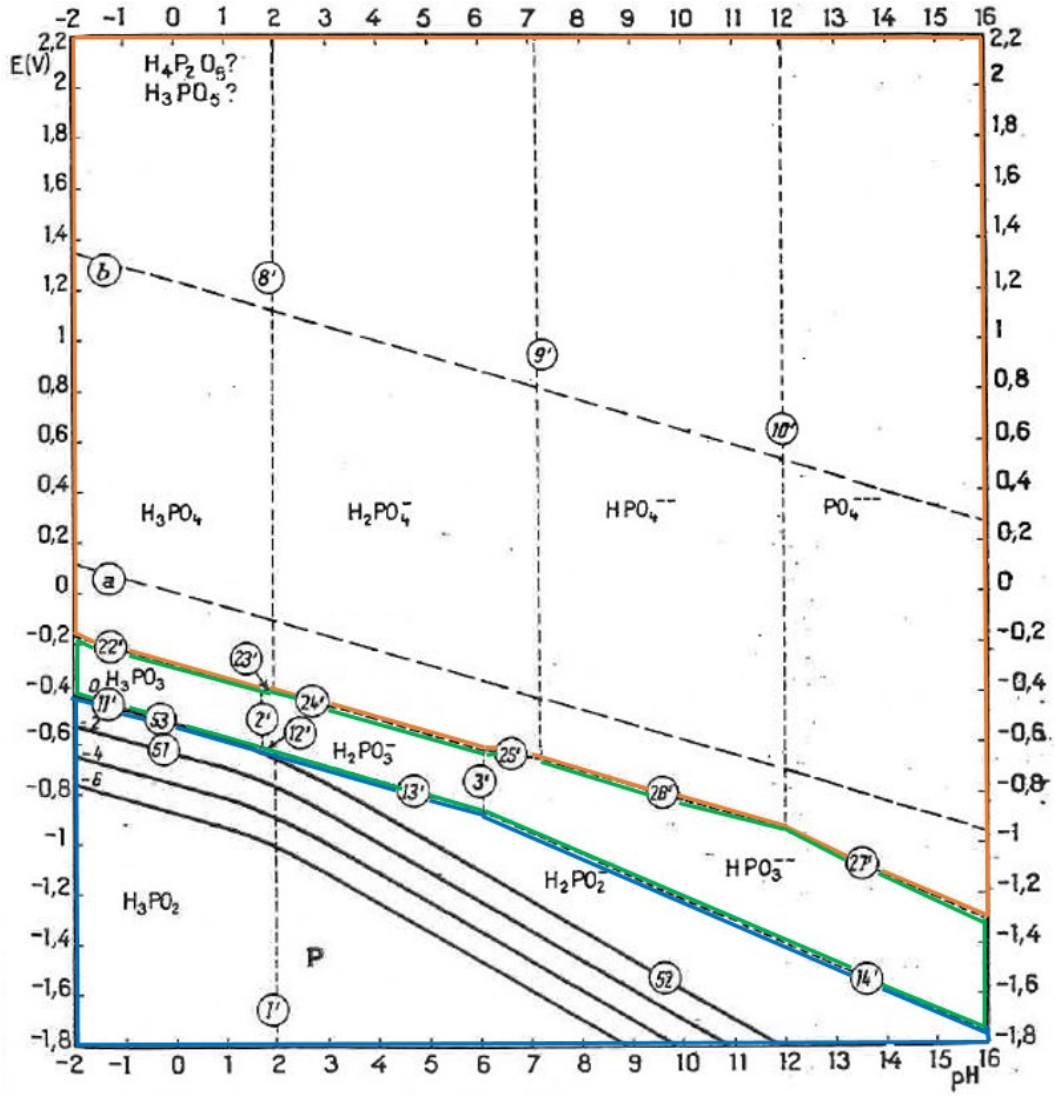

Blue area: oxidation degree I

Green area: oxidation degree III

Orange area: oxidation degree V

Appendix G

Electrochemical Impedance Spectroscopy (EIS) method

This Appendix is based on literature [180]. EIS is a non-steady state technique commonly used to study electrochemical processes at electrode surfaces. Indeed, electrodes are generally subjected to both faradic and non-faradic processes, with various elementary processes not evolving at the same speed, and steady-state techniques do not allow to analyze separately the different contributions involved in the electrochemical process. EIS consists of analyzing the response to a sinusoidal perturbation with a small amplitude. By varying the analysis frequency, fast electrochemical processes occurring at high frequencies can be dissociated from slow processes occurring at low frequencies.

In this work, Staircase Potentio-Electrochemical Impedance Spectroscopy (SPEIS) have been performed. As illustrated in Figure G.1, a sinusoidal potential perturbation x(t), with an amplitude ΔE and a pulsation ω, is applied at different frequencies for each potential step chosen (equation G.1). The pulsation can be expressed according to the frequency (f) such as $\omega = 2\ \Pi f$. In our case, the potential amplitude is 20 mV and the frequency ranges from 0.1 Hz to 500 kHz. The current response y(t) (equation G.2) is analyzed as function of frequency at various potential steps and is characterized by an amplitude ΔI and a dephasing ϕ.

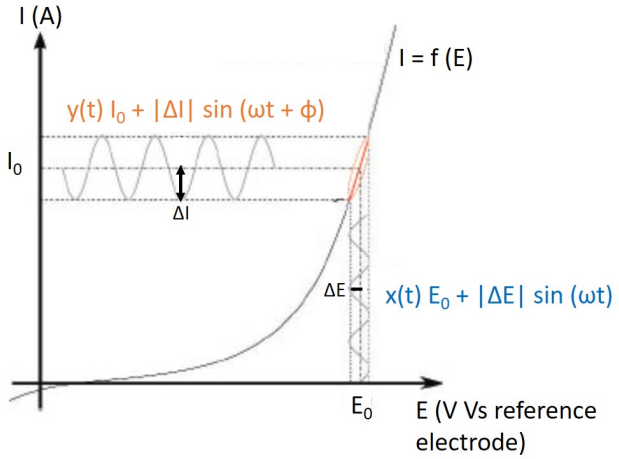

Figure G.1: Working principle of Staircase Potentio-Electrochemical Impedance Spectroscopy (SPEIS).

$$x(t) = |\Delta E| sin(\omega t) \tag{G.1}$$

$$y(t) = |\Delta I| sin(\omega t + \phi) \tag{G.2}$$

The electrochemical impedance Z(t) can be defined as a complex resistance encountered when the current pass through a system composed of different resistances, capacitors and inductors. An analogy with the Ohm's law allows to define Z(t) as the ratio of input voltage and the output measured current such as:

$$Z(t) = \frac{E(t)}{I(t)} = \frac{|\Delta E| sin(\omega t)}{|\Delta I| sin(\omega t + \phi)} = |Z| \frac{sin(\omega t)}{sin(\omega t + \phi)} \tag{G.3}$$

with $|Z|$ the magnitude equal to $\frac{|\Delta E|}{|\Delta I|}$

Then, Euler's relations enable to express the complex form of the impedance with a real and an imaginary part (Z_{real} and Z_{im}) and the global expression is:

$$Z(\omega) = |Z| e^{j\phi} = |Z|(cos(\phi) + j sin(\phi)) = Z_{real}(\omega) + Z_{im}(\omega) \tag{G.4}$$

An electrochemical system can be schematized by an equivalent circuit using different components having their own impedance value. The most commons are:

- **Impedance of a resistance ($\mathbf{Z_R(\omega)}$)(Ω)**: a resistance does not imply a dephasing between the input potential and the output current so $Z_R(\omega)$ is directly equal to the resistance R in Ω;
- **Impedance of a capacitor ($\mathbf{Z_C(\omega)}$)(Ω)**: a capacitor implies a dephasing of 90° and is only characterized by the imaginary component such as $Z_C(\omega) = \frac{1}{jC\omega}$ with C the capacitance in Farad;
- **Impedance of an inductor ($\mathbf{Z_I(\omega)}$)(Ω)**: an inductor implies a dephasing of - 90° and is only characterized by the imaginary component such as $Z_I(\omega) = jL\omega$ with L the inductance in Henry.
- **Impedance of a constant phase element (CPE) ($\mathbf{Z_Q(\omega)}$)($\Omega^{-1}.s^{\alpha}$)**: CPE are used to represent an imperfect capacitor where some properties of the system are not homogeneous. CPE impedance is given by $Z_Q(\omega) = \frac{1}{Q \times (j\omega)^{\alpha}}$ with $0 < \alpha < 1$. $Z_Q(\omega)$ is independent of the frequency and has a value of -($90 \times \alpha$) degrees.

The different components R, C, L and CPE can be determined by fitting the Nyquist and Bode diagrams of the global impedance $Z(\omega)$ with models of equivalent circuits. The Nyquist diagram represents - Z_{im} as a function of Z_{real} and Bode diagram represents ϕ and $\log(|Z|)$ as a function of $\log(\omega)$ (or log(f)). Two common examples, parallel R/C and serie R-C equivalent circuits, are given in Figure G.2. In these cases, R can be easily determined on the Nyquist diagram when ω tends toward zero or infinite. C is calculated by identifying the critical frequency f_c (equation G.5). Indeed, f_c corresponds to the frequency at a phase of 45° by the Bode diagram.

$$f_c = \frac{1}{2\pi RC} \tag{G.5}$$

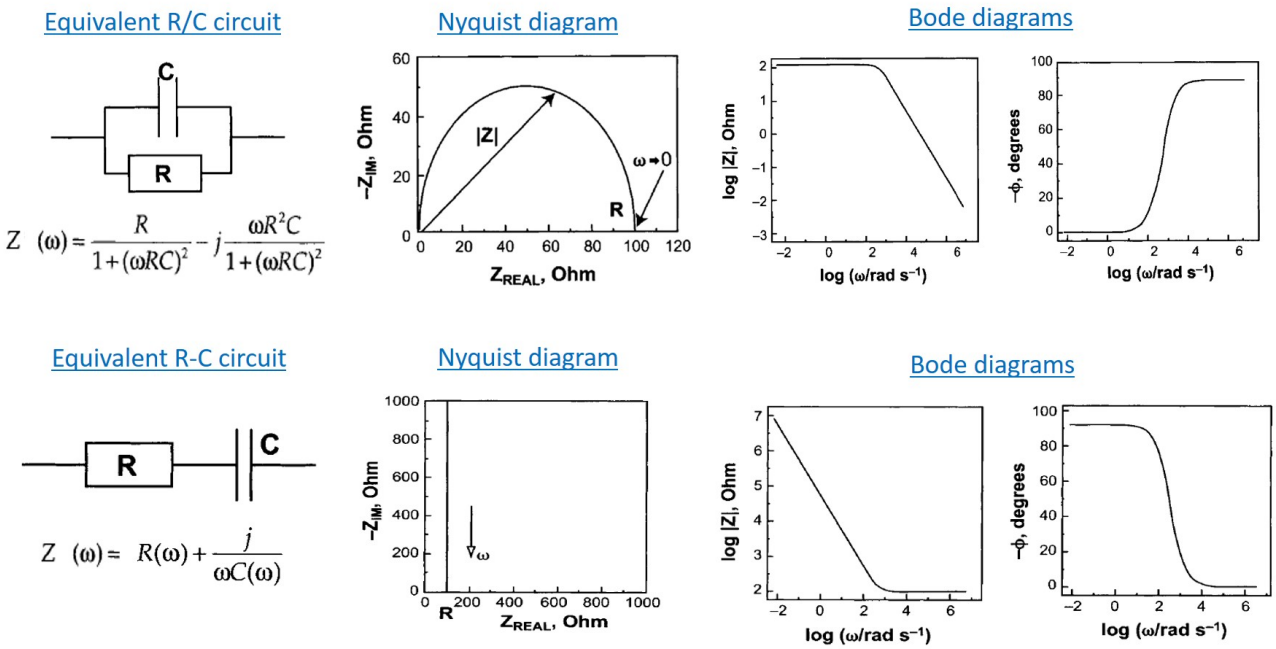

Figure G.2: Illustration of Nyquist and Bode diagrams for R/C and R-C equivalent circuits [180].

Appendix H

Adherence characterization with Acoustic Picoseconds Colored method (APiC)

Elastic properties of materials can be measured by using acoustic wave propagation. Maris et al. have been the first to adapt this method for thin film and at nanoscale by using picosecond ultrasonic technique [210], [211]. Then, it appeared that acoustico-optic detection mechanisms were sensitive to laser wavelength used. Thus, the picosecond ultrasonic technique has been improved by Devos et al. who have developed the so called "Picoseconds Colored method" (APiC) [212].

APiC is a contactless and semi-quantitative optical technique method to measure adherence of thin films [213]. The working principle is schematized in Figure H.1 and described below.

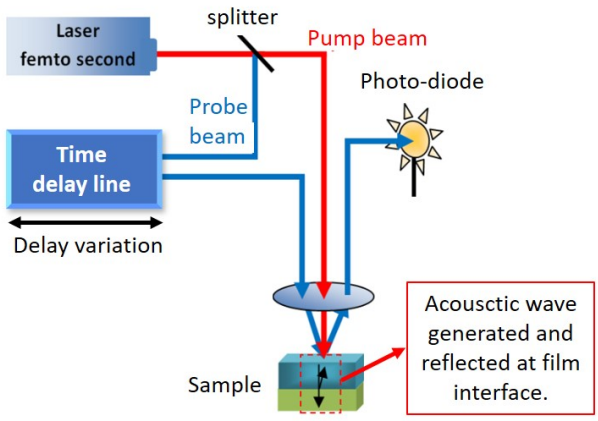

Figure H.1: Working principle of APiC measurements from [214].

A femtosecond laser source is used to generate an optical pulsed beam which is splitted in two parts:

1. One part serves as a pump beam and is focused on the sample surface where it is absorbed. This pulse generates an acoustic wave and propagates in the film at the longitudinal sound velocity. At the sample interfaces, the pulse is reflected and the corresponding echos returns to the surface.
2. The other part serves as probe beam and is focused at the same site on the sample but with a certain delay adjusted to monitor the successive echoes generated by the pump beam. Due to an acoustico-optic coupling between the probe beam and the echoes, the dielectric constant of the film is changed.

Finally, a spectrum representing the transient reflectivity as a function of the time delay is obtained as illustrated in Figure H.2.

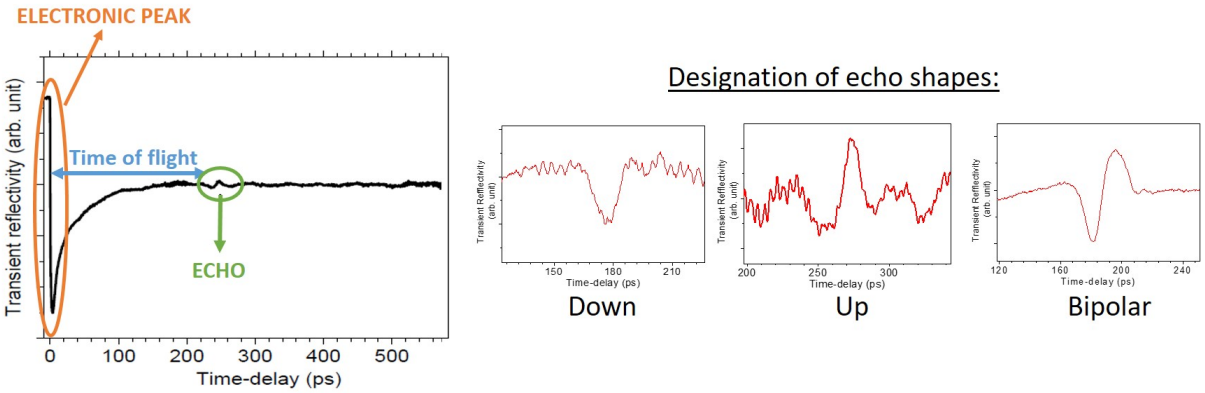

Figure H.2: Typical APiC spectrum: the time delay gives information on film thickness while echo amplitude provides adherence properties.

The first electronic peak is related to the surface chemistry and the echo amplitude allows to assess the film adherence. Indeed, a poor adherence is characterized by a high reflectivity due to defects at the interface [215]. Moreover, the time of flight corresponds to a go and return of the pump beam into the film and therefore enables to calculate the film thickness according to equation H.1.

$$e = \frac{\Delta t \times \nu}{2} \tag{H.1}$$

with e the film thickness, Δ t the time of flight and ν the sound velocity in the film.

Appendix I

Impact of non optimized laser parameters on contact resistivity

This appendix presents the results of TLM measurements after Ni/Cu plating on samples laser opened with two non optimized laser parameters and the two optimized laser parameters determined in Chapter 3. The lowest contact resistivity is obtained with F_{peak} = 0.32 J/cm^2 and 50% overlapping. Line resistivity has been measured and is equal to 3.7.10^{-6} Ω.cm.

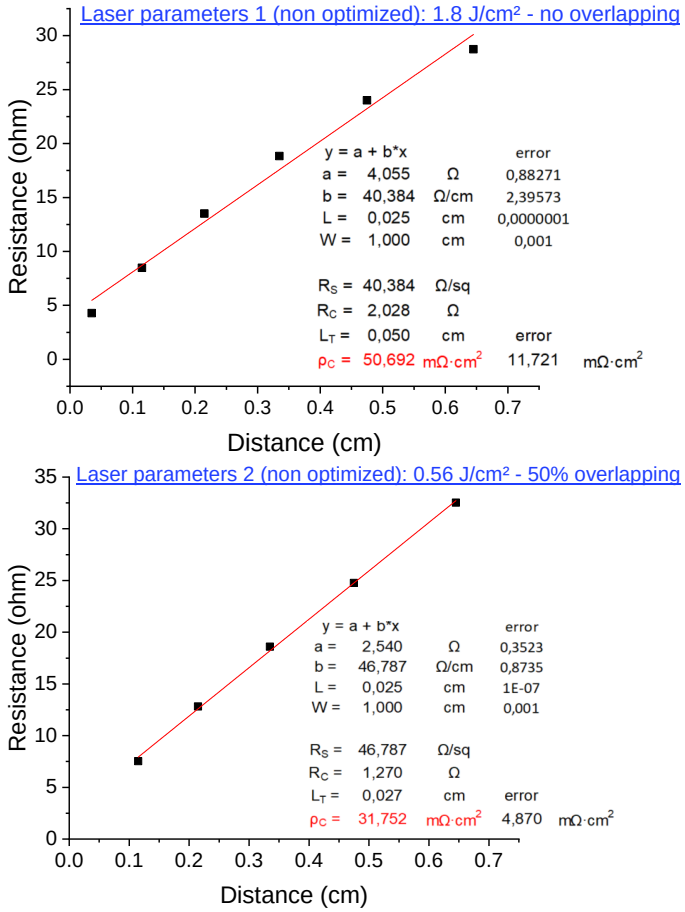

Figure I.1: Results of TLM measurements for samples laser opened with non optimized parameters.

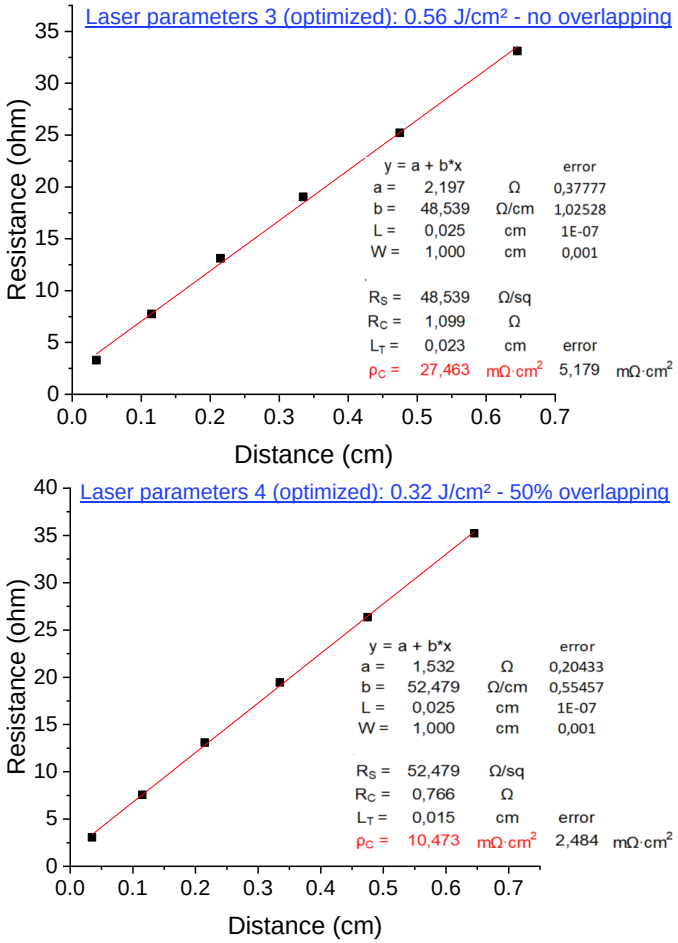

Figure I.2: Results of TLM measurements for samples laser opened with optimized parameters.

Résumé en Français

INTRODUCTION

L'éclairement d'une cellule solaire en silicium cristallin (c-Si) permet de générer des porteurs de charges (paires électron-trou) qui vont être séparés par une jonction p/n puis collectés au niveau de contacts métalliques. Une représentation schématique est donnée sur la Figure 3.

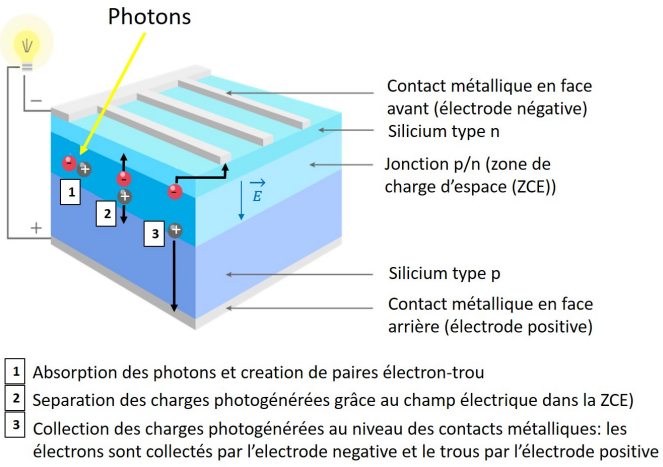

Figure 3: Principe de fonctionnement d'une cellule solaire en silicium cristallin.

Les performances d'une cellule solaire peuvent être déterminées en réalisant des mesures I-V permettant d'extraire les paramètres suivants: le potentiel de circuit ouvert (V_{OC}), le courant de court-circuit (I_{SC}), le Fill Factor (FF), l'efficacité de conversion (η), les résistances séries (R_s) et les résistances parallèles (R_{sh}). L'efficacité maximale pour une cellule solaire c-Si simple jonction est limitée à $\approx$ 30% en raison de pertes intrinsèques. Pour approcher cette limite, les pertes technologiques (pertes optiques, de recombinaison et résistives) peuvent être réduites en améliorant le processus de fabrication de ces cellules.

Dans cette optique, des architectures de cellules avancées (PERC, PERT, IBC, HJT etc.) ont été developpées et les cellules monofaciales, qui collectent uniquement la lumière via la face avant, sont progressivement remplacées par des cellules bifaciales collectant également la lumière réfléchie sur le sol (albedo) par la face arrière. Ainsi, ces travaux de thèse ont été réalisés sur des cellules n-PERT bifaciales. La structure des précurseurs n-PERT utilisés (cellules complètes mais non métallisées) est schématisée sur la Figure 4

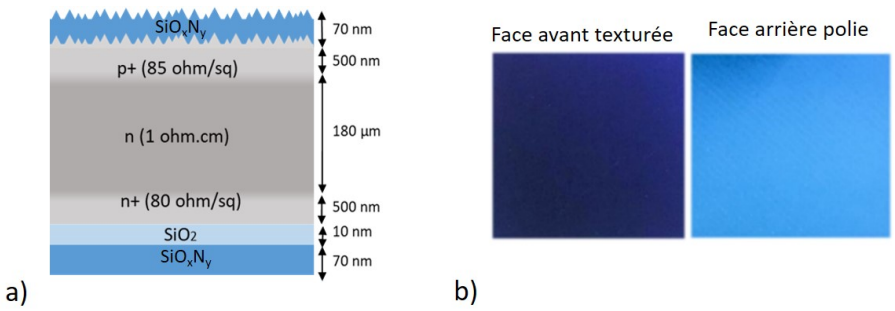

Figure 4: a) Architecture des précurseurs n-PERT commandés chez ISC Konstanz b) Photo des deux faces d'un précurseur.

L'étape de formation des contacts métalliques présente un intérêt particulier car elle a le potentiel d'augmenter l'efficacité des cellules et de réduire les coûts de production. La sérigraphie, qui consiste à appliquer une pâte métallique (généralement à base d'argent) à travers un masque, est aujourd'hui la principale technique utilisée. Ses avantages et inconvenients sont résumés dans le Tableau 1.

Advantages	Inconvénients
- Simple - Rapide - Bien implémentée en industrie	- Pâtes coûteuses (à base d'argent) - 70% des pâtes contiennent du plomb - Contacts poreux - Difficile de réduire la largeur des contacts - Les émetteurs peu dopés sont difficilement contactés - Non adaptée aux cellules à hétérojonction - Précison d'alignement des contacts en mode bifacial doit être améliorée

Table 1: Avantages et inconvénients de la métallisation par sérigraphie pour les cellules solaires c-Si.

La métallisation électrochimique (plaquage Ni/Cu) est une alternative intéressante à la sérigraphie. En effet, cette technique a le potentiel de former des contacts métalliques de meilleure qualité: contacts plus denses, résistivité de contact plus faible, meilleurs ratios hauteur/largueur, émetteurs faiblement dopés plus facilement contactés. De plus, une diminution des coûts de production est envisageable étant donné que le cuivre coûte 100 fois moins cher que l'argent, que les températures de process sont plus basses et que les équipements nécessaires sont potentiellement moins coûteux. Malgré son fort potentiel, la métallisation électrochimique Ni/Cu, présente quelques inconvenients qui doivent être résolus pour une implémentation à l'échelle industrielle. Les avantages et inconvenients de cette technique sont résumés dans le Tableau 2.

Advantages	Inconvénients
Métaux moins coûteux (Ni/Cu) Températures plus faibles (réduction des coûts) - Les deux faces sont métallisées en une fois - Equipements potentiellement moins coûteux - Contacts plus denses (meilleure conductivité) - Largueur de contact plus faible (réduit l'ombrage) - Résistivités de contact plus faibles - Emetteurs faiblement dopés plus facilement contactés	- Procédé laser peut endommager la cellule - Métallisation parasite - Metallisation non homogène - Risques de court-circuits - Problèmes d'adhérence - Fiabilité (diffusion du cuivre)

Table 2: Avantages et inconvenients de la métallisation électrochimique Ni/Cu pour les cellules solaires c-Si.

Le plaquage est le dépôt électrochimique d'un métal sur une surface conductrice ou semiconductrice. La surface est immergée dans un bain d'électrolyte contenant les cations métalliques qui sont réduits et déposés sur la surface. Selon la source d'électrons, on peut distinguer trois types de dépôts illustrés en Figure 5.

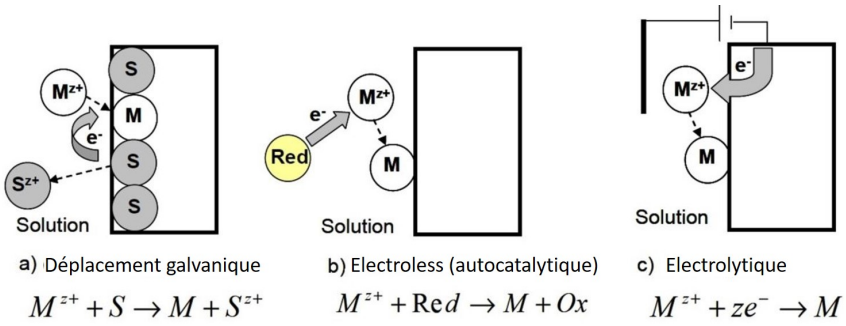

Figure 5: Illustration des trois types de dépôts électrochimiques a) Déplacement galvanique: les électrons proviennent du substrat b) Electroless: les électrons proviennent d'un agent réducteur en solution c) Electrolytique: les électrons proviennent d'une source extèrieure.

Les différentes étapes d'un procédé standard de plaquage Ni/Cu sur une cellule solaire c-Si sont représentées sur la Figure 6.

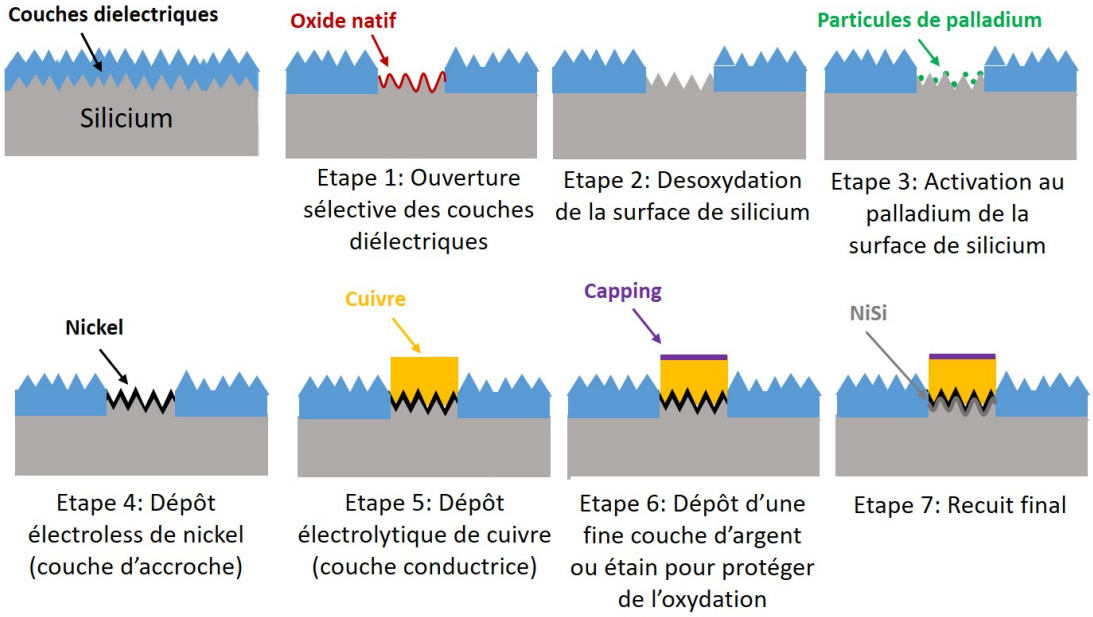

Figure 6: Représentation schématique des différentes étapes du procédé de métallisation électrochimique Ni/Cu.

Ce travail de thèse a pour but de développer un procédé de plaquage Ni/Cu et d'atteindre des rendements de conversion proches des cellules de référence sérigraphiées. Pour ce faire, les différentes étapes sont étudiées afin de comprendre les phénomènes physico-chimiques impliqués et identifier les axes d'amélioration. Ainsi, chacune des étapes du procédé de métallisation électrochimique Ni/Cu pourra être optimisée.

ETUDE DE L'ÉTAPE D'ABLATION LASER DES COUCHES DIÉLECTRIQUES

Les couches diélectriques ont été sélectivement ouvertes par ablation laser en utilisant un laser UV-ps. Afin de comprendre le mécanisme d'ablation et de limiter l'impact sur le silicium sous-jacent, plusieurs paramètres laser ont été testés en faisant varier la fluence pic (F_p) et le recouvrement des spots laser. La caractérisation de la morphologie de surface (MEB, microscope confocal), de la composition et l'environnement chimique (EDS, XPS, Spectrocopie Auger) et des propriétés électriques (Photoluminescence, mesures 4 pointes) ont permis de proposer un mécanisme d'ablation par "lift-off partiel" pour la face arrière polie. Ce mécanisme permet d'expliquer l'apparition de cinq zones concentriques impactées différemment en raison de la distribution spatiale (Gaussienne) de la fluence laser. Ce mécanisme est schématisé en Figure 7. La face avant est plus difficile à étudier, à cause de la texturation (pyramides) et des phénomènes de diffusion optique qui en résultent, mais un mécanisme d'ablation similaire est suspecté.

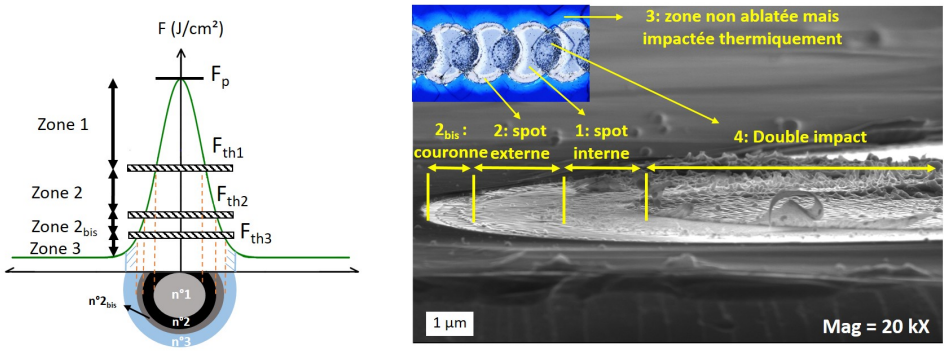

Zone 1 ($F_p > F_{th1}$): Absorption dans le silicium + absorption multiphotonique dans les couches diélectriques. Formation de a-Si + SiO_x en surface (= reste de SiO_x non ablaté + SiO_x formé par le laser)

Zone 2 ($F_{th1} > F_p > F_{th2}$): Absorption dans le silicium + absorption multiphotonique dans la couche SiO_xN_y. Formation de a-Si + reste de SiO_x non ablaté

Zone 2_{bis} ($F_{th2} > F_p > F_{th3}$): Absorption dans le silicium et lift-off des couches diélectriques dû aux contraintes induites à l'interface Si/dielectriques. Formation de a-Si

Zone 3 ($F_p < F_{th3}$): Pas d'ablation mais formation de a-Si

Zone 4: Double impact. Formation de a-Si + SiO_x en surface (= reste de SiO_x non ablaté + SiO_x formé par le laser).

Figure 7: Proposition d'un mécanisme d'ablation laser par "lift-off partiel" en face arrière. Les 5 zones concentriques différemment impactées sont représentées sur les images de microscopie (F_p = 1.809 J/cm^2, 10% recouvrement, $F_{th3} \approx$ 0.269 J/cm^2).

Le recouvrement des spots laser permet de rugosifier la face arrière polie ce qui est favorable pour l'adhérence des contacts métalliques. La rugosité est plus importante sur la face avant texturée avec l'apparition de LIPSS (Laser Induced Periodic Surface Structures) même sans recouvrement des spots laser.

La caractérisation des propriétés électriques (R_{sheet} et temps de vie des porteurs) indique que le temps de vie des porteurs est affecté quelque soit la F_p utilisée et même sans recouvrement. Ceci est probablement dû à la formation de silicium amorphe et à la création de fissures et dislocations. Lorsque les spots laser se recouvrent, R_{sheet} et le temps de vie des porteurs sont tous deux fortement impactés ce qui s'explique par un impact thermique plus important. Ainsi, les spots laser doivent de préférence ne pas se recouvrir, surtout pour l'ablation en face avant texturée où l'impact est amplifié par les phénomènes de diffusion optique.

Il a été démontré qu'un recuit post-laser (750°C) engendre la recristallisation (au moins partiellement)

du silicium amorphe formé durant l'ablation laser. Ce phénomène a été clairement identifié par XPS en face arrière et permet d'améliorer les propriétés électriques de la cellule. De plus, la durée de vie des porteurs est meilleure après un traitement fluoré ($NaHF_2$ 1 $\%_{wt/wt}$ 2 min) gravant la couche SiO_x mais aussi l'extrême surface du silicium qui a été endommagée.

Finalement, deux paramètres laser optimisés ont été proposés: F_p = 0.56 J/cm^2 sans recouvrement et F_p = 0.32 J/cm^2 avec 50% de recouvrement. Les images MEB après ouvertures des deux faces des précurseurs n-PERT sont données en Figure 8.

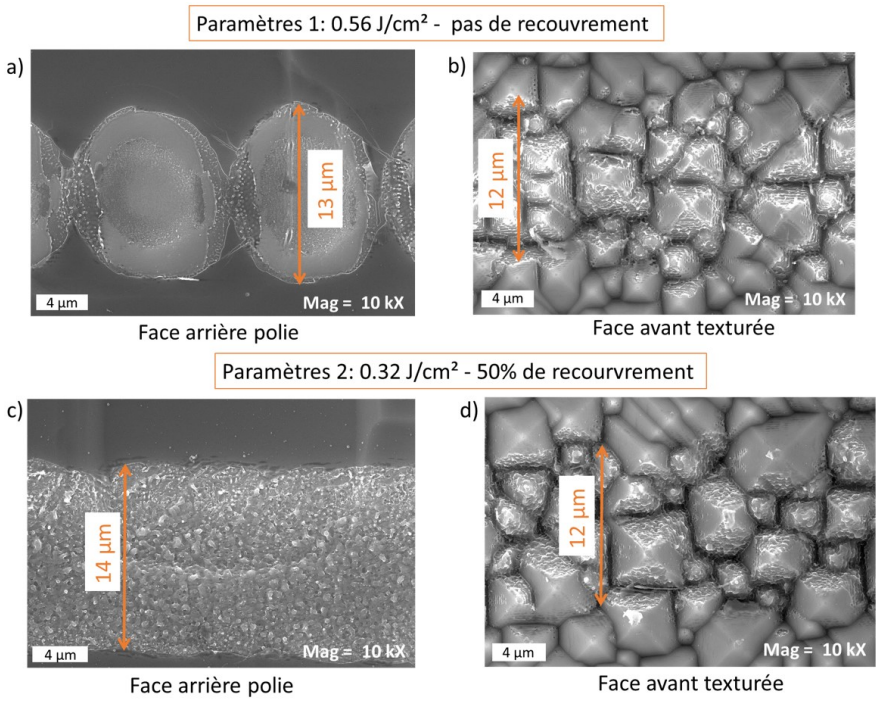

Figure 8: Images MEB après ouverture laser des deux faces d'un précurseur n-PERT avec les deux paramètres optimisés.

ETUDE DES ÉTAPES DE DESOXYDATION ET D'ACTIVATION

Deux étapes sont nécessaires pour permettre de déposer la couche d'accroche de nickel par la suite:

- L'étape de désoxydation qui permet de graver la couche de SiO_x présente en surface après ouverture laser. En effet, la présence d'une couche d'oxyde entre le silicium et le nickel causerait un mauvais contact métallique. Cette couche d'oxyde peut même empêcher le dépôt de nickel si elle est trop couvrante et isolante.
- L'activation de la surface de silicium par le dépôt de particules de palladium par déplacement galvanique. Le palladium a un effet catalytique et permet d'accelérer le dépôt electroless de nickel. Sur un silicium dopé au bore (p^+), les porteurs majoritaires sont des trous alors que le dépôt de nickel requière des électrons. Ainsi, l'activation est nécessaire pour permettre le dépôt de nickel sur la face avant des précuseurs n-PERT.

La désoxydation et l'activation sont toutes deux réalisées en milieux fluorés, connus pour aussi graver les couches de nitrure de silicium. Il est donc important d'optimiser les conditions de désoxydation et d'activation pour limiter la gravure des couches de nitrure de silicium tout en gravant le SiO_x et en activant efficacement la surface de silicium. Deux milieux fluorés ont été étudiés: l'acide fluorhydrique (HF) bien connu et le bifluorure de sodium ($NaHF_2$), moins étudié dans la littérature.

La vitesse de gravure d'un SiO_x déposé par PECVD a été étudiée par ellipsométrie et une relation linéaire a été mise en évidence entre la vitesse de gravure et les concentrations de HF et $NaHF_2$ (Figure 9 a)). En parallèle, la vitesse de gravure d'un SiO_x anodique a été étudiée en élaborant une méthodologie basée sur la spectroscopie d'impédance électrochimique. Les résultats ont apporté les conclusions suivantes:

1. La gravure du SiO_x déposé par PECVD est non uniforme et la porosité de la couche augmente avec le temps de gravure, que ce soit en milieu HF ou $NaHF_2$.
2. Le SiO_x deposé par PECVD et le SiO_x anodique sont tous deux gravés au moins deux fois plus vite en milieu $NaHF_2$.

Ensuite, la vitesse de gravure des couches diélectriques SiO_xN_y des précurseurs n-PERT a été étudiée par des mesures de réflectivité. Une relation linéaire a été établie entre la vitesse de gravure et les concentrations de HF et $NaHF_2$ (Figure 9 b)). Deux conclusions majeures ont été établies:

1. La couche diélectrique SiO_xN_y en face avant texturée est gravée 3 à 4 fois plus vite que celle en face arrière polie. Ceci est principalement attribué à l'indice de réfraction et la densité plus elevés de la couche SiO_xN_y en face arrière.
2. Les vitesses de gravures des couches SiO_xN_y sont identiques en milieu HF et $NaHF_2$ pour une même concentration molaire.

Ces résultats indiquent une meilleure sélectivité vis à vis du SiO_x en travaillant en milieu $NaHF_2$. Ainsi, il est préférable d'utiliser $NaHF_2$ au lieu de HF car le temps d'immersion nécessaire pour graver la couche de SiO_x peut être réduit ce qui limite l'endommagement des couches diélectriques SiO_xN_y et donc le risque de métallisation parasite par la suite.

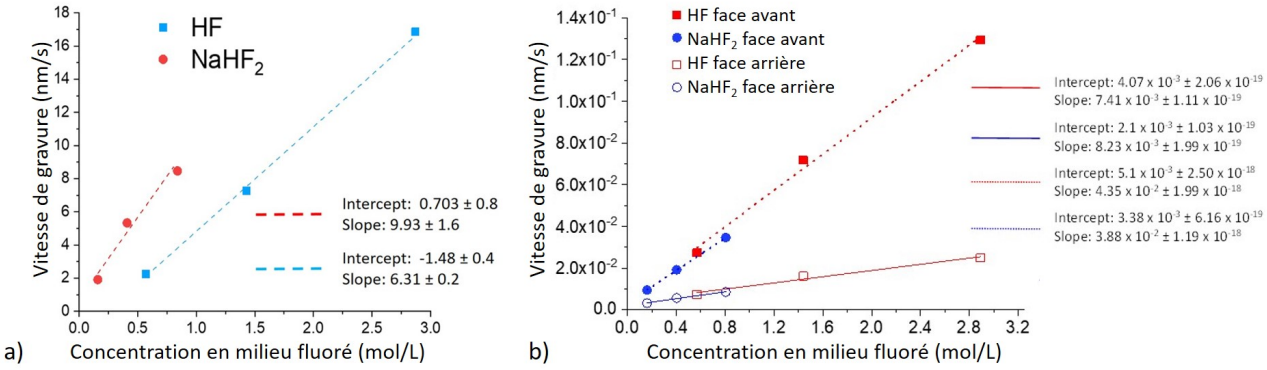

Figure 9: Evolution de la vitesse de gravure d'un SiO_x déposé par PECVD (a) et des couches dielectriques SiO_xN_y des précurseurs n-PERT (b) en fonction de la concentration en HF et $NaHF_2$.

Ensuite, une étude statistique a été réalisée en étudiant le dépôt de palladium par déplacement galvanique sur des échantillons de silicium de type n poli miroir. L'influence de divers paramètres sur la densité et la taille des particules de Pd a été mise en évidence tel que: le temps d'immersion, la [$PdSO_4$], l'agitation de la solution, la [HF] et [$NaHF_2$].

La désoxydation et l'activation ont ensuite été optimisés sur les précurseurs n-PERT après ouverture laser avec les paramètres laser optimisés précédemment. Dans un premier temps, les paramètres optimisés lors de l'étude sur échantillons de silicium poli miroir ont été appliqués (immersion 30 sec dans $NaHF_2$ 0.16 M + $PdSO_4$ 2.5.10^{-4} M). Comme on peut le voir sur la Figure 10, le dépôt de palladium n'est pas homogène mais dépend des différentes zones identifiées après ouvertures laser lorsque les spots ne se recouvrent pas en face arrière (zone 1, 2, 2_{bis} et 4). Ceci s'explique par une différence de composition chimique (plus ou moins de SiO_x) et de rugosité dans ces différentes zones. La couche de SiO_x dans les zones 1 et 2 a résistée au traitement fluoré et empêche le dépôt de palladium. En revanche, le dépôt de palladium est satisfaisant en face avant et en face arrière avec recouvrement des spots laser.

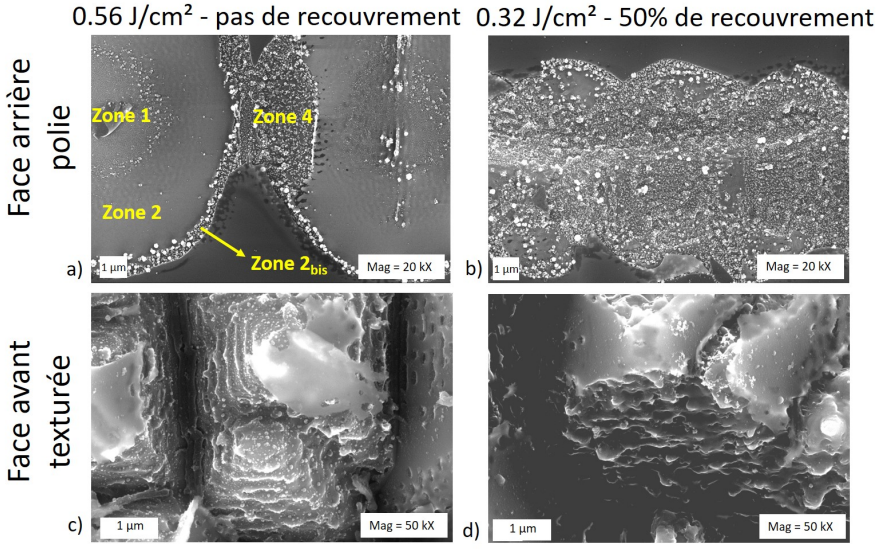

Figure 10: Images MEB après 30 sec d'immersion dans NaHF 0.16 M + $PdSO_4$ 2.5.10^{-4} M des précurseurs n-PERT ouverts avec les paramètres laser optimisés.

Malheureusement, l'étape de désoxydation nécessaire pour retirer la couche de SiO_x dans les zones 1 et 2 et permettre un dépôt de palladium homogène s'est révélée trop agressive pour les couches diélectriques (causant beaucoup de metallisation parasite). Cependant, des conditions de désoxydation ont été trouvées telles que les couches diélectriques sont préservées tandis que quelques particules de Pd sont déposées dans les zones 1 et 2. Ces conditions sont les suivantes: immersion 1 min 30 dans $NaHF_2$ 0.16 M (désoxydation) puis activation 30 sec dans $NaHF_2$ 0.16 M + $PdSO_4$ 5.10^{-5} M. Ces conditions sont également satisfaisantes pour la face avant et la face ariière ouverte avec 50% de recouvrement. Les images MEB correspondantes sont données sur la Figure 11.

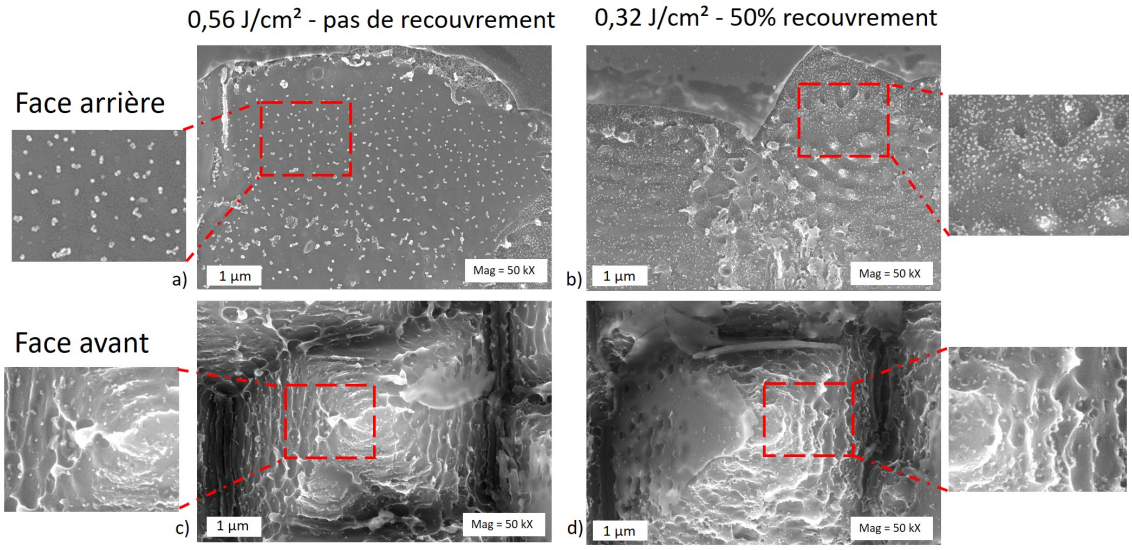

Figure 11: Images MEB après 1 min 30 d'immersion dans $NaHF_2$ 0.16 M (desoxydation) suivit de 30 sec d'immersion dans $NaHF_2$ 0.16 M + $PdSO_4$ 5.10^{-5} M des précurseurs n-PERT ouverts avec les paramètres laser optimisés.

Finalement, les conditions optimisées sont différentes et dépendent des paramètres laser utilisés tel que:

- Cas 1: Desoxydation 1 min 30 dans $NaHF_2$ 0.16 M puis activation 30 seconds dans $NaHF_2$ 0.16 M + $PdSO_4$ 5.10^{-5} M. Conditions satisfaisantes pour les deux faces et avec les deux paramètres laser.
- Cas 2: Desoxydation 30 seconds dans $NaHF_2$ 0.16 M puis activation 30 seconds dans $NaHF_2$ 0.16 M + $PdSO_4$ 5.10^{-5} M. Conditions non adaptées pour la face arrière ouverte sans recouvrement mais ces conditions sont satisfaisantes pour la face avant, avec ou sans recouvrement, et la face arrière ouvertes avec recouvrement. Dans ce cas, le temps de desoxydation est limité et donc les couches diélectriques sont moins endommagées.

DÉPÔT NI/CU ET MESURES D'EFFICACITÉS

Le dépôt electroless de Ni a ensuite été étudié et les facteurs impactant l'homogéneité ont été mis en évidence. Ainsi, le vitesse de dépôt dépend de la géométrie de la zone à métalliser. Les fingers (zones étroites) sont métallisés plus rapidement que les busbars (zones plus larges). Les conditions d'illumination impactent également le dépôt sur la face avant p+. Ceci s'explique par la décourbure des bandes au sein du silicium associé à une augmentation de la densité de trous sur la face avant p^+. Cela ralentit voir empêche la réduction des ions Ni^{2+} c'est pourquoi il est préférable de réaliser le dépôt de Ni à l'obscurité.

De plus, la morphologie et la composition de la surface après ablation laser sur la face arrière polie sans recouvrement (zone 1, 2 et 2_{bis}) conduisent à un dépôt de Ni non homogène avec un effet de bords et probablement une mauvaise adhérence au centre des fingers en raison de la couche SiO_x restante dans les zones 1 et 2. Parmi les deux paramètres laser optimisés précédemment, le paramètre F_p = 0,32 J/cm^2, 50% de recouvrement est donc plus adapté pour limiter les problèmes d'adhérence en face arrière.

L'adhérence de couches de Ni obtenues en utilisant différentes conditions de dépôt electroless (collaboration avec le Fraunhofer ISE) a également été étudiée en utilisant la technique APiC. Pour tous les échantillons, l'adhérence est meilleure sur la face texturée grâce à une rugosité de surface plus importante. Après recuit, l'interdiffusion Ni/Si n'est pas uniforme, notamment sur les cellules métallisées à l'IPVF, conduisant a des problèmes d'adhérence en face arrière polie (délamination des fingers). Cela peut être lié à la présence de SiO_x natif formé dans le bain de Ni avant le dépôt des premiers germes. Une solution pour une future étude serait d'ajouter un composé fluoré comme NH_4F dans le bain de Ni. Ces résultats ont conduit à utiliser des précurseurs n-PERT double texturés pour la suite de ce travail.

Des mesures TLM ont ensuite été réalisées pour déterminer les résistivités de contact (ρ_c) et de ligne après dépôt electroless de Ni en fonction de l'épaisseur de la couche de Ni, de la température de recuit et de la durée du plateau de recuit. Malgré une surestimation des valeurs de ρ_c, en raison d'une chute de tension dans la couche de Ni, une tendance a pu être soulignée. Parmis les conditions testées, les plus faibles valeurs de ρ_c sont obtenues pour un plateau de recuit court (3 min) et un recuit à 230 ou 450 °C.

Avec les conditions optimisées jusqu'à présent pour les différentes étapes de métallisation électrochimique Ni/Cu, des pré-cellules n-PERT double texturées (50 × 50 mm ^{2}) ont été métallisées selon le procédé détaillé en Figure 13. Les images MEB obtenues après dépôts de Ni et de Cu sont données sur la Figure 12.

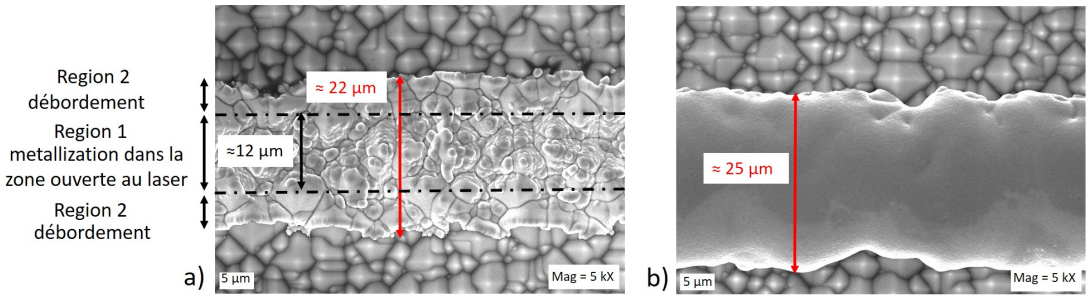

Figure 12: Image MEB après dépôt de nickel et de cuivre avec le procédé détaillé sur la Figure 13.

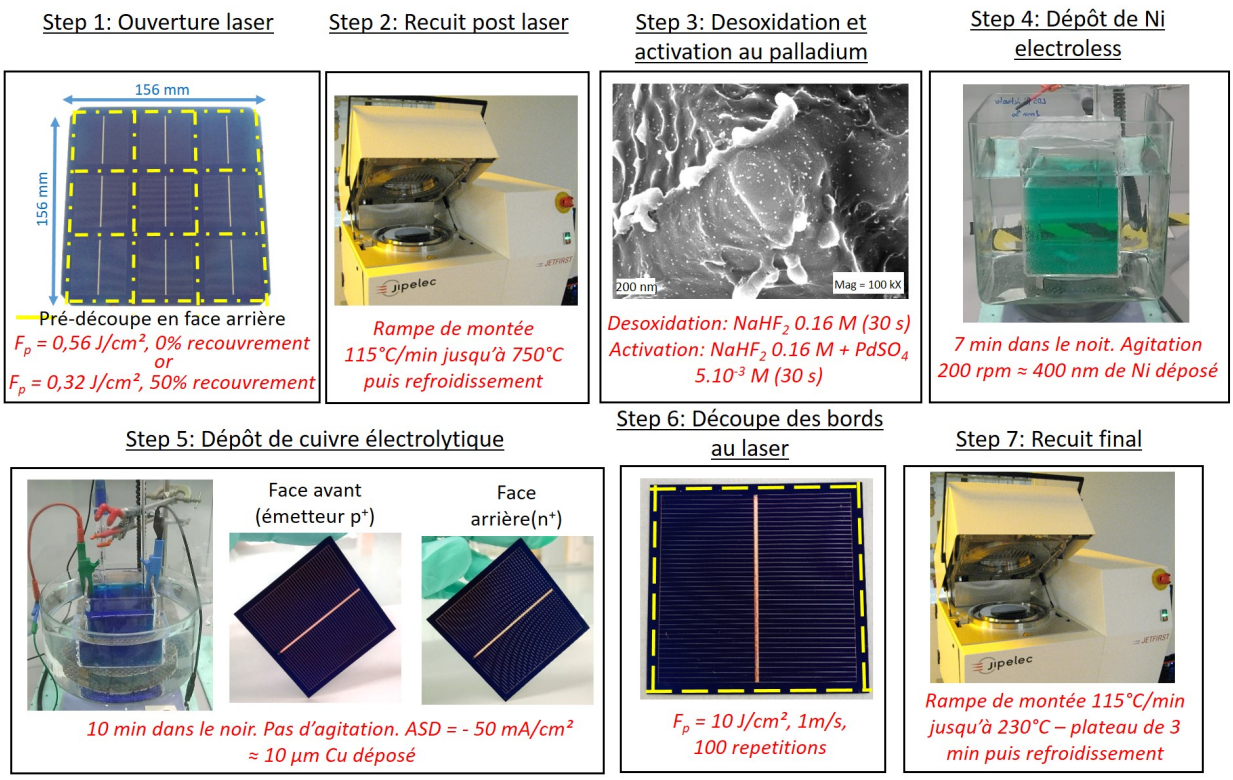

Figure 13: Procédé de métallisation électrochimique Ni/Cu sur cellule n-PERT double texturée après optimization des différentes étapes.

Enfin, des mesures I-V ont été effectuées sur les cellules ainsi métallisées dans les conditions optimisées. Parmi les deux paramètres lasers, la meilleure cellule a été obtenue avec F_p = 0,32 J/cm^2. Les résultats, donnés dans le Tableau 3, sont prometteurs puisque les paramètres obtenus sont similaires à ceux des cellules de référence sérigraphiées. La plupart des paramètres sont même meilleurs avant le recuit final.

	J_{SC} (mA/cm^2)	V_{OC} (mV)	FF (%)	η (%)	R_S (Ω.cm^2)	R_{Sh} (Ω.cm^2)
Face avant (NR)	38.99	629.25	71.07	17.44	1.77	35855.99
Face avant (R)	38.87	625.87	70.06	17.04	1.63	2006.41
Face arrière (NR)	36.95	628.17	72.02	16.71	1.72	34916.87
Face arrière (R)	37.00	625.16	70.27	16.25	1.71	1978.10
SP reference	35.94 $\pm$ 0.053	618 $\pm$ 0.3	78.11 $\pm$ 1	17.35 $\pm$ 0.3	0.75 $\pm$ 0.13	25408 $\pm$ 20400

Table 3: Comparaison des paramètres I-V obtenus pour la meilleure cellule métallisée selon le procédé en Figure 13 avec les cellules de référence sérigraphiées. Les mesures sont réalisées sur la face avant puis la face arrière, avant (NR) et après (R) recuit final.

L'impact de paramètres lasers et d'une température de recuit non optimisés sur les paramètres I-V ont aussi été mis en évidence. Par exemple, à une température de recuit de 380°C, les paramètres I-V sont sévèrement impactés, ce qui est probablement lié à la diffusion de cuivre dans le Si durant le recuit. Une alternative pour une future étude serait d'effectuer l'étape de recuit juste après le dépôt electroless de Ni. Cependant, cela implique de stopper le procédé de métallisation entre le dépôt électrochimique de Ni et celui de Cu ce qui peut impliquer d'autres problèmes.

Bibliography

[1] P. Shabecoff and S. T. t. N. Y. Times, "Global Warming Has Begun, Expert Tells Senate," *The New York Times*, Jun. 1988, ISSN: 0362-4331.

[2] H. Ritchie and M. Roser, "CO2 and Greenhouse Gas Emissions," *Our World in Data*, May 2017. [Online]. Available: https://ourworldindata.org/co2-and-other-greenhouse-gas-emissions.

[3] *Paris Climate Agreement*. [Online]. Available: https://www.worldwildlife.org/pages/paris-climate-agreement.

[4] C. McGlade and P. Ekins, "The geographical distribution of fossil fuels unused when limiting global warming to 2 °C," *Nature*, vol. 517, no. 7533, pp. 187–190, Jan. 2015, ISSN: 0028-0836, 1476-4687. DOI: 10.1038/nature14016.

[5] *BP Statistical Review of World Energy - Main Indicators*. [Online]. Available: https://knoema.fr//BPWES2017/bp-statistical-review-of-world-energy-main-indicators.

[6] REN21, "Renewables 2019: Global status report," Tech. Rep., Jun. 2019, ISBN: 978-3-9818911-7-1, p. 336.

[7] *Renewable Power Generation Costs in 2018*, ISBN: 978-92-9260-126-3.

[8] "IRENA (2017), Electricity Storage and Renewables: Costs and Markets to 2030, International Renewable Energy Agency, Abu Dhabi.," Tech. Rep.

[9] *New Energy Outlook 2019 - Bloomberg NEF*. [Online]. Available: https://about.bnef.com/new-energy-outlook/.

[10] *ITRPV Roadmap 2019 - Tenth edition - 2018 results*, Mar. 2019. [Online]. Available: https://itrpv.vdma.org/.

[11] J. A. Christians, S. N. Habisreutinger, J. J. Berry, and J. M. Luther, "Stability in Perovskite Photovoltaics: A Paradigm for Newfangled Technologies," *ACS Energy Letters*, vol. 3, no. 9, pp. 2136–2143, Sep. 2018, ISSN: 2380-8195, 2380-8195. DOI: 10.1021/acsenergylett.8b00914.

[12] *Silver Mining Stocks, Companies, Prices and News*. [Online]. Available: http://www.infomine.com/investment/silver/.

[13] V.-K. Bajpai, P. Pant, and C.-S. Solanki, "Thin uniform nickel seed layer formation and its impact on Ni-Cu contact adhesion for c-Si solar cell applications," *Solar Energy*, vol. 155, pp. 62–74, Oct. 2017, ISSN: 0038092X. DOI: 10.1016/j.solener.2017.06.002.

[14] L. Tous, J.-F. Lerat, T. Emeraud, R. Negru, K. Huet, A. Uruena, M. Aleman, R. Russell, J. John, J. Poortmans, and R. Mertens, "Nickel Silicide Formation Using Excimer Laser Annealing," *Energy Procedia*, vol. 27, pp. 503–509, 2012, ISSN: 18766102. DOI: 10.1016/j.egypro.2012.07.101.

[15] A. H. M. Smets, K. Jäger, O. Isabella, R. A. v. Swaaij, and M. Zeman, *Solar energy: the physics and engineering of photovoltaic conversion, technologies and systems*. 2016, OCLC: 951110054, ISBN: 978-1-906860-32-5.

[16] L. C. Andreani, A. Bozzola, P. Kowalczewski, M. Liscidini, and L. Redorici, "Silicon solar cells: Toward the efficiency limits," *Advances in Physics: X*, vol. 4, no. 1, p. 1 548 305, Jan. 2019. DOI: 10.1080/23746149.2018.1548305.

[17] P. Yoon, H. Chung, H.-e. Song, J. H. Seo, and S. Shin, "Investigation of the controlling parameters on the bowing phenomenon in ultra-thin crystalline silicon solar cells," *Applied Thermal Engineering*, vol. 90, pp. 559–570, Nov. 2015, ISSN: 1359-4311. DOI: 10.1016/j.applthermaleng.2015.07.034.

[18] S. Kalogirou, Ed., *Mcevoy's Handbook of Photovoltaics: Fundamentals and Applications*, Third edition. London ; San Diego: Academic Press, an imprint of Elsevier, 2018, OCLC: ocn974699127, ISBN: 978-0-12-809921-6.

[19] *The Highs and Lows of Photovoltaic System Calculations*, Jul. 2012. [Online]. Available: https://www.ecmweb.com/green-building/highs-and-lows-photovoltaic-system-calculations.

[20] I. M. Peters and T. Buonassisi, "Energy Yield Limits for Single-Junction Solar Cells," *Joule*, vol. 2, no. 6, pp. 1160–1170, Jun. 2018, ISSN: 25424351. DOI: 10.1016/j.joule.2018.03.009.

[21] R. M. Swanson, "Approaching the 29% limit efficiency of silicon solar cells," in *Conference Record of the Thirty-first IEEE Photovoltaic Specialists Conference, 2005.*, Jan. 2005, pp. 889–894. DOI: 10.1109/PVSC.2005.1488274.

[22] T. Tiedje, E. Yablonovitch, G. Cody, and B. Brooks, "Limiting efficiency of silicon solar cells," *IEEE Transactions on Electron Devices*, vol. 31, no. 5, pp. 711–716, May 1984, ISSN: 0018-9383. DOI: 10.1109/T-ED.1984.21594.

[23] S. Glunz, R. Preu, and D. Biro, "Crystalline Silicon Solar Cells," in *Comprehensive Renewable Energy*, Elsevier, 2012, pp. 353–387, ISBN: 978-0-08-087873-7. DOI: 10.1016/B978-0-08-087872-0.00117-7.

[24] P. Löper, D. Pysch, A. Richter, M. Hermle, S. Janz, M. Zacharias, and S. W. Glunz, "Analysis of the Temperature Dependence of the Open-Circuit Voltage," *Energy Procedia*, Proceedings of the 2nd International Conference on Crystalline Silicon Photovoltaics SiliconPV 2012, vol. 27, pp. 135–142, Jan. 2012, ISSN: 1876-6102. DOI: 10.1016/j.egypro.2012.07.041.

[25] H. Hanifi, C. Pfau, D. Daßler, J. Schneider, S. Schindler, M. Turek, and J. Bagdahn, "Investigation of cell-to-module (CTM) ratios of PV modules by analysis of loss and gain mechanisms," *Photovoltaic International*, vol. 32, pp. 90–98, Jun. 2016. [Online]. Available: https://www.pv-tech.org/technical-papers/investigation-of-cell-to-module-ctm-ratios-of-pv-modules-by-analysis-of-los.

[26] A. Mahmoud Al and B. Lahlouh, "Silicon Pyramid Structure as a Reflectivity Reduction Mechanism," *Journal of Applied Sciences*, vol. 17, no. 8, pp. 374–383, Jul. 2017, ISSN: 18125654. DOI: 10.3923/jas.2017.374.383.

[27] S. Duttagupta, F. Ma, B. Hoex, T. Mueller, and A. G. Aberle, "Optimised Antireflection Coatings using Silicon Nitride on Textured Silicon Surfaces based on Measurements and Multidimensional Modelling," *Energy Procedia*, vol. 15, pp. 78–83, 2012, ISSN: 18766102. DOI: 10.1016/j.egypro.2012.02.009.

[28] B. Swatowska, T. Stapinski, K. Drabczyk, and P. Panek, "The Role of Antireflection Coatings in Silicon Solar Cells – The Influence on Their Electrical Parameters," *Optica Applicata*, vol. XLI, p. 487, Jan. 2011.

[29] M. Müller, G. Fischer, B. Bitnar, S. Steckemetz, R. Schiepe, M. Mühlbauer, R. Köhler, P. Richter, C. Kusterer, A. Oehlke, E. Schneiderlöchner, H. Sträter, F. Wolny, M. Wagner, P. Palinginis, and D. H. Neuhaus, "Loss analysis of 22% efficient industrial PERC solar cells," *Energy Procedia*, vol. 124, pp. 131–137, Sep. 2017, ISSN: 18766102. DOI: 10.1016/j.egypro.2017.09.322.

[30] J. Schmidt, R. Peibst, and R. Brendel, "Surface passivation of crystalline silicon solar cells: Present and future," *Solar Energy Materials and Solar Cells*, vol. 187, pp. 39–54, Dec. 2018, ISSN: 0927-0248. DOI: 10.1016/j.solmat.2018.06.047.

[31] L. Tous, "Nickel/Copper Plated Contacts as an Alternative to Silver Screen Printing for the Front Side Metallization of Industrial High Efficiency Silicon Solar Cells," ISBN 978-94-6018-788-9, PhD thesis, Faculty of Engineering, Leuven (Belgium), Jan. 2014.

[32] A. Kumar and S. N. Melkote, "Diamond Wire Sawing of Solar Silicon Wafers: A Sustainable Manufacturing Alternative to Loose Abrasive Slurry Sawing," *Procedia Manufacturing*, 15th Global Conference on Sustainable Manufacturing, vol. 21, pp. 549–566, Jan. 2018, ISSN: 2351-9789. DOI: 10.1016/j.promfg.2018.02.156.

[33] A. Pietro.P, C. Yifeng, Y. Yang, and F. Zhiqiang, "Riding the workhorse of the industry: PERC," Photovoltaics international, vol. 41, Sep. 2018. [Online]. Available: https://www.pv-tech.org/technical-papers/riding-the-workhorse-of-the-industry-perc.

[34] K. C. Shravan and M. Schmela, "PERC Solar Cell Technology Report 2018 —," en-US, Tech. Rep., p. 57. [Online]. Available: http://taiyangnews.info/reports/perc-solar-cell-technology-report-2018/.

[35] K. Davis, M. Rodgers, G. Scardera, R. Brooker, H. Seigneur, N. Mohajeri, N. G. Dhere, J. Wohlgemuth, E. Schneller, N. Shiradkar, A. C. Rudack, and W. Schoenfeld, "Manufacturing metrology for c-Si module reliability and durability Part II: Cell manufacturing," *Renewable and Sustainable Energy Reviews*, vol. 59, pp. 225–252, Jun. 2016. DOI: 10.1016/j.rser.2015.12.217.

[36] K. Hyung Kim, C. Sub Park, J. Doo Lee, J. Youb Lim, J. Min Yeon, I. Hwan Kim, E. Joo Lee, and Y. Hyun Cho, "Record high efficiency of screen-printed silicon aluminum back surface field solar cell: 20.29%," *Japanese Journal of Applied Physics*, vol. 56, 08MB25, Aug. 2017. DOI: 10.7567/JJAP.56.08MB25.

[37] S. Xiao and S. Xu, "High-Efficiency Silicon Solar Cells—Materials and Devices Physics," *Critical Reviews in Solid State and Materials Sciences*, vol. 39, no. 4, pp. 277–317, Jul. 2014, ISSN: 1040-8436, 1547-6561. DOI: 10.1080/10408436.2013.834245.

[38] B. Demaurex, R. Bartlome, J. P. Seif, J. Geissbühler, D. T. L. Alexander, Q. Jeangros, C. Ballif, and S. De Wolf, "Low-temperature plasma-deposited silicon epitaxial films: Growth and properties," *Journal of Applied Physics*, vol. 116, no. 5, Aug. 2014, ISSN: 0021-8979, 1089-7550. DOI: 10.1063/1.4892095.

[39] R. Léal, F. Haddad, G. Poulain, J.-L. Maurice, and P. Roca i Cabarrocas, "High quality boron-doped epitaxial layers grown at 200°C from SiF_4 /H_2 /Ar gas mixtures for emitter formation in crystalline silicon solar cells," *AIP Advances*, vol. 7, no. 2, p. 025 006, Feb. 2017, ISSN: 2158-3226. DOI: 10.1063/1.4976685.

[40] *LONGi Solar sets new bifacial mono-PERC solar cell world record at 24.06 percent*. [Online]. Available: https://en.longi-solar.com/Home/Events/press_detail/id/89.html.

[41] *Meyer Burger Technology Ltd*. [Online]. Available: http://www.meyerburger.com/en/.

[42] *News release - Imec and Jolywood achieve a record of 23.2 percent with bifacial n-PERT solar cells*. [Online]. Available: https://www.imec-int.com/en/articles/imec-and-jolywood-achieve-a-record-of-23-2-percent-with-bifacial-n-pert-solar-cells.

[43] C. Kuo, T. Kuan, W. Chueh, L. Wu, C. Huang, and C. Yu, "Impact of Laser-Doped Selective Emitters Parameter for Industrial Mono PERC Solar Cells," in *2018 IEEE 7th World Conference on Photovoltaic Energy Conversion (WCPEC)*, Jun. 2018, pp. 1029–1032. DOI: 10.1109/PVSC.2018.8547466.

[44] J. Melskens, B. W. H. van de Loo, B. Macco, L. E. Black, S. Smit, and W. M. M. Kessels, "Passivating Contacts for Crystalline Silicon Solar Cells: From Concepts and Materials to Prospects," *IEEE Journal of Photovoltaics*, vol. 8, no. 2, pp. 373–388, Mar. 2018, ISSN: 2156-3381, 2156-3403. DOI: 10.1109/JPHOTOV.2018.2797106.

[45] A. Louwen, W. van Sark, R. Schropp, and A. Faaij, "A cost roadmap for silicon heterojunction solar cells," *Solar Energy Materials and Solar Cells*, vol. 147, pp. 295–314, Apr. 2016, ISSN: 09270248. DOI: 10.1016/j.solmat.2015.12.026.

[46] J. Haschke, O. Dupré, M. Boccard, and C. Ballif, "Silicon heterojunction solar cells: Recent technological development and practical aspects - from lab to industry," *Solar Energy Materials and Solar Cells*, vol. 187, pp. 140–153, Dec. 2018, ISSN: 09270248. DOI: 10.1016/j.solmat.2018.07.018.

[47] B. Strahm, D. Lachenal, D. Bätzner, W. Frammelsberger, B. Legradic, J. Meixenberger, P. Papet, G. Wahli, E. Vetter, M. Despeisse, A. Faes, A. Lachowicz, C. Allebé, P.-J. Alet, M. Bonnet-Eymard, C. Ballif, Y. Yao, C. Rychen, T. Söderström, J. Heiber, G. Schiltges, S. Leu, J. Hiller, and V. Fakhfouri, "The Swiss Inno-HJT Project: Fully Integrated R&D to Boost Si-HJT Module Performance," *29th European Photovoltaic Solar Energy Conference and Exhibition; 467-471*, 5 pages, 3569 kb, 2014. DOI: 10.4229/eupvsec20142014-2bo.4.1.

[48] Y. Tao and A. Rohatgi, "High-Efficiency Front Junction n-Type Crystalline Silicon Solar Cells," in *Nanostructured Solar Cells*, N. Das, Ed., InTech, Feb. 2017, ISBN: 978-953-51-2935-6 978-953-51-2936-3. DOI: 10.5772/65023.

[49] K. Yoshikawa, H. Kawasaki, W. Yoshida, T. Irie, K. Konishi, K. Nakano, T. Uto, D. Adachi, M. Kanematsu, H. Uzu, and K. Yamamoto, "Silicon heterojunction solar cell with interdigitated back contacts for a photoconversion efficiency over 26%," *Nature Energy*, vol. 2, no. 5, p. 17 032, May 2017, ISSN: 2058-7546. DOI: 10.1038/nenergy.2017.32.

[50] A. us and P. a. C. Policy, *30.2% Efficiency For Bifacial Tandem Solar Cell*. [Online]. Available: http://taiyangnews.info/technology/30-2-efficiency-for-bifacial-tandem-solar-cell/.

[51] Q. Jeangros, M. Bräuninger, T. Yang, J. Werner, F. Sahli, and P. Fiala, "Perovskite Cells for Tandem Applications," Tech. Rep., 2016. [Online]. Available: https://www.epfl.ch.

[52] R. Guerrero-Lemus, R. Vega, T. Kim, A. Kimm, and L. E. Shephard, "Bifacial solar photovoltaics – A technology review," *Renewable and Sustainable Energy Reviews*, vol. 60, pp. 1533–1549, Jul. 2016, ISSN: 1364-0321. DOI: 10.1016/j.rser.2016.03.041.

[53] R. Kopecek, Y. Veschetti, E. Gerritsen, A. Schneider, C. Comparotto, V. Mihailetchi, J. Lossen, and J. Libal, "Bifaciality: One small step for technology, one giant leap for kWh cost reduction," Photovoltaic International, Tech. Rep., Jan. 2015. [Online]. Available: http://www.pv-tech.org.

[54] M. A. Green, E. D. Dunlop, D. H. Levi, J. Hohl-Ebinger, M. Yoshita, and A. W. Ho-Baillie, "Solar cell efficiency tables (version 54)," *Progress in Photovoltaics: Research and Applications*, vol. 27, no. 7, pp. 565–575, Jul. 2019, ISSN: 10627995. DOI: 10.1002/pip.3171.

[55] E. Schneller, R. Brooker, N. S. Shiradkar, M. Rodgers, N. G. Dhere, K. Davis, H. P. Seigneur, N. Mohajeri, J. Wohlgemuth, G. Scardera, A. C. Rudack, and W. Schoenfeld, "Manufacturing metrology for c-Si module reliability and durability Part III: Module manufacturing," *Renewable and Sustainable Energy Reviews*, vol. 59, pp. 992–1016, Jun. 2016. DOI: 10.1016/j.rser.2015.12.215.

[56] G. Beaucarne, G. Schubert, L. Tous, and J. Hoornstra, "Summary of the 6 th Workshop on Metallization and Interconnection for Crystalline Silicon Solar Cells," *Energy Procedia*, vol. 98, pp. 2–11, Nov. 2016, ISSN: 18766102. DOI: 10.1016/j.egypro.2016.10.089.

[57] T. Söderström, P. Papet, and J. Ufheil, "Smart Wire Connection Technology," *28th European Photovoltaic Solar Energy Conference and Exhibition; 495-499*, p. 5, 2013. DOI: 10.4229/28theupvsec2013-1cv.2.17.

[58] G. Beaucarne, "Materials Challenge for Shingled Cells Interconnection," *Energy Procedia*, vol. 98, pp. 115–124, Nov. 2016, ISSN: 18766102. DOI: 10.1016/j.egypro.2016.10.087.

[59] D. Tonini, G. Cellere, M. Bertazzo, A. Fecchio, L. Cerasti, and M. Galiazzo, "Shingling Technology For Cell Interconnection: Technological Aspects And Process Integration," *Energy Procedia*, vol. 150, pp. 36–43, Sep. 2018, ISSN: 18766102. DOI: 10.1016/j.egypro.2018.09.010.

[60] M. Mittag, T. Zech, M. Wiese, D. Blasi, M. Ebert, and H. Wirth, "Cell-to-Module (CTM) Analysis for Photovoltaic Modules with Shingled Solar Cells," in *2017 IEEE 44th Photovoltaic Specialist Conference (PVSC)*, Washington, DC: IEEE, Jun. 2017, pp. 1531–1536, ISBN: 978-1-5090-5605-7. DOI: 10.1109/PVSC.2017.8366260.

[61] *Shingled cell solar modules pave way for higher outputs*, Jun. 2016. [Online]. Available: https://greenmonde.wordpress.com/2016/06/18/shingled-cell-solar-modules-pave-way-for-higher-outputs/.

[62] R. Deng, N. L. Chang, Z. Ouyang, and C. M. Chong, "A techno-economic review of silicon photovoltaic module recycling," *Renewable and Sustainable Energy Reviews*, vol. 109, pp. 532–550, Jul. 2019, ISSN: 13640321. DOI: 10.1016/j.rser.2019.04.020.

[63] J. Tao and S. Yu, "Review on feasible recycling pathways and technologies of solar photovoltaic modules," *Solar Energy Materials and Solar Cells*, vol. 141, pp. 108–124, Oct. 2015, ISSN: 0927-0248. DOI: 10.1016/j.solmat.2015.05.005.

[64] D. Schroder and D. Meier, "Solar cell contact resistance—A review," *IEEE Transactions on Electron Devices*, vol. 31, no. 5, pp. 637–647, May 1984, ISSN: 0018-9383. DOI: 10.1109/T-ED.1984.21583.

[65] W. Shockley, "Research and Investigation of Inverse Epitaxial UHF Power Transistors," Ohio, Tech. Rep. No. ALTOR-64-207, 1964.

[66] H. Berger, "Contact resistance on diffused resistors," in *1969 IEEE International Solid-State Circuits Conference. Digest of Technical Papers*, Philadelphia, PA, USA: IEEE, 1969, pp. 160–161. DOI: 10.1109/ISSCC.1969.1154702.

[67] H. Berger, "Models for contacts to planar devices," *Solid-State Electronics*, vol. 15, no. 2, pp. 145–158, Feb. 1972, ISSN: 00381101. DOI: 10.1016/0038-1101(72)90048-2.

[68] H. H. Berger, "Contact Resistance and Contact Resistivity," *Journal of The Electrochemical Society*, vol. 119, no. 4, p. 507, 1972, ISSN: 00134651. DOI: 10.1149/1.2404240.

[69] S. Guo, G. Gregory, A. M. Gabor, W. V. Schoenfeld, and K. O. Davis, "Detailed investigation of TLM contact resistance measurements on crystalline silicon solar cells," *Solar Energy*, vol. 151, pp. 163–172, Jul. 2017, ISSN: 0038092X. DOI: 10.1016/j.solener.2017.05.015.

[70] D. Guyomard, "Mise au Principes de base de l'électrochimie des semi-conducteurs," *Journal de Chimie Physique*, vol. 83, pp. 355–391, 1986, ISSN: 0021-7689. DOI: 10.1051/jcp/1986830355.

[71] P. I. Gorostiza Langa, "Metal Deposition on Silicon from Fluoride Solution.," Ph.D. Thesis, Universitat de Barcelona, Feb. 2000. [Online]. Available: https://www.tdx.cat/handle/10803/1504.

[72] A. Mette, *New concepts for front side metallization of industrial silicon solar cells*, 1. Aufl, ser. Ingenieurwissenschaften. München: Dr. Hut, 2007, OCLC: 845367093, ISBN: 978-3-89963-650-5.

[73] X. G. Zhang, *Electrochemistry of silicon and its oxide*. New York: Springer Science + Business Media, 2013, OCLC: 958277879, ISBN: 978-1-4757-7494-8.

[74] Krishnan Rajeshwar, "Fundamentals of Semiconductor Electrochemistry and Photoelectrochemistry," in *Encyclopedia of Electrochemistry*, A. J. Bard, Ed., Weinheim, Germany: Wiley-VCH Verlag GmbH & Co. KGaA, Dec. 2007, ISBN: 978-3-527-61042-6. DOI: 10.1002/9783527610426.bard060001.

[75] J. Kang, J. Wen, S. H. Jayaram, A. Yu, and X. Wang, "Development of an equivalent circuit model for electrochemical double layer capacitors (EDLCs) with distinct electrolytes," *Electrochimica Acta*, vol. 115, pp. 587–598, Jan. 2014, ISSN: 00134686. DOI: 10.1016/j.electacta.2013.11.002.

[76] I. Yun and Y. Tao, *Screen Printed Front Junction n-Type Silicon Solar Cells*. InTech, Sep. 2016, ISBN: 978-953-51-2301-9 978-953-51-2527-3. DOI: 10.5772/63198.

[77] J. D. Fields, M. I. Ahmad, V. L. Pool, J. Yu, D. G. Van Campen, P. A. Parilla, M. F. Toney, and M. F. A. M. van Hest, "The formation mechanism for printed silver-contacts for silicon solar cells," *Nature Communications*, vol. 7, no. 1, p. 11 143, Sep. 2016, ISSN: 2041-1723. DOI: 10.1038/ncomms11143.

[78] A. Mostafa and M. Medraj, "Binary Phase Diagrams and Thermodynamic Properties of Silicon and Essential Doping Elements (Al, As, B, Bi, Ga, In, N, P, Sb and Tl)," *Materials*, vol. 10, no. 6, p. 676, Jun. 2017, ISSN: 1996-1944. DOI: 10.3390/ma10060676.

[79] S. H. Lee, D. W. Lee, and S. H. Lee, "Review of Conductive Copper Paste for c-Si Solar Cells," *Korean Journal of Metals and Materials*, vol. 55, no. 9, Sep. 2017, ISSN: 17388228, 22888241. DOI: 10.3365/KJMM.2017.55.9.637.

[80] D. Rudolph, S. Olibet, J. Hoornstra, A. Weeber, E. Cabrera, A. Carr, M. Koppes, and R. Kopecek, "Replacement of Silver in Silicon Solar Cell Metallization Pastes Containing a Highly Reactive Glass Frit: Is it Possible?" *Energy Procedia*, vol. 43, pp. 44–53, 2013, ISSN: 18766102. DOI: 10.1016/j.egypro.2013.11.087.

[81] S. Fritz, E. Emre, J. Engelhardt, S. Ebert, N. Nowak, J. Booth, and G. Hahn, "Contacting BBr3-based Boron Emitters with Aluminium-free Screen-printing Paste," *Energy Procedia*, vol. 92, pp. 925–931, Aug. 2016, ISSN: 18766102. DOI: 10.1016/j.egypro.2016.07.103.

[82] S. K. Chunduri and M. Schmela, *Market Survey on Screen Printers*, 2018. [Online]. Available: http://taiyangnews.info/reports/market-survey-on-screen-printers-2018/.

[83] H. E. Çiftpınar, M. K. Stodolny, Y. Wu, G. J. Janssen, J. Löffler, J. Schmitz, M. Lenes, J.-M. Luchies, and L. Geerligs, "Study of screen printed metallization for polysilicon based passivating contacts," *Energy Procedia*, vol. 124, pp. 851–861, Sep. 2017, ISSN: 18766102. DOI: 10.1016/j.egypro.2017.09.242.

[84] G. Beaucarne, G. Schubert, L. Tous, and J. Hoornstra, "Summary of the 8th Workshop on Metallization and Interconnection for Crystalline Silicon Solar Cells," Perak, Malaysia, 2019, p. 020 001. DOI: 10.1063/1.5125866.

[85] ——, "Summary of the 7th Workshop on Metallization and Interconnection for Crystalline Silicon Solar Cells," 2018. DOI: 10.2139/ssrn.3151953.

[86] Y. Zhang, *Knotless Screen Printing for Crystalline Silicon Solar Cells*, Oct. 2017.

[87] H. Hannebauer, T. Falcon, J. Cunnusamy, and T. Dullweber, "Single Print Metal Stencils for High-efficiency PERC Solar Cells," *Energy Procedia*, vol. 98, pp. 40–45, Nov. 2016, ISSN: 18766102. DOI: 10.1016/j.egypro.2016.10.079.

[88] A. Lorenz, C. Gredy, A. Senne, S. Beyer, Y. Yao, P. Papet, J. Ufheil, H. Reinecke, and F. Clement, "Flexo-printed Busbarless Solar Cells for Multi-wire Interconnection," *Energy Procedia*, vol. 98, pp. 46–60, Nov. 2016, ISSN: 18766102. DOI: 10.1016/j.egypro.2016.10.080.

[89] A. Lorenz, A. Senne, J. Rohde, S. Kroh, M. Wittenberg, K. Krüger, F. Clement, and D. Biro, "Evaluation of Flexographic Printing Technology for Multi-busbar Solar Cells," *Energy Procedia*, vol. 67, pp. 126–137, Apr. 2015, ISSN: 18766102. DOI: 10.1016/j.egypro.2015.03.296.

[90] C. Kunpai, M. G. Kang, H.-e. Song, and D.-Y. Shin, "Fine front side metallisation by stretching the dispensed silver paste filament with graphite nanofibres," *Solar Energy Materials and Solar Cells*, vol. 169, pp. 167–176, Sep. 2017, ISSN: 09270248. DOI: 10.1016/j.solmat.2017.05.010.

[91] J. Lossen, M. Matusovsky, A. Noy, C. Maier, and M. Bähr, "Pattern Transfer Printing (PTPTM) for c-Si Solar Cell Metallization," *Energy Procedia*, vol. 67, pp. 156–162, Apr. 2015, ISSN: 18766102. DOI: 10.1016/j.egypro.2015.03.299.

[92] C. Boulord, "Développement de techniques de métallisation innovantes pour cellules photovoltaïques à haut rendement," Thèse de doctorat, Institut national des sciences appliquées de Lyon, Lyon, France, 2011.

[93] C. Carraro, R. Maboudian, and L. Magagnin, "Metallization and nanostructuring of semiconductor surfaces by galvanic displacement processes," *Surface Science Reports*, vol. 62, no. 12, pp. 499–525, Dec. 2007, ISSN: 0167-5729. DOI: 10.1016/j.surfrep.2007.08.002.

[94] M. Ciobanu, J. P. Wilburn, M. L. Krim, and D. E. Cliffel, "1 - Fundamentals," in *Handbook of Electrochemistry*, C. G. Zoski, Ed., Amsterdam: Elsevier, Jan. 2007, pp. 3–29, ISBN: 978-0-444-51958-0. DOI: 10.1016/B978-044451958-0.50002-1.

[95] M. Gebhardt, T. Kießling, and M. Grimm, "Laser Contact Opening of High Efficient Solar Cells: On the fly laser processing of PERC solar cells," *Laser Technik Journal*, vol. 11, no. 1, pp. 18–20, Jan. 2014, ISSN: 16137728. DOI: 10.1002/latj.201400016.

[96] M. Pourbaix, *Atlas of electrochemical equilibria in aqueous solutions*. National Association of Corrosion Engineers, 1974, Google-Books-ID: QjxRAAAAMAAJ.

[97] K. Kolasinski, "Etching of silicon in fluoride solutions," *Surface Science*, vol. 603, pp. 1904–1911, Jun. 2009. DOI: 10.1016/j.susc.2008.08.031.

[98] D. Martin Knotter and T. J. J. (Dee) Denteneer, "Etching Mechanism of Silicon Nitride in HF-Based Solutions," *Journal of The Electrochemical Society*, vol. 148, no. 3, F43, 2001, ISSN: 00134651. DOI: 10.1149/1.1348262.

[99] C.-W. Hsu, W.-Y. Wang, S.-H. Wang, Y.-H. Kao, and T.-C. Wei, "Adhesive nickel-phosphorous electroless plating on silanized silicon wafer catalyzed by reactive palladium nanoparticles," in *2015 10th International Microsystems, Packaging, Assembly and Circuits Technology Conference (IMPACT)*, Oct. 2015, pp. 245–249. DOI: 10.1109/IMPACT.2015.7365244.

[100] S. Hsieh, J. Hsieh, W. Chen, and C. Chuang, "Electroless Nickel Deposition for Front Side Metallization of Silicon Solar Cells," *Materials*, vol. 10, no. 8, p. 942, Aug. 2017, ISSN: 1996-1944. DOI: 10.3390/ma10080942.

[101] F. Delaunois, V. Vitry, and L. Bonin, *Electroless Nickel Plating: Fundamentals to Applications*. CRC Press, Nov. 2019, Google-Books-ID: yHm6DwAAQBAJ, ISBN: 978-0-429-88113-8.

[102] M. Navlani-García, K. Mori, D. Salinas-Torres, Y. Kuwahara, and H. Yamashita, "New Approaches Toward the Hydrogen Production From Formic Acid Dehydrogenation Over Pd-Based Heterogeneous Catalysts," *Frontiers in Materials*, vol. 6, p. 44, Mar. 2019, ISSN: 2296-8016. DOI: 10.3389/fmats.2019.00044.

[103] X. Zhang, F. Ren, M. Goorsky, and K. Tu, "Study of the initial stage of electroless Ni deposition on Si (100) substrates in aqueous alkaline solution," *Surface and Coatings Technology*, vol. 201, no. 6, pp. 2724–2732, Dec. 2006, ISSN: 02578972. DOI: 10.1016/j.surfcoat.2006.05.025.

[104] E. Ochoa-Martínez, N. Wehkamp, J. Ramos-Barrado, and J. Bartsch, "Progress on Laser Assisted Nickel Seed Layer Deposition for Front Contact Copper Plating," *Energy Procedia*, vol. 38, pp. 777–786, 2013, ISSN: 18766102. DOI: 10.1016/j.egypro.2013.07.346.

[105] G. O. Mallory and J. B. Hajdu, *Chapter 1: the Fundamental Aspects Of Electroless Nickel Plating*. New York: American Electroplaters and Surface Finishers, 2009, OCLC: 900928495, ISBN: 978-0-8155-1277-6.

[106] M. Schlesinger and M. Paunovic, Eds., *Modern electroplating*, 5th ed, ser. The electrochemical society series 52. Hoboken, NJ: Wiley, 2010, ISBN: 978-0-470-16778-6.

[107] A. u. Rehman and S. H. Lee, "Review of the Potential of the Ni/Cu Plating Technique for Crystalline Silicon Solar Cells," *Materials*, vol. 7, no. 2, pp. 1318–1341, Feb. 2014. DOI: 10.3390/ma7021318.

[108] M. Kamp, *Electrochemical processes for metallization of novel silicon solar cells*, ser. Solare Energie- und Systemforschung/Solar energy and systems research / Fraunhofer-Institut für Solare Energiesysteme ISE. Stuttgart: Fraunhofer Verlag, 2016, OCLC: 964637998, ISBN: 978-3-8396-1055-8.

[109] J. Reid, "Copper Electrodeposition: Principles and Recent Progress," *Japanese Journal of Applied Physics*, vol. 40, no. Part 1, No. 4B, pp. 2650–2657, Apr. 2001, ISSN: 0021-4922, 1347-4065. DOI: 10.1143/JJAP.40.2650.

[110] X. Li, T. O. Drews, E. Rusli, F. Xue, Y. He, R. Braatz, and R. Alkire, "Effect of Additives on Shape Evolution during Electrodeposition," *Journal of The Electrochemical Society*, vol. 154, no. 4, p. D230, 2007, ISSN: 00134651. DOI: 10.1149/1.2434686.

[111] R. Rohit, A. Rodofili, G. Cimiotti, J. Bartsch, and M. Glatthaar, "Selective plating concept for silicon heterojunction solar cell metallization," *Energy Procedia*, vol. 124, pp. 901–906, Sep. 2017, ISSN: 18766102. DOI: 10.1016/j.egypro.2017.09.289.

[112] J. K. Jhothiraman and R. Balachandran, "Electroplating: Applications in the Semiconductor Industry," *Advances in Chemical Engineering and Science*, vol. 9, no. 2, pp. 239–261, Feb. 2019. DOI: 10.4236/aces.2019.92018.

[113] S. Kluska, J. Bartsch, A. Büchler, G. Cimiotti, A. A. Brand, S. Hopman, and M. Glatthaar, "Electrical and Mechanical Properties of Plated Ni/Cu Contacts for Si Solar Cells," *Energy Procedia*, vol. 77, pp. 733–743, Aug. 2015, ISSN: 18766102. DOI: 10.1016/j.egypro.2015.07.104.

[114] A. Mondon, D. Wang, A. Zuschlag, J. Bartsch, M. Glatthaar, and S. Glunz, "Nanoscale investigation of the interface situation of plated nickel and thermally formed nickel silicide for silicon solar cell metallization," *Applied Surface Science*, vol. 323, pp. 31–39, Dec. 2014, ISSN: 01694332. DOI: 10.1016/j.apsusc.2014.08.157.

[115] A. Marshall, "Nickel Silicide as a Contact and Diffusion Barrier for Copper Metallization in Silicon Photovoltaics," *Theses*, May 2017. [Online]. Available: https://scholarworks.rit.edu/theses/9472.

[116] E. Bahette, J. F. Michaud, D. Certon, D. Gross, and D. Alquier, "Progresses in cMUT device fabrication using low temperature processes," *Journal of Micromechanics and Microengineering*, vol. 24, no. 4, p. 045 020, Apr. 2014, ISSN: 0960-1317, 1361-6439. DOI: 10.1088/0960-1317/24/4/045020.

[117] S. Abhaya, G. Amarendra, S. Kalavathi, P. Gopalan, M. Kamruddin, A. Tyagi, V. Sastry, and C. Sundar, "Silicidation in Ni/Si thin film system investigated by X-ray diffraction and Auger electron spectroscopy," *Applied Surface Science*, vol. 253, no. 8, pp. 3799–3802, Feb. 2007, ISSN: 01694332. DOI: 10.1016/j.apsusc.2006.07.091.

[118] G. Cimiotti, J. Bartsch, A. Kraft, A. Mondon, and M. Glatthaar, "Design Rules for Solar Cells with Plated Metallization," *Energy Procedia*, vol. 67, pp. 84–92, Apr. 2015, ISSN: 1876-6102. DOI: 10.1016/j.egypro.2015.03.291.

[119] J. Burschik, Y. Shengzhao, N. Bay, K. Crouse, A. De Rose, A. Hoffmann, H. Kühnlein, B. Lee, A. Letize, M. Passig, D. Pysch, M. Sieber, P. Verlinden, and K. Vosteen, "Transition to 4 and 5 BB Designs for Ni/Cu/Ag Plated Cells," *Energy Procedia*, vol. 98, pp. 66–73, Nov. 2016, ISSN: 18766102. DOI: 10.1016/j.egypro.2016.10.082.

[120] A. u. Rehman and S. H. Lee, "Crystalline Silicon Solar Cells with Nickel/Copper Contacts," *Solar Cells - New Approaches and Reviews*, Oct. 2015. DOI: 10.5772/59008.

[121] E. Cornagliotti, L. Tous, R. Russell, A. Uruena, P. Choulat, A. van der Heide, M. Aleman, F. Duerinckx, E. Voroshazi, and J. Szlufcik, "High efficiency bifacial n-PERT cells with co-plated Ni/Ag contacts for multi-wire interconnection," *Energy Procedia*, Proceedings of the SNEC 11th International Photovoltaic Power Generation Conference & Exhibition, SNEC 2017 Scientific Conference, vol. 130, pp. 50–54, Sep. 2017, ISSN: 1876-6102. DOI: 10.1016/j.egypro.2017.09.413.

[122] A. Descoeudres, C. Allebé, N. Badel, L. Barraud, J. Champliaud, G. Christmann, F. Debrot, A. Faes, J. Geissbühler, J. Horzel, A. Lachowicz, J. Levrat, S. Martin de Nicolas, S. Nicolay, B. Paviet-Salomon, L.-L. Senaud, C. Ballif, and M. Despeisse, "Low-temperature processes for passivation and metallization of high-efficiency crystalline silicon solar cells," *Solar Energy*, vol. 175, pp. 54–59, Nov. 2018, ISSN: 0038092X. DOI: 10.1016/j.solener.2018.01.074.

[123] A. Dabirian, A. Lachowicz, J.-W. Schüttauf, B. Paviet-Salomon, M. Morales-Masis, A. Hessler-Wyser, M. Despeisse, and C. Ballif, "Metallization of Si heterojunction solar cells by nanosecond laser ablation and Ni-Cu plating," *Solar Energy Materials and Solar Cells*, vol. 159, pp. 243–250, Jan. 2017, ISSN: 09270248. DOI: 10.1016/j.solmat.2016.09.021.

[124] M. Kim, D. Kim, D. Kim, and Y. Kang, "Analysis of laser-induced damage during laser ablation process using picosecond pulse width laser to fabricate highly efficient PERC cells," *Solar Energy*, vol. 108, pp. 101–106, Oct. 2014, ISSN: 0038092X. DOI: 10.1016/j.solener.2014.06.020.

[125] C. Dang, R. Labie, L. Tous, R. Russell, M. Recaman, J. Deckers, A. Uruena, F. Duerinckx, and J. Poortmans, "Investigation of Laser Ablation Induced Defects in Crystalline Silicon Solar Cells," *Energy Procedia*, vol. 55, pp. 649–655, Aug. 2014. DOI: 10.1016/j.egypro.2014.08.040.

[126] A. Frey, J. Engelhardt, G. Micard, G. Hahn, and B. Terheiden, "Investigation of fill factor losses on 20.2% efficient n-type mono-like silicon solar cells with laser contact opening," *physica status solidi (RRL) - Rapid Research Letters*, vol. 10, no. 2, pp. 143–147, Feb. 2016, ISSN: 1862-6270. DOI: 10.1002/pssr.201510334.

[127] J. Thorstensen and S. E. Foss, "Investigation of Depth of Laser Damage to Silicon as Function of Wavelength and Pulse Duration," *Energy Procedia*, Proceedings of the 3rd International Conference on Crystalline Silicon Photovoltaics (SiliconPV 2013), vol. 38, pp. 794–800, Jan. 2013, ISSN: 1876-6102. DOI: 10.1016/j.egypro.2013.07.348.

[128] G. Poulain, "Procédés laser pour la réalisation de cellules photovoltaïques en silicium à haut rendement," PhD thesis, Lyon, INSA, Oct. 2012. [Online]. Available: http://www.theses.fr/2012ISAL0099.

[129] A. Lennon, J. Colwell, and K. P. Rodbell, "Challenges facing copper-plated metallisation for silicon photovoltaics: Insights from integrated circuit technology development," *Progress in Photovoltaics: Research and Applications*, vol. 27, no. 1, pp. 67–97, Jan. 2019, ISSN: 10627995. DOI: 10.1002/pip.3062.

[130] C. Dang, R. Labie, E. Simoen, and J. Poortmans, "Detailed structural and electrical characterization of plated crystalline silicon solar cells," *Solar Energy Materials and Solar Cells*, vol. 184, pp. 57–66, Sep. 2018, ISSN: 09270248. DOI: 10.1016/j.solmat.2018.04.016.

[131] A. Mondon, J. Bartsch, M. Kamp, A. Brand, B. Steinhauser, N. Bay, J. Horzel, M. Glatthaar, and S. Glunz, "Plated Nickel-Copper Contacts on c-Si: From Microelectronic Processing to Cost Effective Silicon Solar Cell Production," *29th European Photovoltaic Solar Energy Conference and Exhibition; 1286-1291*, 6 pages, 6313 kb, 2014. DOI: 10.4229/EUPVSEC20142014-2CV.4.7.

[132] A. Buechler, S. Kluska, F. Meyer, A. Brand, G. Cimiotti, J. Bartsch, and M. Glatthaar, "Interface oxides in femtosecond laser structured plated Ni-Cu-Ag contacts for silicon solar cells," *Solar Energy Materials and Solar Cells*, vol. 166, pp. 197–203, Jul. 2017. DOI: 10.1016/j.solmat.2017.03.016.

[133] A. Mondon, M. Jawaid, J. Bartsch, M. Glatthaar, and S. Glunz, "Microstructure analysis of the interface situation and adhesion of thermally formed nickel silicide for plated nickel–copper contacts on silicon solar cells," *Solar Energy Materials and Solar Cells*, vol. 117, pp. 209–213, Oct. 2013, ISSN: 09270248. DOI: 10.1016/j.solmat.2013.06.005.

[134] C. Dang, R. Labie, E. Simoen, L. Tous, R. Russell, F. Duerinckx, R. Mertens, and J. Poortmans, "Insights into the reliability of Ni/Cu plated p-PERC silicon solar cells," *Energy Procedia*, vol. 124, pp. 862–868, Sep. 2017, ISSN: 18766102. DOI: 10.1016/j.egypro.2017.09.243.

[135] J. Colwell, P.-C. Hsiao, X. Shen, W. Zhang, X. Wang, S. Lim, and A. Lennon, "Impact of contact integrity during thermal stress testing on degradation analysis of copper-plated silicon solar cells," *Solar Energy Materials and Solar Cells*, vol. 174, pp. 225–232, Jan. 2018, ISSN: 09270248. DOI: 10.1016/j.solmat.2017.09.005.

[136] A. Kraft, C. Wolf, J. Bartsch, M. Glatthaar, and S. Glunz, "Long term stability of copper front side contacts for crystalline silicon solar cells," *Solar Energy Materials and Solar Cells*, vol. 136, pp. 25–31, May 2015, ISSN: 09270248. DOI: 10.1016/j.solmat.2014.12.024.

[137] M. Schulz-Ruhtenberg, D. Trusheim, J. Das, S. Krantz, and J. Wieduwilt, "Influence of Pulse Duration in Picosecond Laser Ablation of Silicon Nitride Layers," *Energy Procedia*, Proceedings of the SiliconPV 2011 Conference (1st International Conference on Crystalline Silicon Photovoltaics), vol. 8, pp. 614–619, Jan. 2011, ISSN: 1876-6102. DOI: 10.1016/j.egypro.2011.06.191.

[138] S. Binetti, A. Le Donne, A. Rolfi, B. Jäggi, B. Neuenschwander, C. Busto, C. Frigeri, D. Scorticati, L. Longoni, and S. Pellegrino, "Picosecond laser texturization of mc-silicon for photovoltaics: A comparison between 1064 nm, 532 nm and 355 nm radiation wavelengths," *Applied Surface Science*, vol. 371, pp. 196–202, 2016, ISSN: ISSN 0169-4332. DOI: 10.1016/j.apsusc.2016.02.187.

[139] K. Mangersnes, S. Erik Foss, and A. Thogersen, "Damage free laser ablation of SiO2 for local contact opening on silicon solar cells using an a-Si:H buffer layer," *Journal of Applied Physics*, vol. 107, no. 4, p. 043 518, Feb. 2010, ISSN: 0021-8979. DOI: 10.1063/1.3309382.

[140] M. S. Bailly, J. Karas, H. Jain, W. J. Dauksher, and S. Bowden, "Damage-free laser patterning of silicon nitride on textured crystalline silicon using an amorphous silicon etch mask for Ni/Cu plated silicon solar cells," *Thin Solid Films*, vol. 612, pp. 243–249, Aug. 2016, ISSN: 00406090. DOI: 10.1016/j.tsf.2016.06.011.

[141] N. Bay, A. A. Brand, A. Büchler, J. Burschik, S. Kluska, H. H. Kuehnlein, M. Passig, D. Pysch, and M. Sieber, "Benefits of different process routes for industrial direct front side plating," *Energy Procedia*, 7th International Conference on Silicon Photovoltaics, SiliconPV 2017, 3-5 April 2017, Freiburg, Germany, vol. 124, pp. 823–828, Sep. 2017, ISSN: 1876-6102. DOI: 10.1016/j.egypro.2017.09.353.

[142] S. Kluska, A. Büchler, J. Bartsch, B. Grübel, A. A. Brand, S. Gutscher, G. Cimiotti, J. Nekarda, and M. Glatthaar, "Easy Plating—A Simple Approach to Suppress Parasitically Metallized Areas in Front Side Ni/Cu Plated Crystalline Si Solar Cells," *IEEE Journal of Photovoltaics*, vol. 7, no. 5, pp. 1270–1277, Sep. 2017, ISSN: 2156-3381. DOI: 10.1109/JPHOTOV.2017.2720461.

[143] T. Kim, J.-K. Lim, H.-N.-R. Shin, D. Kyeong, J. Cho, M. Kim, J. Lee, H. Park, K. Lee, W.-j. Lee, and E.-C. Cho, "21%-efficient PERL Solar Cells with Plated Front Contacts on Industrial 156mm p-type Crystalline Silicon Wafers," *Energy Procedia*, Proceedings of the 4th International Conference on Crystalline Silicon Photovoltaics (SiliconPV 2014), vol. 55, pp. 431–436, Jan. 2014, ISSN: 1876-6102. DOI: 10.1016/j.egypro.2014.08.123.

[144] C. M. Chong, A. Wenham, R. Chen, S. Wang, J. Ji, Z. Shi, L. Mai, B. Tjahjono, B. Hallam, A. Sugianto, and S. Wenham, "Improved adhesion for plated Solar cell metallisation," in *2015 IEEE 42nd Photovoltaic Specialist Conference (PVSC)*, New Orleans, LA: IEEE, Jun. 2015, pp. 1–4, ISBN: 978-1-4799-7944-8. DOI: 10.1109/PVSC.2015.7355882.

[145] Z. Hameiri, L. Mai, T. Puzzer, and S. Wenham, "Influence of laser power on the properties of laser doped solar cells," *Solar Energy Materials and Solar Cells*, vol. 95, no. 4, pp. 1085–1094, Apr. 2011, ISSN: 09270248. DOI: 10.1016/j.solmat.2010.12.006.

[146] N. Song, P.-C. Hsiao, W. Zhang, X. Wang, J. Colwell, Z. Li, and A. Lennon, "Post-plating Annealing of Light Induced Plated Copper Fingers: Implications for Reliable Metallization," *Energy Procedia*, vol. 98, pp. 136–141, Nov. 2016, ISSN: 18766102. DOI: 10.1016/j.egypro.2017.03.1299.

[147] C. Molto, J. E. Lee, J. Nekarda, V. Arya, S. Bechu, M. Bouttemy, A. Etcheberry, E. Drahi, P.-P. Grand, and A.-M. Goncalves, "Investigation of dielectric layers laser ablation mechanism on n-PERT silicon solar cells for (Ni) plating process: Laser impact on surface morphology, composition, electrical properties and metallization quality," *Solar Energy Materials and Solar Cells*, vol. 202, p. 110 149, Nov. 2019, ISSN: 09270248. DOI: 10.1016/j.solmat.2019.110149.

[148] D. Bäuerle, *Laser processing and chemistry*, 3rd rev. enlarged ed. Berlin ; New York: Springer, 2000, ISBN: 978-3-540-66891-6.

[149] K. Sugioka and Y. Cheng, "Femtosecond laser processing for optofluidic fabrication," *Lab on a Chip*, vol. 12, no. 19, p. 3576, 2012, ISSN: 1473-0197, 1473-0189. DOI: 10.1039/c2lc40366h.

[150] B. N. Chichkov, C. Momma, S. Nolte, F. von Alvensleben, and A. Tünnermann, "Femtosecond, picosecond and nanosecond laser ablation of solids," *Applied Physics A: Materials Science & Processing*, vol. 63, pp. 109–115, Aug. 1996, ISSN: 0947-8396. DOI: 10.1007/BF01567637.

[151] Z. Du, N. Palina, J. Chen, M. Hong, and B. Hoex, "Rear-Side Contact Opening by Laser Ablation for Industrial Screen-Printed Aluminium Local Back Surface Field Silicon Wafer Solar Cells," *Energy Procedia*, vol. 25, pp. 19–27, 2012, ISSN: 18766102. DOI: 10.1016/j.egypro.2012.07.003.

[152] D. Suh, "Influence of laser damage and contact geometry on the performance of passivated emitter and rear cell solar cells," *Thin Solid Films*, vol. 668, pp. 45–49, Dec. 2018, ISSN: 00406090. DOI: 10.1016/j.tsf.2018.10.020.

[153] Z. Sun and M. C. Gupta, "A study of laser-induced surface defects in silicon and impact on electrical properties," *Journal of Applied Physics*, vol. 124, no. 22, p. 223 103, Dec. 2018, ISSN: 0021-8979, 1089-7550. DOI: 10.1063/1.5058143.

[154] D. Walter, A. Fell, E. Franklin, D. Wang, K. Fong, T. Kho, K. Weber, and A. W. Blakers, "Damage-free ultraviolet nanosecond laser ablation for high efficiency back contact solar cell fabrication," *Solar Energy Materials and Solar Cells*, vol. 136, pp. 1–10, May 2015, ISSN: 09270248. DOI: 10.1016/j.solmat.2014.12.030.

[155] G. Heinrich and A. Lawerenz, "Non-linear absorption of femtosecond laser pulses in a SiNx layer - Influence of silicon doping type," *Solar Energy Materials and Solar Cells*, vol. 120, pp. 317–322, Jan. 2014. DOI: 10.1016/j.solmat.2013.05.004.

[156] G. Heinrich, M. Bähr, K. Stolberg, T. Wütherich, M. Leonhardt, and A. Lawerenz, "Investigation of ablation mechanisms for selective laser ablation of silicon nitride layers," *Energy Procedia*, vol. 8, pp. 592–597, Dec. 2011. DOI: 10.1016/j.egypro.2011.06.188.

[157] G. Heinrich, I. Hšger, M. BŠhr, K. Stolberg, T. WŸtherich, M. Leonhardt, A. Lawerenz, and G. Gobsch, "Investigation of Laser Irradiated Areas with Electron Backscatter Diffraction," *Energy Procedia*, Proceedings of the 2nd International Conference on Crystalline Silicon Photovoltaics SiliconPV 2012, vol. 27, pp. 491–496, Jan. 2012, ISSN: 1876-6102. DOI: 10.1016/j.egypro.2012.07.099.

[158] G. Heinrich, M. Wollgarten, M. Bähr, and A. Lawerenz, "Ultra-short pulsed laser ablation of silicon nitride layers: Investigation near threshold fluence," *Applied Surface Science*, vol. 278, pp. 265–267, Aug. 2013, ISSN: 01694332. DOI: 10.1016/j.apsusc.2012.10.122.

[159] S. Hermann, N.-P. Harder, R. Brendel, D. Herzog, and H. Haferkamp, "Picosecond laser ablation of SiO2 layers on silicon substrates," *Applied Physics A*, vol. 99, no. 1, pp. 151–158, Apr. 2010, ISSN: 0947-8396, 1432-0630. DOI: 10.1007/s00339-009-5464-z.

[160] L. Chahed, M. Thèye, and B. Bourdon, "Effets du recuit sur les propriétés optiques du silicium amorphe hydrogéné," *Journal de Physique*, vol. 44, no. 3, pp. 387–392, 1983. DOI: 10.1051/jphys:01983004403038700.

[161] A. Knorz, M. Peters, A. Grohe, C. Harmel, and R. Preu, "Selective laser ablation of SiNx layers on textured surfaces for low temperature front side metallizations," *Progress in Photovoltaics: Research and Applications*, vol. 17, no. 2, pp. 127–136, 2009, ISSN: 1099-159X. DOI: 10.1002/pip.856.

[162] M. S. Trtica, B. M. Gakovic, B. B. Radak, D. Batani, T. Desai, and M. Bussoli, "Periodic surface structures on crystalline silicon created by 532nm picosecond Nd:YAG laser pulses," *Applied Surface Science*, vol. 254, no. 5, pp. 1377–1381, Dec. 2007, ISSN: 0169-4332. DOI: 10.1016/j.apsusc.2007.06.050.

[163] T. Schutz-Kuchly, A. Slaoui, J. Zelgowski, A. Bahouka, M. Pawlik, J.-P. Vilcot, E. Delbos, M. Bouttemy, and R. Cabal, "UV and IR laser induced ablation of Al_2O_3 /SiN:H and a-Si:H/SiN:H," *EPJ Photovoltaics*, vol. 5, p. 55 201, 2014, ISSN: 2105-0716. DOI: 10.1051/epjpv/2013027.

[164] J. F. Moulder, *Handbook of XRay Photoelectron Spectroscopy*. 1992. [Online]. Available: https://fr.scribd.com/document/311527850/John-F-Moulder-PHI-Handbook-of-XRay-Photoelectron-Spectroscopy.

[165] J.-W. He, X. Xu, J. S. Corneille, and D. W. Goodman, "X-ray photoelectron spectroscopic characterization of ultra-thin silicon oxide films on a Mo(100) surface," *Surface Science*, vol. 279, no. 1, pp. 119–126, Dec. 1992, ISSN: 0039-6028. DOI: 10.1016/0039-6028(92)90748-U.

[166] E. Dehan, P. Temple-Boyer, R. Henda, J. Pedroviejo, and E. Scheid, "Optical and structural properties of SiOx and SiNx materials," *Thin Solid Films*, vol. 266, no. 1, pp. 14–19, Sep. 1995, ISSN: 00406090. DOI: 10.1016/0040-6090(95)06635-7.

[167] J. R. Shallenberger, D. A. Cole, and S. W. Novak, "Characterization of silicon oxynitride thin films by x-ray photoelectron spectroscopy," *Journal of Vacuum Science & Technology A*, vol. 17, no. 4, pp. 1086–1090, Jul. 1999, ISSN: 0734-2101. DOI: 10.1116/1.582038.

[168] L. Csepregi, E. F. Kennedy, J. W. Mayer, and T. W. Sigmon, "Substrate-orientation dependence of the epitaxial regrowth rate from Si-implanted amorphous Si," *Journal of Applied Physics*, vol. 49, no. 7, pp. 3906–3911, Jul. 1978, ISSN: 0021-8979, 1089-7550. DOI: 10.1063/1.325397.

[169] V. A. Dao, J. Heo, Y. Kim, K. Kim, N. Lakshminarayan, and J. Yi, "Optimized surface passivation of n and p type silicon wafers using hydrogenated SiNx layers," *Journal of Non-Crystalline Solids*, vol. 356, no. 50-51, pp. 2880–2883, Nov. 2010, ISSN: 00223093. DOI: 10.1016/j.jnoncrysol.2010.09.025.

[170] V. N. Kruchinin, T. V. Perevalov, G. N. Kamaev, S. V. Rykhlitskii, and V. A. Gritsenko, "Optical Properties of Nonstoichiometric Silicon Oxide SiOx (x ¡ 2)," *Optics and Spectroscopy*, vol. 127, no. 5, pp. 836–840, Nov. 2019, ISSN: 1562-6911. DOI: 10.1134/S0030400X19110183.

[171] X. Y. Chen, Y. F. Lu, L. J. Tang, Y. H. Wu, B. J. Cho, X. J. Xu, J. R. Dong, and W. D. Song, "Annealing and oxidation of silicon oxide films prepared by plasma-enhanced chemical vapor deposition," *Journal of Applied Physics*, vol. 97, no. 1, p. 014 913, Dec. 2004, ISSN: 0021-8979. DOI: 10.1063/1.1829789.

[172] J. J. Low, M. L. Kreider, D. P. Pulsifer, A. S. Jones, and T. Gilani, "Band Gap Energy in Silicon," *American Journal of Undergraduate Research*, vol. 7, Jun. 2008. DOI: 10.33697/ajur.2008.010.

[173] R. A. Street, *Hydrogenated amorphous silicon*, New ed, ser. Cambridge solid state science series. Cambridge u.a: Cambridge Univ. Press, 2005, OCLC: 845372037, ISBN: 978-0-521-01934-7.

[174] K. Williams and R. Muller, "Etch rates for micromachining processing," *Microelectromechanical Systems, Journal of*, vol. 5, pp. 256–269, Jan. 1997. DOI: 10.1109/84.546406.

[175] D. J. Monk, D. S. Soane, and R. T. Howe, "A review of the chemical reaction mechanism and kinetics for hydrofluoric acid etching of silicon dioxide for surface micromachining applications," *Thin Solid Films*, vol. 232, no. 1, pp. 1–12, Sep. 1993, ISSN: 00406090. DOI: 10.1016/0040-6090(93)90752-B.

[176] K. W. Kolasinski, "The Composition of Fluoride Solutions," *Journal of The Electrochemical Society*, vol. 152, no. 9, J99, 2005, ISSN: 00134651. DOI: 10.1149/1.1952787.

[177] H. Kikuyama, M. Waki, I. Kawanabe, M. Miyashita, T. Yabune, N. Miki, J. Takano, and T. Ohmi, "Etching Rate and Mechanism of Doped Oxide in Buffered Hydrogen Fluoride Solution," *Journal of The Electrochemical Society*, vol. 139, no. 8, pp. 2239–2243, Jan. 1992, ISSN: 0013-4651, 1945-7111. DOI: 10.1149/1.2221208.

[178] J. S. Judge, "A Study of the Dissolution of SiO2 in Acidic Fluoride Solutions," *Journal of The Electrochemical Society*, vol. 118, no. 11, pp. 1772–1775, Jan. 1971, ISSN: 0013-4651, 1945-7111. DOI: 10.1149/1.2407835.

[179] P. Allongue, V. Kieling, and H. Gerischer, "Etching mechanism and atomic structure of H-Si(111) surfaces prepared in NH4F," *Electrochimica Acta*, vol. 40, no. 10, pp. 1353–1360, Jul. 1995, ISSN: 00134686. DOI: 10.1016/0013-4686(95)00071-L.

[180] V. F. Lvovich, *Impedance spectroscopy: applications to electrochemical and dielectric phenomena*. Hoboken, N.J: Wiley, 2012, OCLC: ocn668195856, ISBN: 978-0-470-62778-5.

[181] M. Hecini, A. Khelifa, B. Palahouane, S. Aoudj, and H. Hamitouche, "A new advance in the study of p-type silicon/electrolyte interface by electrochemical impedance spectroscopy," *Research on Chemical Intermediates*, vol. 41, Jan. 2013. DOI: 10.1007/s11164-013-1195-z.

[182] E. Mahé, F. Rouelle, I. Darolles, and D. Devilliers, "Electrochemical characterization of silicon electrodes: Part 1: Capacitance-Voltage Method," *J. New Mat. Electrochem. Sys.*, vol. 9, no. 3, p. 257, 2006. [Online]. Available: https://hal.archives-ouvertes.fr/hal-00163656.

[183] T. Longjuan, Z. Yinfang, Y. Jinling, L. Yan, Z. Wei, X. Jing, L. Yunfei, and Y. Fuhua, "Dependence of wet etch rate on deposition, annealing conditions and etchants for PECVD silicon nitride film," *Journal of Semiconductors*, vol. 30, no. 9, p. 096 005, Sep. 2009, ISSN: 1674-4926. DOI: 10.1088/1674-4926/30/9/096005.

[184] E. A. Taft, "Characterization of Silicon Nitride Films," *Journal of The Electrochemical Society*, vol. 118, no. 8, p. 1341, 1971, ISSN: 00134651. DOI: 10.1149/1.2408318.

[185] V. K. Rathi, M. Gupta, and O. P. Agnihotri, "The dependence of etch rate of photo-CVD silicon nitride films on NH4f content in buffered HF," *Microelectronics Journal*, vol. 26, no. 6, pp. 563–567, Sep. 1995, ISSN: 0026-2692. DOI: 10.1016/0026-2692(95)00017-C.

[186] C. A. Deckert, "Etching of CVD Si3 N 4 in Acidic Fluoride Media," *Journal of The Electrochemical Society*, vol. 125, no. 2, pp. 320–323, Jan. 1978, ISSN: 0013-4651, 1945-7111. DOI: 10.1149/1.2131436.

[187] L.-H. Liu, D. J. Michalak, T. P. Chopra, S. P. Pujari, W. Cabrera, D. Dick, J.-F. Veyan, R. Hourani, M. D. Halls, H. Zuilhof, and Y. J. Chabal, "Surface etching, chemical modification and characterization of silicon nitride and silicon oxide—selective functionalization of Si_3N_4 and SiO_2," *Journal of Physics: Condensed Matter*, vol. 28, no. 9, p. 094 014, Mar. 2016, ISSN: 0953-8984, 1361-648X. DOI: 10.1088/0953-8984/28/9/094014.

[188] M. Brunet, D. Aureau, P. Chantraine, F. Guillemot, A. Etcheberry, A. C. Gouget-Laemmel, and F. Ozanam, "Etching and Chemical Control of the Silicon Nitride Surface," *ACS Applied Materials & Interfaces*, vol. 9, no. 3, pp. 3075–3084, Jan. 2017, ISSN: 1944-8244. DOI: 10.1021/acsami.6b12880.

[189] *Standard Solar Spectra — PVEducation*. [Online]. Available: https://www.pveducation.org/pvcdrom/appendices/standard-solar-spectra.

[190] K. Williams, K. Gupta, and M. Wasilik, "Etch rates for micromachining processing-part II," *Journal of Microelectromechanical Systems*, vol. 12, no. 6, pp. 761–778, Dec. 2003, ISSN: 1057-7157. DOI: 10.1109/JMEMS.2003.820936.

[191] P. Gorostiza, P. Allongue, R. Díaz, J. R. Morante, and F. Sanz, "Electrochemical Characterization of the Open-Circuit Deposition of Platinum on Silicon from Fluoride Solutions," *The Journal of Physical Chemistry B*, vol. 107, no. 26, pp. 6454–6461, Jul. 2003, ISSN: 1520-6106, 1520-5207. DOI: 10.1021/jp030071v.

[192] A. Pimpinelli and J. Villain, *Physics of Crystal Growth*, 1st ed. Cambridge University Press, Dec. 1998, ISBN: 978-0-521-55198-4 978-0-521-55855-6 978-0-511-62252-6. DOI: 10.1017/CBO9780511622526.

[193] S.-H. Huh, S.-H. Choi, A.-S. Shin, S.-J. Ham, S. Moon, and H.-J. Lee, "Nucleation and Growth Behaviors of Pd Catalyst and Electroless Ni Deposition on Cu (111) Surface," *Journal of The Electrochemical Society*, vol. 163, no. 2, pp. D49–D53, Jan. 2016, ISSN: 0013-4651, 1945-7111. DOI: 10.1149/2.0641602jes.

[194] K. Hermann, *Crystallography and surface structure: an introduction for surface scientists and nanoscientists*. Weinheim, Germany: Wiley-VCH, 2011, OCLC: ocn664325855, ISBN: 978-3-527-41012-5.

[195] W.-p. Wu and J.-j. Jiang, "Effect of plating temperature on electroless amorphous Ni–P film on Si wafers in an alkaline bath solution," *Applied Nanoscience*, vol. 7, no. 6, pp. 325–333, Aug. 2017, ISSN: 2190-5509, 2190-5517. DOI: 10.1007/s13204-017-0575-x.

[196] F. A. Harraz, J. Sasano, T. Sakka, and Y. H. Ogata, "Different Behavior in Immersion Plating of Nickel on Porous Silicon from Acidic and Alkaline Fluoride Media," *Journal of The Electrochemical Society*, vol. 150, no. 5, p. C277, 2003, ISSN: 00134651. DOI: 10.1149/1.1562595.

[197] Y. Ogata, K. Kobayashi, and M. Motoyama, "Electrochemical metal deposition on silicon," *Current Opinion in Solid State and Materials Science*, vol. 10, no. 3-4, pp. 163–172, Jun. 2006, ISSN: 13590286. DOI: 10.1016/j.cossms.2007.02.001.

[198] M. C. Raval and C. S. Solanki, *Review of Ni-Cu Based Front Side Metallization for c-Si Solar Cells*, Research article, 2013. DOI: 10.1155/2013/183812.

[199] Y. B. Amor, I. Frateur, P. Mat, and M. Boualam, "Dépôt chimique de nickel : Synthèse bibliographique," *Matériaux & Techniques*, vol. 102, no. 1, p. 101, 2014, ISSN: 0032-6895, 1778-3771. DOI: 10.1051/mattech/2014004.

[200] G. Hu, H. Wu, and F. Yang, "Direct electroless nickel plating on silicon surface," *Chinese Science Bulletin*, vol. 49, no. 22, pp. 2363–2367, Nov. 2004, ISSN: 1001-6538, 1861-9541. DOI: 10.1007/BF03183423.

[201] K.-C. Lai, P.-Y. Wu, C.-M. Chen, T.-C. Wei, C.-H. Wu, and S.-P. Feng, "Interfacial Characterizations of a Nickel-Phosphorus Layer Electrolessly Deposited on a Silane Compound-Modified Silicon Wafer Under Thermal Annealing," *Journal of Electronic Materials*, vol. 45, no. 10, pp. 4813–4822, Oct. 2016, ISSN: 0361-5235, 1543-186X. DOI: 10.1007/s11664-016-4708-x.

[202] S. Zamani Javid, "Copper Diffusion through Plated Nickel Barrier Layers for Laser-Doped Selective-Emitter Silicon Solar Cells," PhD thesis, University of New South Wale, Sydney, Australia, 2012.

[203] Seok-Hwan Huh, Sung-Ho Choi, An-Seob Shin, Gi-Ho Jeong, Suk-Jin Ham, and Keun-Soo Kim, "Characterization of the surface morphology of electroless NiP deposited on conductive Cu film," *Circuit World*, vol. 41, no. 4, pp. 137–146, Nov. 2015, ISSN: 0305-6120. DOI: 10.1108/CW-01-2015-0003.

[204] H. Philipsen, H. Jehoul, F. Inoue, K. Vandersmissen, L. Yang, H. Struyf, and D. Van Dorp, "Nucleation and growth kinetics of electrodeposited Ni films on Si(100) surfaces," *Electrochemical acta*, vol. 230, pp. 407–417, 2017. DOI: 10.1016/j.electacta.2017.02.010.

[205] E. Delbos, D. Aureau, H. E. Belghiti, J. Vigneron, M. Bouttemy, and A. Etcheberry, "Localised metallisation process for silicon solar cells," *physica status solidi (c)*, vol. 12, no. 12, pp. 1427–1432, Dec. 2015, ISSN: 1610-1642. DOI: 10.1002/pssc.201510106.

[206] D. Levy, A. Grob, J. J. Grob, and J. P. Ponpon, "Formation of palladium silicide by rapid thermal annealing," *Applied Physics A Solids and Surfaces*, vol. 35, no. 3, pp. 141–144, Nov. 1984, ISSN: 0721-7250, 1432-0630. DOI: 10.1007/BF00616966.

[207] B. Inkson, "Scanning electron microscopy (SEM) and transmission electron microscopy (TEM) for materials characterization," in *Materials Characterization Using Nondestructive Evaluation (NDE) Methods*, Elsevier, 2016, pp. 17–43, ISBN: 978-0-08-100040-3. DOI: 10.1016/B978-0-08-100040-3.00002-X.

[208] A. Razdan, K. Patel, G. E. Farin, and D. G. Capco, "Volume visualization of multicolor laser confocal microscope data," *Computers & Graphics*, vol. 25, no. 3, pp. 371–382, Jun. 2001, ISSN: 00978493. DOI: 10.1016/S0097-8493(01)00061-9.

[209] *Department of Chemistry and Biochemistry – University of Maryland, College Park MD Surface Analysis Center - Department of Chemistry and Biochemistry - University of Maryland, College Park MD*. [Online]. Available: http://www.chem.umd.edu/sharedinstrumentation/surface-analysis-center,%20http://www.chem.umd.edu/sharedinstrumentation/surface-analysis-center.

[210] C. Thomsen, J. Strait, Z. Vardeny, H. J. Maris, J. Tauc, and J. J. Hauser, "Coherent Phonon Generation and Detection by Picosecond Light Pulses," *Physical Review Letters*, vol. 53, no. 10, pp. 989–992, Sep. 1984, ISSN: 0031-9007. DOI: 10.1103/PhysRevLett.53.989.

[211] C. Thomsen, H. T. Grahn, H. J. Maris, and J. Tauc, "Surface generation and detection of phonons by picosecond light pulses," *Physical Review B*, vol. 34, no. 6, pp. 4129–4138, Sep. 1986, ISSN: 0163-1829. DOI: 10.1103/PhysRevB.34.4129.

[212] A. Devos, "Colored ultrafast acoustics: From fundamentals to applications," *Ultrasonics*, vol. 56, pp. 90–97, Feb. 2015, ISSN: 0041624X. DOI: 10.1016/j.ultras.2014.02.009.

[213] P. Emery, D. G. Seiler, A. C. Diebold, R. McDonald, A. Chabli, and E. M. Secula, "Thin Films Mechanical Characterization Using Colored Picosecond Acoustics," Grenoble (France), 2011, pp. 176–179. DOI: 10.1063/1.3657886.

[214] F. Casset, "Caractérisation par acoustique picoseconde des propriétés mécaniques du PZT déposé en couches minces pour des applications MEMS," thesis, Lille 1, Jun. 2014. [Online]. Available: http://www.theses.fr/2014LIL10040.

[215] A. Devos and P. Emery, "Thin-film adhesion characterization by Colored Picosecond Acoustics," *Surface and Coatings Technology*, vol. 352, pp. 406–410, Oct. 2018, ISSN: 02578972. DOI: 10.1016/j.surfcoat.2018.07.097.

université PARIS-SACLAY
ÉCOLE DOCTORALE
Interfaces:
matériaux, systèmes, usages

Titre : Compréhension des mécanismes réactionnels des procédés de métallisation électrochimique utilisés pour les cellules solaires en silicium.

Mots clés : Silicium, Photovoltaïque, Ablation laser, Métallisation électrochimique, Bifacial, Interfaces.

Résumé : Pour ce travail de thèse, la métallisation électrochimique de Ni/Cu (« plating ») est étudié en tant qu'alternative à la sérigraphie à base de pâtes d'Ag et Al pour métalliser les cellules solaires en silicium. Cette technique a le potentiel d'améliorer la qualité des contacts métalliques et d'augmenter l'efficacité des cellules solaires en silicium. Les métaux utilisés étant moins coûteux, une diminution des coûts de production est envisageable. Cependant, le plating Ni/Cu doit être amélioré pour une application industrielle dans le domaine photovoltaïque.
L'objectif de cette thèse est d'étudier les différentes étapes du procédé de plating Ni/Cu sur des cellules solaires n-PERT bifaciales afin de comprendre les mécanismes physicochimiques impliqués et résoudre les différents problèmes relatifs à cette technique.
La première étape, qui consiste à ouvrir selectivement les couches diélectriques par ablation laser, a été optimisée en choisissant des paramètres limitant l'endommagement du silicium sous-jacent. Un mécanisme d'ablation a également été proposé. La désoxydation et l'activation au palladium du silicium, ont été étudiés dans deux milieux fluorés (HF et $NaHF_2$). De meilleurs résultats en terme de gravure du SiO_x et d'activation ont été obtenus avec $NaHF_2$. L'inhomogénité du dépôt de nickel a soulignée l'importance de réaliser ce dépôt à l'obscurité. Une mauvaise adhérence sur surface polie a été observée et des axes d'amélioration ont été proposés. L'impact de paramètres de recuit non adaptés sur le rendement des cellules a été étudié. Un procédé de plating Ni/Cu optimisé a été developpé et des rendements similaires aux références sérigraphiées ont été obtenus.

Title: Understanding reaction mechanisms of electrochemical metallization processes used for silicon photovoltaic cells.

Keywords: Silicon, Photovoltaic, Laser ablation, Electrochemical metallization, Bifacial, Interfaces.

Abstract: In this thesis, Ni/Cu electrochemical metallization ("plating") is studied as an alternative to mainstream screen-printing technique based on Ag and Al metallic pastes to produce industrial c-Si solar cells. Ni/Cu plating has the potential to improve the quality of metallic contacts and increase c-Si solar cell efficiency. The use of cheaper metals is a strong asset to reduce the production costs. However, Ni/Cu plating is still at an introductory phase and there are some issues to deal with.
The goal of this thesis is to investigate the successive steps of Ni/Cu plating process for bifacial n-PERT c-Si solar cells and understand the physico-chemical phenomena involved to address the related issues.
As a first step, laser ablation parameters have been optimized to selectively ablate the dielectric layers while limiting the impact on the underlying Si. An ablation mechanism has also been proposed. Next steps of deoxidation and Pd activation of Si surface have been studied in two fluoride media (HF and $NaHF_2$). $NaHF_2$ provided higher SiO_x etching rates and better Si surface activation. Next, homogeneity issues of Ni electroless deposition have been found, highlighting the need to make the deposition in the dark. Poor adherence on a polished surface has been observed and areas of improvement have been suggested. The impact of non-optimized annealing parameters on cells conversion efficiencies has been demonstrated. The Ni/Cu plating process has been improved and similar efficiencies than those of screen-printed reference cells have been achieved.

Université Paris-Saclay
Espace Technologique / Immeuble Discovery
Route de l'Orme aux Merisiers RD 128 / 91190 Saint-Aubin, France